SEISMIC RETROFIT AND REPAIR OF REINFORCED CONCRETE BRIDGE COLUMNS USING SHAPE MEMORY ALLOY SPIRALS

BY

MOOCHUL SHIN

DISSERTATION

Submitted in partial fulfillment of the requirements
for the degree of Doctor of Philosophy in Civil Engineering
in the Graduate College of the
University of Illinois at Urbana-Champaign, 2012

Urbana, Illinois

Doctoral Committee:

Assistant Professor Bassem Andrawes, Chair and Director of Research
Professor Amr S. Elnashai
Professor Glaucio H. Paulino
Associate Professor John S. Popovics

ABSTRACT

This research focuses on examining the use of shape memory alloy (SMA) spirals in the seismic retrofitting and repair of reinforced concrete (RC) bridge columns. The thermally triggered recovery stress of prestrained SMA spirals is utilized to apply large active confinement pressure at the column's plastic hinge zone to enhance the flexural ductility of vulnerable columns and limit their post-earthquake damage. Although research has proven that concrete active confinement is a more superior technique to passive confinement, its field application using conventional materials is hindered due to several complications related to the method of application. This research focuses on investigating the new concrete active confinement technique using SMA spirals numerically and experimentally, which is rapid, robust and simple. The research work comprises of: 1) Performing numerical analysis on RC columns retrofitted using SMA spirals (active confinement) and Fiber Reinforced Polymer (FRP) wraps (passive confinement) to examine the superiority of the suggested new confinement technique over current confinement techniques, 2) Investigating experimentally the thermo-mechanical behavior of NiTiNb SMA which is used for this research, 3) Testing concrete cylinders wrapped with SMA spirals and Glass-FRP (GFRP) wraps, 4) Conducting quasi-static lateral cyclic tests on four 1/3-scale RC columns retrofitted with SMA spirals and GFRP wraps, 5) Conducting quasi-static lateral cyclic tests on two severely damaged columns that were repaired using SMA spirals as an emergency repair technique, 6) Utilizing the experimental results of the tested columns to develop and validate numerical models for RC columns retrofitted with SMA spirals, and 7) Utilizing the validated

models to conduct a comprehensive parametric study on columns retrofitted with SMA spirals. The results of this experimental and numerical work clearly illustrate that using thermally prestressed SMA spirals to apply external active confinement pressure on concrete columns is an effective, simple, robust, and rapid approach to improve the performance of RC bridge columns.

To My Family

ACKNOWLEDGMENTS

I owe my deepest gratitude to those who have supported me as I completed this thesis. Without their help, this thesis would not have been possible. First of all, it is with great pleasure that I give many thanks to my advisor, Professor Bassem Andrawes. While working with him, I have learned invaluable things that I could not learn elsewhere: passion, enthusiasm, pioneering spirit as well as knowledge and wisdom. He has tremendously contributed to my development as an engineer and researcher along my Ph.D journey. I want to thank my thesis committee members, Professor Amr Elnashai, Professor Glaucio Paulino, and Professor John Popovics for their time and input. I also cannot forget Professor Taehyo Park who encouraged me to be a good scholar and I owe a great debt to him.

In so many ways, Dr. Grezgorz Banas assisted me to conduct the successful experimental testing including material testing and column testing. He is a truly part of the success of this research. And also, without the help of my fellow graduate students, namely, Pablo Caiza, Nick Wierschem, and Yong-Wan Kim, preparing and conducting the testing could not have been completed.

When looking back on my Ph.D journey in Champaign-Urbana, I owe a great deal of thanks to numerous friends. Among them, I would like to thank my roommates: Daniel Kim, Josh Tice, Paul Toh, Joseph Choi, and Elijah Kim. They have helped me to exercise to stay strong when I was exhausted and have prayed for me to do well. I owe a particular debt of gratitude to my brothers and sisters in Christ who prayed for me to finish this journey by faith. Some of them are from the U of I ministry, some from Hanyang, and some from Toledo, and I especially thank Dr. Samuel A. Lee who has helped me to see

the words of God every week for the last six years. Additionally, I want to thank Jeremiah Cowen, Jeremiah Park, Ryan Boyd, Robin Kim, Abraham Jeon, Yunho, David and many U of I students who have studied the Bible together with me. Also, I would like to thank all the members of Korean Students Association in Civil and Environmental Engineering. Especially, I am grateful to those who helped me to adjust to Champaign-Urbana when I got here in 2006. Without their friendship and practical help from Dr. Kyu-Sik Park's family and Professor Kyoungsoo Park's family, I cannot imagine what I would have gone through when I did not know much about the life in Champaign. My gratitude is extended to Seung Jae Lee, Jaehyuk Kwack, Young Joo Lee, Do Soo Moon, Hongki Jo, Sungwoo Moon, Byungmin Kim, Robin Kim, Fernando Moreu, Hyungchul Yoon as well as many others that have shared their joy of life here. Furthermore, I thank Professor Sung-Han Sim who made my life in Champaign more fun and joyful while we were exercising together, sharing meals, and talking about many things in life.

To my beloved family members, parents, and sister: at this moment I can say only one thing, "We are family, and I love you all." You make me realize how important family is. To my wife, Haemin Lee: without your love, and unconditional support and prayers, it would have been impossible to complete this journey. You make me grow as a man, and you are the source of my joy and life.

Most importantly, I would like to thank my LORD who has guided and supported me in every way of my life. He has helped me to grow as his son, and there is no single word to express my heart to him. He is my Savior, and I am his son.

This study was supported in part by the National Cooperative Highway Research Program through its Innovations Deserving Exploratory Analysis project (NCHRP-IDEA) under project no. 135.

TABLE OF CONTENTS

LIST OF FIGURES

LIST OF TABLES

CHAPTER 1 INTRODUCTION

1.1 PROBLEM DESCRIPTION

Insuring the resilience of lifeline infrastructures against high seismic events in highly populated areas is of high priority in any seismic design and mitigation plan. Bridges are among the most critical elements in any transportation infrastructure network. Therefore, a large number of studies focus on identifying the main causes of the collapse of bridges during earthquakes. These studies showed that many of the bridge failures that occurred during past earthquakes were due to the collapse of one or more of the bridge reinforced concrete (RC) columns or piers. Several historic earthquakes have shed light on the problems of old bridge seismic design provisions that were developed based on the elastic seismic design concept (prior to 1971). Research studies have shown that the main factors causing the failures of RC columns are their insufficient flexural ductility and/or inadequate shear capacity (Chai et al. 1991; Priestley et al. 1994a,b; Maekawa and An 2000; fib 2007 among others). Lack of concrete confinement due to the use of insufficient transverse reinforcement and the use of insufficient lap splice length at the plastic hinge region of the columns had been identified as the main reasons for the poor flexural ductility and/or insufficient shear capacity observed in many of the collapsed bridge columns (Priestley and Seible 1995; Haroun and Elsanadedy 2005; fib 2007).

A common approach that is currently used to address the issue of poorly designed RC columns is by providing additional (external) confinement for the concrete at the potential plastic hinge region of the columns. This could be conducted through the use of either concrete, steel, or fiber reinforced polymer (FRP) jackets. Confinement methods

could be divided into two main types: 1) Passive confinement and 2) Active confinement. Previous studies have demonstrated that under the same confinement pressure, active confinement approach is superior to passive confinement in terms of increasing the concrete strength and ultimate strain (Richart et al. 1928 & 1929). A key factor behind such superiority is the delay in the damage sustained by the concrete as a result of the early application of confinement pressure in the case of active confinement; while in the case of passive confinement, the concrete would have to deform laterally (i.e. dilate) in order for the confinement pressure to be fully activated.

The superiority of active confinement to passive confinement motivated several researchers to investigate it analytically and experimentally. Although the methodology for the application of active confinement pressure varied in each study, most of them attempted to use prestressed steel strands or FRP bands. Using such conventional methods to apply active confinement resulted in many practical problems related to the excessive use of mechanical hardware, labor, and time to apply moderate confinement pressures in the field (Saatcioglu and Yalcin 2003; Nesheli and Meguro 2006). For these practical reasons and despite the advantages associated with using active confinement, its widespread application has been hindered, and conventional passive confinement using steel or FRP jackets has become more popular. To allow active confinement to reach its full potential, there is a dire need for a simple, practical, and robust method that could be used for applying active confinement easily in the field.

1.2 SCOPE OF RESEARCH

This research focuses on studying and testing a new method for applying active confinement using Shape Memory Alloys (SMAs). SMAs are a class of metallic alloys that exhibit unique capability of recovering their original (undeformed) shape after being excessively deformed. The shape recovery could be attained by heating the alloy to a temperature above the transformation temperature, A_f, which is a material property of the alloy predetermined by the user/manufacturer. What makes the shape recovery phenomenon appealing is the induction of large recovery stress in the SMAs when the prestrained alloy is heated while restrained. This thesis will present an investigation on the feasibility and features of using the thermally induced recovery stress as an innovative means for performing seismic retrofit or repair of vulnerable or damaged RC bridge columns. The research uses thermally prestressed SMA spirals as external supplementary reinforcement for the retrofitted or repaired columns. The recovery stress is utilized to exert active confinement pressure externally on the columns at the location where confinement is needed the most (i.e. plastic hinge zone). The ease of installation and prestressing (using temperature) provides SMA spirals with an advantage over steel strands and FRP straps in terms of eliminating the need for excessive use of mechanical devices to apply the prestressing force and limiting the labor and time needed for on-site installation.

This dissertation will present experimental results related to the new technique and its effectiveness in increasing the flexural ductility and drift capacity of retrofitted and repaired columns compared to conventional retrofit techniques. The experimental results will then be utilized to develop and validate numerical models for RC bridge

columns retrofitted using the proposed SMA spirals. The validated models will be used in a series of advanced nonlinear analyses using the finite element program OpenSees. To further investigate the efficacy of the proposed technique under cyclic loading, extensive parametric study is conducted to provide practical information that is useful in setting a design guideline for retrofitted bridge columns.

1.3 DISSERTATION OUTLINE

The contents of this dissertation consist of the following:

Chapter 2: An overview of the problems of the insufficient flexural ductility and/or inadequate shear capacity of RC bridge columns during past earthquakes is presented. An overview of past studies of retrofitting and repair techniques on RC columns is also presented.

Chapter 3: The concept behind the new active confinement technique using SMA spirals is discussed, and details are presented on the thermo-mechanical characteristics of SMAs in general, and the NiTiNb alloy in particular, which is utilized in this research.

Chapter 4: The effectiveness of the new active confinement technique is first proved analytically. Numerical models of RC columns confined using FRP jackets and SMA spirals are developed, analyzed, and their cyclic and seismic behaviors are compared.

Chapter 5: Material tests conducted on SMA wires and concrete cylinders confined with active and/or passive confinement techniques are described and the testing results are presented.

Chapter 6: Details and results of the lateral cyclic experimental tests conducted on reduced-scale RC columns retrofitted with SMA spirals and Glass-FRP (GFRP) sheets are discussed.

Chapter 7: An emergency repair technique using SMA spirals is proposed for severely damaged RC columns. Experimental test results of two repaired columns are presented.

Chapter 8: A simplified modeling methods for RC columns retrofitted with SMA spirals is presented and validated using the experimental test data presented in chapter 6.

Chapter 9: The modeling technique proposed in Chapter 8 is used to conduct an extensive parametric study to investigate the impact of various design and geometric parameters on the cyclic behavior of RC columns retrofitted with SMA spirals.

Chapter 10: Conclusions and recommendations for future work are presented.

CHAPTER 2 LITERATURE REVIEW

2.1 OLD SEISMIC DESIGN CRITERIA

Bridge columns designed before the 1971 San Fernando earthquake typically contain very little transverse reinforcement. This is mainly attributed to the application of elastic design philosophy. A common detail for both circular and rectangular columns consisted of 12.7 mm (0.5 in) dia. (No. 4) transverse hoops at 305mm (12 in.) regardless of the column size and area of the main reinforcement (AASHO, 1969). This reinforcement resulted in many cases in a very low transverse reinforcement ratio (approx. 0.2% or less), especially for columns with larger diameters. This led to the unsatisfactory flexural and shear behaviors and the catastrophic collapse of many of these columns during past earthquakes. The following section provides an overview of the performance of bridge columns/piers during major historic earthquakes.

2.2 PERFORMANCE OF BRIDGE COLUMNS DURING PAST EARTHQUAKES

2.2.1 1971 San Fernando earthquake

This earthquake with a moment magnitude of 6.6 occurred on February 9, 1971 near Sylmar, California causing significant damages and casualties. The earthquake resulted in the death of 65 people and the damage and collapse of several bridge structures. The total cost of the damage resulted from the earthquake was estimated to be 500 million dollars (Jennings et al., 1971). One of the main reasons for bridge failures was the excessive damage sustained by the bridges RC columns. Figure 2.1 shows a

picture of a damaged column on Interstates 5 and 14. Due to inadequate transverse reinforcement, the developed plastic hinge at the column was severely damaged leading to the fracture of the transverse reinforcement, buckling of the longitudinal reinforcement and crushing of cover and core concrete.

Figure 2.1 Damaged RC column on Interstates 5 and 14 during the San Fernando earthquake, 1971 (USGS, 2006a).

2.2.2 1989 Loma Prieta earthquake

The Loma Prieta earthquake which occurred on October 17, 1989 with a moment magnitude of 6.9 was one of the most notorious earthquakes that caused severe damages to the transportation network in California. This devastating event resulted in 63 deaths, 12,000 damaged homes, 40 collapsed buildings, and damage to two major bridges. Among these bridges is the Cypress Street Viaduct of Interstate 880 in West Oakland which experienced several failures that resulted in the deaths of 42 people. Figure 2.2 shows picture of the damage sustained by the RC columns and the collapse of the Cypress viaduct of Interstate 880. The viaduct was built on 1950 with insufficient transverse reinforcement, which was deemed as one of the main reasons for RC columns' failures.

Figure 2.2 Failures of RC columns and collapsed upper deck on the Cypress viaduct of Interstate 880 (USGS, 2006b).

2.2.3 1994 Northridge earthquake

The main shock of this 6.7 moment magnitude earthquake struck in Northridge, California near the city of Los Angeles and lasted for about 45 seconds. The ground accelerations measured during this earthquake were among the highest that were ever recorded in the United States. The estimated damage cost was $20 billion, which was almost 40 times the damage cost of the 1971 San Fernando earthquake. It was reported that at least 72 people got killed during the earthquake. The failures and collapses on bridges, highways, and the main transportation networks were observed on the interchange of Interstate 5 with California State Route 14, Interstate 10, and California State Route 118. Figure 2.3 is one example of the failed RC columns under the Simi Valley Freeway at the north end of the San Fernando Valley. The plastic hinges were formed at the base of the damaged columns, and it should be noted that the low level of transverse reinforcement was the primary reason for the severe damage sustained by these hinges.

Figure 2.3 Failed RC columns under the Simi Valley Freeway as a result of the 1994 Northridge earthquake (Southern California Earthquake Data Center, 2011).

2.2.4 1995 Kobe earthquake, Japan

The Kobe earthquake struck the area of Kobe and Osaka, Japan on Tuesday, January 17, 1995. The earthquake magnitude was reported as 6.8 on the moment magnitude scale (USGS, 2010). This earthquake was one of the most devastating seismic events that occurred in highly populated and industrialized areas. Almost 55,000 deaths and 35,000 injuries were reported, while several important highways either sustained severe damage or collapsed entirely. Figure 2.4 shows one exemplary picture of the severely damaged expressway due to the collapse of the support RC columns. The damage of the columns which led to their failure was localized at the base due to the lack of sufficient transverse reinforcement at this critical region (Kawashima, 2009)

Figure 2.4 Severely damaged Hanshin expressway due to the 1995 Kobe earthquake (Kawashima, 2009)

2.2.5 2004 Niigata-Ken Chuetsu earthquake, Japan

The Chuetsu earthquake occurred on Saturday, October 23, 2004 in Japan. The magnitude of the earthquake was recorded as 6.9 in moment magnitude. It was the first incident where the Shinkasen train (high-speed train) derailed in the history of Japan due to seismic activities. The earthquake's main shock along with the aftershocks brought the death toll to 40. Furthermore, several highways, houses, and buildings were destroyed (Shanmuganathan, 2005). The damage experienced in many cases was due to the lack of flexural ductility of RC columns. Figure 2.5 shows an example of the damaged RC column of Uonogawa Bullet Train Bridge as a result of the earthquake.

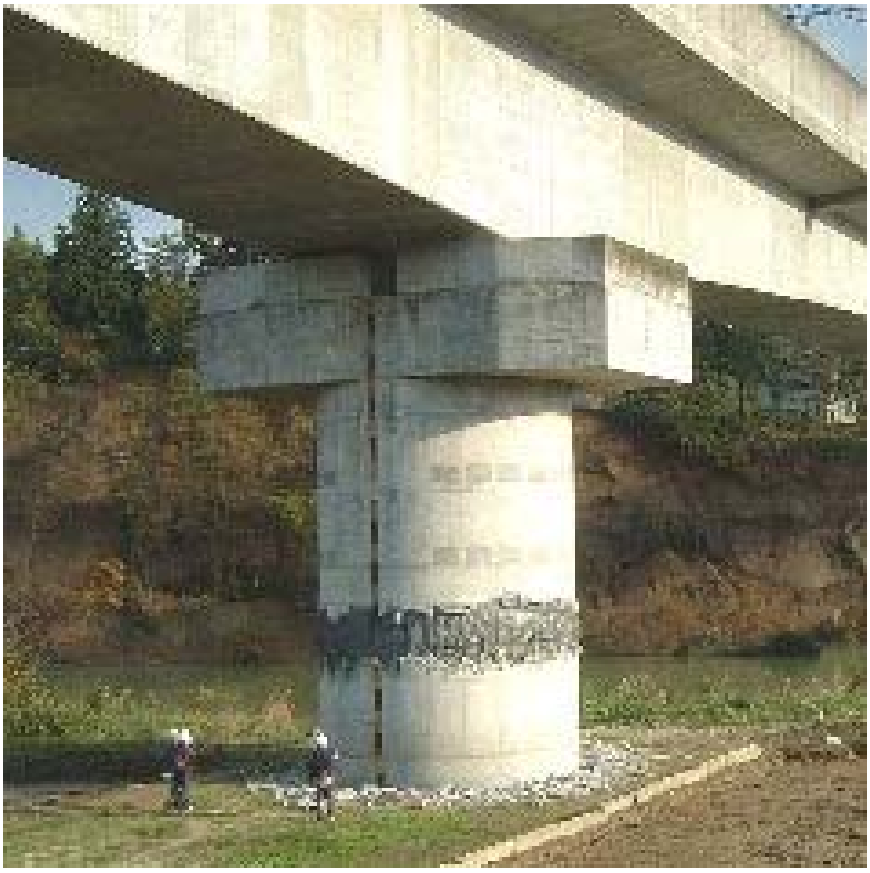

Figure 2.5 Damaged RC column of Uonogawa Bullet Train Bridge due to the 2004 Chuetsu earthquake in Japan (Shanmuganathan, 2005).

2.2.6 2010 Chile earthquake, Chile

On February 27, 2010, a moment magnitude 8.8 earthquake occurred off shore of the Biobio region of Chile. The earthquake was recorded as one of the top 10 largest earthquakes in history. Strong after-shocks whose magnitudes were greater than 5.0 also followed within an hour. The casualties were devastating, and USGS (2011) reported that at least 521 people were killed, 56 missing and about 12,000 injured. Damage of structures was also severe. Many houses, buildings, highways and bridges were damaged and some of them even collapsed. The Juan Pablo II bridge is an example of one of the damaged bridges. Earthquake Engineering Research Institute (EERI)/Pacific Earthquake

Engineering Research (Peer)/Federal Highway Administration (FHWA) bridge team reported that RC columns of the bridge showed shear failure due to insufficient transverse reinforcement (EERI et.al, 2010). Figure 2.6 shows an exemplary picture of the failed RC columns of the bridge.

Figure 2.6 Damaged RC columns of Juan Pable II bridge during 2010 Chile earthquake (EERI et.al, 2010).

2.3 RETROFIT TECHNIQUES

As illustrated in the previous section, past earthquakes have demonstrated the shortcomings of old bridge seismic design provisions (prior to 1971). Research studies have shown that the main factors causing the failures of RC columns are their insufficient flexural ductility and/or inadequate shear capacity (Chai et al. 1991; Priestley et al.

1994a,b; Maekawa and An 2000; fib 2007 among others). Lack of concrete confinement due to the use of insufficient transverse reinforcement and/or insufficient lap splice length at the plastic hinge region of the columns had been identified as the main reasons for the poor flexural ductility observed in many of the collapsed bridge columns (Priestley and Seible 1995; Haroun and Elsanadedy 2005; fib 2007).

The poor seismic performance of structures in the past brought the attention of engineers and researchers to the field of structural retrofitting. Among the most common retrofitting measures that are used to boost the ductility capacity of vulnerable bridge columns is providing additional confinement for the concrete by using external wraps or jackets. The concrete confinement techniques that have been applied to date can be categorized as: 1) Passive confinement and 2) Active confinement. Figure 2.7.a and b show schematics of cross sections of passively and actively confined concrete cylinders, respectively. The major difference between both techniques is the lateral confining pressure which is exerted on the section prior to axial loading in the case of active confinement. In the passive confinement technique the confining pressure is exerted only as a direct result of the lateral dilation of concrete. Hence, in order for the passive confinement technique to be fully engaged, the concrete has to undergo some sort of damage. However, the confining pressure is applied before concrete gets damage via the active confinement technique. Figure 2.7.c depicts typical stress versus volumetric strain behaviors of unconfined, passively confined, and actively confined concrete. The unconfined concrete experiences volumetric compaction in the elastic region, after which it starts expanding rapidly until reaching failure. Similarly, under axial stress, the volume

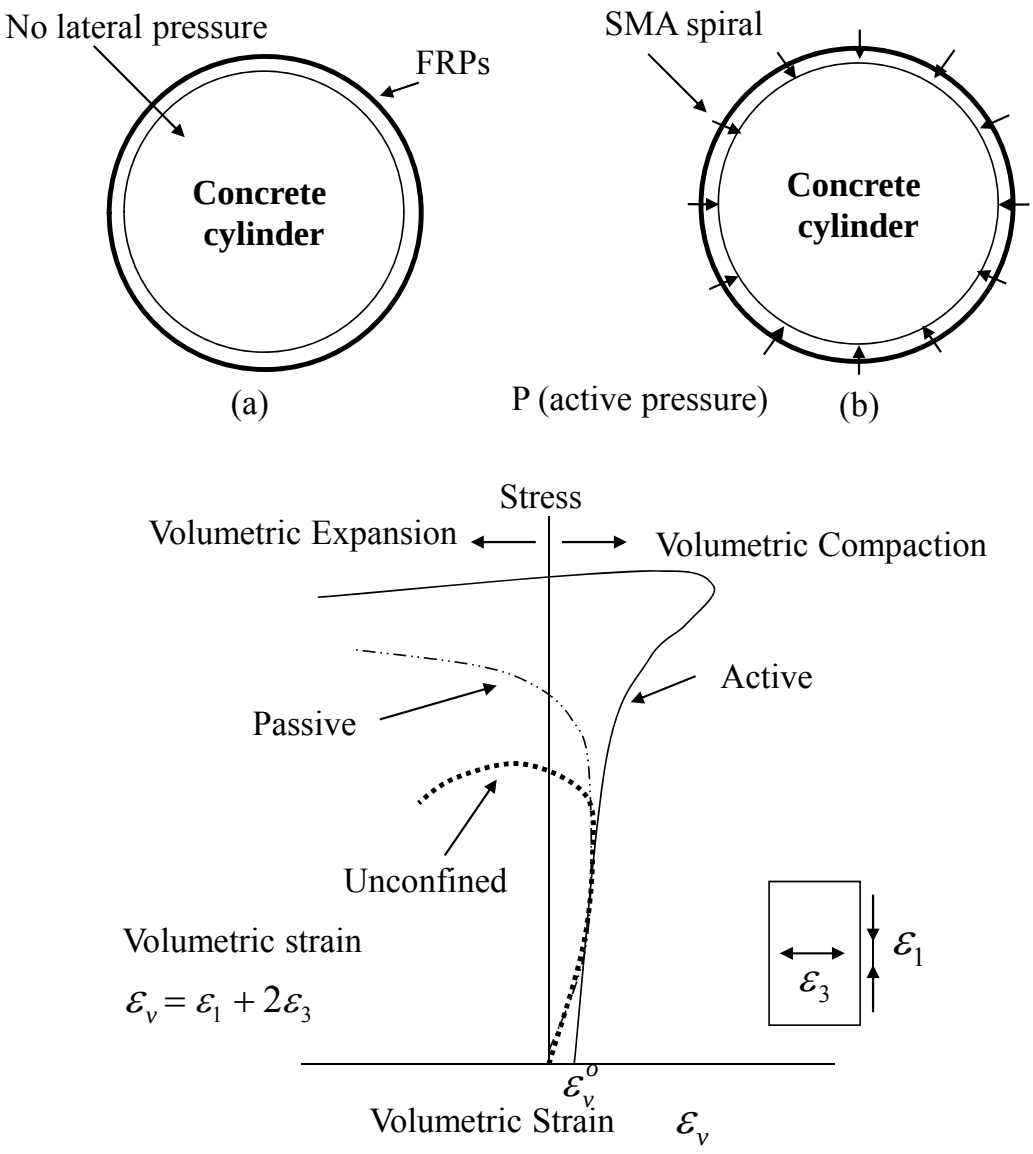

Figure 2.7 Schematics of the cross section of passively and actively confined concrete before loading (a and b) and stress vs. volumetric strain curves of unconfined, passively confined, and actively confined concrete (c).

of a passively confined concrete reduces in the elastic region and the passive confining pressure helps in delaying the point where the concrete starts expanding volumetrically.

In the active confinement case, the confining pressure which is applied as a prestress on the concrete element laterally prior to loading exerts an initial volumetric strain ε_v^o due to compaction. In order to overcome the effect of this strain, extra axial strain and stress are needed, and thus the failure point of the concrete is further delayed compared to the passively confined concrete.

2.3.1 Passive confinement techniques

During the past few decades, several passive confinement retrofit techniques have been developed, studied, and applied to enhance the strength and flexural ductility of vulnerable RC columns during earthquakes. In the following sub-sections, a background of two of the most commonly used passive confinement techniques is discussed, namely steel reinforcement/jackets and FRP wraps (Moehle 2000; fib 2003). Figure 2.8 shows pictures of two examples of RC columns confined with FRP wraps and steel jackets. RC columns of Sakawa-gawa bridge, Tomei Expressway in Japan were confined with Carbon FRP wraps (see Figure 2.8.a) and the columns of Metropolitan Expressway in Japan were confined with steel jackets (see Figure 2.8.b).

(a) (b)

Figure 2.8 Examples of passive confinement techniques: (a) using FRP wraps, (b) using steel jackets (fib 2003).

2.3.1.1 Steel Reinforcement/Jackets

One of the very early studies that focused on investigating the behavior of concrete passively confined with steel wire or bar reinforcement was conducted by Richart et al. (1929). In their early research, they concluded that using spiral reinforcement helped in increasing the strength of concrete columns. Later, Roy and Sozen (1964) studied experimentally the improvement in concrete ductility through confinement using internal ties. In 1971 Kent and Park (1971) suggested an analytical model for confined concrete with rectangular steel ties based on the data from Roy and

Sozen (1964). Park et al. (1982) later improved the Kent and Park analytical model by incorporating the effect of increased strength in confined concrete which was ignored in the earlier version of the model. Many studies also were conducted on full scale concrete columns reinforced with rectangular hoops (e.g. Vellenas et al. 1977, Sheikh and Uzumeri 1979). Scott et al. (1982) later suggested that the ultimate strain of confined concrete column with rectangular internal hoop is a function of the volumetric ratio and yielding stress of the hoops. Other researchers had also examined the effects of confinement using a spiral type of reinforcement, which was a common practice used in a circular column of a building or a bridge. Ahmad and Shah (1982) were among the researchers who examined the behavior of concrete cylinders confined with varying yielding strengths of steel spirals. They carried out some experiments and proposed a stress-strain relationship of confined concrete with the steel spirals. One of their conclusions was that the effectiveness of the confinement would be less when lightweight aggregates were used.

Among the most popular models is the one by Mander et al. (1988a) who proposed a general stress-strain curve of concrete confined with circular and rectangular hoops or spirals. In order to estimate the increased peak strength of the confined concrete, they adopted a yielding surface with five parameters based on the work of Willam and Warnke (1975). In their model, Mander et al. used the triaxial test data from Schickert and Winkler (1977). Also, an energy method was proposed to estimate the ultimate strain of the confined concrete with steel lateral reinforcement. Furthermore, in a following paper (Mander et al. 1988b), the authors conducted experimental studies to verify their analytical model through the testing of rectangular walls reinforced with ties, and circular

concrete columns reinforced with spirals. Later, Chang and Mander (1994) updated their analytical model of concrete confined with high strength lateral reinforcement, and studied the impact of high strength reinforcement on the post-peak softening behavior of the confined concrete. Also, Martinez-Rueda and Elnashai (1997) reviewed the concrete model proposed by Mander et al. (1988a), and improved the analytical concrete model by modifying the cyclic behavior of concrete. They proposed slightly different rules for cyclic degradation of strength, inelastic strain, and the shape of unloading branches. The improved concrete model was implemented into a nonlinear program utilizing a fiber element approach. The authors concluded that the model had high numerical stability, and it produced proper behaviors with RC members under flexural and axial loading conditions.

In addition to using internal steel reinforcement to provide confining effects on concrete, researchers have also studied the application of external steel in the form of jackets or shells. Priestly et al. (1994a, 1994b) studied theoretically and experimentally the retrofit of bridge columns using steel jackets. Circular and rectangular columns were prepared and tested in as-built and retrofitted conditions. The results showed that the columns retrofitted with steel jackets performed better than the as-built columns in terms of exhibiting greater flexural ductility and more stable energy absorption capacity, while the as-built columns failed in a brittle manner. Daudey and Filiatrault (2000) conducted an experimental study to investigate the seismic performances of RC columns retrofitted with steel jackets. Figure 2.9 depicts schematics of the cross section of the retrofitted RC columns. The cross section of the RC columns was a grooved rectangular section that was a typical type in eastern Canada. To retrofit the RC column using steel jackets, either

circular or elliptical shape was used. The authors concluded that steel jackets improved the flexural ductility of the RC columns with the grooved rectangular shape, and the effects of using either elliptical or circular shape of the steel jackets were similar in terms of improving the flexural ductility of the columns.

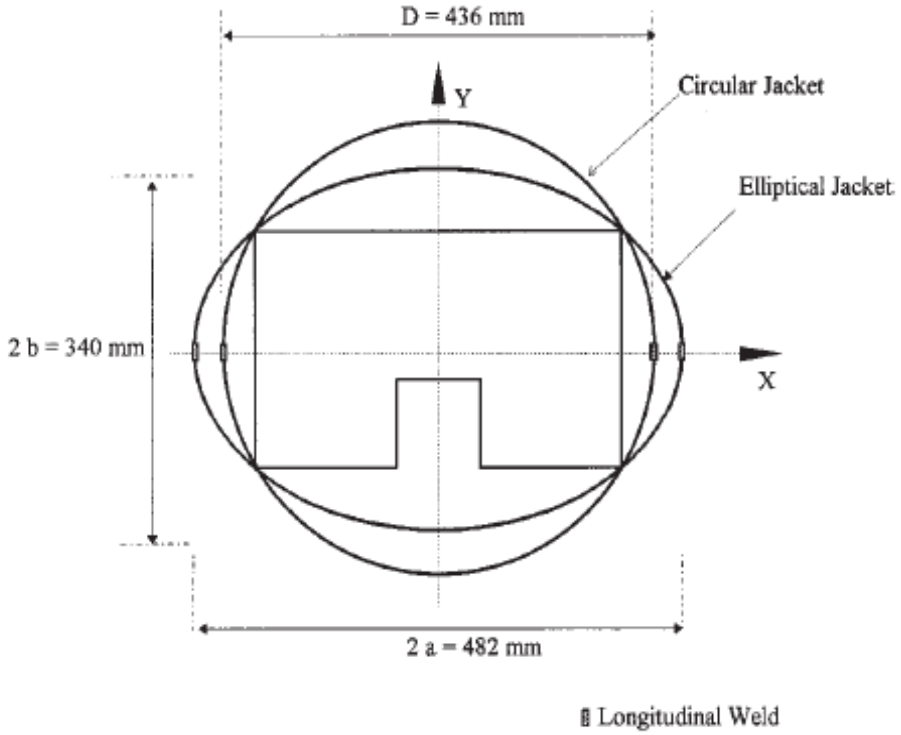

Figure 2.9 Cross section of the RC columns and the shapes of steel jackets used in the study by Daudey and Filiatrault (2000).

An experimental test on square RC columns was also carried out by Xiao and Wu (2003). A total of five 1/3-scale RC columns were prepared and tested. To retrofit the square RC columns, thin steel plates were welded, and additional stiffeners (plate stiffener, angle stiffener, or pipe stiffener) were attached at the plastic hinge region. In

conclusion, the welded steel jackets were able to enhance the performance of the square RC columns showing maximum lateral drift of 8.0%. In 2005, Li et al. (2005) obtained stress-strain relationships of concrete confined with steel jackets with various thicknesses in addition to different types of internal reinforcement including spirals, hoops, and steel wires. The authors concluded that the steel jackets improved the strength and the ductility of concrete cylinders, and that the peak strength of confined concrete was highly dependent on the type of internal reinforcement. They also concluded that the spiral reinforcement was the most effective reinforcement among the studied types of reinforcement.

2.3.1.2 Fiber Reinforced Polymers

Fiber-reinforced polymers (FRPs) are composite materials that have been used in several engineering applications such as in the aerospace, auto-mobile, and construction industries. Also it has been widely adopted in the field of retrofit and repair of RC structures, due to their small weight-to-strength ratio and high corrosion resistance. These characteristics encouraged many practitioners to use FRP jackets/wraps for concrete passive confinement instead of steel jackets.

In 1981, Fardis and Khalili (1981) attempted to use glass-FRP (GFRP) to encase concrete cylinders. The results showed that the strength and the ductility of the concrete confined with GFRPs were improved. Saadatmanesh et al. (1994) also, carried out large scale tests on RC columns retrofitted with carbon or glass FRP straps. It was concluded that the flexural strength and the ductility of retrofitted RC columns increased and that the increase rate of ductility decreased as the spacing of the straps increased. Moreover,

the authors developed an analytical model to predict the behavior of confined concrete with FRPs as modifying the Mander et al. model. Toutanji (1999) conducted experimental tests on concrete cylinders wrapped with carbon and glass FRPs and developed an analytical model to describe the stress-strain relationship of the confined concrete based on the Mander et al. model. The author observed that the strength and ductility of the confined concrete had improved significantly, and that using carbon FRPs helped the concrete possess slightly higher strength than when using glass FRPs.

Haroun and Elsanadedy (2005) studied the impact of using glass or carbon FRP jackets on the cyclic behavior of RC column which would have failed in a brittle manner due to poor lap splice length. A total of 13 scaled columns were prepared and tested. Three of them were tested in as-built condition, and eight columns were retrofitted with FRPs. Among the 13 columns, 5 were square columns and 8 were circular columns. In conclusion, the authors found that flexural ductility of the retrofitted circular columns was improved significantly while the retrofitted square columns exhibited limited improvement in their ductility.

Although some early studies attempted to extend the model that was developed by Mander et al. to describe the behavior of concrete confined with FRPs, this approach was deemed by many researchers as inappropriate since as stated earlier, the Mander et al. model was formulated using the triaxial test data which is characterized by a constant confining pressure unlike the constantly increasing confining pressure applied by the FRP wraps. In addition, the Mander et al. model adopted the stress-strain curve proposed by Popovics (1973), which was inappropriate for describing the bilinear behavior of concrete confined by FRPs. The bilinear behavior of the confined concrete was exhibited and

confirmed experimentally by many studies. Figure 2.10 shows schematics of the stress-strain relationships of concrete confined with FRPs. While strain hardening is observed with high confinement pressure, softening is observed with low confinement pressure after reaching the transient point (f_t and ε_t).

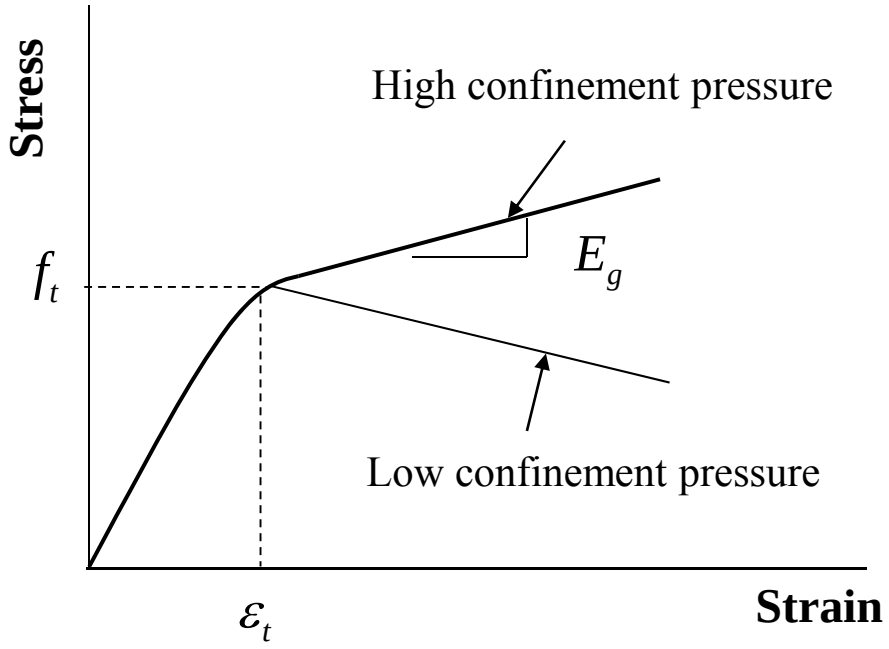

Figure 2.10 Stress-strain relationship of concrete confined with FRPs.

The discrepancies between the behaviors of concrete confined with FRPs and steel ties motivated many researchers to work on developing more accurate models for concrete confined with FRPs. For example, Samaan et al. (1998) developed a simple model for concrete confined with FRPs based on the unique dilation properties of concrete encased with FRPs from the study by Mirmiran and Shahawy (1997). In the study, the authors compared several existing confinement models including the models

by Ahmad and Shah (1982), Fardis and Khalili (1982), Mander et al. (1988a), and Monti and Spoelstra (1997). They concluded that there existing models were not able to predict the failure point (ultimate point) of the concrete with FRPs. They also compared their model with the experimental results conducted by others, and their model showed good agreement with the experimental results.

Also, Spoelstra and Monti (1999) noticed that just adopting the Mander et al. model was not suitable for the FRP confinement which behaves as an elastic material until it fails. Therefore, they proposed a confined concrete model with FRPs that takes into account the continuously increasing confinement pressure from FRPs while satisfying the equilibrium state of concrete through iterative process. In their research, the proposed analytical model was compared with other experimental data, and the results showed good agreement.

In 2003 Lam and Teng (2003) suggested a model that is considered among the most accurate models that is capable of predicting the failure (ultimate) point successfully. To develop the model, the authors examined and observed the published data of 76 tests conducted on concrete cylinders confined with various types of FRPs from 14 different studies. In their model, the actual hoop rupture point of FRP and the effect of the confinement stiffness on the ultimate point of the confined concrete were carefully incorporated.

Some other researchers used simplified approaches to develop their models such as Saiidi et al. (2005) who suggested a bilinear confined concrete model with carbon FRPs based on the work of Kawashima et al. (2001). Unlike most other models which

describe the ascending branch of the stress-strain curve as a polynomial function, Saiidi et al. used a simple linear function to describe the ascending branch.

Most of the previously discussed models aimed at predicting the behavior of concrete confined with FRP only without taking into account the effect of internal transverse steel reinforcement. Therefore, these models were viewed by some researchers as incapable of accurately describing the realistic behavior of RC elements retrofitted with FRPs. To illustrate this limitation further, Figure 2.11 shows a schematic of concrete section confined with both internal steel ties and external FRPs. As shown herein, the core concrete is affected by the confining pressures from internal steel and external FRP, and the cover concrete is only affected by the outside confining pressure from the FRPs. Although the previously discussed models are applicable to the cover concrete, the behavior of core concrete should be addressed taking into account both internal and external confining pressures. To address this limitation, few studies have focused on incorporating the effect of internal steel reinforcement in the models.

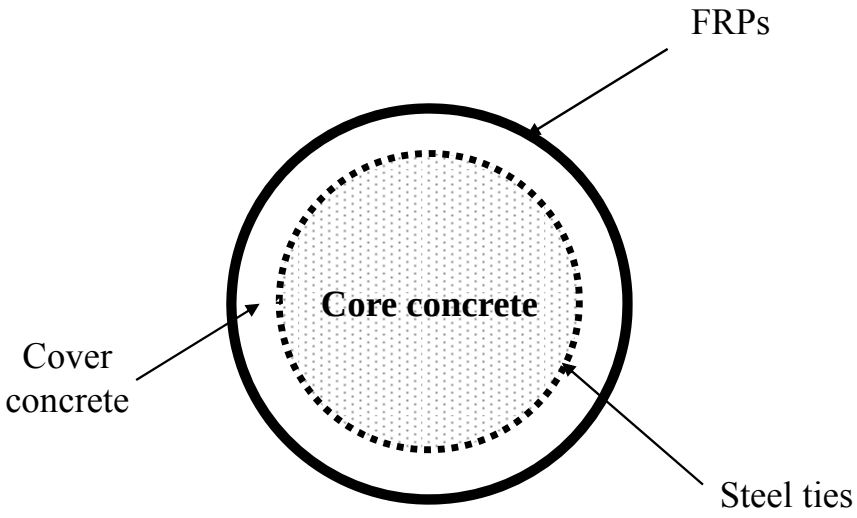

Figure 2.11 Schematic of concrete confined with internal steel ties and external FRPs.

Kawashima et al. (2001) proposed an analytical model which is able to describe the stress-strain relationship of the core concrete when confined with internal steel ties and external carbon FRPs. The behavior of the cover concrete is obtained when taking out the effects of the internal steel. Also, the authors assumed that the failure point of core concrete coincides with the point when the external FRPs fail. In other words, the effect of internal transverse steel was ignored in predicting the ultimate point of the core concrete.

Eid and Paultre (2008) also developed an analytical model for concrete confined with both external FRPs and internal ties. In their study, the equation to capture the failure point of core concrete took into account the effect of both FRPs and internal ties, unlike the Kawashima et al. (2001) model. Finally, the authors compared their analytical model with various experimental data conducted by Demers and Neale (1999), Xiao and Wu (2000), Lam and Teng (2004) and Eid et al. (2006), and the analytical model showed good agreement with the experimental data.

2.3.2 Active confinement techniques

The study by Richart et al. (1928) was one of the pioneer works in the field of concrete confinement, especially under triaxial stress state. The authors used a triaxial pressure vessel to exert active confining pressure on concrete cylinders. Lateral confining pressure was widely varied from 7% to 570% of the compressive strength of unconfined concrete. The following simple equations were suggested to estimate the peak strength, f_{cc} and strain of the confined concrete, ε_{cc} under a lateral confining pressure, f_l:

$$f_{cc} = f_{co} + k_1 f_l , \qquad (2.1)$$

$$\varepsilon_{cc} = \varepsilon_{co}(1 + k_2 \frac{f_l}{f_{co}}) , \qquad (2.2)$$

where f_{co} and ε_{co} are the strength and strain of the unconfined concrete at the peak point, when it reaches the peak strength, and k_1 and k_2 are coefficient values that account for the effect of active confining pressure. The average values suggested for k_1 and k_2, respectively are 4.1 and $5k_1$. These simple equations have become the basis for many analytical models. After the study by Richart et al. (1928) early experimental work was conducted on concrete cylinders or blocks subjected to biaxial and/or triaxial state of stress using a biaxial pressure machine, a three axis independent pressure machine, or a triaxial pressure vessel (Balmer 1949, Bellamy 1961, Kupfer et al. 1969, Mills and Zimmerman 1970, Launay and Gachon 1972, and Kupfer and Gerstle 1973). These studies demonstrated that the strength and the strain of concrete are improved dramatically by increasing the confining pressure.

The superiority of active confinement compared to passive confinement encouraged some researchers to investigate the feasibility of applying active confinement in the field of seismic retrofit. The methodology of which the active confinement pressure was applied varied in each study. Some of the studies attempted using lateral prestressed steel strands to confine RC columns (Gamble et al. 1996, Saatcioglu and Yalcin 2003). Gamble et al. (1996) constructed full scale RC circular columns to examine the spliced regions at the base of the columns. They confined the RC columns using externally

tensioned steel bands and prestressing strands. The results showed that the performance of the RC columns was improved with the presstressing strands. Saaticoglu and Yalcin (2003) tested full scale RC column tests. A total of seven columns (2 square and 5 circular) were tested. In order to install external prestressing strands, a special anchor and device were used. Figure 2.12 shows the hardware used for the installation of the prestressing strands. The confined columns were tested under lateral cyclic loadings with a constant compression loading. The results showed that the flexural behavior was improved, and the shear failure was prevented.

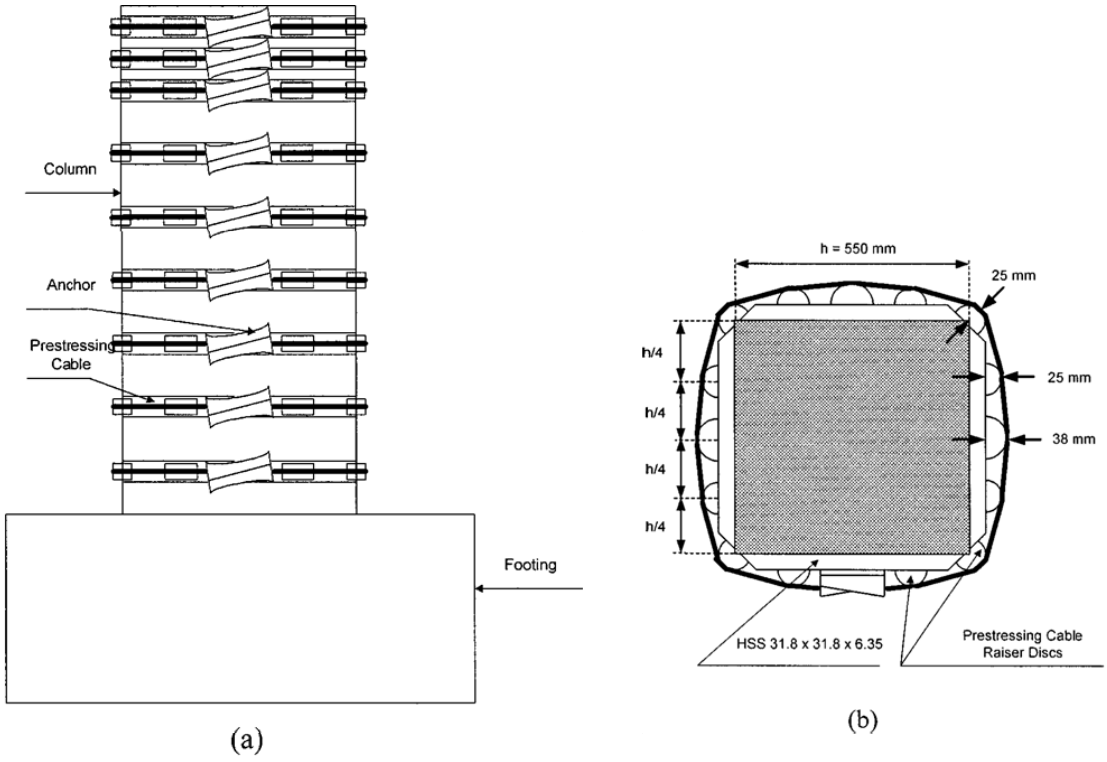

Figure 2.12 Hardware used for applying prestressing confining cables: (a) RC column with confinement and (b) cross section of the column (Saaticoglu and Yalcin, 2003).

Others investigated the feasibility of using prestressed FRP belts (straps) to apply the confinement pressure (Yamakawa et al. 2004; Nesheli and Meguro 2006). In Nesheli and Meguro's study (2006), five square columns were cast and tested under cyclic lateral loading. To confine the RC columns, FRP belts with three-centimeter width made of carbon and aramid/epoxy composite were used. Two of the specimens were wrapped with prestressed FRP belts. The results of the study showed that shear failure was prevented and flexural behavior of confined columns was improved.

There have also been a few studies that focused on exploring experimentally the effect of active confinement on the material level (Krstulovic-Opara and Thiedeman 2000, Hussain and Driver 2005). Other studies attempted to describe analytically the constitutive behavior of concrete when subjected to active confinement (Malvar et al. 2004; Cho et al. 2005; Wolf 2008). Malvar et al. (1997) developed finite element model for concrete under multiaxial loadings. Based on the plasticity theory, basic yielding failure surfaces were defined, and the surfaces were calibrated with the existing data obtained from the concrete cylinder tests under multiaxial loading states. Shear dilation and a fracture energy dependent strain in tension were also incorporated in the model. In 2005, Cho et al. (2005) suggested a concrete confined model under multiaxial stress states. The peak strength and strain were calculated based on the triaxial failure surfaces. They assumed concrete as an orthotropic material subjected to a triaxial constitutive law. More recently, Wolf (2008) developed a generalized analytical model, which is able to predict an entire stress-strain relationship of concrete confined with any type of confinement (passive or active). The model was designed to capture the behavior of the concrete under multiaxial loading state. It was developed based on the plasticity model by

Malver et al. (1994). The author combined two flow rules to capture the plastic deformation (strain) of concrete: 1) an associated flow rule which allows plastic volume expansion, and 2) Prandtl-Reuss flow rule (Chen 1982) which does not allow any plastic volume expansion. Based on the experimental data from other researchers, the author obtained reasonable loading surfaces and implemented the theory into a FE program.

2.4 REPAIR TECHNIQUES

Among the common application fields for concrete confinement is the field of structural damage repair. The majority of the damage repair techniques currently at hand suggest the use of either FRP sheets or concrete jackets. Figure 2.13 shows schematics of these two repairing techniques. One of the recent studies that explored the use of carbon-FRP (CFRP) sheets to repair already damaged columns was conducted by Vosooghi et al. (2008). To reduce the repair time, the researchers utilized accelerated curing techniques to elevate the columns temperatures between 94^0C-100^0C and reduce the ambient relative humidity to 10%. Such accelerated curing techniques are only feasible in laboratory environment and thus would be difficult to apply in real applications. Prior to this study there was another study (Saadatmanesh et al. 1997) that focused on using prefabricated FRP composite straps for seismic damage repair of circular and rectangular sections. The used straps were slightly oversized, and the gap between the column and the straps was filled with pressurized epoxy grout to apply confining pressure on the column. Similar studies were conducted in different parts of the world including Japan (Fukuyama et al. 2000), Italy (Balsamo et al. 2005), and South Korea (Youm et al. 2006). All of these studies reported improvements in the strength and ductility of the repaired columns.

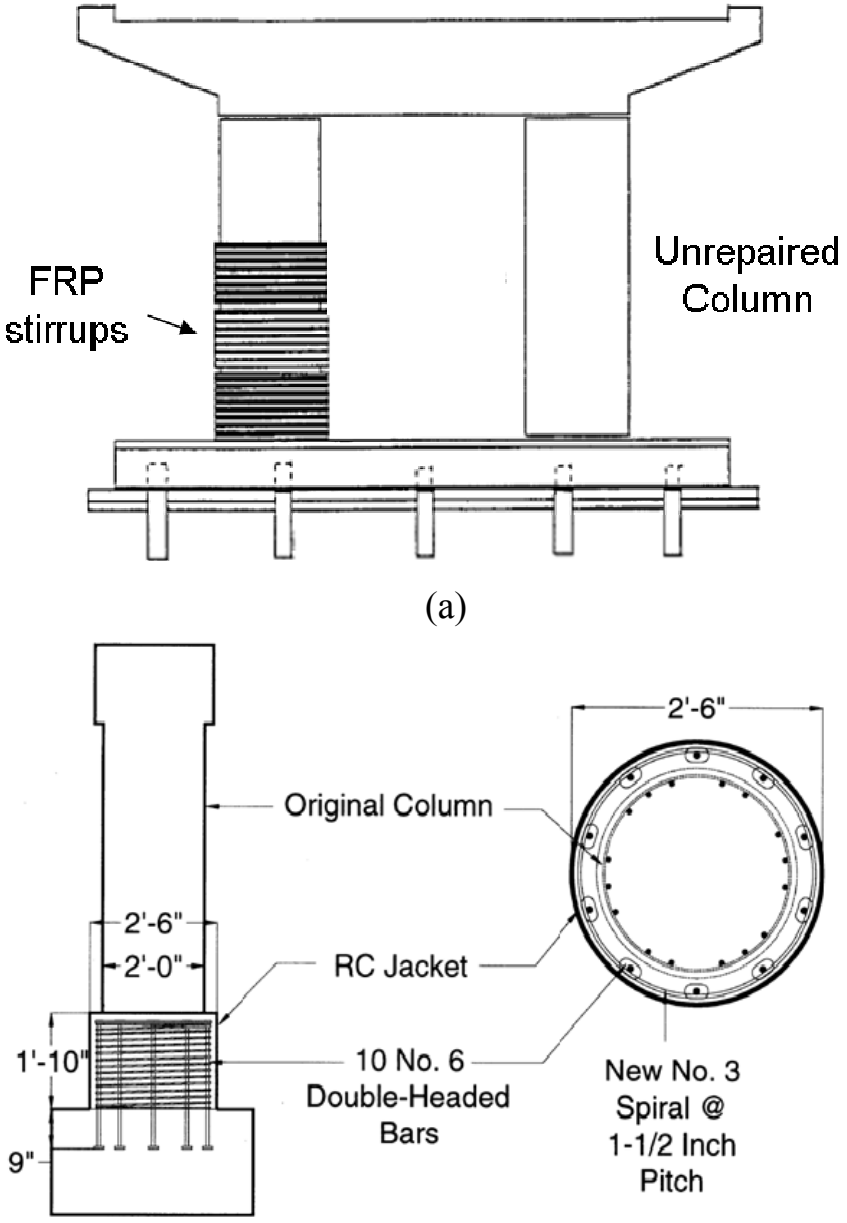

Figure 2.13 Schematics of different RC column repairing techniques using: (a) FRP stirrups (Saadatmanesh et al. 1997), and (b) RC jackets (Lehman et al. 2001).

However, a major problem with using FRP sheets for rapid repair is the time required for resins to cure under ambient climate conditions which could extend up to a week.

On the other hand, fewer studies focused on investigating the approach of using concrete jackets for repair (see Figure 2.13 (b)). Among these studies are the ones by Bett et al. (1988), Fukuyama et al. (2000), and Lehman et al. (2001). They utilized strong concrete jackets and designed the stiffness of the jacket such that the plastic hinge would either develop at or above the repaired location. The results of the studies were satisfactory; however, this technique has two major limitations: 1) The design and construction of the concrete jackets will require considerable labor and time, which will impose significant delays in the opening of the damaged structure 2) Adding concrete jackets at the base will increase the stiffness of the column, and this will change the dynamic properties of the entire structure which could significantly increase the strength and ductility demands on the columns. To the best of the author's knowledge there is no published work on the application of active confinement for damage repair.

2.5 LIMITATIONS OF CURRENT ACTIVE CONFINEMENT TECHNIQUES

Despite the widely accepted fact that active confinement is superior to passive confinement, the application of active confinement in the retrofit or repair of real bridge columns has been hindered due to many practical reasons associated with the techniques used in applying active confinement in the field. A major drawback in most of the used techniques is the need for excessive mechanical hardware, required labor and time to apply a moderate level of active confinement pressure. The amount of hardware and labor

involved with active confinement application using conventional materials is typically far more than is needed to install conventional passive steel or FRP jackets. Another crucial reason is the long-term performance of the prestressed steel or FRP materials used for applying active confinement pressure. In the 1990's, the attempts conducted by the California Department of Transportation (Caltrans) to retrofit bridge columns using active confinement applied with prestressed E-glass FRP wraps yielded unsatisfactory results. This was mainly due to the premature fracture of the prestressed wraps after three years of installation due to creep rupture (Hawkins et al. 1996). For these practical reasons and despite the advantages associated with using active confinement, its widespread application has been hindered, and the passive confinement approach using steel or FRP jackets has become more popular over the last several decades. To allow active confinement to reach its full potential in the fields of seismic retrofit and repair, there is a dire need for a more simple and robust method to apply active confinement on-site with minimal hardware and labor. This research focused on presenting and testing a new methodology for applying active confinement using shape memory alloys.

CHAPTER 3 NEW TECHNIQUE FOR ACTIVE CONFINEMENT

3.1 PROPOSED CONCEPT

The idea of using SMAs in providing active confinement for concrete is based on utilizing the recovery stress associated with the shape recovery of the SMAs when heated. SMAs are known to be capable of recovering their original shape after experiencing large deformations up to 8%-strain (Vokoun et al. 2003). The shape memory phenomenon is associated with large recovery stress if the alloy is restrained from restoring its original shape. The recovery stress highly depends on the material composition, manufacturing procedure, and the level of deformation experienced prior to shape recovery (Otsuak and Wayman, 2002). In the proposed application, prestrained SMA wires as a spiral will be wrapped around the most critical zone of the column (e.g. plastic hinge) and heated using a fire torch or electrical current. The heated SMA spirals will attempt to shrink to their original length. Since the SMA spirals are anchored at both ends and the concrete column they are wrapped around is essentially incompressible, the induced shrinkage causes the SMA spirals to squeeze the concrete column. This squeezing effect provides the active confinement pressure to the column. The proposed concept for applying active confinement using SMA spirals is depicted in Figure 3.1. Unless the SMA spirals are heated, no active confinement pressure is applied to the column (see. Figure 3.1.a), but after heating, the active confinement pressure is activated (see Figure 3.1.b). A key element in the success of this technique is the thermo-mechanical properties of the SMAs.

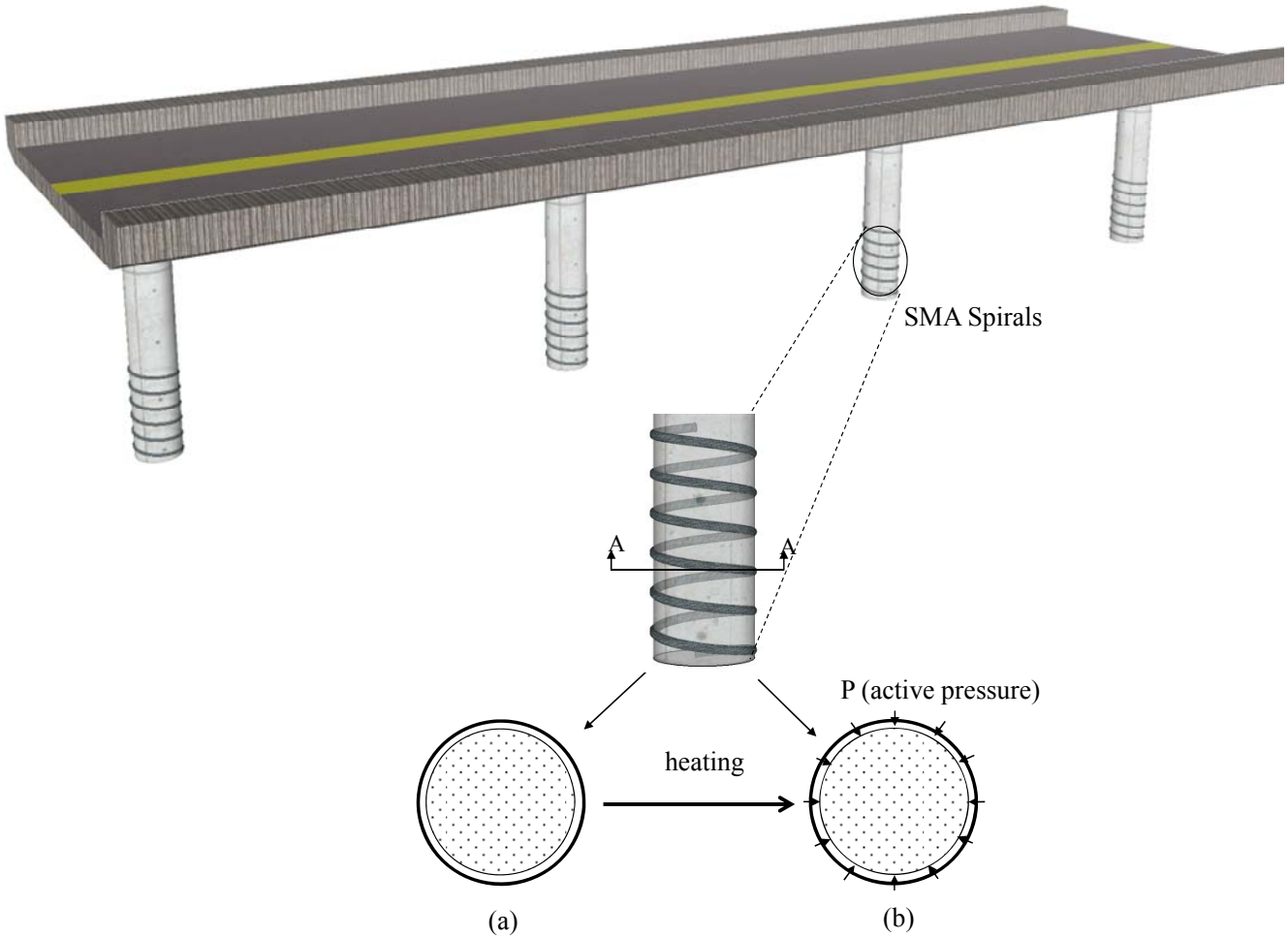

Figure 3.1 Schematic of RC bridge columns retrofitted with SMA spirals: (a) before the spirals are activated and (b) after the spirals are activated.

A brief background on the thermo-mechanical behavior of SMAs is presented in the following subsections.

3.2 SHAPE MEMORY ALLOYS

Shape memory alloys (SMAs) possess two unique phenomena; shape memory effect (SME), and superelasticity. SME is the ability of the alloy to recover its original shape by heating after being excessively deformed. Superelasticity on the other hand is the ability of the alloy to sustain large strains (e.g. 6-8% strain) and still recover its original shape upon unloading. These phenomena had been discovered in various alloys such as the Au-Cu alloy in 1930s, the In-Ti alloy in 1950s, and the Ni-Ti alloy in 1963 (Tadaki, 1988; Otsuka and Wayman, 2002).

The key factor behind the unique thermo-mechanical behavior of SMAs is the phase transformation that occurs between the two distinct phases that exist on the atomic level: 1) Austenitic phase, which exists at high temperatures and 2) Martensitic phase, which exists at low temperatures. As an example, Figure 3.2 shows the atomic structures of binary NiTi SMAs in the austenitic and martensitic phases. As it is shown in the figure, the atomic matrix of SMAs in the austenite phase is symmetrical, and thus, the austenite phase is often known as the parent phase. However, the atomic structure of the martensite phase is less symmetrical, and in some cases it takes a rhombic or monoclinic shape (see Figure 3.2.b)

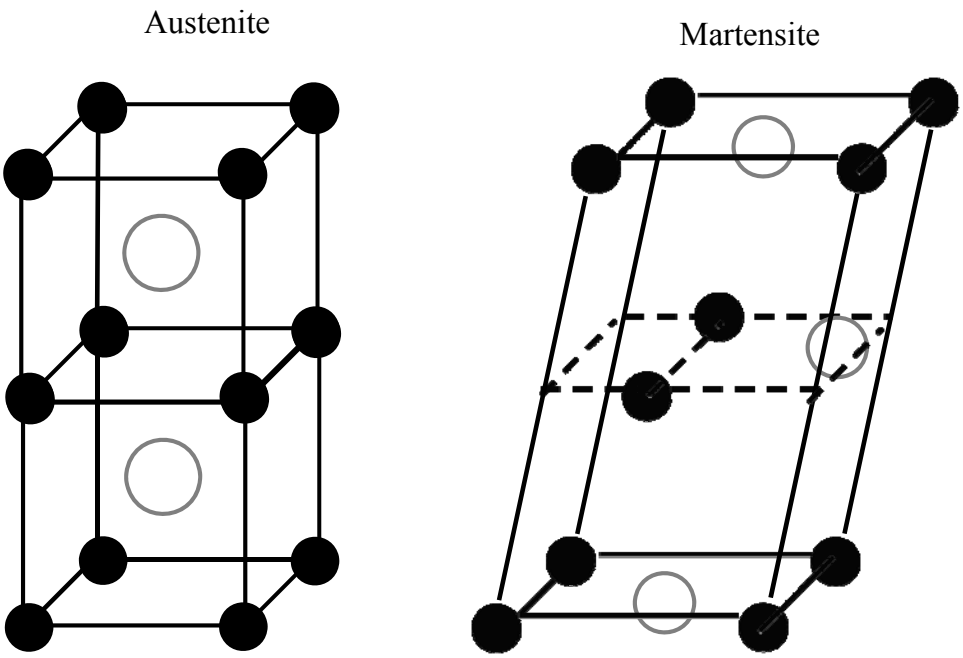

Figure 3.2 Atomic structures of a binary NiTi SMA in the austenite (a) and martensite (b) phases.

One basic principle that enables SMAs to possess the SME and superelasticity phenomena is that the alloys can be transformed from one phase to the other either by applying thermal load, mechanical load, or both. Figure 3.3 shows the atomic matrix during the martensitic transformation (i.e. austenite to martensite) and reverse transformation (i.e. martensite to austenite). The laws that govern the transformation from one phase to the other are highly dependent on the alloy's temperature with respect to four "transformation temperatures" which are unique properties for every alloy. These transformation temperatures are: 1) the austenite start temperature (A_s), where the reverse transformation of martensite to austenite starts, 2) the austenite finish temperature (A_f),

where the reverse transformation of martensite to austenite finishes, and beyond A_f, the alloys are completely austenite, 3) the martensite start temperature (M_s), where the martensitic transformation of austenite to martensite starts, and 4) the martensite finish temperature (M_f), where the martensitic transformation of austenite to martensite finishes, and below M_f the alloys are completely martensite (see Figure 3.4).

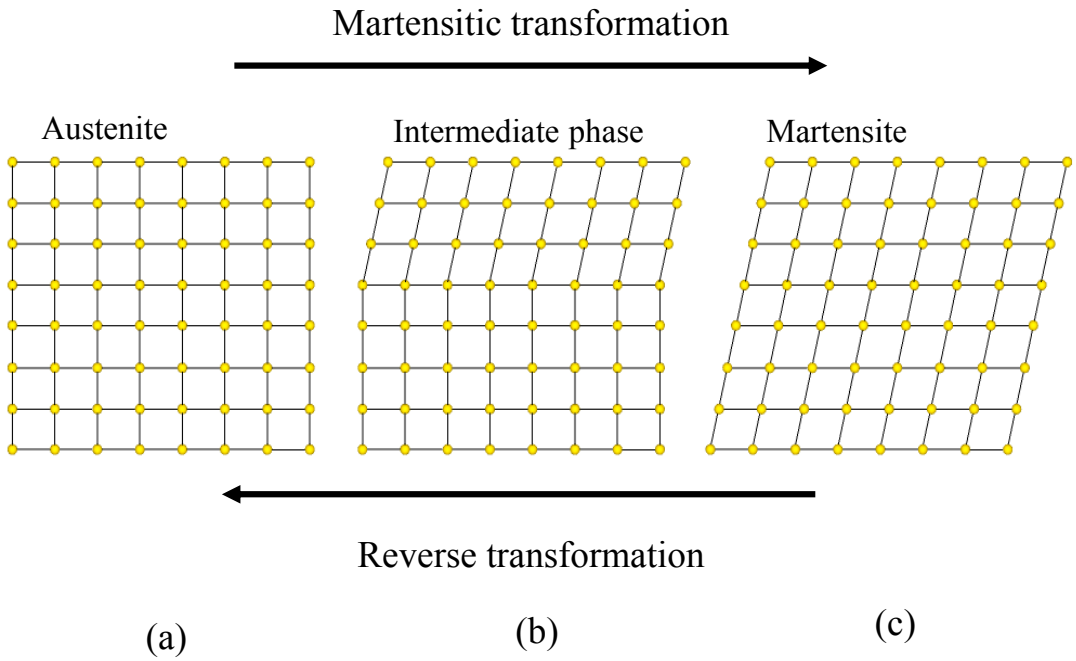

Figure 3.3 Matrix of the atoms at different phases: austenite (a), intermediate (b) and martensite (c) phase.

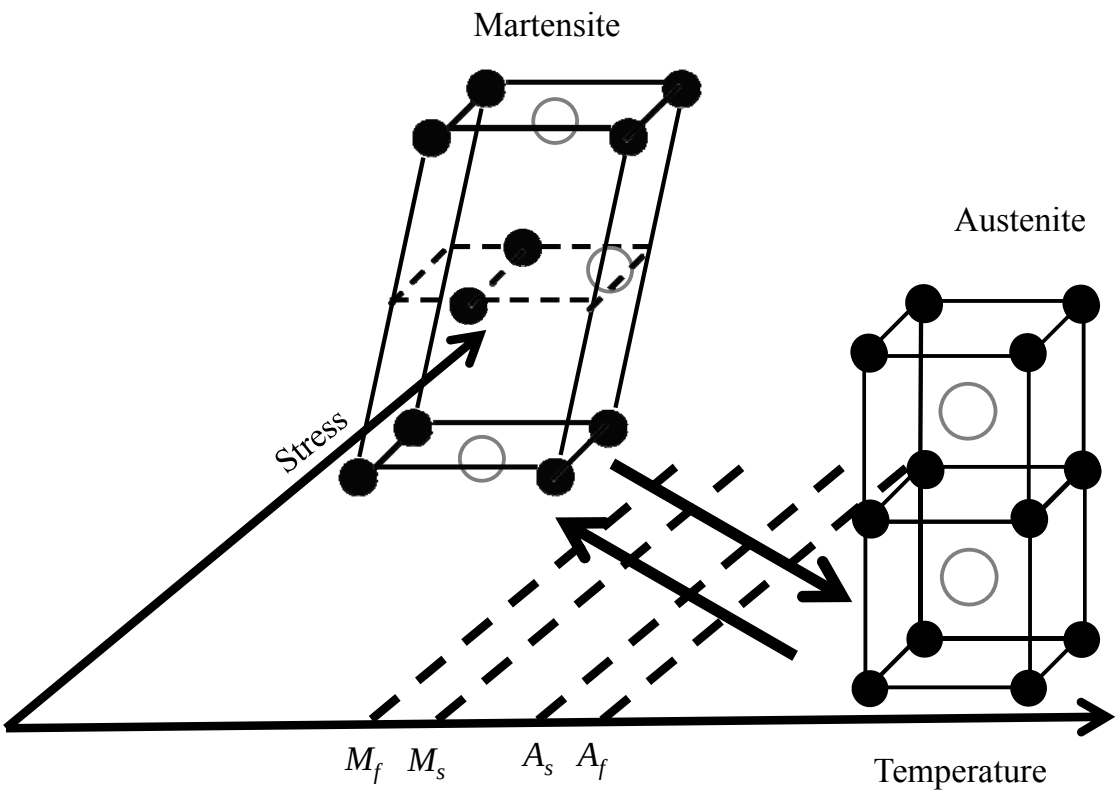

Figure 3.4 Four transformation temperatures.

Furthermore, it should be noted that there are two possible phases of martensite: 1) twinned martensite and 2) deformed or detwinned martensite. Since austenite is more symmetrical than martensite, the two different martensite phases could be formed after the martensitic transformation. The two different shapes of martensite are depicted in Figure 3.5 in two dimensional spaces.

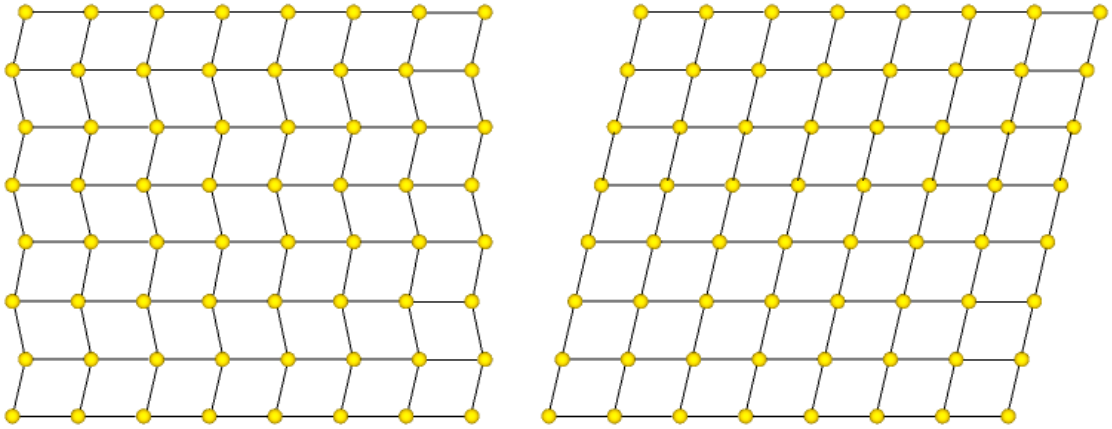

(a) (b)

Figure 3.5 Twinned (a) and detwinned martensite (b).

3.2.1 Shape memory effect

In order for SME to be observed, the alloy has to be at temperature below M_f, where the SMA is found in the twinned martensite phase, and this is often referred to as the "original shape". Then, the twinned martensite becomes detwinned martensite when the SMA sustains stress or is deformed. Finally, the original shape is fully recovered when the temperature of the alloy is raised above the austenite finish temperature (A_f). Figure 3.6 describes a typical process of the shape recovery (shape memory effect) in SMAs.

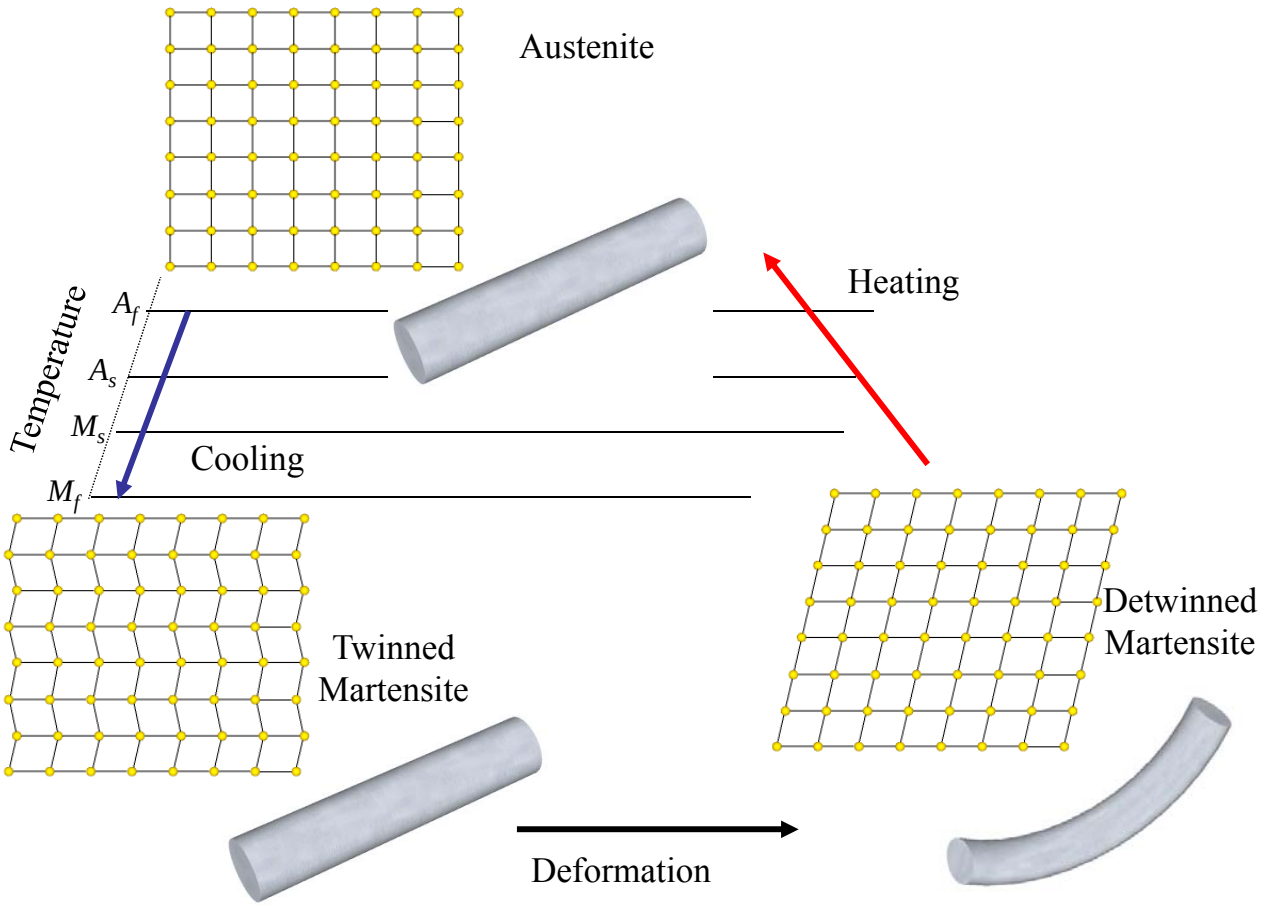

Figure 3.6 Shape recovery process in SMAs.

3.2.2 Superelasticity

The Superelasticity (SE) phenomenon is observed when SMAs undergo a process of loading and unloading in an austenite phase; hence, the alloy has to be at temperature above $A_{f,}$. In the process of martenstic transformation (austenite to martensite), decreasing temperature induces an equivalent effect of increasing stress (Wayman and Duerig, 1990). Therefore, when the austenite SMA is under increasing stress, the austenite SMA can be transformed into twinned followed by detwinned martensite phase. Martensite that is induced due to mechanical loading is often known as stress-induced martensite (SIM). Then, once the stress is removed, the reverse transformation from the detwinned martensite to the austenite starts, and thus the original shape of the alloy is restored. Without temperature changes, austenite SMA behaves like an elastic material, but loading and unloading follow different paths. A typical stress-strain curve of SMAs in an austenite phase looks like a flag (see Figure 3.7).

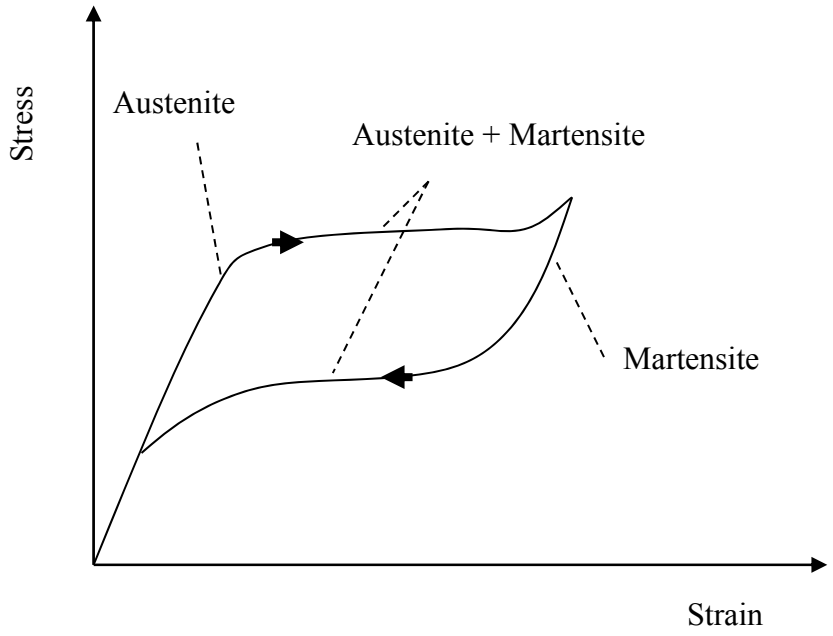

Figure 3.7 Typical flag-shaped stress-strain curve of SMAs in the austenite phase.

3.2.3 Mechanical properties of SMAs

Thermo-mechanical behavior of a typical SMA in a martensite and austenite phases are presented in Figure 3.8 in three dimensional spaces of deformation, force and temperature. A SMA in a twinned martensite phase behaves similar to any other metallic material where at the beginning of the deformation, the behavior is linear due to the elastic behavior of the twinned martensite. However, the behavior becomes nonlinear once the detwinning process begins. When the alloy is fully transformed into the detwinned martensite, it starts exhibiting nonlinear behavior again. Therefore, SMA in the martensite phase exhibits residual deformation due to the loading-unloading process. The residual deformation can be eliminated by increasing the temperature of the SMA above A_f.

As it was described in section 3.2.2, a typical stress-strain relationship of a SMA in an austenite phase has a flag shape (see Figure 3.7 and Figure 3.8). The stress strain relationship shows two stress plateau levels (upper and lower) due to forward and reverse phase transformations during loading and unloading, respectively.

Since the discovery of the Au-Cu alloy in 1930's, many types of SMAs have been developed. However, a few of them such as NiTi-based, Cu-based and Fe-based alloys have been most used among all SMA products. Table 3.1 summarizes the properties of several of the SMAs that are most commonly used commercially or that are being studied extensively in research. These alloys include NiTi, NiTiNb, Cu-based and Fe-based SMAs based on the data from literatures (Cai et al. 1994; Humbeeck and Stalmans 1998; Andrawes 2005; Janke et al. 2005; Wei and Xinqing 2009; Shin and Andrawes 2010).

The properties in the table show wide ranges, and the variations depend mainly on alloys' compositions, manufacturing processes, and loading rate and cycles.

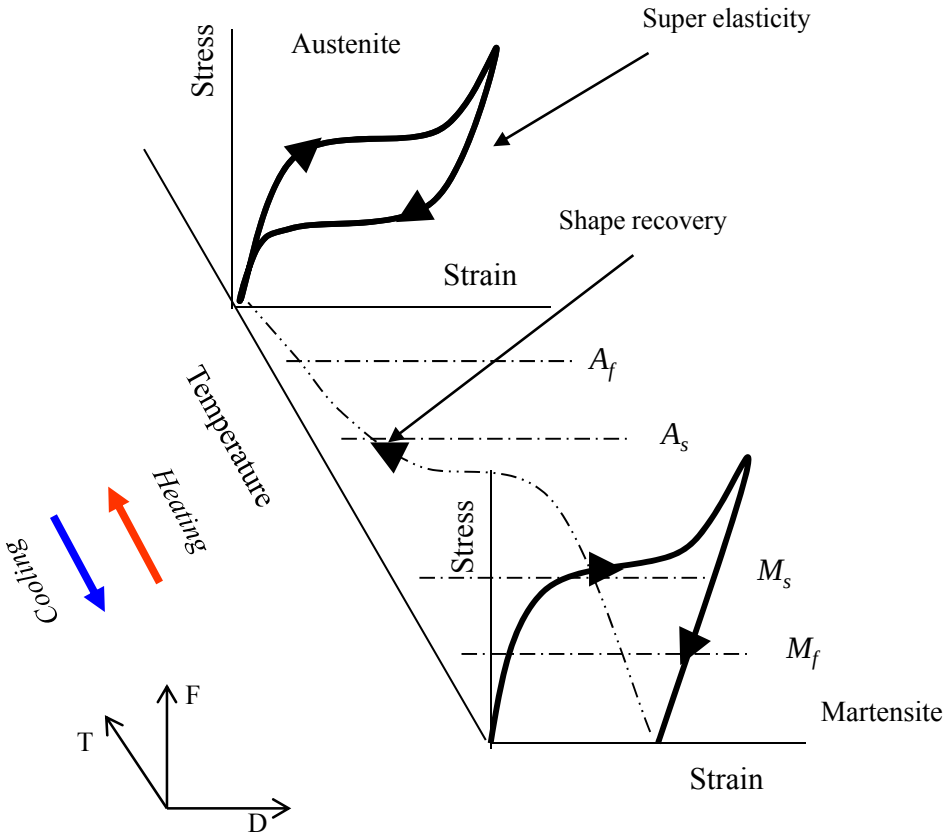

Figure 3.8 Thermo-mechanical behavior of a typical SMA.

Table 3.1 Mechanical properties of different SMAs

	NiTi		**NiTiNb**	
	Austenite	**Martensite**	**Austenite**	**Martensite**
Young's modulus (GPa)	30-80	21-41	-	-
Yielding Strength(MPa)	170-800	50-300	520-620	103-280
Ultimate tensile strength(MPa)	895-1900	895-1900	-	-
Recoverable strain (%)	6-8	6-8	8-9	8-9
Elongation at failure (%)	15-20	30-50	30-50	30-50
Max recovery stress (MPa)	620-865		480-565	
	CuZnAl		**FeMnSiCr**	
	Austenite	**Martensite**	**Austenite**	**Martensite**
Young's modulus (GPa)	70-100	70	140	
Yielding Strength(MPa)	150-350	80-300	200	
Ultimate tensile strength(MPa)	400-900	700-800	650	
Recoverable strain (%)	4-6	4-6	29	
Elongation at failure (%)	10-15	10-15	3.4	
Max recovery stress (MPa)	400-700		400	

3.2.3.1 Recovery stress

As explained earlier, the recovery stress of SMAs is associated with the shape memory effect. Figure 3.9 describes how the recovery stress could be induced in a SMA bar. At temperatures below M_f (martensite phase), the undeformed SMA bar is pre-strained (elongated) (see Figure 3.9.b). If the deformed (elongated) bar is fully constrained, and heated, high recovery stress, σ_R will induce in the bar (see Figure 3.9.c). This recovery stress will vary depending on the composition and processing procedure of each alloy. For example, as listed in Table 3.1 the recovery stress of NiTi-based alloys can reach up to 865 MPa (125 ksi).

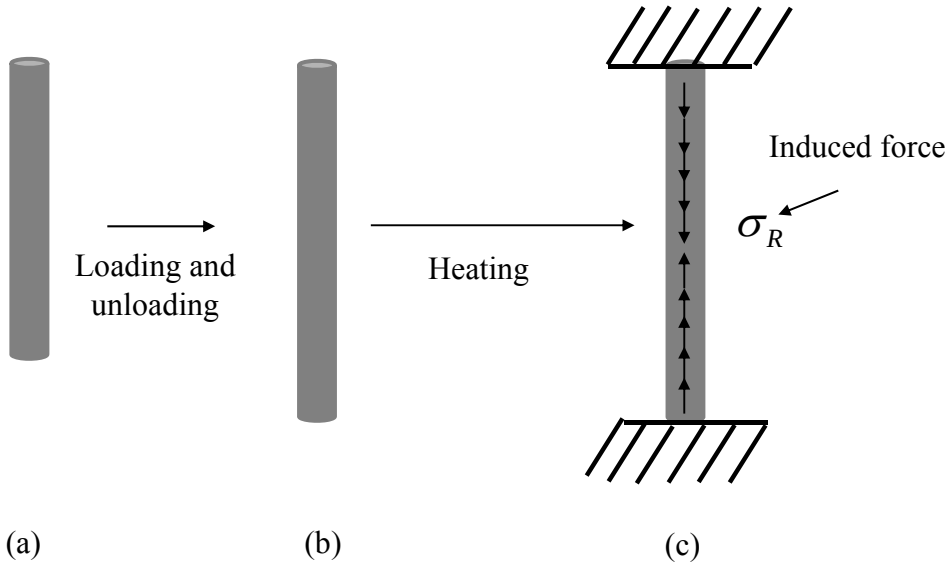

Figure 3.9 Schematics showing the procedure for inducing recovery stress in SMA bar: Undeformed bar (a), deformed bar (b) and constrained bar (c).

3.2.3.2 Thermal hysteresis width

The thermal hysteresis of an SMA is a key characteristic that defines the alloys thermo-mechanical behavior. To understand the definition of thermal hysteresis, Figure 3.10 is presented. It shows the change in the martensitic fraction of the SMA with respect to the temperature. The alloy's thermal hysteresis is often defined by the temperate between A_s and M_s, or the temperature width of the thermal hysteresis loop at 50% martensitic fraction (see Figure 3.10). There are alloys with narrow thermal hysteresis width such as the NiTi alloy whose thermal hysteresis width is typically 20~40^{o}C (Wayman and Duerig, 1990). Other ternary alloys such as NiTiNb possess a larger hysteresis of more than 130^{o}C (Cai et al. 1994; Dong et al. 2002; Zhao et al. 2006). The SMA spirals application that will be the focus of this work requires alloys with relatively large thermal hysteresis width. This is crucial for the spiral to maintain its recovery stress throughout the service life of the application. Figure 3.11 shows a schematic of the variation of recovery stresses of SMAs with narrow and wide thermal hysteresis. In the case of narrow hysteresis, the majority of the recovery stress is lost when the temperature drops to typical ambient temperatures, while in the wide hysteresis case, the recovery stress is more stable.

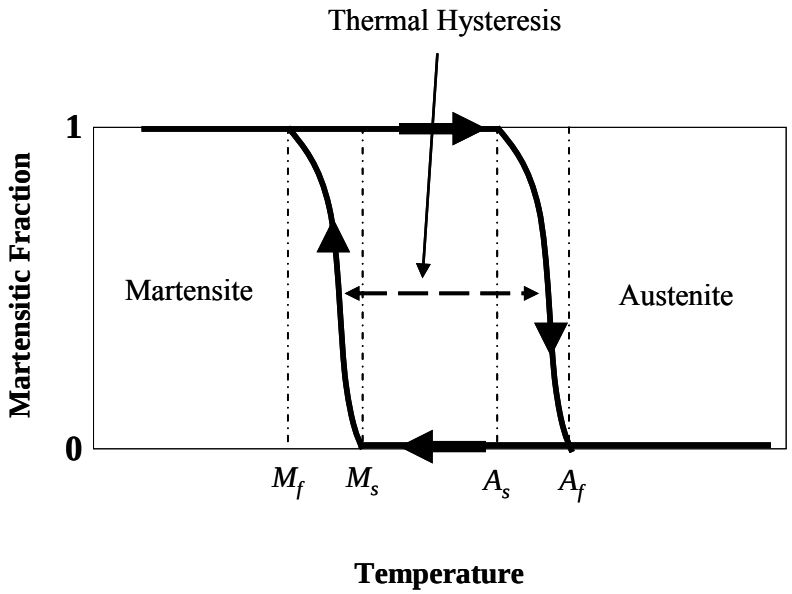

Figure 3.10 Typical relationship between martensitic fraction and temperature for an SMA.

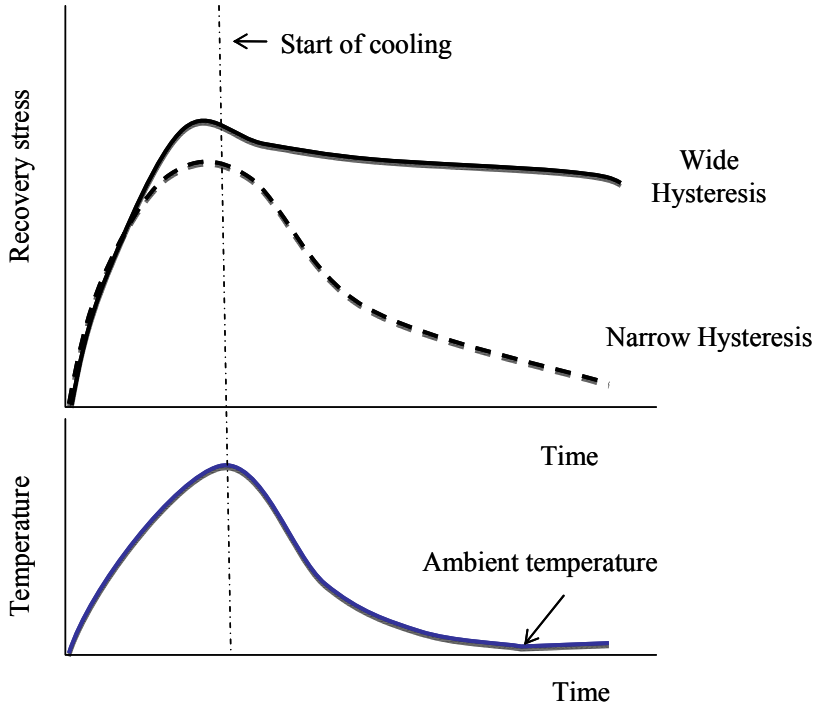

Figure 3.11 Variation of recovery stresses of SMAs with a wide hysteresis and a narrow hysteresis with respect to temperature.

3.2.4 NiTiNb alloy

Beside the studies of binary NiTi SMA, many researchers also have focused on developing and studying ternary NiTiX shape memory alloys. "X" denotes a possible third element. Some of the motivations of the studies on the ternary NiTiX alloys were to control hysteresis width, to increase austenitic strength and to increase corrosion resistance. With the effort of adding a third element into the binary NiTi, there are successfully developed ternary applications such as NiTiFe, NiTiNb, NiTiCr, NiTiCo and NiTiV (Duerig et al. 2011).

In this research, the NiTiNb alloy was used due to its wide thermal hysteresis and high recovery stress. The NiTiNb alloy had been studied with the aim of using it for developing couplers and fasteners. In order for the coupling made of SMAs to be useful for daily applications, the thermal properties of SMA should not be sensitive to the wide ranges of ambient temperature changes.

The first effort of studying the effect of adding niobium (Nb) into NiTi was done by Melton et al. (1986). NiTiNb is comprised of NiTi (reversible) and Nb (irreversible), and the atomic structure of NiTiNb comprises B2 structure (NiTi) and BCC structure (Nb). Figure 3.12 shows the schematics of microstructures of NiTiNb in martensite phase. As the figure shows, Nb particles are located intermittently in NiTi lattice. When the detwinned martensite (see Figure 3.12.b) is heated above A_s, the matrix of NiTi begins to recover, but Nb hinders the recovery process. This irreversible deformation induces delay in the total strain recovery and a temporary increase in the austenite start and finish temperature (i.e. from A_s to A'_s) as shown in Figure 3.13. After the first thermal cycle, the original A_s is restored, which results in the shrinking of the thermal

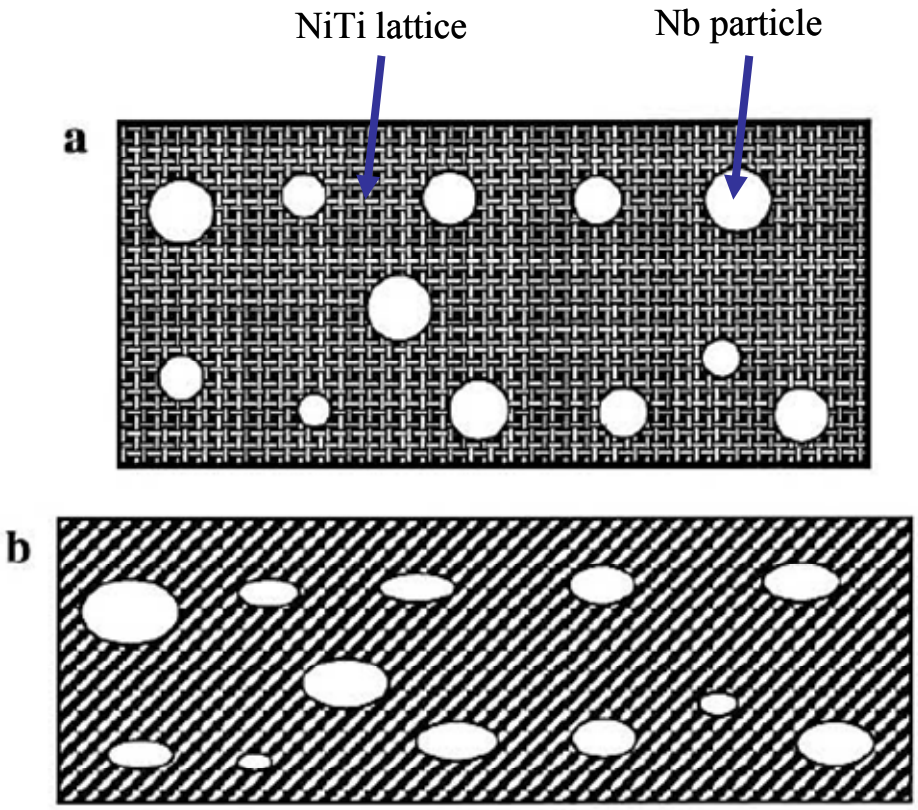

Figure 3.12 Schematics of microstructures of NiTiNb: a) twinned NiTiNb and b) detwinned NiTiNb (Duerig et al., 1990).

hysteresis (Duerig et al. 1990). NiTiNb can exhibit about 130~150 ^{o}C (266 ~ 302 ^{o}F) of thermal hysteresis width (M_s~A'_s) (Melton et al. 1986). Since the expected range of ambient temperatures is greater than M_s, SMA should remain in the austenite phase when temperature of SMA falls into the expected temperature range after it was heated above A'_f. Thus, even when the temperature drops to typical low ambient temperatures, the alloy still maintains its recovery stress. Therefore, the thermo-mechanical behaviors of NiTiNb can be explained by examining its microstructures in multiple phases such as in twinned martensite phase, in detwinned martensite phase or in austenite phase, with Nb

particles. In order to model materials with multiple phases, micromechanical finite element models have been suggested by researchers (Hirano et al. 1991; Reiter and Dvorak, 1998). Also Yin et al. (2004) proposed a micromechanical framework for materials with multiple phases while taking into account the local particle interactions and gradient effects of phase volume fractions.

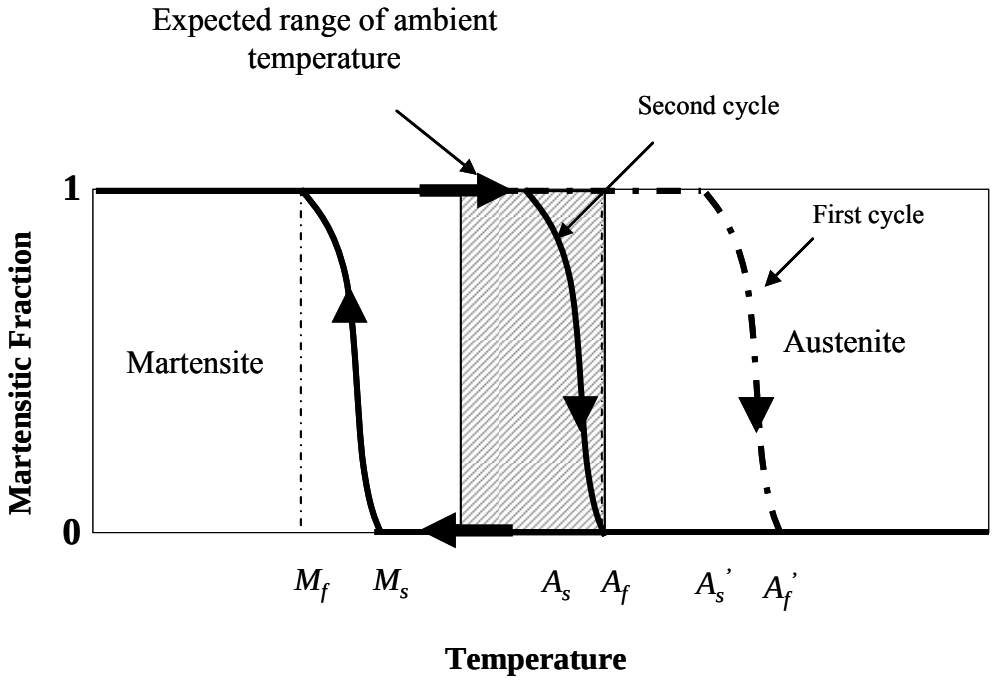

Figure 3.13 Typical thermal hysteresis of NiTiNb alloy.

Figure 3.14 shows the variations of transformation temperature with respect to the amount of Nb. In general, the more amount of Nb was added into NiTi, the lower martensite start (M_s) temperature was observed. Also, the martensite start temperature highly depends on the Ni/Ti ratios as well. The results in the figure indicated that some

NiTiNb SMAs would not be transformed back into martensite after SMAs transformed into austenite even if the temperature drops to -125°C.

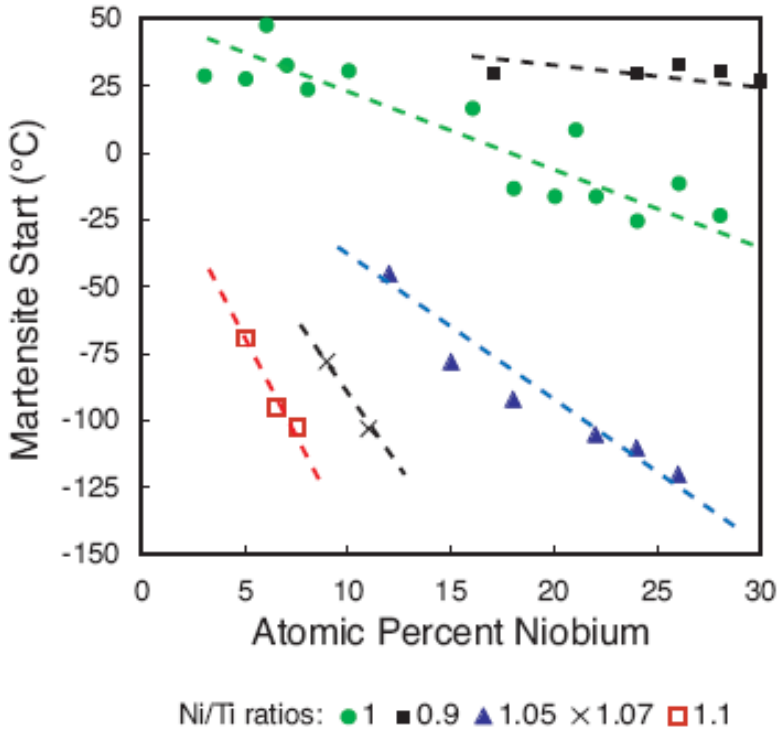

Figure 3.14 Variations of transformation temperature with respect to amount of Nb (Duerig et al., 2011).

A study conducted by Cai et al. (1994) revealed that the recovery stress of NiTiNb SMA prestrained to 9%-strain was approximately 480MPa (69.7ksi). The study showed that the recovery stress increases as prestrain value increases until a strain of 9%; after which it starts to decrease. Also, by adding niobium into NiTi, not only was the hysteresis width increased, but also corrosion resistance, machinability, ductility of SMA and plateau stress of loading and unloading were enhanced (Besselink, 1997; Duerig et al.

2011). Figure 3.15 shows the comparisons of the plateau stress of the loading and unloading branches of NiTi SMA and NiTiNb SMA. NiTiNb exhibits much higher plateau stresses compared with those of NiTi.

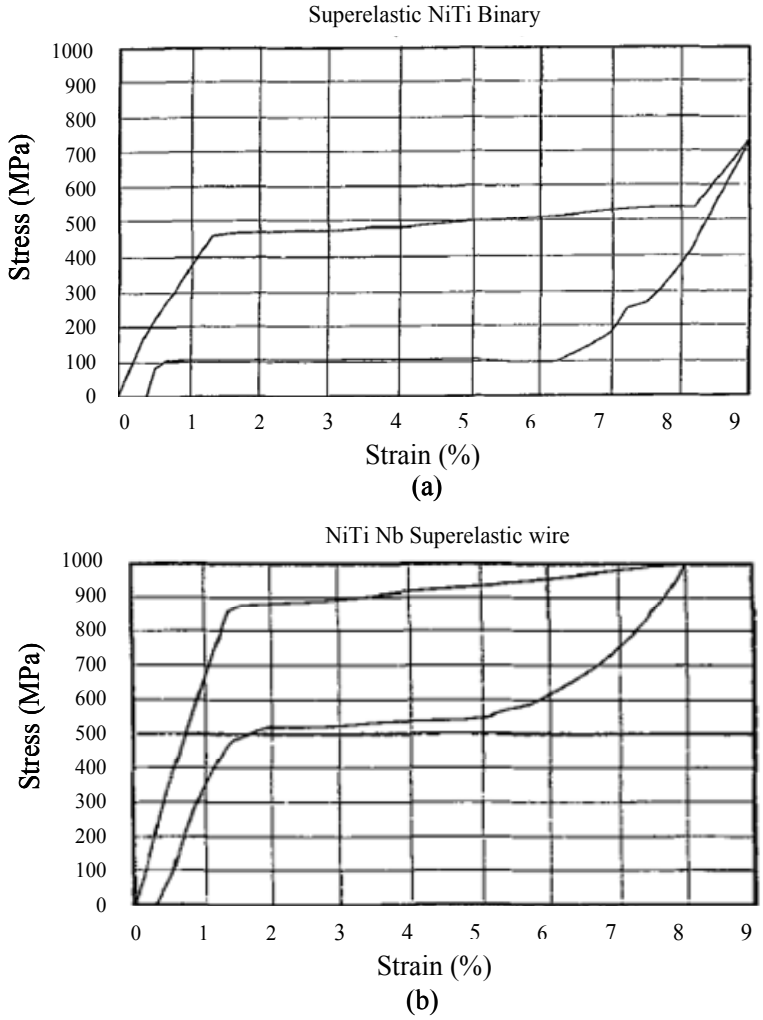

Figure 3.15 Loading and unloading stress plateau of: a) NiTi and b) NiTiNb (Besselink, 1997).

Fu et al. (2009) examined the effect of the amount of Nb on yielding strength of NiTiNb alloy. As indicated in Figure 3.16, when the alloy is in the martensite phase, the yielding strength of the alloy varies with respect to the amount of Nb. The yield strength

increases when adding 5% ~ 15% of Nb. However, the yielding strength starts decreasing when the Nb exceeds 15% of the alloy's composition. Cai et al. (2005) investigated damping capacity of NiTiNb. In their study, NiTiNb was reported having high damping capacity either while the SMA was transforming into martensite or when the SMA was in austenite phase and in martensite phase. Therefore, the author concluded that NiTiNb has great potential for engineering applications.

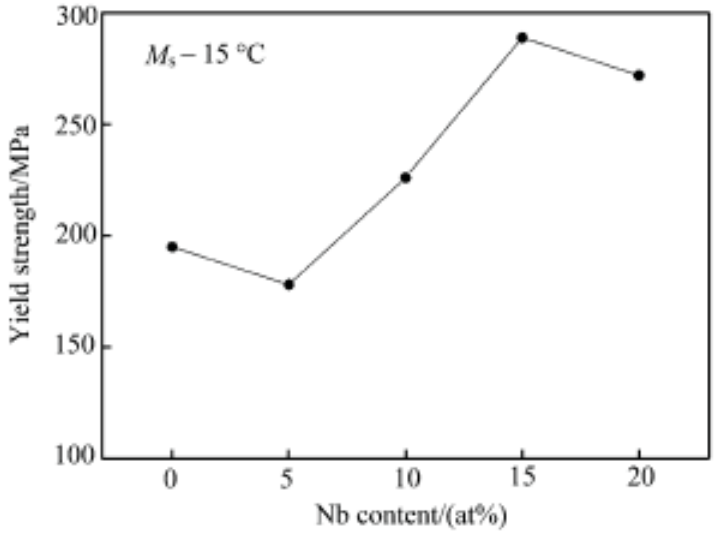

Figure 3.16 Variation of yield strength of NiTiNb in martensite phase with Nb content (Fu et al. 2009).

3.2.4.1 Engineering applications of NiTiNb

Among the most successful applications using shape memory recovery of SMAs are couplings and fasteners. SMA couplings have been used for hydraulic tubes and different sizes of pipes (Harrison and Hodgson 1975; Benson et al. 1983; Duerig 1990). However, the procedure of mounting SMA couplings was complicated, since Ni-Ti based couplings were very sensitive to the temperature variations. In order to pre-deform

couplings and fasteners and to store the pre-deformed applications, liquid nitrogen was necessary for the SMA products to remain in martensite phase. Then the products were exposed to the ambient temperatures to take the advantage of shape recovery phenomenon of the product. Therefore, NiTiNb couplings and fasteners whose thermal hysteresis is wide enough for the applications had been developed and utilized successfully (Duerig 1990; Dong et al. 2002; Wang et al. 2005). NiTiNb couplings or fasteners can be easily shipped without any extra equipment controlling temperature, and whole mounting procedures become easier than using typical temperature sensitive NiTi couplings or fasteners. Figure 3.17 depicts the concept of NiTiNb couplings. Pre-deformed NiTiNb coupling is placed to the smaller diameter pipes (see Figure 3.17.a) and the shape memory force after the couplings heated up (beyond A_f') will be exerted on the subassemblies (see Figure 3.17.b). Due to its wide hysteresis temperature, the shape memory force will not lose its force even after the temperature drops into ambient temperature (see Figure 3.17.c).

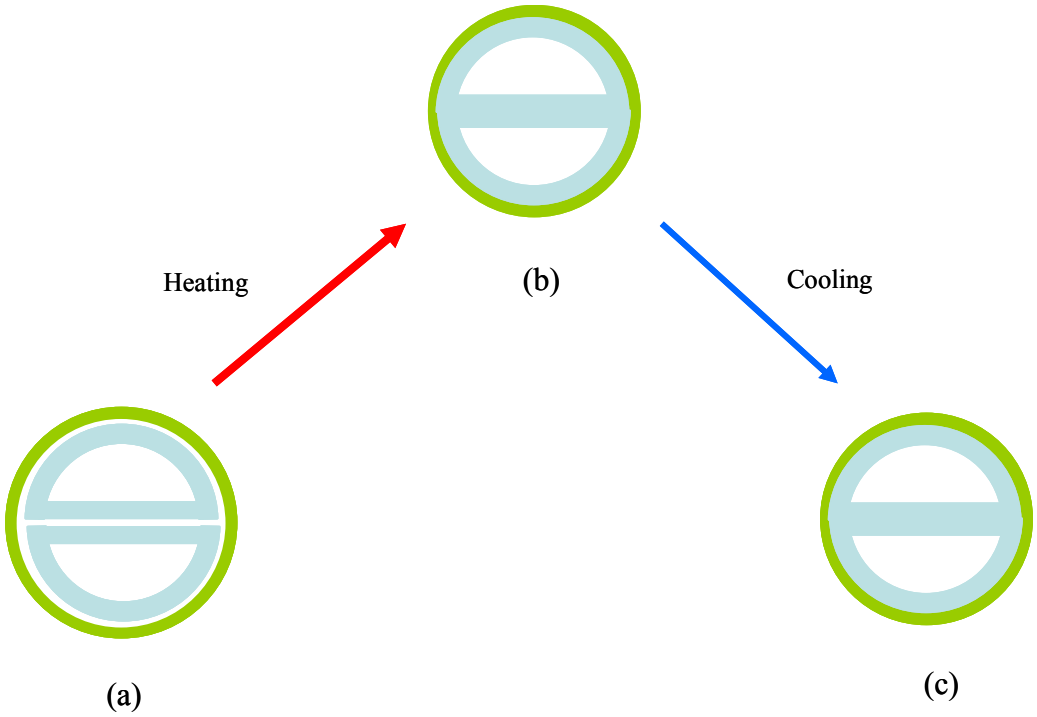

Figure 3.17 Schematics of NiTiNb couplings.

Medical devices such as stent, guide-wires for catheters have been made using NiTi SMAs (Stice, 1990; Miyazaki, 1998; Duerig et al. 1999; Otsuka and Ren, 1999). However, the medical devices made of the binary NiTi required some improvements due to their serviceability. For instance, a stent has been developed using a binary NiTi as a means of creating a self-expanding stent. This stent, however, is hard to install and has the possibility of damaging an artery when first installed since the stent would suddenly expand by itself. To overcome these shortcomings, a stent made of NiTiNb has been suggested to utilize its wide hysteresis characteristics in Japan (Takagi et al. 2005). Figure 3.18 shows schematics of two stents when installed: a) Using conventional NiTi stent and b) NiTiNb stent. The conventional NiTi stent must be delivered in a strong sheath, which must have a higher strength than the recovery force of the NiTi stent. NiTi

stent has to be deformed in martensite phase and be encapsulated in the delivery sheath prior to the shape recovery effect taking place. Since body temperature is about 37^{o}C and it is normally higher than A_f of NiTi stent, the stent expands by itself due to a superelastic phenomenon once it is placed into the target area. As described, placing a self-expanding stent in the target area with high precision has been challenging, and high possibility to damage other areas of the artery has been observed. On the other hand, a NiTiNb stent can be delivered in martensite phase without a special delivery sheath, so placing the NiTiNb stent into the target area is very precise and easy when using a typical placing tool such as a balloon tube. Then, pouring a warm physiological salt solution into the balloon or using high frequency magnetic field to the stent, the NiTiNb stent can be transformed into the austenite phase. In this application, A_f of the NiTiNb stent used in their study was 42^{o}C, and this temperature has been known to be safe enough for a normal organisms. Finally, NiTiNb stents remain in austenite phase throughout its service life since human body temperature is 37^{o}C which is higher than M_s (-43.5^{o}C) of the NiTiNb stent.

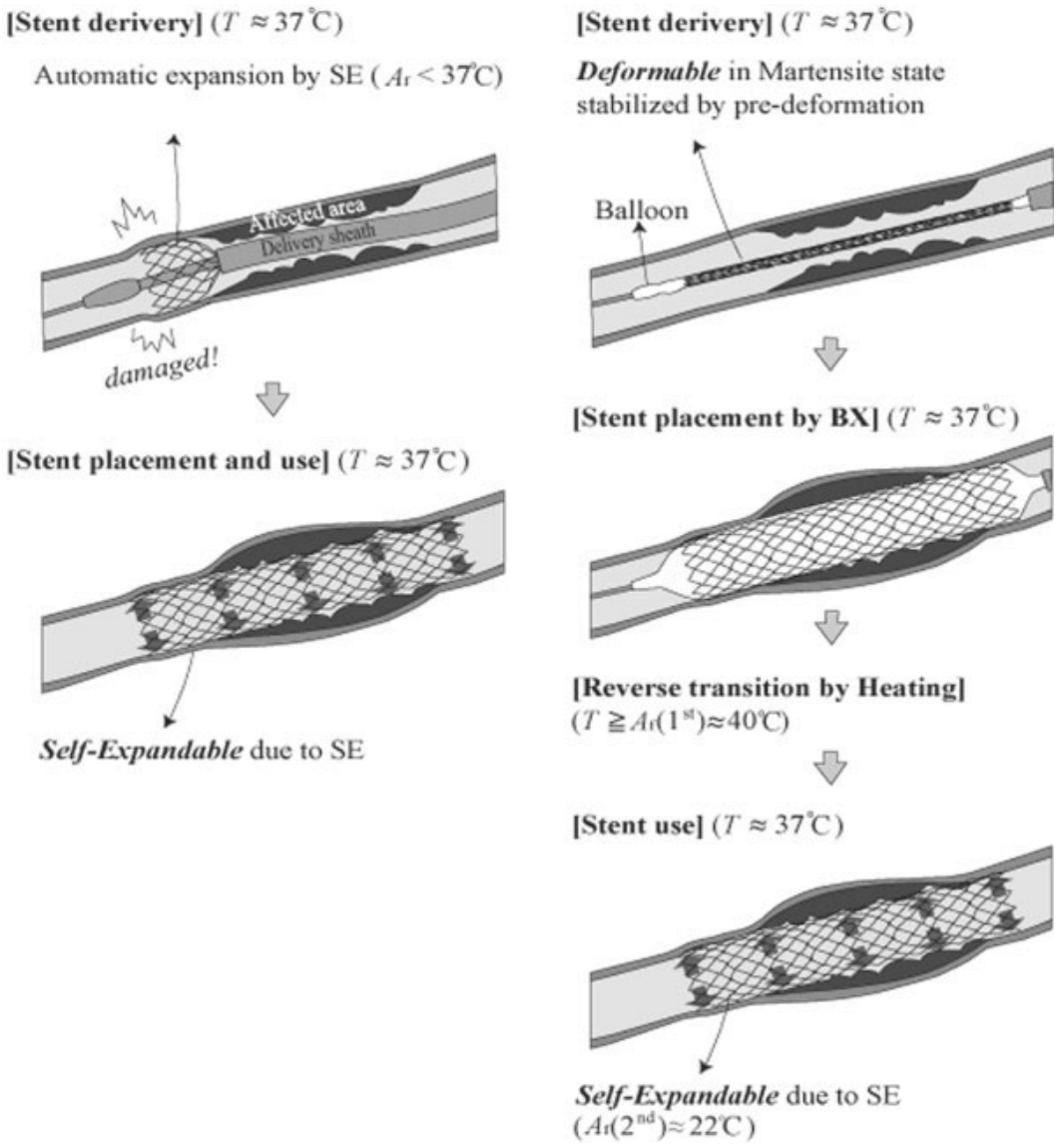

(a) Conventional Stent (b) NiTiNb Stent

Figure 3.18 Schematics of installing stents: a) conventional NiTi stent and b) NiTiNb stent (Takagi et al., 2005).

A plug for sealing high-pressure fuel passage in diesel fuel injectors is another successful application of using NiTiNb SMA (Wu and Wu 2000). Figure 3.19 depicts a typical diesel fuel injector. The fuel passage connects the valve and the cylinder, and should be designed to endure high pressure while fuel has been injected into engine. Since the fuel passage is manufactured with an open end, it requires a secure sealing tool. The sealing plug has been often made of brazing steel, and the plug has sometimes failed due to high pressure. However, in introducing NiTiNb as a sealing tool for the fuel passage, sealing has become more reliable. The martensite NiTiNb plug is stretched longitudinally and manufactured to have a smaller diameter than the passage, and it is inserted into the fuel passage. After the installation, the NiTiNb plug is heated and the plug is able to seal the passage tight due to its shape memory effect. A NiTiNb plug has been very effective in withstanding high pressure in the fuel injector. Figure 3.20 shows NiTiNb plugs used to seal the fuel passage in the diesel fuel injector.

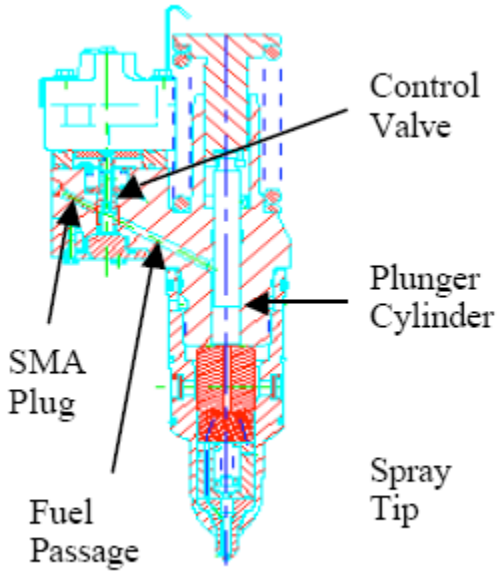

Figure 3.19 Typical fuel injector (Wu and Wu, 2000).

Figure 3.20 NiTiNb plugs (Wu and Schetky, 2000).

CHAPTER 4 PROOF OF CONCEPT – A NUMERICAL APPROACH

4.1 INTRODUCTION

The proposed technique of using SMA spirals for retrofitting of RC bridge columns was first explored analytically. Numerical analyses were conducted to evaluate the performance of the new retrofitting technique compared to one of the currently used techniques using carbon-FRP (CFRP) wraps under cyclic and seismic loadings prior to performing real column tests. The following subsections present description of these analyses and the obtained results.

4.2 MATERIAL MODELING

An important task in this study was to develop analytical models that are capable of describing the uniaxial stress-strain behavior of confined concrete and steel reinforcement. Different models were used to describe the behavior of passively confined concrete using CFRP and actively confined concrete using SMA spirals. The following is a description of the different constitutive material models used in the study.

4.2.1 Concrete confined with CFRP

Previous studies have shown that concrete confined with external CFRP sheets exhibits a stress-strain behavior with an ascending branch followed by either descending or ascending branch with reduced modulus depending on the wraps volumetric ratio (see Figure 2.10) (Mirmiran and Shahawy 1997; Saiidi et. al 2005; Carey and Harries 2005). When the CFRP sheets reach their ultimate strain they rupture suddenly causing the

concrete to fail in a brittle manner. Kawashima et al. (2001) developed an experimental-based model to describe this behavior. This model was adopted during the early stages of this research due to its simplicity and ease of implementation. Kawashima et al. suggested the following equations for the stress f_t and strain ε_t values (See Figure 2.10) at the point where the concrete modulus of elasticity starts degrading:

$$f_t = f_{co} + 1.93\rho_{CF} \cdot \varepsilon_{CFt} \cdot E_{CF} + 2.2\rho_S \cdot f_{yh} \qquad (4.1)$$

$$\varepsilon_t = \varepsilon_{co} + 0.00939\frac{\rho_{CF} \cdot \varepsilon_{CFt} \cdot E_{CF}}{f_{co}} + 0.0107\frac{\rho_S f_{yh}}{f_{co}} \qquad (4.2)$$

where f_{co} and ε_{co} are the strength and strain of the unconfined concrete at the peak point, ρ_{CF} is the volumetric ratio of the CFRP sheets, ε_{CFt} is the spherical strain of CFRP sheets at the point where the modulus of the confined concrete starts degrading (1,800~1,900 μ), E_{CF} is the elastic modulus of CFRP sheets, ρ_s is the volumetric ratio of transverse reinforcement, and f_{yh} is the yield strength of the transverse reinforcement. The concrete modulus during the strain hardening E_g and the ultimate strain of the concrete ε_{cu} could be computed using the following equations:

$$E_g = -0.658\frac{f_{co}^2}{\rho_{CF} \cdot \varepsilon_{CFt} \cdot E_{CF} + 0.098\rho_s f_{yh}} + 0.078\sqrt{\rho_{CF}} \cdot E_{CF} \qquad (4.3)$$

$$\varepsilon_{cu} = 0.00383 + 0.1014\left(\frac{\rho_{CF} \cdot f_{CF}}{f_{co}}\right)^{\frac{3}{4}}\left(\frac{f_{CF}}{E_{CF}}\right)^{\frac{1}{2}} \quad (4.4)$$

where, f_{CF} is the ultimate strength of the CFRP sheets. Finally, Eqs. (4.1)-(4.4) were implemented into the finite element program OpenSees (Mazzoni et al. 2009), which is widely known and used in performing advanced nonlinear seismic analysis on concrete and steel structures based on a fiber section model. The Concrete01 uniaxial material model from the OpenSees material library was utilized after being modified to account for the rupture of the CFRP sheets since the Concrete01 material was not able to capture the rupture of CFRP. The backbone curve of the Concrete 01 material model can be described as an ascending branch following a polynomial equation and a linear descending branch. Also, the cyclic behavior of the concrete model follows the work of Karsan-Jirsa (1969) with the simplified linear unloading/reloading stiffness. In the model, the tensile strength of concrete is ignored. Numerically, concrete strength (f_{co}) and the corresponding strain (ε_{co}), and stress (f_{cu}) and strain (ε_{cu}) at the crushing (ultimate) point of concrete are needed as input in this model. Schematics illustrating the typical behavior of Concrete01 uniaxial material in OpenSees before and after modification (Figure 4.1.a and Figure 4.1.b, respectively), and the constitutive stress-strain relationships used to describe the behavior of cover and core concrete are shown in Figure 4.1c and d, respectively. After the CFRP rupture, a residual stress equal to 20% of the ultimate strength f_{cu} was assumed. In the case of cover concrete, this residual stress was eliminated.

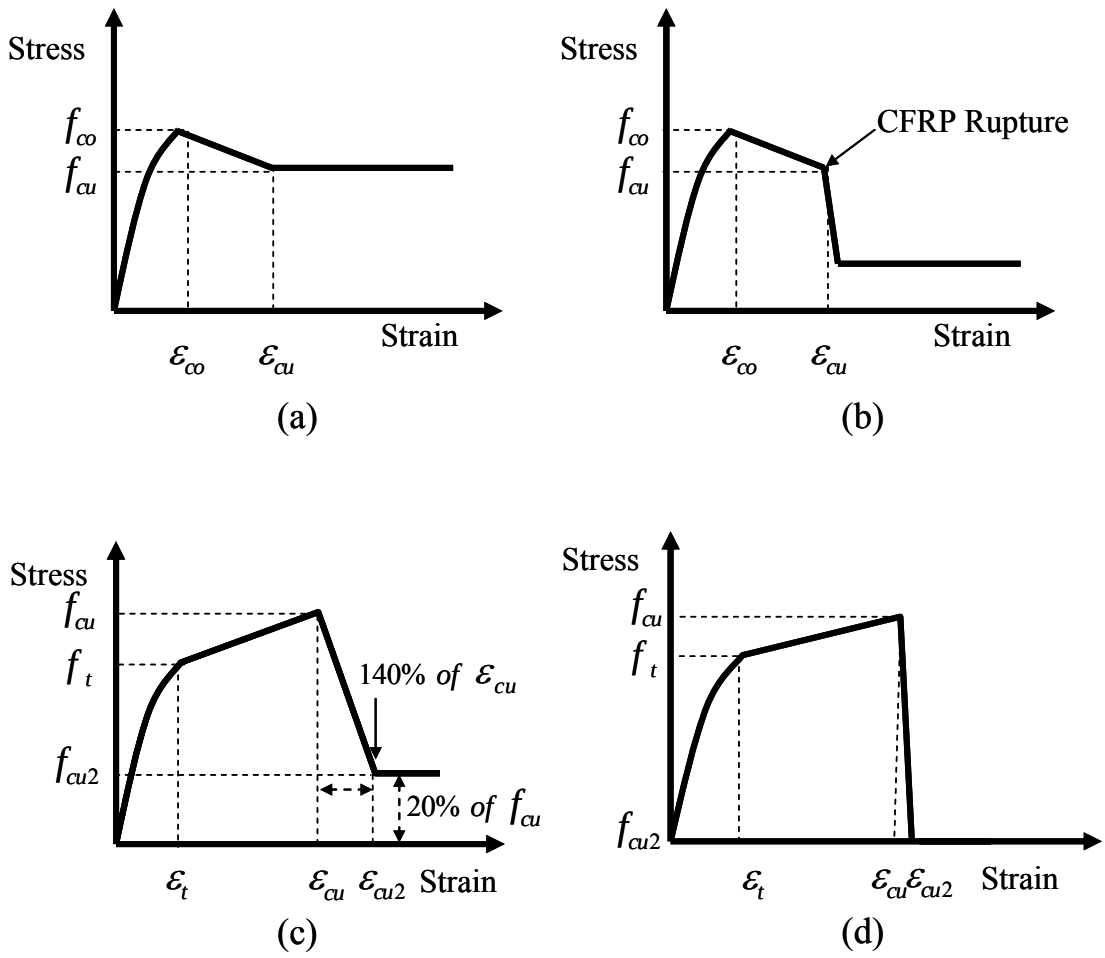

Figure 4.1 Constitutive behaviors of OpenSees Concrete01 material model before (a) and after (b) modification, and backbone stress-strain curves of the concrete core (c) and cover (d) that were used in the analyses.

4.2.2 Concrete confined with SMAs

To incorporate the effects of active lateral pressure developed by the external SMA spiral wrapped around the studied columns. A modified version of the model that was developed by Mander et al. (1998a) was utilized. The main reason for using this model is that in their model, Mander et al. assumed a constant confinement pressure resulting from the yielding of the steel lateral reinforcement. Furthermore, the model was

calibrated using the test data obtained from multiaxial concrete cylinders subjected to active confinement (Schickert and Winkler 1977). The intrinsic feature of the Mander et al. model as an active confinement model has been acknowledged by other researchers including Madas and Elnashai (1992). According to Mander et al., the stress f_{cc} and strain ε_{cc} values at the peak point on the curve could be computed as follows:

$$f_{cc} = f_{co}\left(-1.254 + 2.254\sqrt{1+\frac{7.94 f_l}{f_{co}}} - 2\frac{f_l}{f_{co}}\right) \quad (4.5)$$

$$\varepsilon_{cc} = \varepsilon_{co}\left[1+5\left(\frac{f_{cc}}{f_{co}}-1\right)\right] \quad (4.6)$$

where f_{cc} and ε_{cc} are the peak strength and strain of the confined concrete, respectively, f_{co} and ε_{co} are the peak strength and strain of the unconfined concrete, respectively, and f_l is the effective lateral stress from internal ties and external active confinement using SMA wires. In order to include the effect of active confinement using SMA wires, the lateral pressure f_l was written as

$$f_l = f_{l\_tie} + f_{l\_SMA} \quad (4.7)$$

where f_{l_tie} is the confining pressure induced by the ties at yielding and f_{l_SMA} is the confining pressure induced by the SMA wires. Confining pressure by the ties was computed as follows:

$$f_{l\_tie} = \frac{1}{2} k_e \rho_s f_{yh} \quad (4.8)$$

where ρ_s is the volumetric ratio of the ties, f_{yh} is the yielding strength of the ties, and k_e is a correction factor suggested by Mander et al. to account for the reduction in the confining pressure due to the spacing between the ties. Figure 4.2 shows the schematics of the efficacy of the confining pressure when concrete is confined with internal ties. The correction factor k_e is computed using Eq. 4.9, for circular hoop ties, and Eq. 4.10, for circular spirals:

$$k_e = \frac{(1 - \frac{s'}{2d_s})^2}{1 - \rho_{cc}} \quad (4.9)$$

$$k_e = \frac{1 - \frac{s'}{2d_s}}{1 - \rho_{cc}} \quad (4.10)$$

where ρ_{cc} is the volumetric ratio of longitudinal reinforcement to the core concrete.

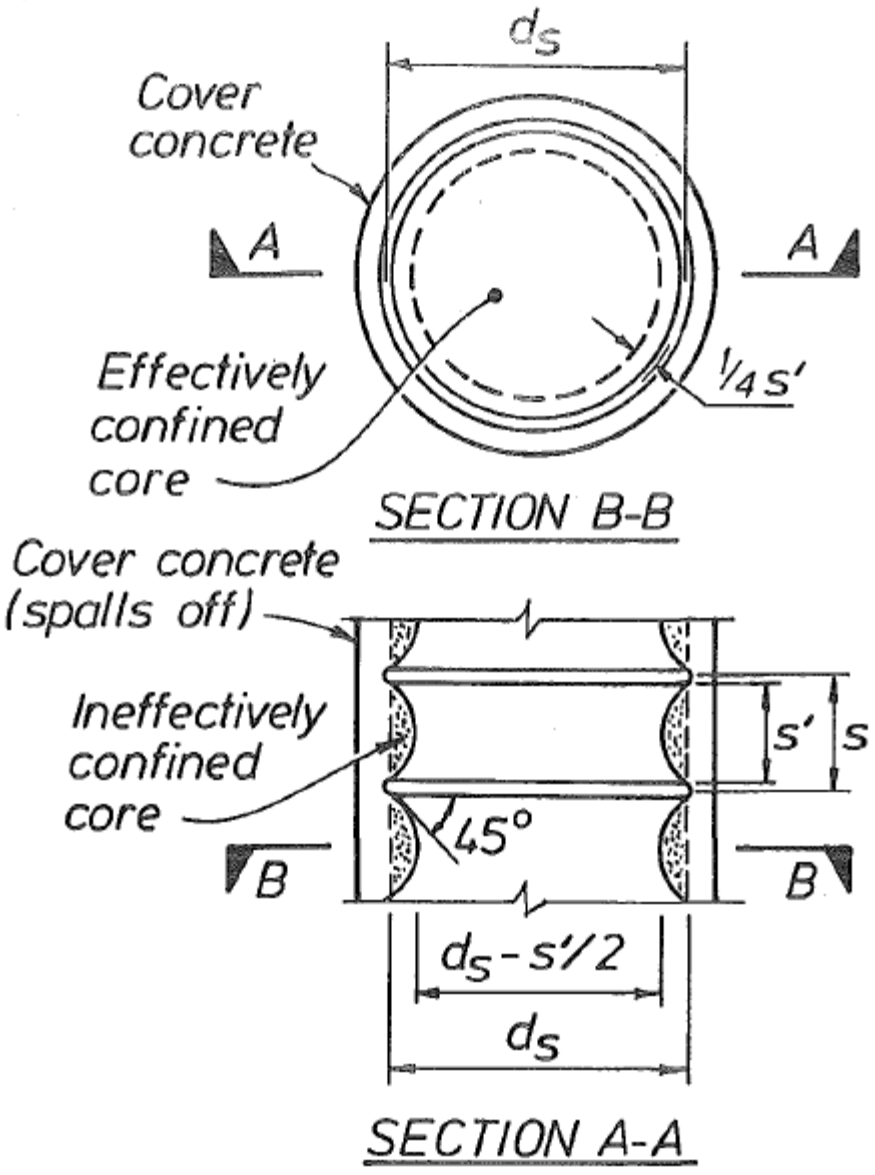

Figure 4.2 Effective confining region of confined concrete with internal ties (Mander at el. 1988a).

The f_{l_SMA} parameter in Eq. 4.7 is directly related to the properties of the SMA wire using the following formula:

$$f_{l\_SMA} = k_e^{SMA}(2A_{SMA}\sigma_{SMA}) / (d \times s) \qquad (4.11)$$

where A_{SMA} is the cross sectional area of the SMA wire, σ_{SMA} is the SMAs recovery stress, d is the diameter of the circular column, and s is the spacing between the spirals, k_e^{SMA} is a correction factor to account for the reduction in the active confining pressure due to the spacing between the SMA spirals, and it follows the same principle described for k_e. The equation for k_e^{SMA} is described in Eq.4.12:

$$k_e^{SMA} = \frac{1 - \frac{s'}{2d}}{1 - \rho_{cc}} \qquad (4.12)$$

where s' is a clear spacing of the SMA spirals.

In order to calculate the ultimate strain of the confined concrete, the energy balance approach which was suggested by Mander et al. was adopted. The additional ductility of confined concrete is expected due to extra energy stored in SMA spirals and internal transverse ties. The energy equilibrium in the confined concrete is assumed when SMA spirals are ruptured:

$$U_{SMA} + U_{sh} = U_{con} + U_{sc} \qquad (4.13)$$

where U_{SMA}, U_{sh}, U_{con}, and U_{sc} are the ultimate strain energy capacity per unit volume of concrete for SMA spiral, transverse reinforcements, concrete and longitudinal reinforcements, respectively. By computing the total area under the stress-strain curve of the SMA spiral until it ruptures, U_{SMA} can be expressed as:

$$U_{SMA} = \rho_{SMA} \int_0^{\varepsilon_{sf}} f_{SMA} d\varepsilon \qquad (4.14)$$

where ε_{sf} is the rupture strain of SMAs and ρ_{SMA} is the volumetric ratio of SMA spirals. Also, U_{sh} can be obtained by multiplying ρ_s (the volumetric ratio of ties) and the area of stress-strain curve of steel ties. U_{con} and U_{sc} are expressed in Eqs. 4.15 and 4.16, respectively:

$$U_{con} = \int_o^{\varepsilon_{cu}} f_c d\varepsilon \qquad (4.15)$$

$$U_{sc} = \rho_{cc} \int_o^{\varepsilon_{cu}} f_{sl} d\varepsilon \qquad (4.16)$$

The OpenSees uniaxial Concrete04 material model was used to describe the behavior of concrete confined with SMA since the Concrete04 model follows the stress-strain curve proposed by Popovics (1973), which the confined model by Mander et al. also follows. The proposed equation by Popovics is presented as:

$$f_c = \frac{f_{cc} xr}{r - 1 + x^r} \qquad (4.17)$$

where $x = \frac{\varepsilon_c}{\varepsilon_{cc}}$ and $r = \frac{E_c}{E_c - E_{\sec}}$. Also E_{sec} is the secant modulus of concrete at the peak point. Figure 4.3 shows the constitutive behavior of the Concrete04 material model. The Concrete04 model adopted the work by Karsan and Jirsa (1964) to describe the cyclic behavior of concrete. Based on experimental results, Karsan and Jirsa (1964) introduced a relationship between the concrete plastic strain and the strain at the unloading point as follows:

$$S_p = 0.145 S_{un}^2 + 0.13 S_{un} \qquad (4.18)$$

where S_p is a ratio of plastic strain to peak strain ($\varepsilon_{pl} / \varepsilon_{cc}$), and S_{un} is the ratio of the strain at the unloading point to the peak strain ($\varepsilon_{un} / \varepsilon_{cc}$).

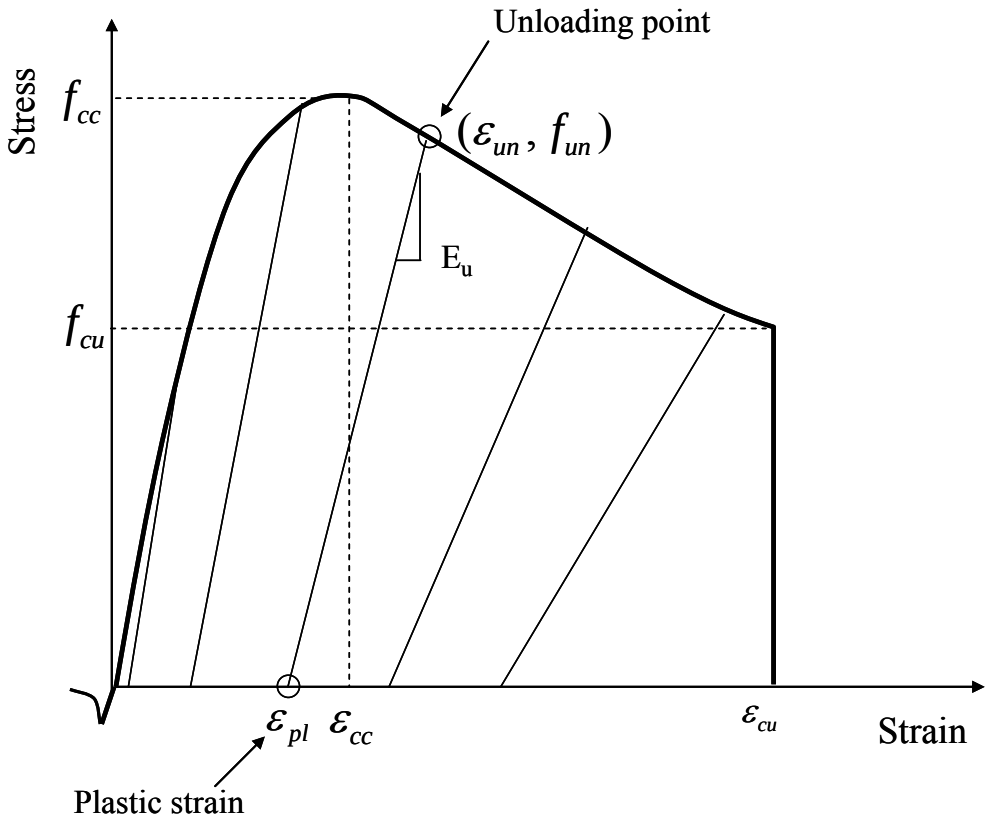

Figure 4.3 Stress-strain constitutive behavior of Concrete04.

Although Karsan and Jirsa expressed a cyclic behavior of concrete with different loading and unloading curves like several other cyclic models (e.g. Mander et al. 1988a model shown in Figure 4.4), the Uniaxial Concrete04 model simplified the cyclic behavior with degraded linear loading/unloading path based on Eq. 4.18. The loading and unloading slope was computed as follows:

$$E_u = (\varepsilon_{un} - \varepsilon_{pl}) f_{un} \qquad (4.19)$$

The Concrete04 material model is also capable of capturing the tensile strength of concrete. in this model, the initial Young's modulus of concrete, and the stresses and strains at the peak and ultimate points of the concrete are the main input parameters.

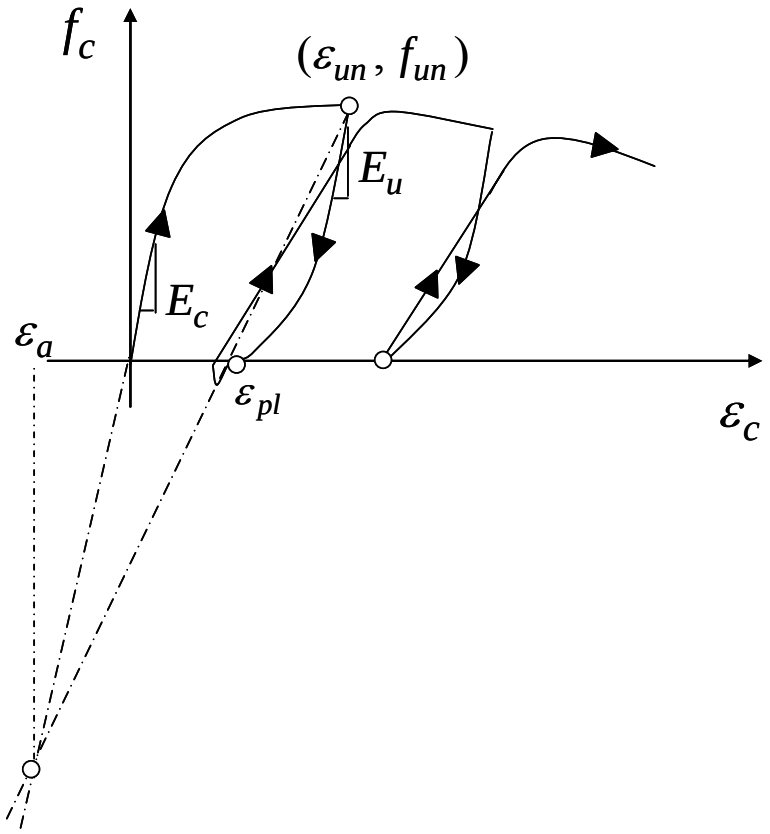

Figure 4.4 Typical cyclic model of concrete.

4.2.3 Steel reinforcement

The behavior of the longitudinal steel reinforcement was described in this study using the uniaxial material OpenSees Steel02 model, which is often known as the Giuffré-Menegotto-Pinto model (Menegotto and Pinto 1973). The model is capable of simulating the hysteretic behavior of steel reinforcement under cyclic loading. The envelop stress-strain curve is bilinear with a clear yielding point and transient region from elastic to plastic behavior. The equation that represented the transient behavior was proposed as follows:

$$\sigma^* = b\varepsilon^* + \frac{(1-b)\varepsilon^*}{(1+\varepsilon^{*R})^{1/R}} \qquad (4.20)$$

where $\varepsilon^* = \frac{(\varepsilon - \varepsilon_r)}{(\varepsilon_o - \varepsilon_{r)}}$, $\sigma^* = \frac{(\sigma - \sigma_r)}{(\sigma_o - \sigma_r)}$, σ_o and ε_o are the stress and strain at a intersection point where the elastic and the strain hardening asymptotes meet, and σ_r and ε_r are the point at the last reversal. Also, b is a hardening ratio of steel and R is an independent parameter which defines the curvature of the transition region. Figure 4.5 shows a typical hysteretic behavior of the Steel02 model under cyclic loading.

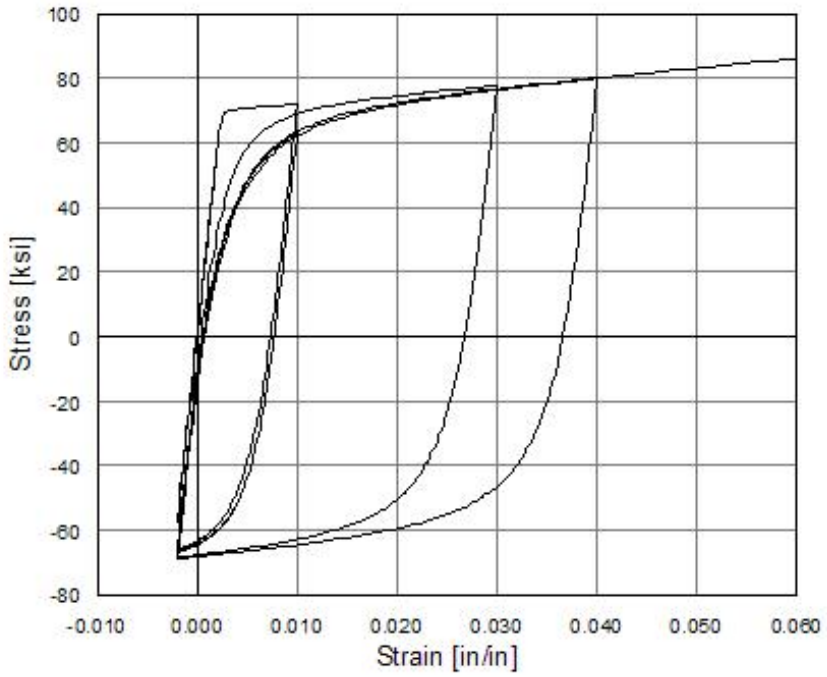

Figure 4.5 Hysteretic behavior of steel reinforcement based on Giuffré-Menegotto-Pinto model under cyclic loading - Steel02 (OpenSees, 2010).

4.3 BRIDGE COLUMN MODELING

Nonlinear reinforced concrete bridge column model was defined based on the geometry and properties of the columns that were tested by Kawashima et al. (2001). In that study, the authors conducted a series of quasi-static lateral cyclic tests on CFRP wrapped columns. This helped in validating the analytical model using the experimental results published by Kawashima et al. (2001).

4.3.1 Model description

Schematics showing the adopted bridge column and its numerical model are presented in Figure 4.6. Table 4.1 also presents a summary of the column's properties and dimensions. As illustrated in the figure and table, the column had a circular section with a diameter equal to 400 mm (15.7 in) and a concrete cover of 35 mm (1.4 in). The effective height of the column was 1350 mm (53.1 in) and the length of the confined region where the CFRP sheets were applied was 1000 mm (39.3 in) from the base. An axial compression load of 185 kN (41.6 kips) representing 5% of the column's gross sectional nominal capacity was applied at the top of the column. The compressive strength of the unconfined concrete was 30 MPa (4350 psi) and the yield strength of the longitudinal and lateral steel reinforcements were 374 MPa (54 ksi) and 363 MPa (53 ksi), respectively. The OpenSees nonlinear displacement-based beam-column element, which assumes displaced shapes of a structure in a displacement field and requires several elements to represent the deformation of a structure with acceptable accuracy (Scott and Fenves 2006), was utilized with five integration points to develop the numerical model of the column at the confined region (elements E1-E3 in Figure 4.6.b) and the footing (element E4). A fiber section was assigned to the beam-column elements to describe their nonlinear behavior. In the fiber section, different constitutive relations are utilized for the cover concrete, core concrete, and steel reinforcement fibers (see Figure 4.6.c). As it was discussed earlier, the Concrete01 material was used after being modified for concrete confined with CFRP. The values obtained from the modified Mander et al. model was implemented in the OpenSees Concrete04 uniaxial material model and used in the analysis for concrete confined with SMA spirals. An elastic beam-column element was

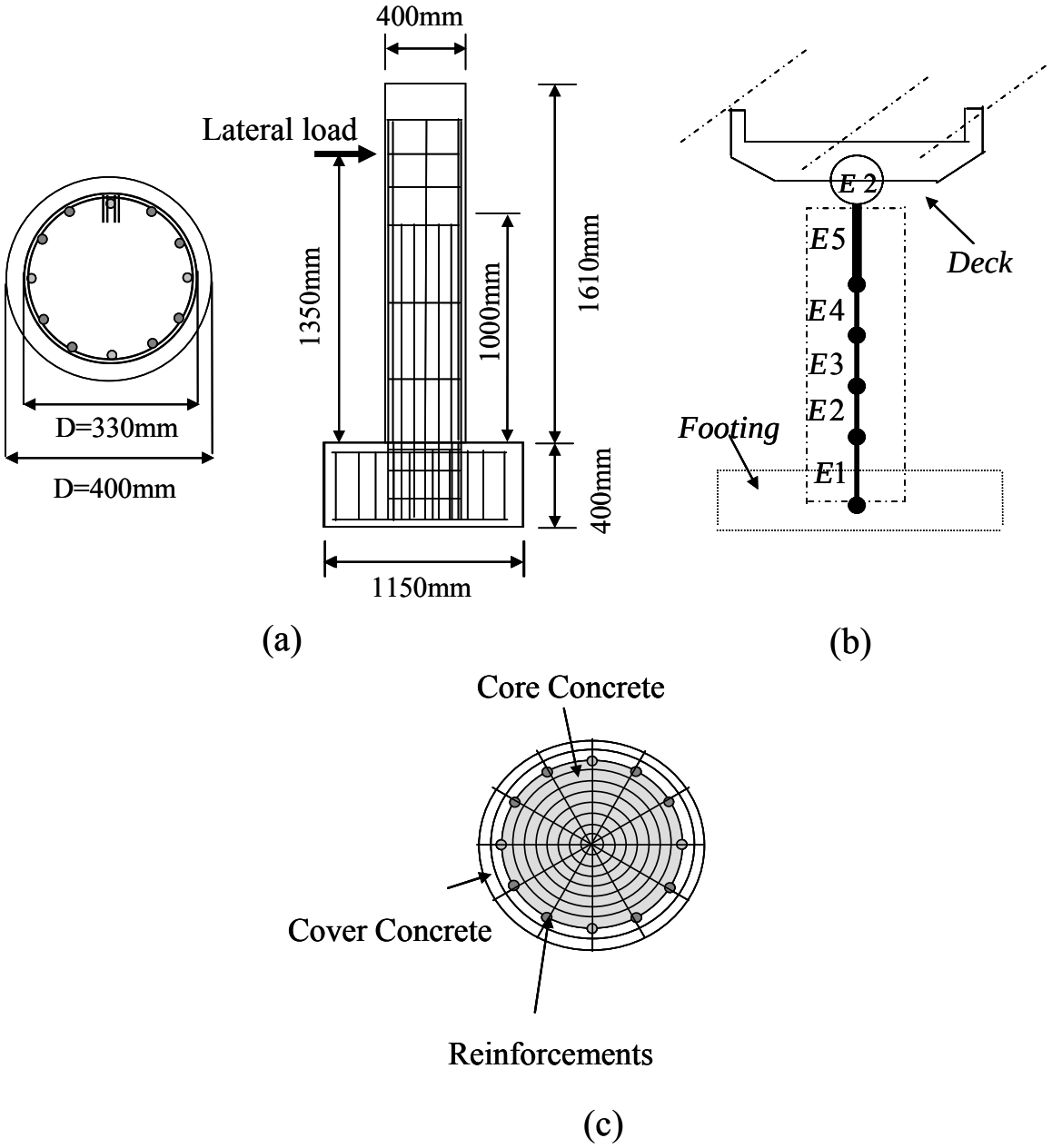

Figure 4.6 Schematic of the column tested by Kawashima et al. (a) and its analytical column (b) and fiber section of the analytical column (c).

Table 4.1 Material properties used in the reinforced concrete column adopted in the study

Property	Value
Section Diameter (mm)	400
Effective Height , h(mm)	1350
Longitudinal Reinforcement ratio (%)	1.89
Volumetric Ratio of Tie Reinforcement (%)	0.13
Compressive Strength of Concrete (MPa)	30
Longitudinal Reinforcement	Yield Strength =374MPa
Tie Reinforcement	Yield Strength =363MPa
Axial Force (kN)	185

used for the remaining part of the column (element E5). A uniaxial material model with isotropic strain hardening (Steel02) was used to describe the behavior of the longitudinal reinforcement (see Figure 4.5). A mass of 18,858 kg (41575 lb) was lumped at the top of the column. For the SMA spiral, f_{l_SMA} was designed to be the same amount of the passive lateral pressure provided from CFRP wraps at the onset of CFRP's rupture.

4.3.2 Numerical model validation

The bridge column model used in this study was validated by comparing its behavior with the experimental behavior reported by Kawashima et al. (2001) for a

column wrapped with one layer of CFRP (0.11 mm thick.), which represents a volumetric ratio of 0.11%. The analytical model was subjected to the same displacement-controlled cyclic loading protocol that was used during the test. The column was displaced with an increment of 0.5%-drift until reaching a maximum drift of 5%. Figure 4.7 shows a comparison between the force-displacement relationships resulting from the analysis and experiment. The figure shows that the analytical model was capable of capturing the behavior of the experimental column throughout the loading protocol with an acceptable level of accuracy in terms of strength and stiffness. Only 4% difference was observed between the peak strength values of the analytical and experimental columns.

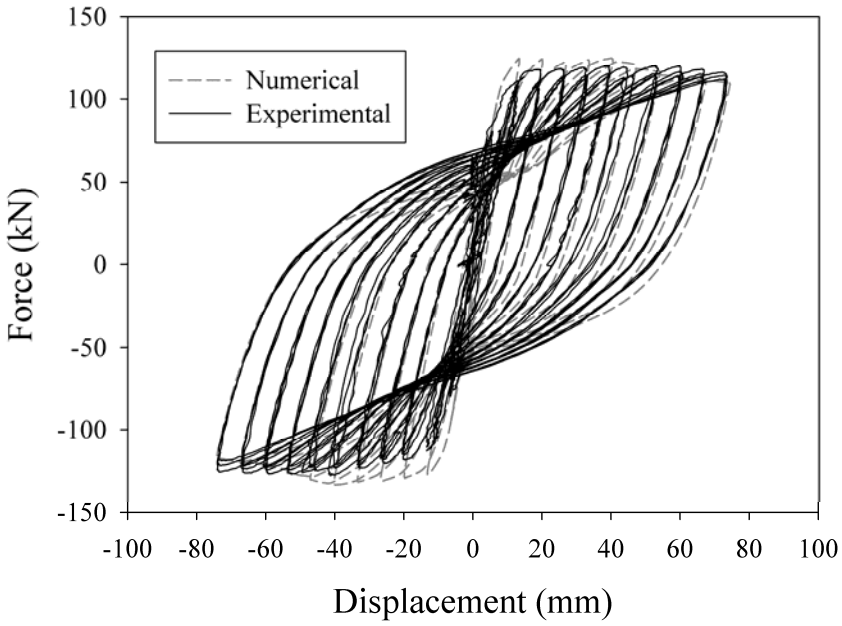

Figure 4.7 Comparison between the analytical and experimental force-displacement results.

Since no experimental data on RC columns confined with SMA spirals was available at the time this analysis was conducted, the numerical model of concrete confined with SMA spirals based on the modified Mander et al. model was validated using the results of uniaxial compression tests conducted on concrete cylinders confined with SMA spirals (Andrawes et al. 2010). 152 mm x 305 mm (6 in x 12 in) concrete cylinders were cast and cured in a moisture controlled room, and the cylinders were confined with 3 mm (0.12 in) diameter SMA wires. Figure 4.8 shows the prepared concrete cylinder before testing.

Figure 4.8 Concrete cylinder confined with SMA spirals (Andrawes et al. 2010).

Figure 4.9 shows that the analytical model was able to successfully capture the experimental behavior, and thus, the modified Mander et al. model was adopted for the rest of the analysis. The result in the figure showed that the confining pressure and recovery stress of SMAs were found to be 0.903 MPa (130 psi) and 255 MPa (37 ksi) respectively in Eq. 4.11 of the suggested modified Mander model. In the application of the active lateral pressure (f_{l_SMA}), the spacing of the SMA wires is considered a key variable in controlling the active pressure according to Eq. 4.11. In this numerical analysis, therefore, the recovery stress of SMAs was assumed to be 255 MPa (37 ksi) based on the calibrated result of the uniaxial concrete cylinder test conducted by Andrawes et al. 2010.

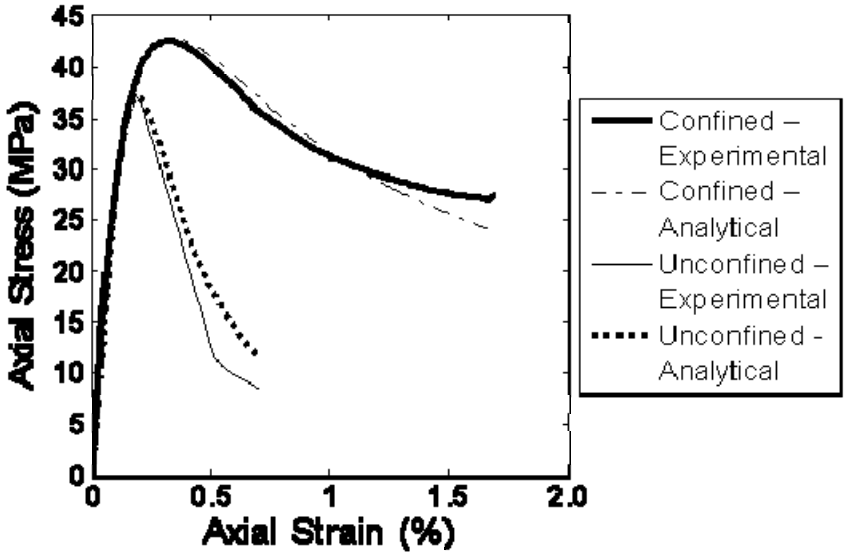

Figure 4.9 Experimental and analytical stress-strain results for SMA confined and unconfined concrete cylinders (Andrawes et al. 2010).

4.4 NUMERICAL STUDY

After the numerical model was validated it was utilized to conduct a comparison between the efficacy of SMA spirals and CFRP wraps in improving the behavior of RC columns under cyclic and seismic loadings. The amount of confinement of the CFRP retrofitted columns was varied by using one, two, and three 0.11 mm (0.0043 in)-thick CFRP sheets, which correspond to a volumetric ratio of 0.11% (Case I), 0.22% (Case II) and 0.33% (Case III) respectively. Similarly, the amount of SMA confinement was varied by changing the pitch spacing of the SMA spiral. In order to provide a common base for the comparison between the two retrofitting techniques, the amount of active confining pressure provided by the SMA spiral was taken equal to the passive confining pressure provided by the CFRP wraps just before their rupture. Table 4.2 shows the number of CFRP wraps, CFRP volumetric ratio, SMA spiral pitch spacing, and lateral confining pressure corresponding to each of the three studied cases.

Table 4.2 Properties of the CFRP sheets and SMA spirals used in the three studied cases

Case No.	**Case I**	**Case II**	**Case III**
No. of CFRP wraps	1	2	3
ρ_{CF} (%)	0.11	0.22	0.33
Thickness of CFRP wraps (mm)	0.11	0.22	0.33
Confining pressure(MPa)	1.2	2.4	3.6
Diameter of SMA wires (mm)	10	10	10
SMA spiral patch spacing (mm)	76	40	27

4.4.1 Cyclic loading analysis

The studied columns were subjected to a displacement-controlled cyclic loading with a 0.5%-drift increment until reaching a maximum drift of 8%. Figure 4.10 shows the force-displacement relationship of the CFRP and SMA retrofitted columns in Case I, Case II and Case III. As shown in the figure, in all three cases, the columns wrapped with SMAs showed superior behavior to CFRP wrapped columns in terms of load-carrying capacity.

The SMA retrofitted columns were able to maintain their load-carrying capacity until the end of the loading protocol, while the CFRP retrofitted columns confined with one, two, and three wraps of CFRP started losing their capacity at drift values of 3%, 4% and 5%, respectively. These drift values correspond to where the CFRP sheets started experiencing significant rupture. At the point of maximum lateral drift (8%-drift), a closer comparison reveals an increase in the peak strength of the SMA wrapped columns relative to the CFRP wrapped columns by 38%, 33% and 26% in Cases I, II, and III, respectively.

In order to obtain a better understanding of the level of damage exerted on the analyzed columns, a comparison between the concrete and longitudinal steel stress-strain behaviors using SMA spirals and CFRP wraps is presented in Figure 4.11. In all three cases (I, II, and III) applying active confinement using SMA spirals resulted in an early increase in the concrete compressive strength compared to the case with CFRP sheets. This boost in strength resulted in a significant reduction in the level of concrete damage, which was assessed by the amount of reduction in the maximum compressive strain. The reduction in concrete maximum strain in Cases I, II, and III was found to be 71%, 71%,

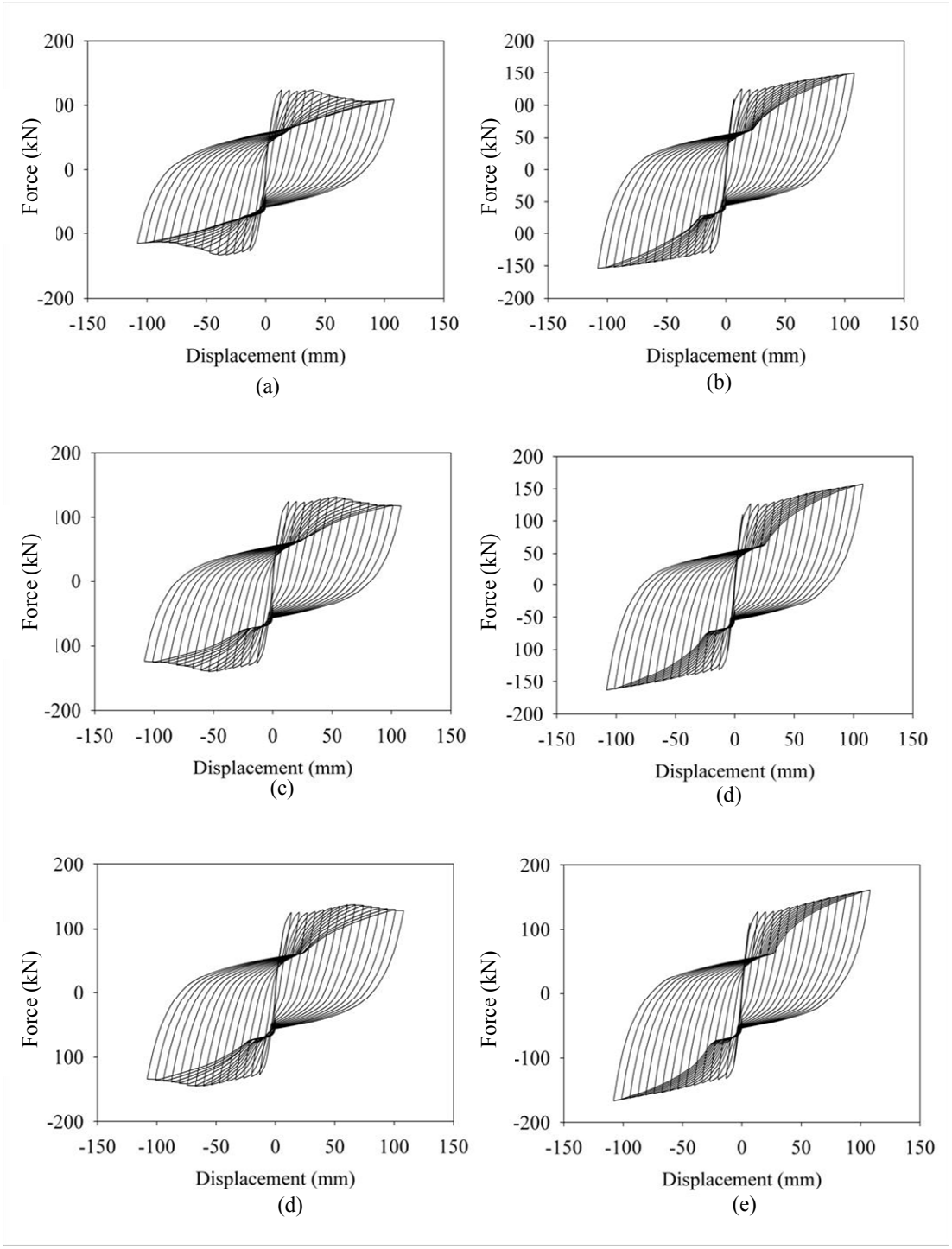

Figure 4.10 Force-displacement relationship of the SMA and CFRP retrofitted columns under cyclic loading: (a) CFRP column - Case I, (b) SMA column - Case I, (c) CFRP column - Case II, (d) SMA Column - Case II, (e) CFRP column - Case III , and (f) SMA column – Case III.

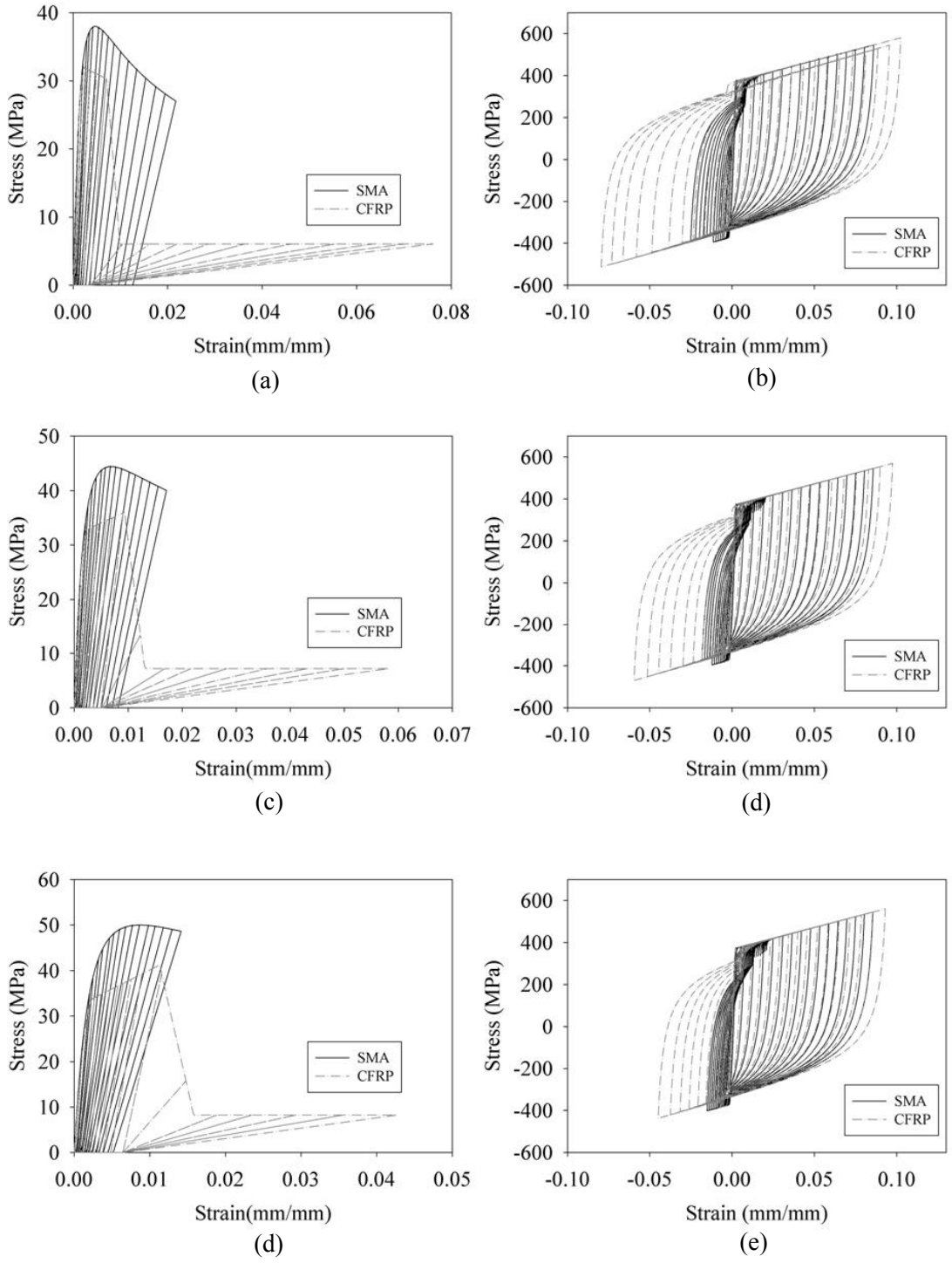

Figure 4.11 Axial stress vs. strain of concrete core and longitudinal steel of the SMA and CFRP retrofitted columns under cyclic loading: (a) Core concrete - Case I, (b) Steel - Case I, (c) Core concrete - Case II, (d) Steel - Case II, (e) Core concrete- Case III , and (f) Steel – Case III.

and 67%, respectively. The results presented in Figure 4.11 also illustrate that using active confinement reduced the deformation demands on longitudinal steel reinforcements by 16%, 12%, and 8% in Cases I, II, and III, respectively.

4.4.2 Seismic analysis

The behaviors of the retrofitted columns were investigated under a suite of six ground motion records from historic earthquakes. Table 4.3 presents a summary of the characteristics of the records used in the analysis. At the fundamental period of the column (T_1 = 0.18sec.), the average spectral acceleration of the records was found to be 0.98g. In order to provide a common base for the comparison between the behaviors of the columns under the six records and to introduce a level of damage to the columns that would make the option of retrofitting necessary and effective, the records were scaled to a spectral acceleration value of 1.5g at the fundamental period of the column. The peak ground acceleration (PGA) values before and after scaling are shown in Table 4.3.

Three types of response parameters were identified in this analytical study as the key factors that would define the efficacy of the proposed SMA retrofitting technique. These response parameters and their definitions are: 1) column strength, represented by the maximum lateral force resisted by the column at the point of maximum drift, 2) effective column stiffness, which is defined as the secant stiffness at the point of maximum drift, and 3) residual column drift, which is defined as the lateral drift of the column at the end of the record. A summary of the results of each of these three response parameters under the six ground motion records are presented in the following subsections.

Table 4.3 Characteristics of the six ground motion records used in the study.

Earthquake	Record Station	Distance (km)	Magnitude (Ms)	Before Scaling PGA (g)	After Scaling PAG(g)	Sa (g) $\|_{T1}$
1980, Victoria	6604 Cerro Prieto	34.8	6.4	0.62	0.99	0.94
1989, Loma Prieta	57217 Coyote Lake Dam	21.8	7.1	0.48	1.03	0.61
1994, Northridge	90014 Beverly Hills	20.8	6.7	0.62	0.7	1.32
1979, Imperial Valley	5115 El Centro Array #2	10.4	6.9	0.32	0.56	0.85
1992, Cape Mendocino	89324 Rio Dell Overpass	18.5	7.1	0.55	0.75	1.1
1980, Mammoth Lakes	54214 Long Valley dam	20.0	6	0.92	1.3	1.07

4.4.2.1 Column strength

Figure 4.12 presents a comparison between the normalized strength values of the columns wrapped with SMA spirals and CFRP wraps under the six scaled records. The strength values were normalized relative to the strength of the as-built column. The effect of changing the level of confining pressure was included in the figure by studying Cases I, II, and III, which represent different values for CFRP volumetric ratio and pitch spacing of SMA spirals (see Table 4.2). The results shown in the figure illustrate that in general, both SMA spirals and CFRP wraps were effective in increasing the column strength compared to the as-built case. However, the average increase in the strength in the case of

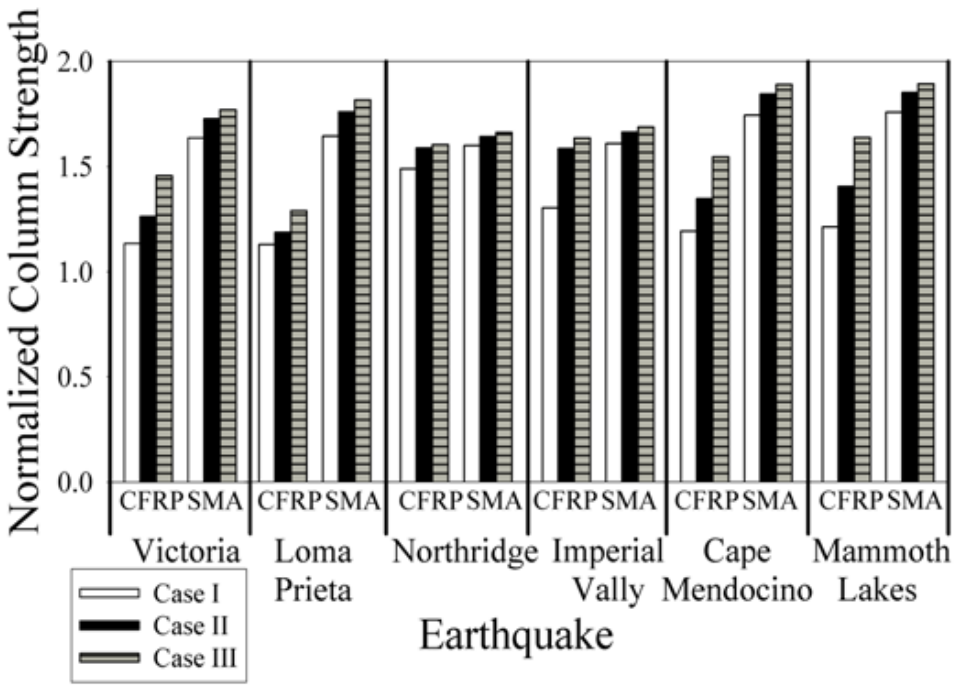

Figure 4.12 Normalized column strength using SMA spirals and CFRP wraps under the six earthquake records.

SMA spirals was 73%, while in the case of CFRP wraps, it was only 39%. Comparing the results of Cases I, II, and III shows that increasing the level of confinement tends to reduce the difference between column strength observed using both retrofitting techniques. This observation was expected since the seismic demand was kept the same in all three cases. On average, applying the active confinement technique using SMA spirals increased the strength of studied columns by 25% compared to passive confinement technique using CFRP wraps. The superior performance of the SMA spirals relative to the CFRP wraps could be attributed to the early increase in concrete strength associated with active confinement. To demonstrate this argument further, Figure 4.13 is presented as an example of the force-displacement relationships typically obtained from this analysis. The behavior shown is for Case-II under the scaled Coyote Lake Dam

Station record from the 1989 Loma Prieta earthquake. The behavior of the as-built column is also shown for comparison.

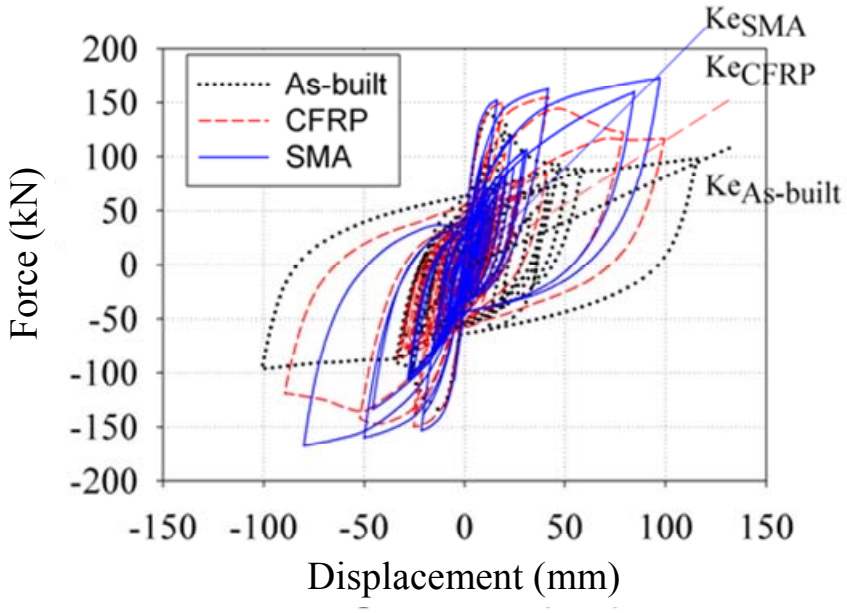

Figure 4.13 Force-displacement relationship of Case II and as-built column under the scaled Coyote Lake Dam Station record from the 1989 Loma Prieta earthquake.

4.4.2.2 Effective stiffness

The degradation in the structural effective stiffness is an indication of the amount of damage experienced by the structure during the earthquake and thus is considered a key factor that defines the seismic behavior of structures. Figure 4.14 shows the normalized effective stiffness of studied RC columns when retrofitted with SMA spirals and CFRP wraps and subjected to the suite of records. In general, it could be observed that in all cases, the effective stiffness of SMA retrofitted columns was higher than that of CFRP wrapped columns. Based on the average of all cases, using SMA spirals improved

the effective strength by 34% compared to CFRP wraps. This result demonstrates the superiority of the SMA confining technique in limiting the progressive damage in the retrofitted column. Taking a closer look at the behaviors shown earlier in Figure 4.13 reveals that such superiority could be attributed to the significant damage encountered due to CFRP rupture. In this particular case shown in Figure 4.13, the effective stiffness of the CFRP wrapped column degraded by 34% more than that of the SMA retrofitted column.

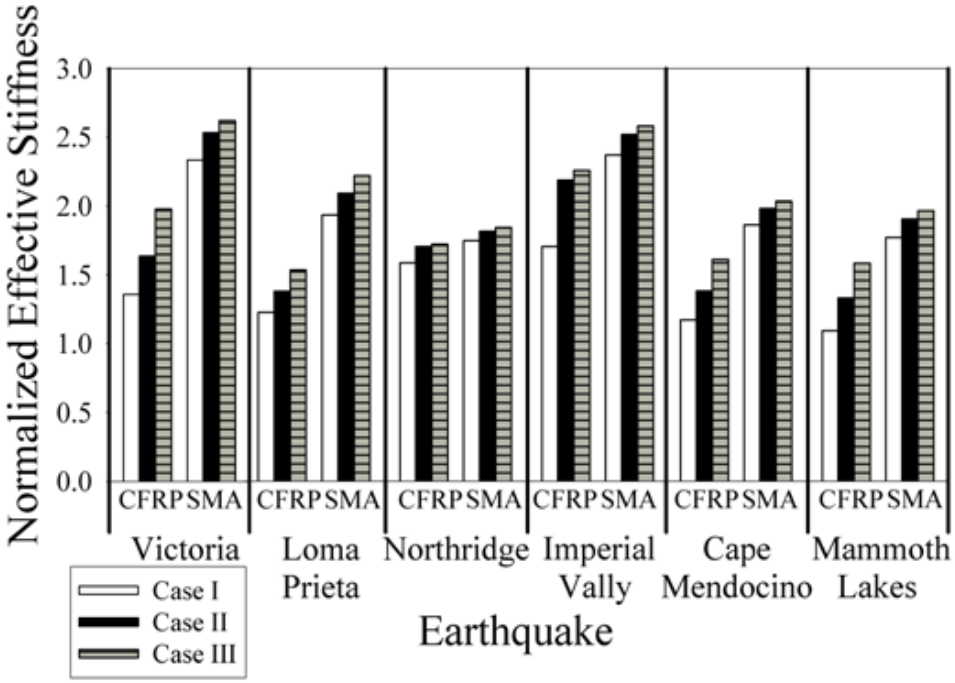

Figure 4.14 Normalized effective stiffness using SMA spirals and CFRP wraps under the six earthquake records.

4.4.2.3 Residual drift

Residual drift of bridge columns is an important factor that governs the functionality of the bridge after an earthquake. The normalized residual drifts of the studied retrofitted columns under the six ground motion records are depicted in Figure 4.15. The average residual drift of the SMA and CFRP retrofitted columns was 66% and 41% smaller than that of the as-built column, respectively. In most of the cases shown in the figure, the SMA retrofitted columns exhibited less residual drifts at the end of the records compared to CFRP retrofitted columns. As illustrated earlier, these less residual drifts of the columns with SMA spirals were expected due to the less demand exerted on the concrete and reinforcing steel, which resulted in a reducing the level of inelastic (permanent) deformations compared to residual drifts of the columns with the CFRP wraps.

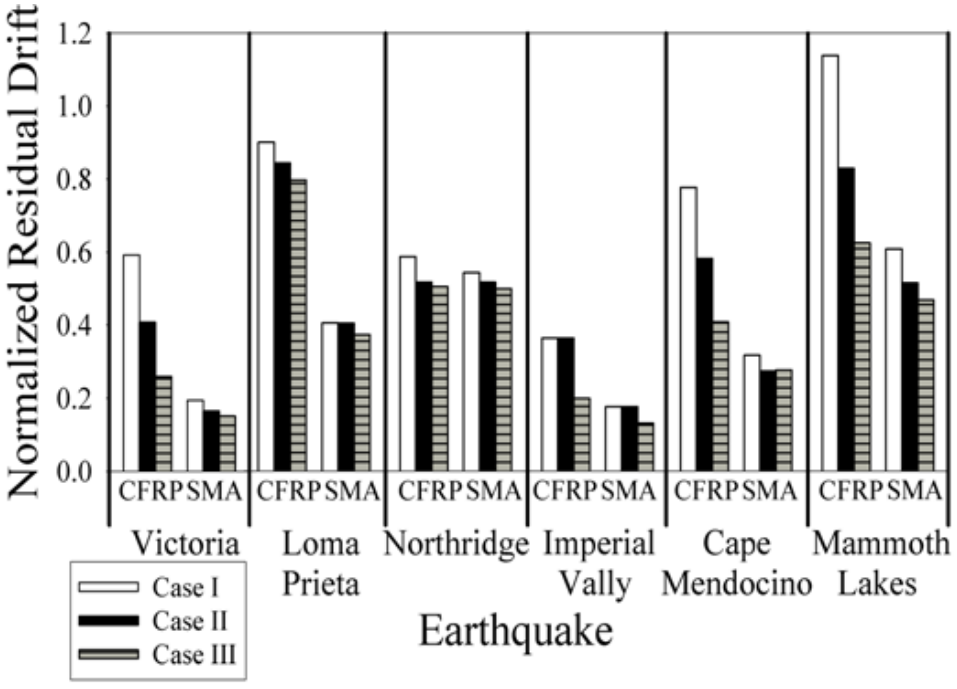

Figure 4.15 Normalized residual column drifts using SMA spirals and CFRP wraps under the six earthquake records.

CHAPTER 5 MATERIAL TESTING

After numerically exploring the new active confinement technique using SMA spirals, it was important to examine experimentally the new confinement technique on the material level. Therefore, a testing program comprising the thermo-mechanical testing of NiTiNb SMA wires and the uniaxial compression testing of concrete cylinders confined with SMA spirals and FRP wraps was conducted. A description of the tests and their results are presented in this chapter.

5.1 DIFFERENTIAL SCANNING CALORIMETER TEST

In order to determine the phase transformation temperatures of the NiTiNb used in this study (i.e. M_f , M_s , A_s , and A_f), differential scanning calorimeter (DSC) testing was conducted with a heating rate of 20 ^{o}C/min. A total of 30 mg (66E-6 lb) of NiTiNb particles were prepared and encapsulated for the DSC testing. Figure 5.1 shows the used DSC testing machine (a) and the prepared NiTiNb sample after encapsulation (b). The original testing plans consisted of two successive thermal cycles. For the first cycle, the testing would start at room temperature (19 ^{o}C (68 ^{o}F)) and then increase to 190 ^{o}C (374 ^{o}F) where the temperature is held constant for two minutes. This is followed by reducing the temperature below -100 ^{o}C (212 ^{o}F), where the temperature is held for two minutes. For the second cycle, the specimen is reheated to 190 ^{o}C (374 ^{o}F). The process of cooling the sample for the second cycle did not need to be carried out during testing since the reheated NiTiNb was found to undergo no more phase transformation.

(a)

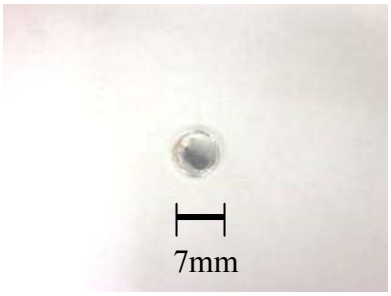

(b)

Figure 5.1 DSC testing machine (a) and the encapsulated NiTiNb sample (b).

The DSC results are shown in Figure 5.2. When increasing the temperature, a clear peak was observed indicating that NiTiNb in the martensite phase transformed into the austenite phase, and the austenite start and finish temperatures (A_s and A_f) were recorded as 68 ^{o}C (154.4 ^{o}F) and 76 ^{o}C (168.8 ^{o}F), respectively; however, determining the martensite start and finish temperatures (M_f and M_s) was not possible since they were both below the lowest temperature that could be recorded by the DSC machine (-125 ^{o}C

(-193 ^{o}F)). During the second cycle, it was concluded that NiTiNb was still in austenite phase although the temperature of the NiTiNb sample dropped below -100 ^{o}C (-148 ^{o}F) since the DSC results did not show any heat flow decrease or increase while cooling (see Figure 5.2.a) or heating (see Figure 5.2.b) the sample.

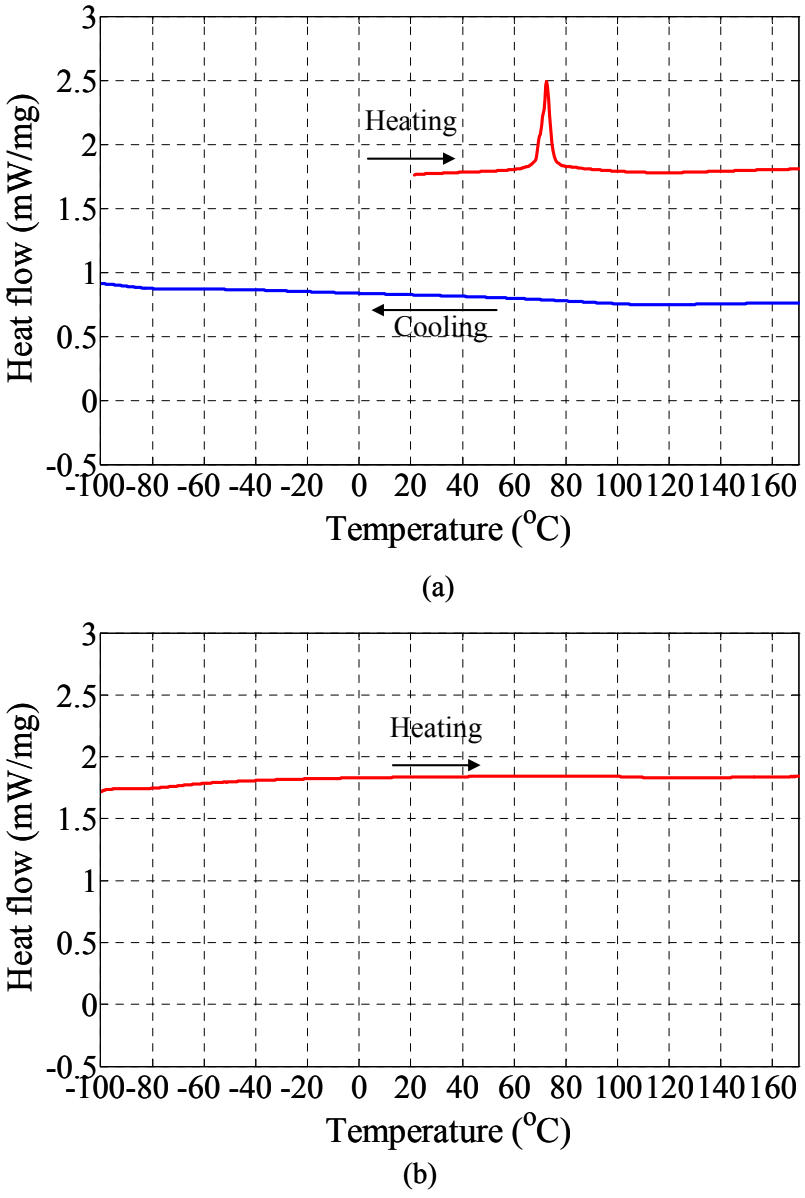

Figure 5.2 DSC result of NiTiNb alloy: (a) first cycle, and (b) second cycle.

5.2 RECOVERY STRESS TESTS OF SHAPE MEMORY ALLOYS

This experimental work focused on examining the recovery stress of NiTiNb SMA wires. The SMA wires used in the study were round with a cross section diameter of 2 mm (0.08 in). They were provided by the manufacturer in a prestrained condition (approximately 6.4% prestrain). In order to examine the recovery stress of the SMA wires at various temperatures, thermo-mechanical tests were conducted using a 89 kN (20 kips) MTS uniaxial servo-controlled hydraulic machine (see Figure 5.3.a). In these tests, the SMA wire was clamped at both ends by the grips of the hydraulic frame then heated as shown in Figure 5.3.b. In order to ensure uniform distribution of the temperature throughout the entire length of the wire, it was heated by passing an electric current throughout its length. Each end of the SMA wire was connected to a power supply that controls the output current. By providing about 20 A of electrical current into the SMA wire, the wire was gradually heated until a maximum recovery stress was observed. Heating the SMA wire triggers its shape recovery, and since the wire was fully restrained at both ends, a recovery stress was induced in the wire. The recovery stress was calculated based on the force measured by the load cell in the hydraulic machine divided by the area of the wire. To monitor the wire's temperature during testing, a thermocouple was attached to the wire.

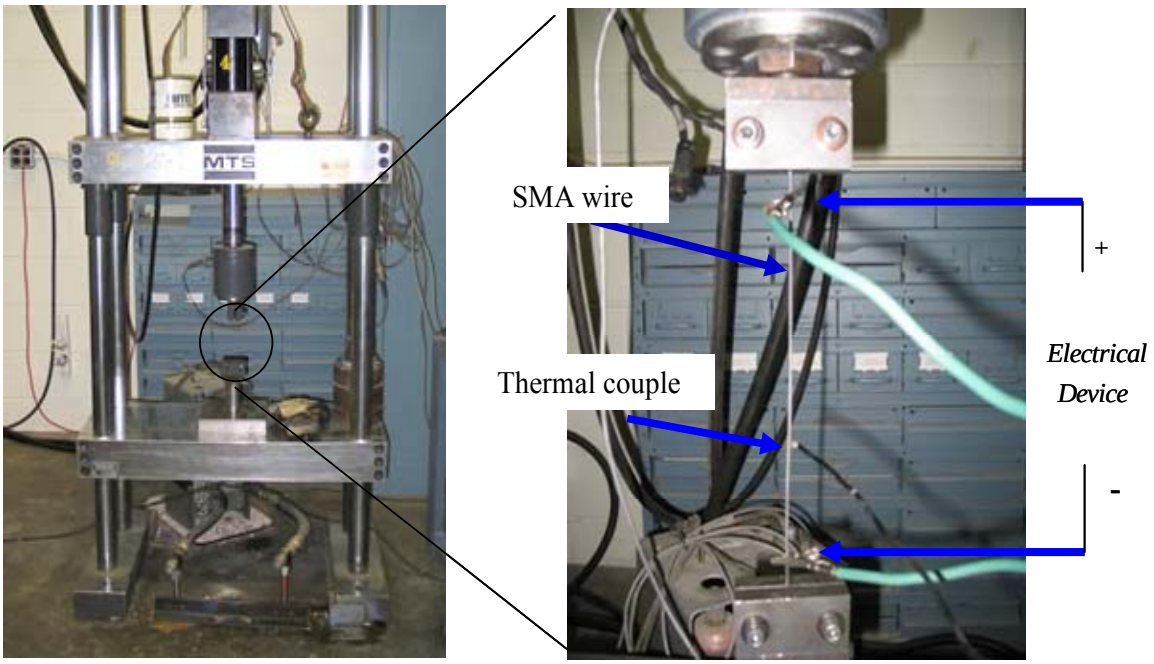

Figure 5.3 89 kN MTS uniaxial servo-controlled hydraulic machine (a) and recovery stress test set up of NiTiNb SMA wire (b).

Figure 5.4 shows the variation of recovery stress with time during the testing of the prestrained SMA wire and the variation of temperature with time. At the onset of heating, the recovery stress started increasing until it reached a maximum value of 565 MPa (82 ksi) at a temperature of 108 ^{o}C (226 ^{o}F). After which, the wire was left to cool. A slight decrease was observed in the recovery stress after the electric source was cut. The recovery stress then converged and became stable at a value of 460 MPa (67 ksi) at a room temperature of 16 ^{o}C (61 ^{o}F).

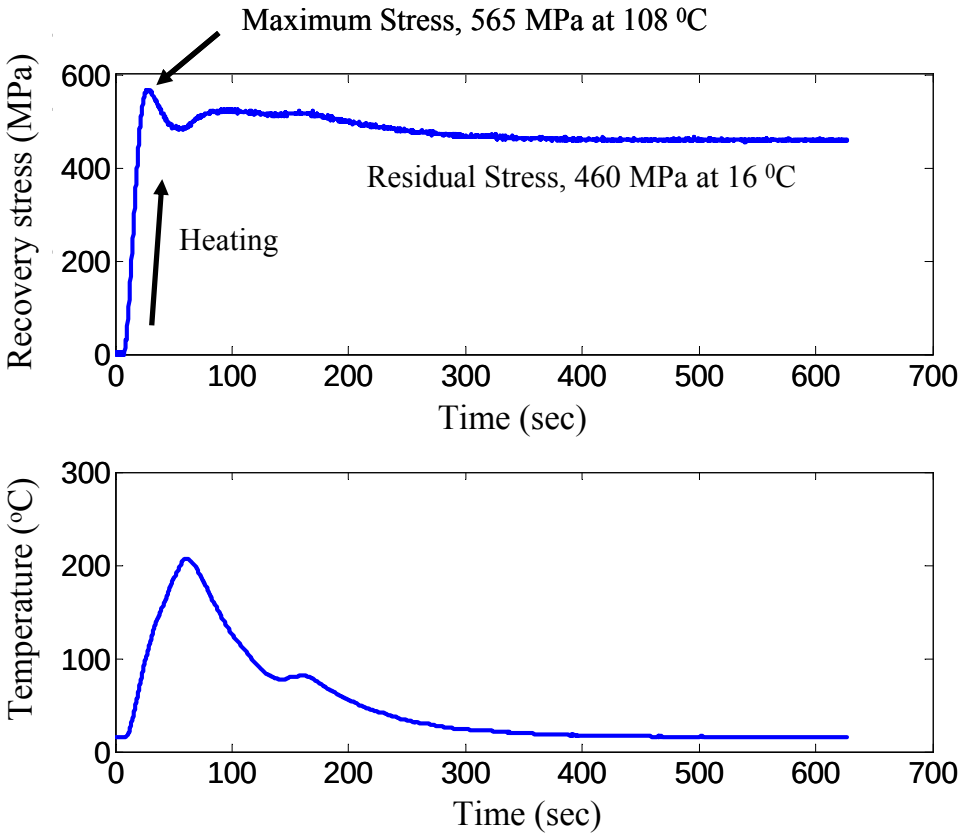

Figure 5.4 Variation of recovery stress (top) and temperature (bottom) with time during recovery stress test.

In order to examine the relationship between the level of the recovery stress induced by heating and the prestrain value, the same recovery stress test described above was conducted on three SMA wire specimens. The three specimens were prestrained to different strain values of approximately 6.4%, 4.5% and 2.8%. Figure 5.5 shows the relationship between the recovery stresses (maximum and residual) and the prestrain value. As shown in the figure, the recovery stress induced in the wires increased linearly with the amount of prestrain. When the level of prestrain of the wire increased from 2.8% to 6.4%, the maximum and residual recovery stress increased by 22% and 17%,

respectively. In general it was observed that the average residual recovery stress was approximately 80% of the maximum recovery stress.

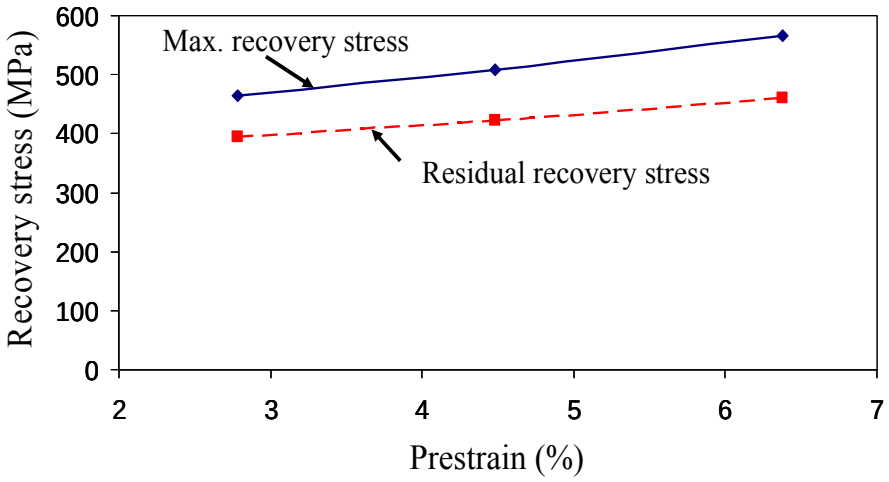

Figure 5.5 Relationship between recovery stress induced in the SMA wire and its prestrain value.

To examine the mechanical behavior of the prestressed SMA wires after reaching a stable recovery stress, the already prestressed wires were subjected to cyclic loading. The displacement-controlled cyclic load was applied using the MTS hydraulic machine with a strain rate of 0.5%/min. Figure 5.6 shows the cyclic behavior of the prestressed SMA wire which had a prestrain value of 6.4%. It might be important to note that prior to applying the cyclic load, the recovery stress developed in the wire will confine the concrete actively. However, when the concrete expands laterally (dilates) under axial loading, additional passive confinement is provided by the SMA spiral as a result of the additional hoop stresses induced in the wires. Therefore, in real applications, the confining pressure provided by the SMA spiral is partially but dominantly active (prior to concrete loading) and partially passive (after concrete loading). The cyclic tests

demonstrated that the confining stress induced in the SMA spiral is stable even when the concrete is subjected to cyclic loading such as in the case of seismic events.

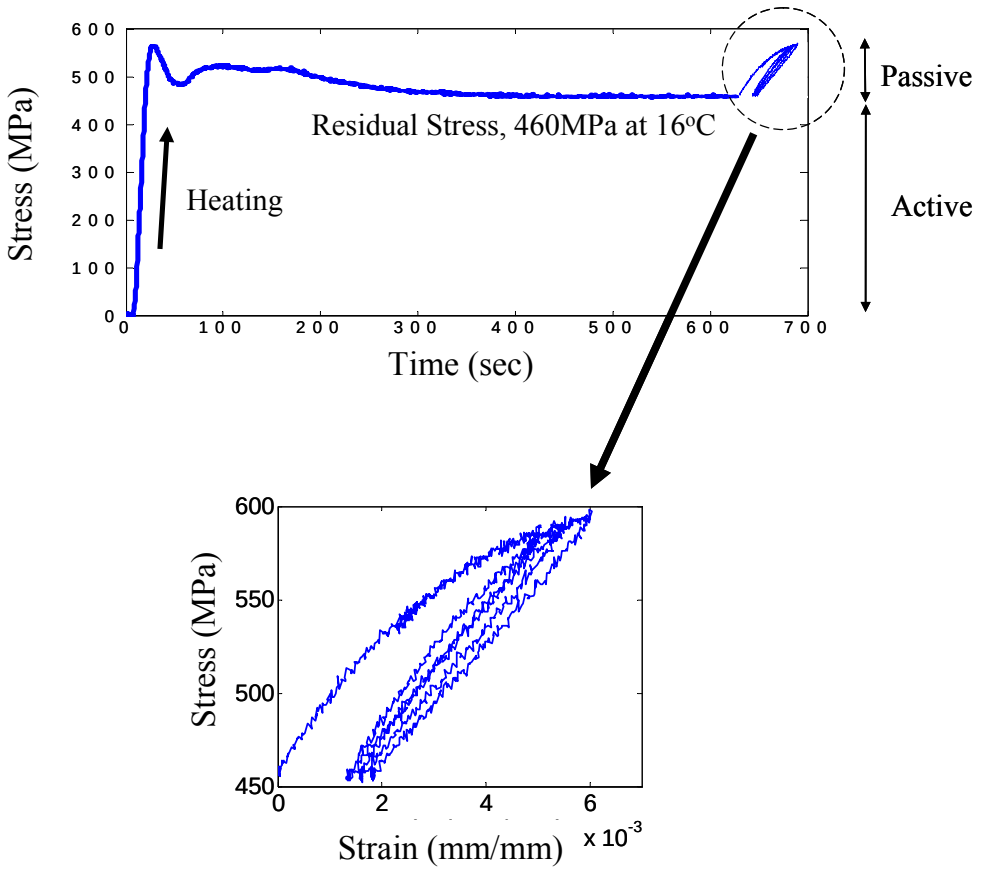

Figure 5.6 Cyclic behavior of prestressed SMA wire.

5.3 CONNECTION TESTS

Spirals made of NiTiNb SMA wires were utilized in this study to confine concrete cylinders. For shipping purposes, the SMA manufacturer was able to provide a maximum of 2400 mm (8 ft) long segments of prestrained wires. Therefore, a splicing technique was established and tested to connect these segments in order to develop the full length of the spiral. Figure 5.7 shows a schematic of a typical SMA wrapped concrete cylinder that was used in the study. As illustrated in the figure, splicing connections were needed at the top and bottom loops of the spiral as well as at the location where two wire segments meet. In order to select a suitable connection for this application an experimental study was conducted.

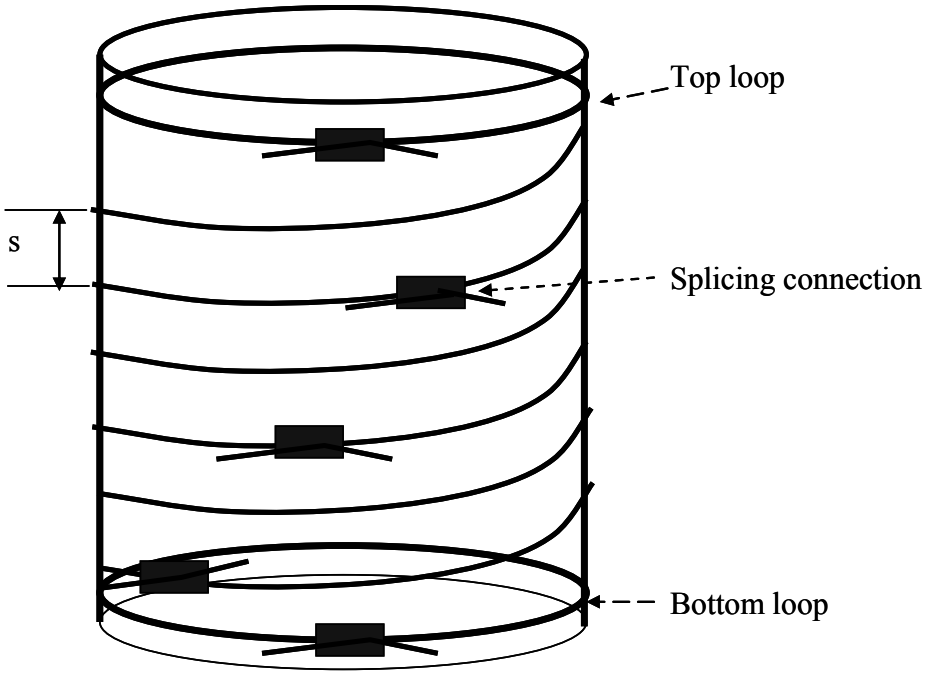

Figure 5.7 Concrete cylinder schematic showing the splicing connections used to develop the full length of the spiral.

To ensure that the selected connection will not fail prematurely during the testing of the cylinders, it should be able to transfer greater force between the two connected wires than the recovery force and the force from passive effect from the wires (see Figure 5.6). Figure 5.8 shows the three connection types that were considered in the study including: 1) Sleeve connection (Figure 5.8.a), 2) U-clamp connection (Figure 5.8.b), and 3) Welded connection, using metal inert gas (MIG) (Figure 5.8.c). The sleeve connection was tested with and without end stoppers. The first two types of connections were tested using different number of sleeves and U-clamps.

(a) Sleeve connection

(b) U-clamp connection

(c) Welded connection

Figure 5.8 Three types of splicing connections.

To examine the mechanical capacity of the connections, a tension test was conducted on the each connection type using the 89 kN (20 kips) MTS uniaxial servo-controlled hydraulic machine. The maximum stress that was developed in the wires prior to the failure of each connection was recorded. The test results are summarized in Table 5.1. The connection made of four U-clamps was able to sustain a maximum force corresponding to a stress equal to 573.3 MPa (83 ksi), which was close enough to the ultimate stress (see Figure 5.6). However, the maximum stresses developed in the wires in the cases of the sleeve and welded connections were 393.0 MPa (57 ksi) and 77.2 MPa (11 ksi), respectively. Therefore, based on these results, the connection with the four U-clamps was deemed suitable for the proposed application and thus was used throughout the rest of the study.

Table 5.1 Results of connection testing

Method		**# of Specimens**	**Avg. Stress Capacity (MPa)**
Sleeve	2 sleeves	2	139.0
	2 sleeves and stoppers	2	177.5
	3 Sleeves	2	265.4
	3 Sleeves and stoppers	2	279.2
	4 Sleeves	2	393.0
U-Clamp	1 U Clamps	2	113.0
	2 U Clamps	2	203.4
	3 U Clamps	2	445.7
	4 U Clamps	2	573.3
Welding		7	77.2

5.4 CONCRETE CYLINDERS TESTS

5.4.1 Preparation of the specimens

The feasibility of the newly developed confinement concept using SMA spirals was first examined on the material level by conducting uniaxial compression tests on confined concrete cylinders. A number of 152 mm (6 in) x 305 mm (12 in) concrete cylinders were cast and cured in a moisture-controlled room in preparation for testing. After the cylinders were cured properly, they were capped using a melted capping compound. A 2.7 MN (600 kips) MTS uniaxial servo-controlled hydraulic machine was used to conduct the uniaxial compression tests with a loading rate of 1 mm (0.04 in)/min at room temperature (see Figure 5.9).

Figure 5.9 2.7 MN (600kips) MTS uniaxial servo-controlled hydraulic machine.

Averaging and circumferential extensometers were attached to the surface of the cylinders to measure the concrete axial and diametric strains, respectively. The specifications of the retrofit schemes used in the tests are summarized in Table 5.2. Three types of wraps were used in the study: (1) SMA spirals, representing the active confinement case. A spiral pitch spacing of 13 mm (0.5 in) was used in this study, (2) SMA spirals plus Glass Fiber Reinforced Polymers (GFRP)/epoxy sheets (SMA-GFRP), representing a hybrid active/passive confinement case. Two pitch spacing values of 13 mm (0.5 in) and 25 mm (1.0 in) were used for the SMA spiral in conjunction with 2 and 4 sheets of GFRP, respectively, and (3) GFRP/epoxy sheets, representing the passive confinement case. GFRP was especially selected in this study due to its relatively large ultimate strain. The thickness of the GFRP sheets used in the study was 0.11 mm (0.0043 in). The hand lay-up method was utilized to apply the GFRP/epoxy sheets, which had a volumetric ratio in the range of 0.58% to 2.86%. After cutting out the glass fabric sheets to the proper size for the concrete cylinder, epoxy resin and hardener were mixed. The GFRP/epoxy sheets were applied one layer at a time using a roller and a brush. The concrete cylinder specimens used in the tests are shown in Figure 5.10. In order to provide evenly distributed heating for the wrapped SMA spiral, an oven was utilized to heat the specimens gradually for 15 minutes until reaching a temperature of 160 ^{o}C (320 ^{o}F). Figure 5.11 shows the oven used for heating.

Table 5.2 Specifications of the confinement techniques examined in the compression tests

Specimen label	Confinement technique
Active-SMA	13mm pitch spacing of SMA spiral
Hybrid-1	25mm pitch spacing of SMA spiral + 2 layers of GFRP
Hybrid-2	13mm pitch spacing of SMA spiral + 4 layers of GFRP
Passive-1	2 layers of GFRP
Passive-2	4 layers of GFRP
Passive-3	8 layers of GFRP
Passive-4	10 layers of GFRP
Unconfined	N/A

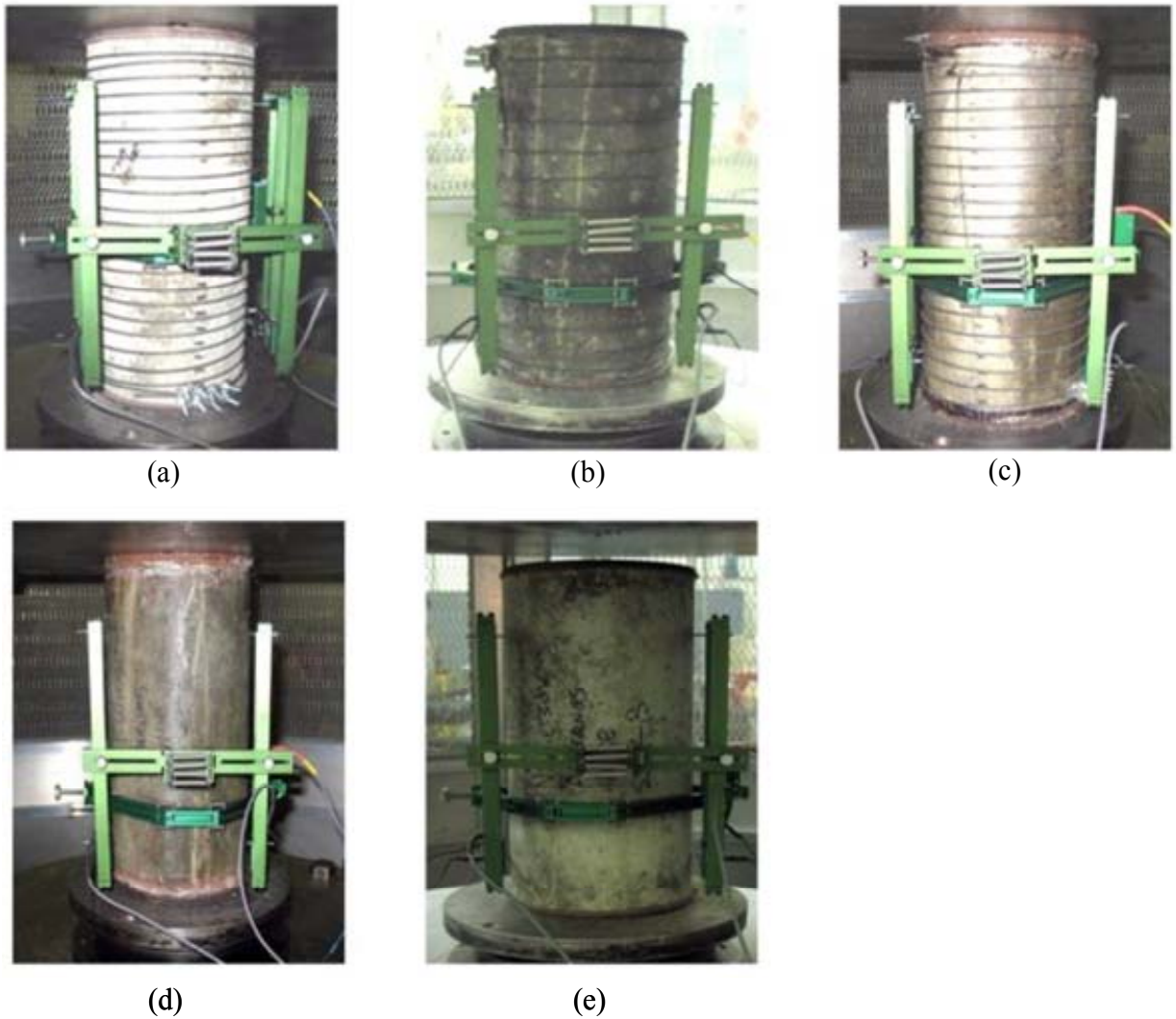

(a) (b) (c)

(d) (e)

Figure 5.10 Concrete cylinders used in testing: (a) Active-SMA, (b) Hybrid-1, (c) Hybrid-2, (d) Passive-4 and (e) Unconfined.

Figure 5.11 Oven used for heating up the concrete cylinders.

Tensile tests were also conducted on six GFRP/epoxy coupons to determine their mechanical properties, and the 89 kN (20 kips) MTS uniaxial servo-controlled hydraulic machine (see Figure 5.3.a) was used. Figure 5.12 shows a GFRP/epoxy coupon in the testing machine when it ruptured (a) and all coupons after testing (b). The tests revealed an ultimate strain of 0.018 mm/mm (0.018 in/in) and the Young's modulus of 19000 MPa (2755 ksi), respectively. The stress-strain result of the coupon test is presented in Figure 5.13.

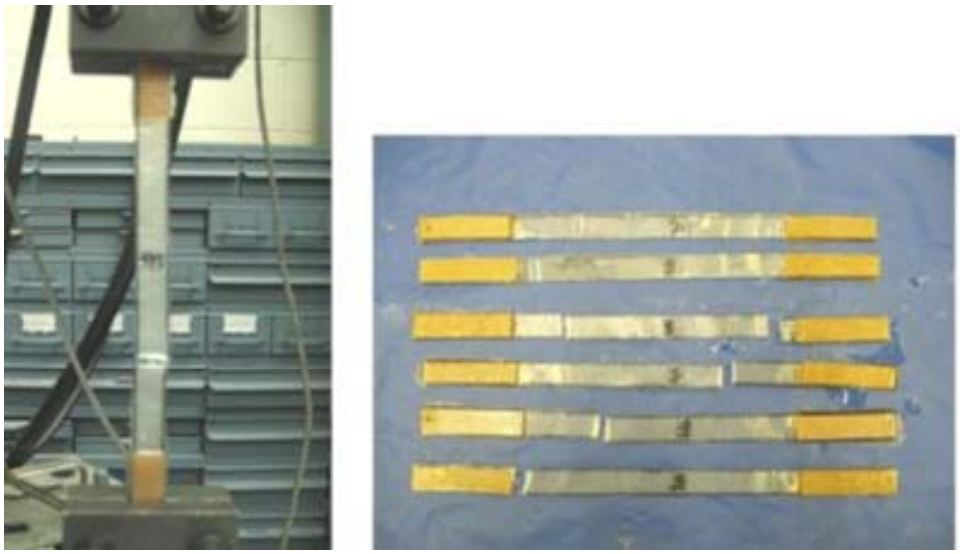

(a) (b)

Figure 5.12 GFRP/epoxy coupon in the testing machine (a) and all specimens after testing (b).

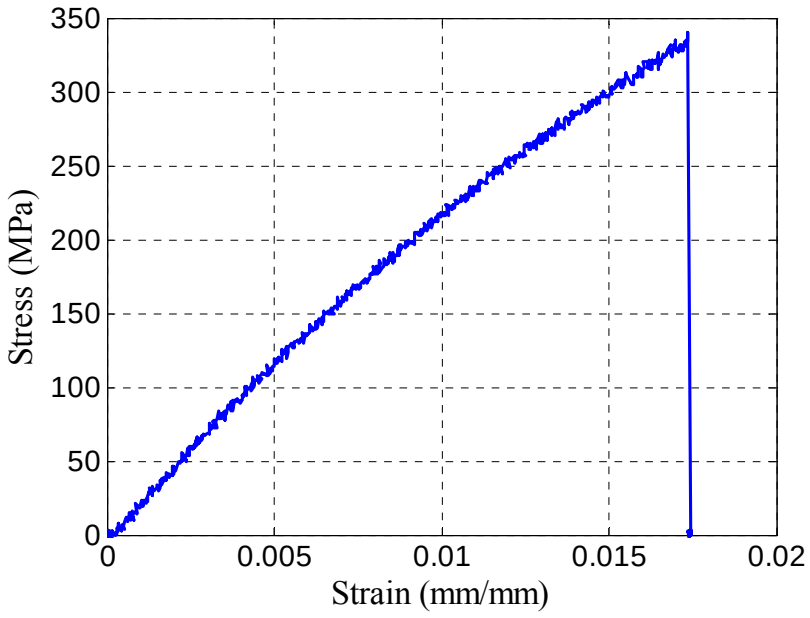

Figure 5.13 Stress-strain result of a GFRP coupon test.

5.4.2 Prestrain losses

Prior to conducting the compression tests, the prestrain loss sustained by the SMA spirals during heating were investigated. This loss could possibly take place as a result of geometric imperfections of the spiral that could cause the spiral to be slack and/or cause wire slippage that could occur at the splicing connections. The residual prestrain after all loss take place will determine the effective amount of confining pressure to be applied to the specimens. Two extensometers were attached to the SMA spiral to monitor the variation of the strain in the spiral while heating the specimens (see Figure 5.14). Figure 5.15 shows the variation of the average prestrain loss from the two extensometers A and B with respect to temperature for the Active-SMA cylinder. After reaching a temperature of 75 ^{o}C (185 ^{o}F), the shape recovery of the spiral was activated and the prestrain loss increased consistently with temperature until reaching a constant value. In this particular case, the maximum prestrain loss recorded was 0.67%. Table 5.3 presents a summary of the average values of the prestrain loss for each of the tested specimens along with the corresponding maximum and residual recovery stress values. The average prestrain loss of Active-SMA, Hybrid-1, and Hybrid-2 specimens were 0.67%, 0.33% and 1.73%, respectively. The recovery stress values were obtained using the recovery stress versus prestrain relationships presented earlier in Figure 5.5.

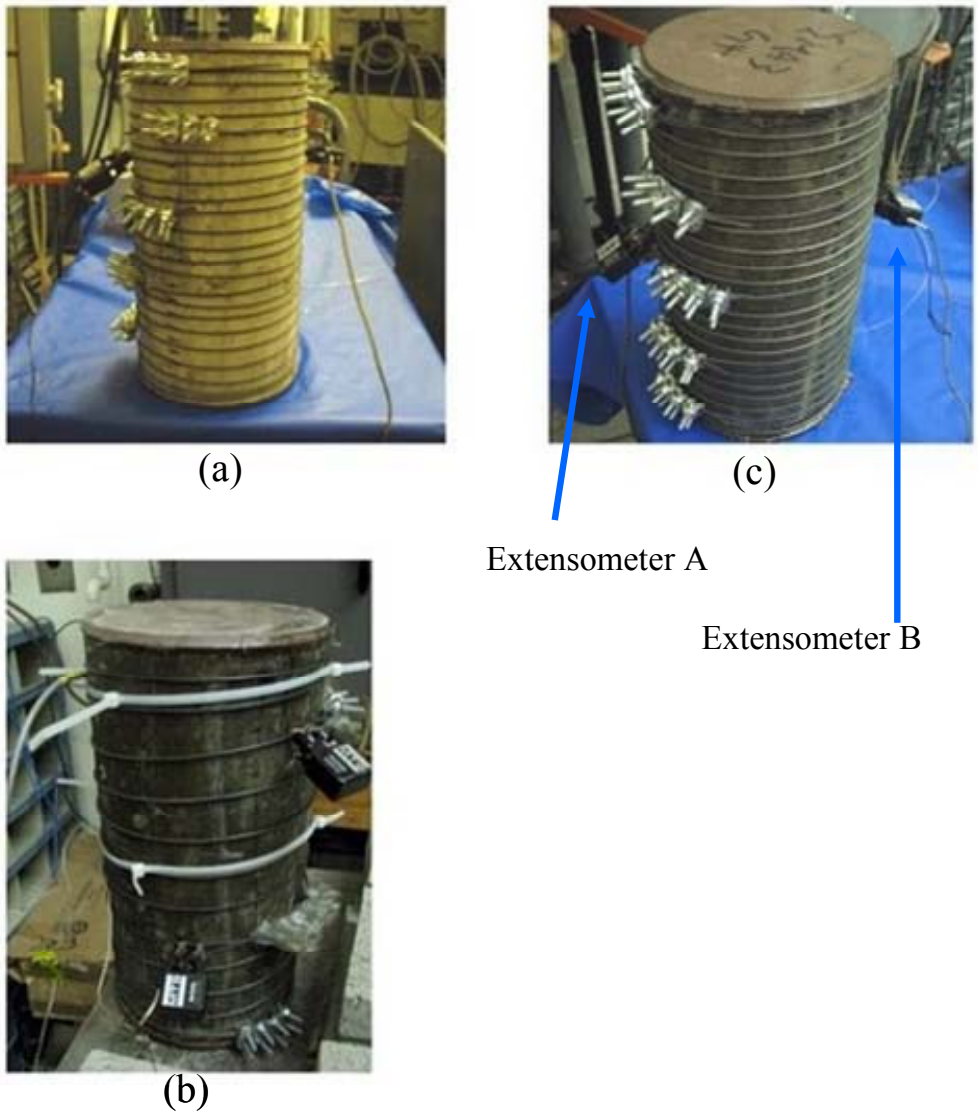

Figure 5.14 Concrete cylinders with two extensometers before heating the cylinders: (a) Active-SMA, (b) Hybrid-1, and (c) Hybrid-2.

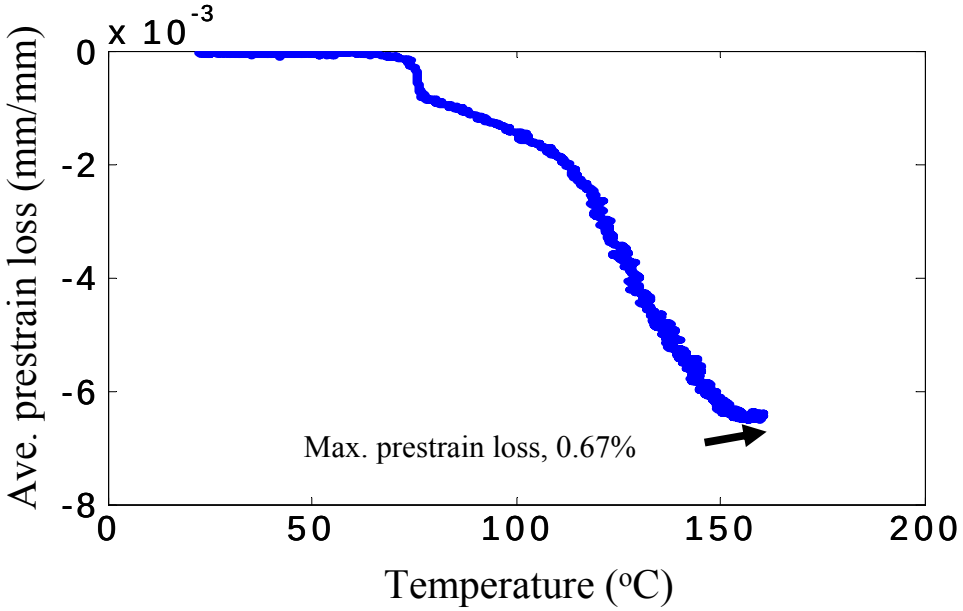

Figure 5.15 Average prestrain losses versus temperature for Active-SMA specimen.

Table 5.3 Prestrain loss (%) and recovery stress of concrete cylinders

Specimen label	**Avg. Prestrain loss (%)**	**Max. recovery stress (MPa)**	**Residual recovery stress (MPa)**
Active-SMA	0.67	546	447
Hybrid-1	0.33	555	453
Hybrid-2	1.73	516	427

5.4.3 Compression test results

5.4.3.1 Results of Active-SMA specimen

Figure 5.16 shows the Active-SMA specimen before, during and after testing. During testing, the concrete cylinder experienced significant cracking and crushing (see Figure 5.16.b), however it remained intact because of the active pressure applied by the SMA spirals. After experiencing excessive deformations, the SMA spiral fractured suddenly and the cylinder failed diagonally as shown in Figure 5.16.c. The stress-strain results obtained from the test is shown in Figure 5.17. The figure demonstrates that the performance of the concrete confined with the SMA spiral improved significantly in terms of strength and ultimate strain. Based on the recovery stress and prestrain loss values that were obtained earlier, the total confining pressure applied on the tested cylinder was approximately 1.42 MPa (206 psi). The peak strengths of the confined concrete cylinder and the unconfined concrete cylinder were 47.3 MPa (6859 psi) and 39.2 MPa (5684 psi), respectively, which indicates that the strength of the concrete confined with the SMA spiral was approximately 21% higher than that of the unconfined concrete. In addition, the ultimate strain of the SMA confined concrete was 24 times that of the unconfined concrete. The smooth and gradual softening of the stress-strain behavior during the post-peak phase of the Active-SMA specimen behavior was due to the cracks which were slowly developing and progressing through the concrete. The active confining pressure applied by the SMA spiral was able to effectively control the opening and propagation of these cracks until the failure point (see Figure 5.16.b). This is illustrated by the plateau which followed the softening branch. Based on the numerical

simulation in Chapter 4, compressive strain of confined concrete reached more than 0.02 mm/mm when the RC column reached at an 8%-drift ratio (see Figure 4.11.a). Therefore, this excessive plateau of actively confined concrete would be beneficial for a RC column under great lateral displacement demand. Even after the concrete had experienced severe damage, the SMA spiral was able to maintain about 55% of the concrete's peak strength until failure occurred.

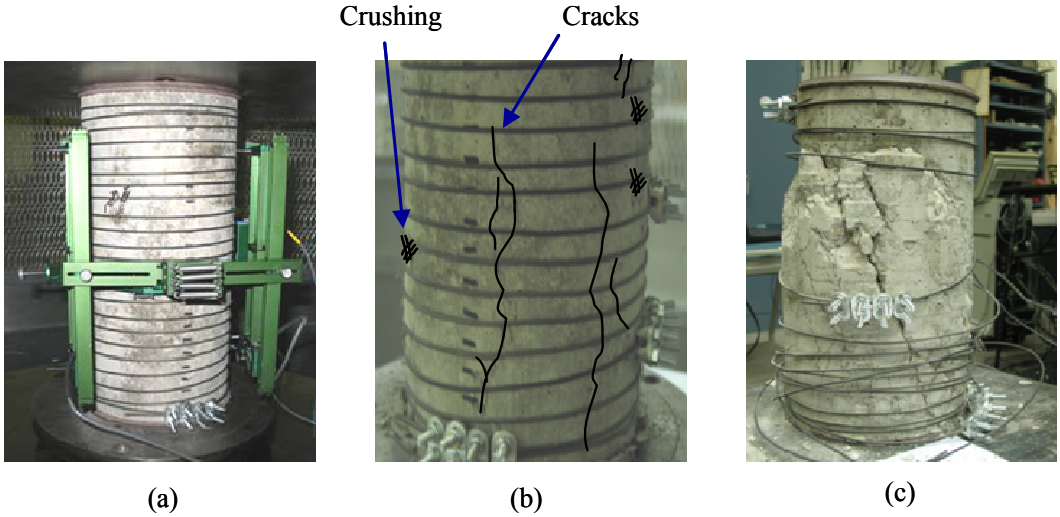

Figure 5.16 Active-SMA specimen before (a), during (b) and after (c) compression testing.

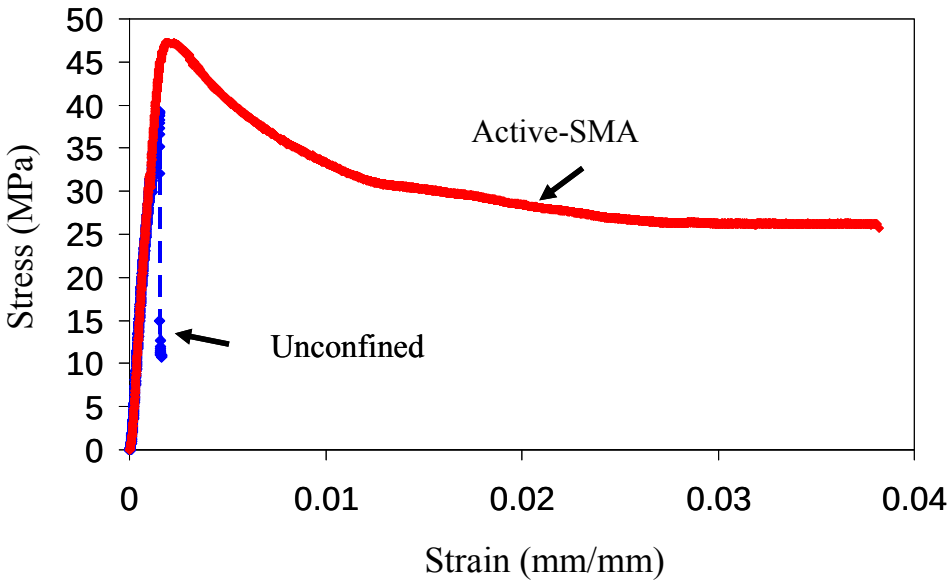

Figure 5.17 Stress-strain relationships of unconfined and Active-SMA specimens.

5.4.3.2 Results of SMA-GFRP wrapped cylinders

The effect of using a hybrid wrapping technique (SMA-GFRP) by combining passive and active confinement techniques was examined. The two specimens labeled Hybrid-1 and Hybrid-2 (see. Figure 5.18) were prepared using the hybrid wrapping technique and tested. Figure 5.18 shows the Hybrid-1 and -2 specimens before, during and after testing. Figure 5.19 shows the compression stress-strain behaviors of the concrete cylinders confined with the hybrid techniques. The peak strengths of the Hybrid-1 and Hybrid-2 specimens were 41.1 MPa (5960 psi) and 42.6 MPa (6177 psi), respectively, which indicates an increase in the strength by 4.8% and 8.7%, respectively compared to that of the unconfined concrete cylinder. For both cases, Hybrid-1 and Hybrid-2, the hybrid technique improved the ultimate strain of the concrete cylinders dramatically by 30 and 25 times, respectively compared to that of the unconfined

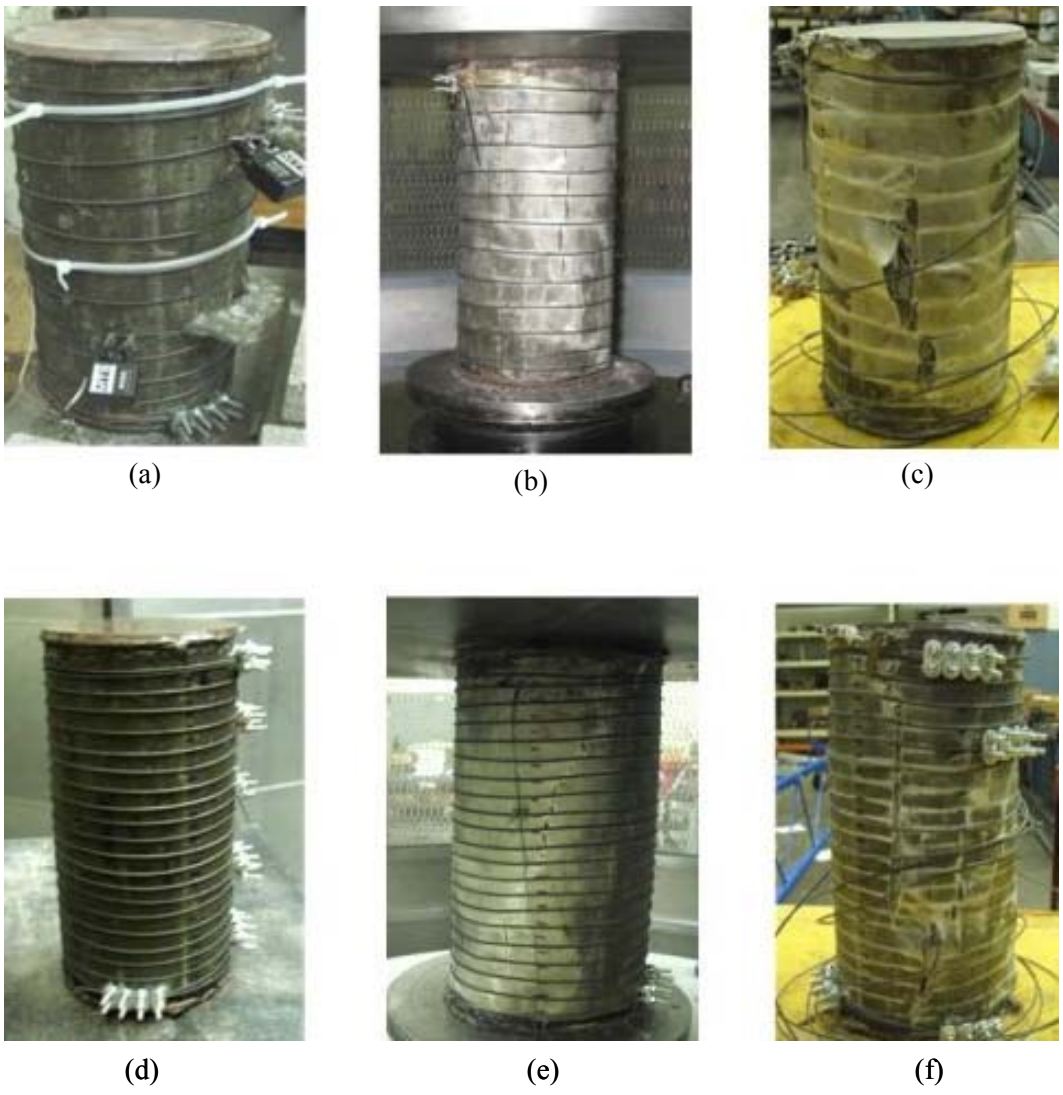

Figure 5.18 Hybrid-1 and -2 specimens before, during and after compression testing: (a) Hybrid-1 before testing, (b) Hybrid-1 during testing, (c) Hybrid-1 after testing, (d) Hybrid-2 before testing, (e) Hybrid-2 during testing and (f) Hybrid-2 after testing.

concrete. Observation of the specimens during testing revealed that the GFRP wraps started rupturing much earlier than the SMA spirals. The points of the rupture of GFRP in both cases are shown in Figure 5.19 and also pictures of Hybrid cylinders with ruptured GFRPs during testing are presented in Figure 5.18.c and d. After the GFRP wraps experienced severe damage, significant softening was observed followed by a slight strain hardening until failure. This strain hardening was a direct result of the contribution of the SMA spiral which solely dominated the behavior of the specimen after the GFRPs' rupture. Finally, the specimens reached their failure point when the SMA spirals failed. It is clear from the behavior shown in the figure, that the SMA spiral played two important roles: 1) delayed the rupture of the GFRP sheets, which was prestressed by the externally applied SMA spiral, and 2) acted as a second line of defense which allowed the specimen to maintain an almost constant level of strength until failure.

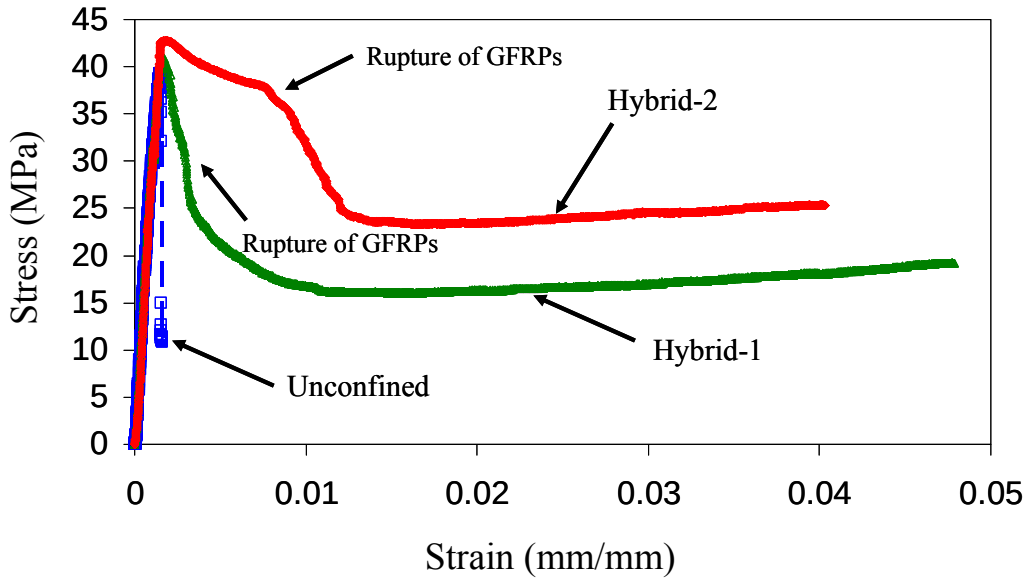

Figure 5.19 Comparison between the stress-strain behaviors of unconfined and SMA-GFRP confined cylinders.

5.4.3.3 Results of GFRP/epoxy confined cylinders

For the purpose of comparison with the behavior of cylinders confined with SMA spirals, several concrete cylinders were tested in compression after being wrapped with GFRP/epoxy sheets. Table 5.4 presents the GFRP's volumetric ratio and the effective confining pressure corresponding to each of the tested specimens. The confining pressure was estimated at the onset of fracture of the wraps using the GFRP mechanical properties obtained from coupon tests after being reduced using an efficiency factor of 0.5.. The efficiency factor value was based on previous studies (Xia and Wu 2000, Lorenzis and Tepfer 2003) and is used to account for the imperfections in the GFRP wraps, and with the efficiency factor, the lateral confining pressure f_l was expressed as:

$$f_l = \frac{2E_f \alpha \varepsilon_f nt}{D} \qquad (5.1)$$

where D is the column diameter, E_f is the Young's modulus of the GFRP, ε_f is the GFRP ultimate strain, n is the number of GFRP sheets, t is the thickness of the GFRP sheet, and α is the jacket efficiency factor which is defined as the ratio between the ultimate circumferential strain of the GFRP jacket and the ultimate strain determined from the coupon test.

Table 5.4 Volumetric ratio and confining pressure of GFRP wrapped specimens

Specimen label	ρ_{GFRP} **(%)**	**Passive lateral pressure (MPa)**
Passive-1	0.58	0.5
Passive-2	1.15	1.0
Passive-3	2.31	2.0
Passive-4	2.89	2.5

Figure 5.20 shows a comparison between the compression stress-strain behaviors of the concrete cylinders wrapped with different numbers of GFRP layers. As shown in the figure, the concrete strength and ultimate strain increased as the number of GFRP layers increased. However, the effect of confinement was more pronounced on the ultimate strain than on the strength. A minor change was observed in the strength of Passive-1 and Passive-2 cylinders, while in the case of Passive-3 and Passive-4, the concrete strength increased by 7% and 18%, respectively compared to that of the unconfined cylinder. The ultimate strain of the Passive-1, Passive-2, Passive-3 and Passive-4 specimens increased by 1.2, 2.1, 2.7 and 5.2 times, respectively compared to that of the unconfined concrete cylinder.

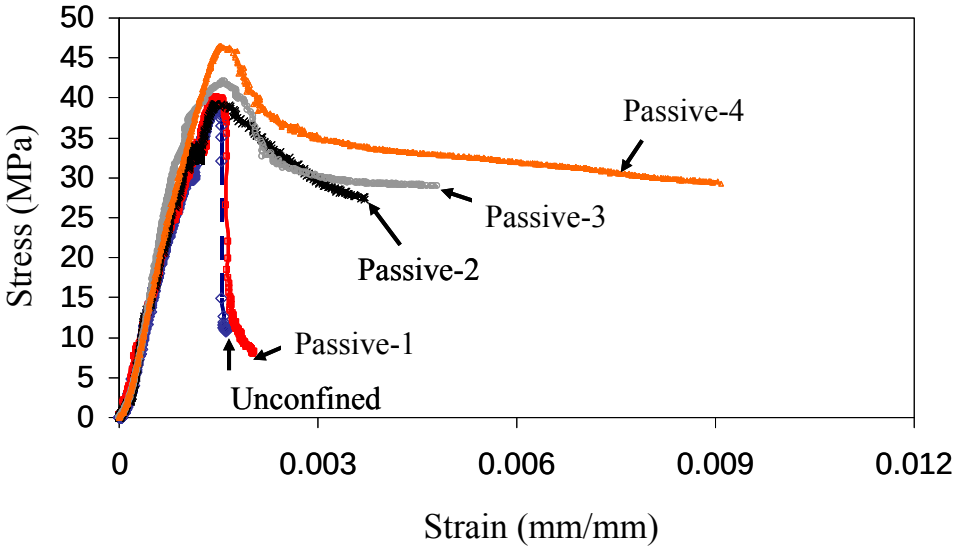

Figure 5.20 Comparison of the stress-strain behaviors of concrete cylinders confined with GFRP wraps.

5.4.4 Comparison of results

In this section, a comparison between the three studied wrapping techniques was conducted. The amount of confining pressure whether active, passive or hybrid was employed as the common base for the comparisons.

5.4.4.1 SMA spiral vs. GFRP/epoxy sheets

As discussed earlier, the total confining pressure applied in the case of Active-SMA specimen was found to be 1.42 MPa (206 psi). This pressure falls between the 1.0 MPa (145 psi) and 2.0 MPa (290 psi) passive pressures applied in the cases of Passive-2 and Passive-3 specimens (see Table 5.4). Therefore, the stress-strain behaviors of the three specimens (i.e. Active-SMA, Passive-2 and Passive-3) were depicted on the same figure (see Figure 5.21) and compared. The figure shows that the active confining

pressure improved the performance of concrete more dramatically compared to passive confinement. The strength of Active-SMA specimen increased by 21% and 12% compared to Passive-2 and Passive-3, respectively. In addition, the ultimate strain of Active-SMA specimen increased by 10 times and 8 times compared to that of Passive-2 and Passive-3, respectively.

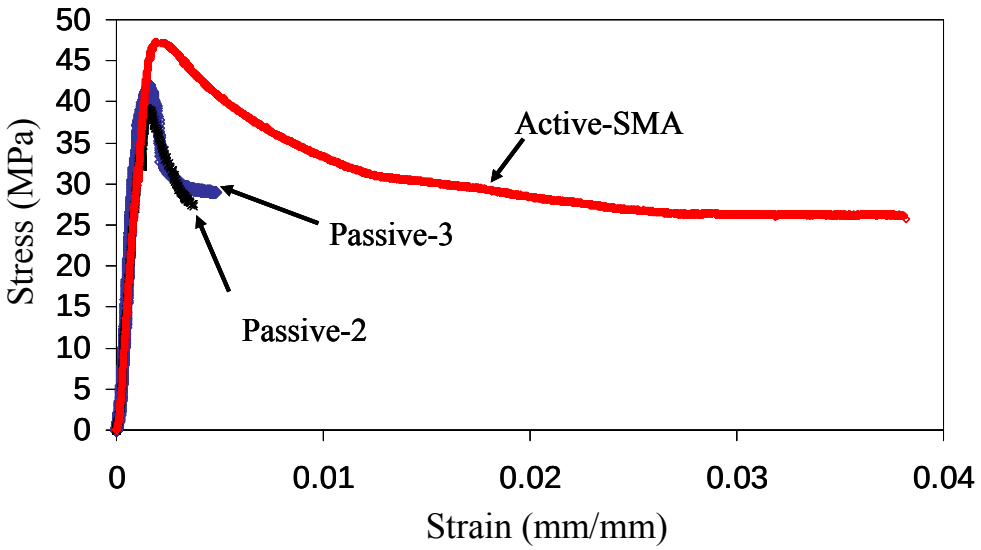

Figure 5.21 Comparison between the stress-strain behaviors of Active-SMA, Passive-2, and Passive-3 specimens.

5.4.4.2 SMA-GFRP vs. GFRP/epoxy sheets

For the cases of the Hybrid specimens, the total confining pressure was defined at the point where the GFRP begins to rupture. Hence, at this point it is expected that the passive pressure applied from the SMA spiral is minimal, and thus, the total confining pressure was determined as the summation of the active pressure from SMA spirals and the passive pressure from GFRPs wraps. For the Hybrid-1 specimen, the total confining

pressure was found to be 1.0 MPa (145 psi), which consisted of 0.5 MPa (72.5 psi) applied as active pressure from the SMA spiral and 0.5 MPa (72.5 psi) applied as passive pressure from the GFRP wraps at the onset of their rupture. The total pressure was equivalent to the passive pressure when using two layers of GFRPs, which was estimated as 1.0 MPa (145 psi) (see Table 5.4). Therefore, the behaviors of the two specimens Hybrid-1, and Passive-2 are presented and compared in Figure 5.22. The behaviors were almost identical until the concrete cylinder confined with four layers of GFRP sheets failed; after which, the behaviors were significantly distinguishable. The hybrid wrapping technique improved dramatically the concrete ultimate strain by approximately 13 times compared to the passively confined specimen. Although the Hybrid-1 specimen comprised half of the GFRP wraps used in the Passive-2 specimen, the GFRP rupture points for both specimens were almost identical. This demonstrates the effectiveness of the SMA spiral in delaying the rupture of the GFRP wraps used in the hybrid specimen. The brittle behavior of the GFRP wraps limited the ability of the Passive-2 specimen to maintain any residual strength. However, the active confining pressure provided by the SMA spiral exhibited an effective role in controlling the residual strength which was almost maintained at a level of 46% of the peak strength.

On the other hand, in the case of the Hybrid-2 specimen, the total confining pressure was found to be 2.1 MPa (305 psi), which comprised 1.1 MPa (160 psi) active pressure and 1.0 MPa (145 psi) passive pressure. This total confining pressure was comparable to the passive pressure of 2.0 MPa (290 psi), which was obtained from using eight layers of GFRPs (see Table 5.4). Therefore, the behaviors of the Hybrid-2 and Passive-3 specimens are presented and compared in Figure 5.22 as well. In terms of the

peak strength, the two specimens were almost identical, however, in terms of the ultimate strain, the hybrid technique showed a superior performance compared to the traditional passive confinement technique. The ultimate strain of the Hybrid-2 specimen was 9 times that of the Passive-3 specimen. One noticeable observation was that eight layers of GFRP (represented by Passive-3) reached their rupture strain much earlier than the four layers of GFRP used in the Hybrid-2 specimen due to the prestressing effect of the SMA spirals. Furthermore, the SMA spiral was successful in maintaining about 60% of the concrete peak strength until failure.

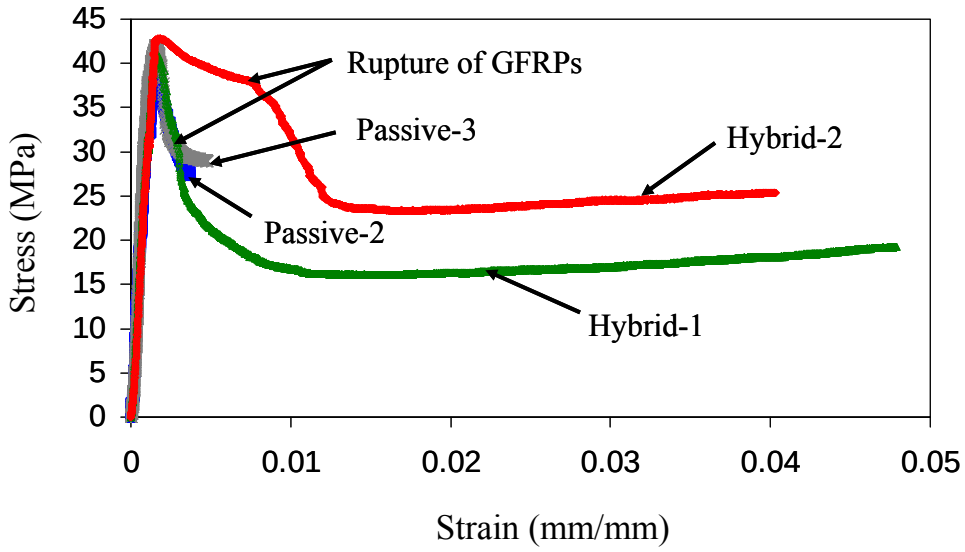

Figure 5.22 Comparison between the stress-strain behaviors of Hybrid-1 and Passive-2 specimens, and of Hybird-2 and Passive-3 specimens.

CHAPTER 6 REINFORCED CONCRETE COLUMNS TESTING

The material tests presented in Chapter 5 demonstrated the effectiveness of the new active confinement technique to conventional passive technique in enhancing the strength and ultimate strain of concrete. This chapter focuses on expanding this research further by examining experimentally the effectiveness of the new technique on the component level through the testing of reduced-scale (1/3-scale) RC single cantilever columns representative of bridge columns. The quasi-static cyclic behavior of columns retrofitted using SMA spirals is studied and discussed in this chapter. The behavior is also compared with that of a column retrofitted using conventional passive confinement applied with glass-FRP (GFRP) wraps.

6.1. SPECIMEN DESCRIPTION

Four reduced-scale (1/3-scale) RC single cantilever columns were built and tested under quasi-static lateral cyclic loading. Figure 6.1 shows the design of the reduced-scale RC cantilever column, and Figure 6.2 depicts the details of reinforcement. The manufacturing process of the RC columns is presented in Figure 6.3. Figure 6.4 shows an isometric view of the column testing. The effective height of the column was 1270 mm (50 in), and its diameter was 254 mm (10 in) with a 25.4 mm (1 in) concrete cover. The column was supported by 1168 mm (46 in) x 1168 mm (46 in) x 406 mm (16 in) footing. To mimic the effect of gravity loads, the axial force on the column was maintained during testing at a value of 116 kN (26 kips), which represents 5% of the column's gross section compressive strength. The axial force was maintained using a 445 kN (100 kips) hydraulic actuator. A load cell was mounted on the top of the column and a 15.2 mm

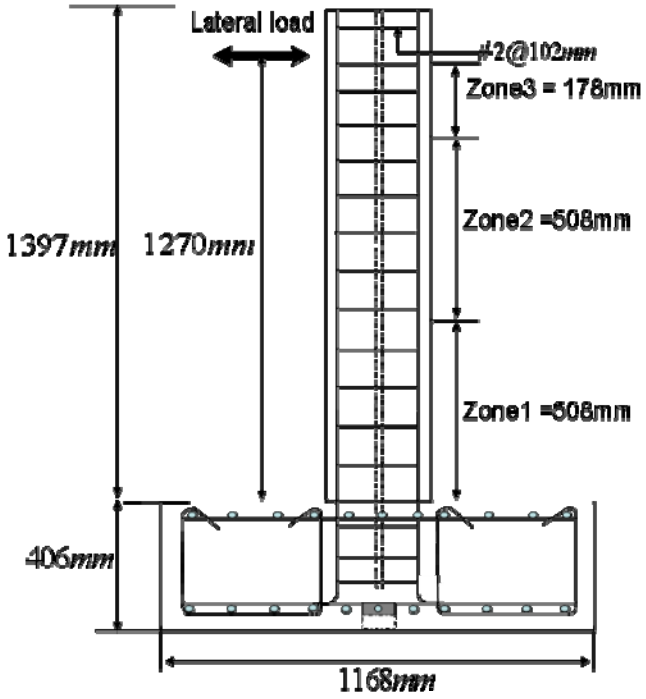

Figure 6.1 Details of reduced-scale reinforced concrete column used in testing.

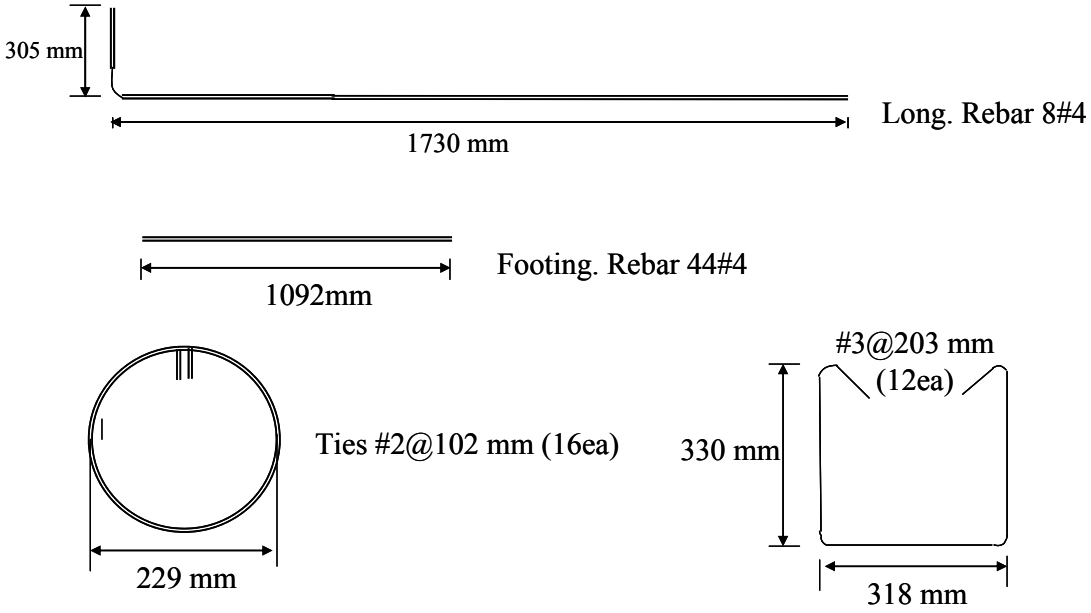

Figure 6.2 Details of column reinforcement.

(a)

(b)

(c)

Figure 6.3 RC column specimen: (a) Reinforcement, (b) Casting concrete and (c) As-built column.

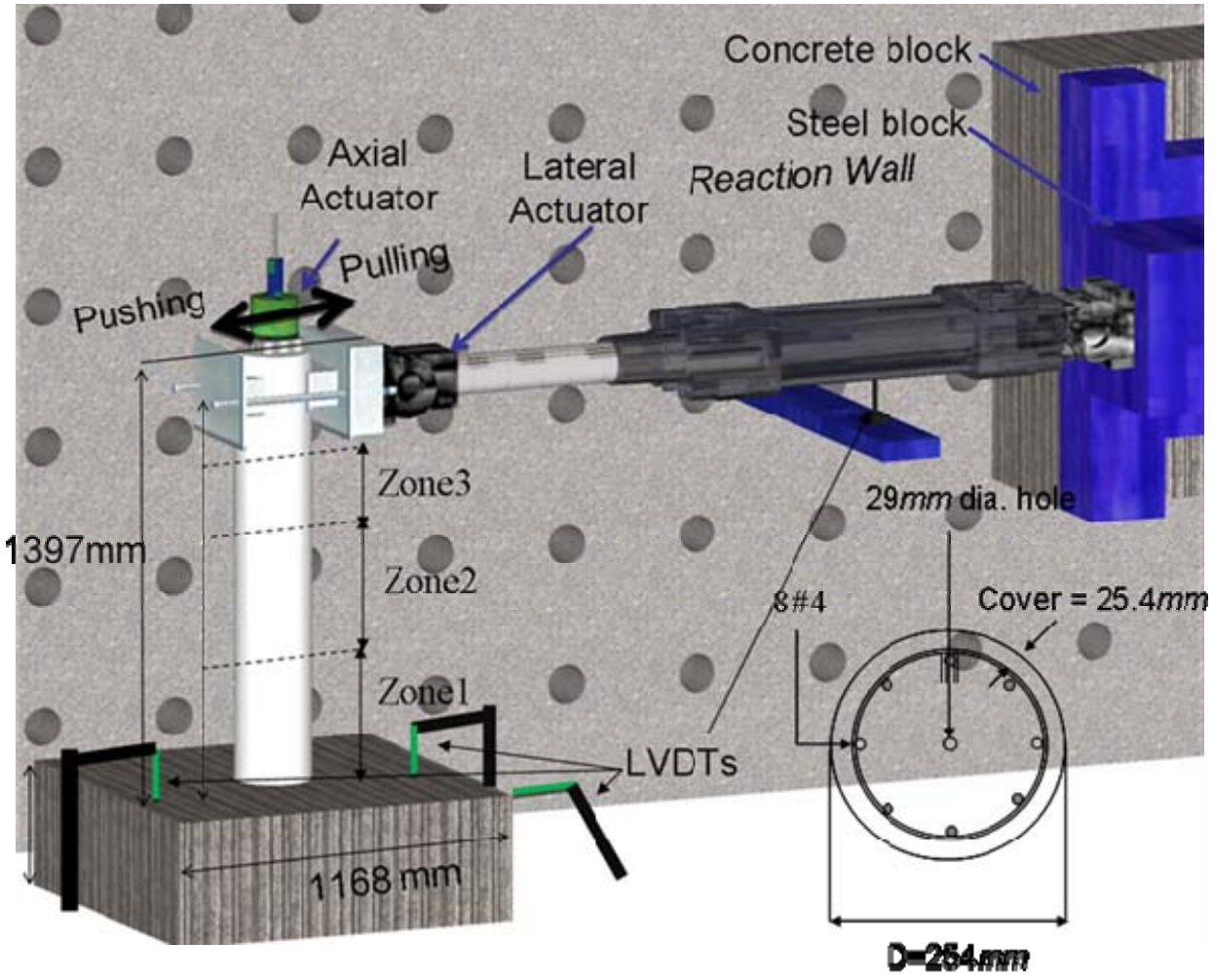

Figure 6.4 Test set-up of RC columns.

(0.6 in) seven wire steel strand was located at the center of the column. Each column was reinforced with 8#4 bars in the longitudinal direction which corresponds to a volumetric ratio of 2%, and #2@102 mm (4 in) hoops placed in the transverse direction, which corresponds to a volumetric ratio of 0.56%. No. 2 bar was used for the transverse reinforcement since it was the smallest size available, and the spacing (102 mm (4 in)) was chosen to avoid brittle shear failure since it represents approximately half of the concrete core diameter. During testing, the lateral force was applied using a 445 kN (100 kips) servo-controlled hydraulic actuator with a stroke of ± 254 mm (10 in). The actuator was anchored to a reaction wall through a steel block and a concrete block (see Figure 6.4). Four Linear Variable Differential Transformers (LVDTs) were installed to measure the net displacements of the column. Three of these LVDTs were placed between the floor and the footing to capture the rotation of the footing and its displacement relative to the floor. The fourth LVDT was used to capture the relative displacement between the reaction wall and the actuator's steel and concrete blocks. In addition, several strain gauges were installed at the plastic hinge zone to monitor the variations of the strains in the steel rebars and hoops, and on the surface of the concrete. Figure 6.5 shows the locations of strain gauges and their labels. 'S' and 'C' stand for strain gauge on steel and concrete, respectively; 'L' and 'H' stand for the longitudinal and horizontal direction, respectively in which the strain gauges were installed, and 'W', 'E' and 'S' indicate the west, east and south direction of the column, respectively. Strain gauges were also installed horizontally on the surface of GFRP, and SMA spirals to monitor their strain variations.

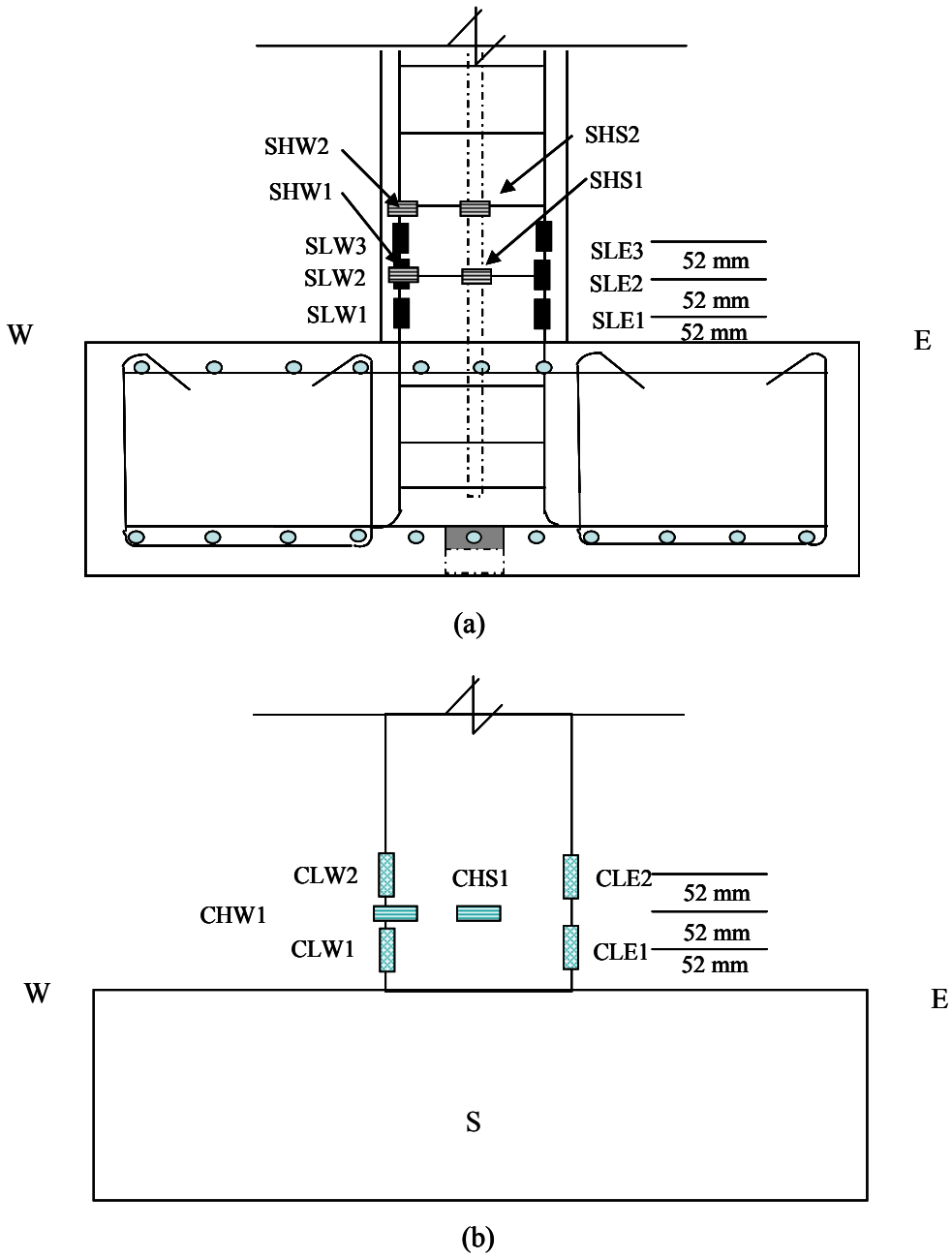

Figure 6.5 Strain gauges on reinforcement (a) and on concrete surface (b).

Figure 6.6 shows the locations and the labels of strain gauges on external GFRP wraps and SMA spiral in the cross-sectional view of the column. The strain gauges on the surface of SMA spirals were installed at the positions as shown in Figure 6.6.b. This is unlike the strain gauges on GFRP wraps due to the conflictions with connectors of SMA spirals and the other strain gauges on the surfaces of the columns.

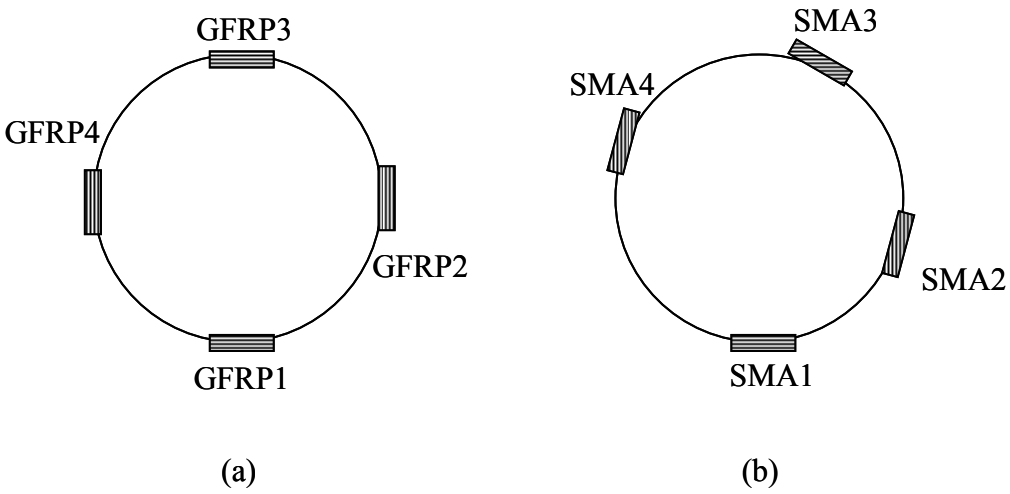

Figure 6.6 Strain gauges on: (a) GFRP and (b) SMA spiral.

Figure 6.7 shows exemplary pictures of single element strain gauges on longitudinal reinforcement and on concrete surface. The reinforcement strain gauges were installed using a strain gauge adhesive after grinding the target surface of reinforcement followed by chemical treatments. Then the strain gauges were protected by covering the gauges and reinforcement with rubber from possible damage when pouring concrete. On the other hand, the surface of the concrete was prepared by sanding the surface followed by chemical treatments for strain gauging. All the strain gauges were connected to data acquisition system (DAQ) and LabView program was used to monitor

and store the data. A total of 24-27 data channels were used for the data acquisition depending on the type of retrofit used, which will be discussed in the following subsection. At the time of testing, the average compressive strength of the concrete was found to be 44.8 MPa (6500 psi). Furthermore, in order for a testing column specimen to be fully mounted to the lateral actuator, some fixture plates were designed and manufactured. The drawings of the fixture plates can be found in Appendix A.

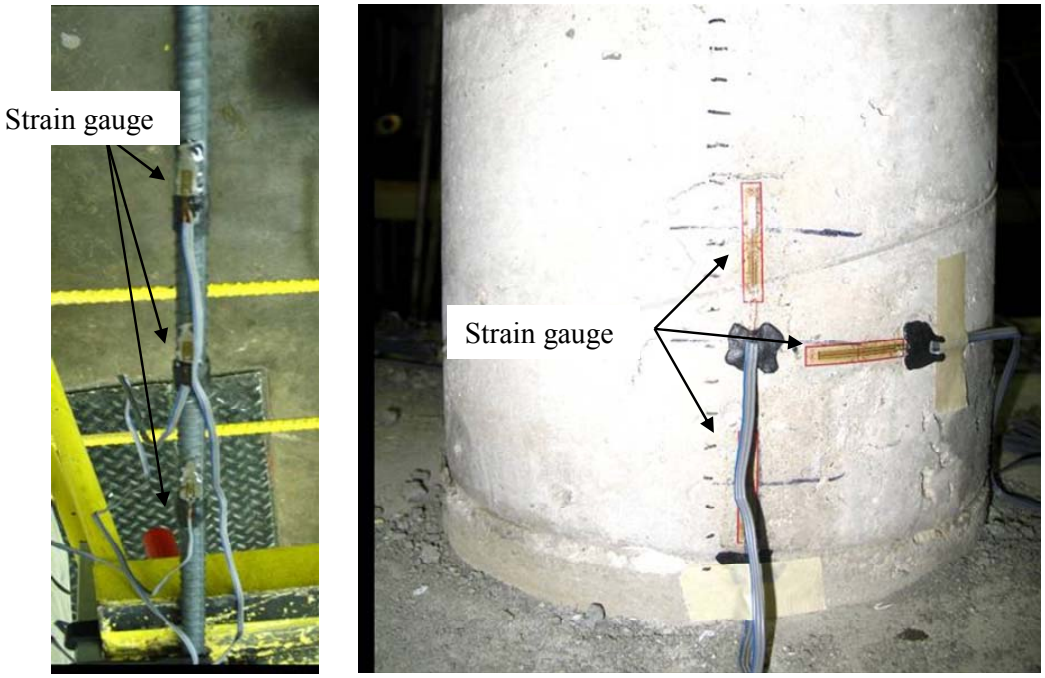

(a) (b)

Figure 6.7 Strain gauges on longitudinal reinforcement (a) and on concrete surface (b).

6.2 RETROFITTING SCHEMES

Three of the columns were retrofitted using different confining techniques while the fourth column was tested in its as-built condition and used as control specimen. Figure 6.8 shows the four columns before testing with schematics of each retrofit scheme.

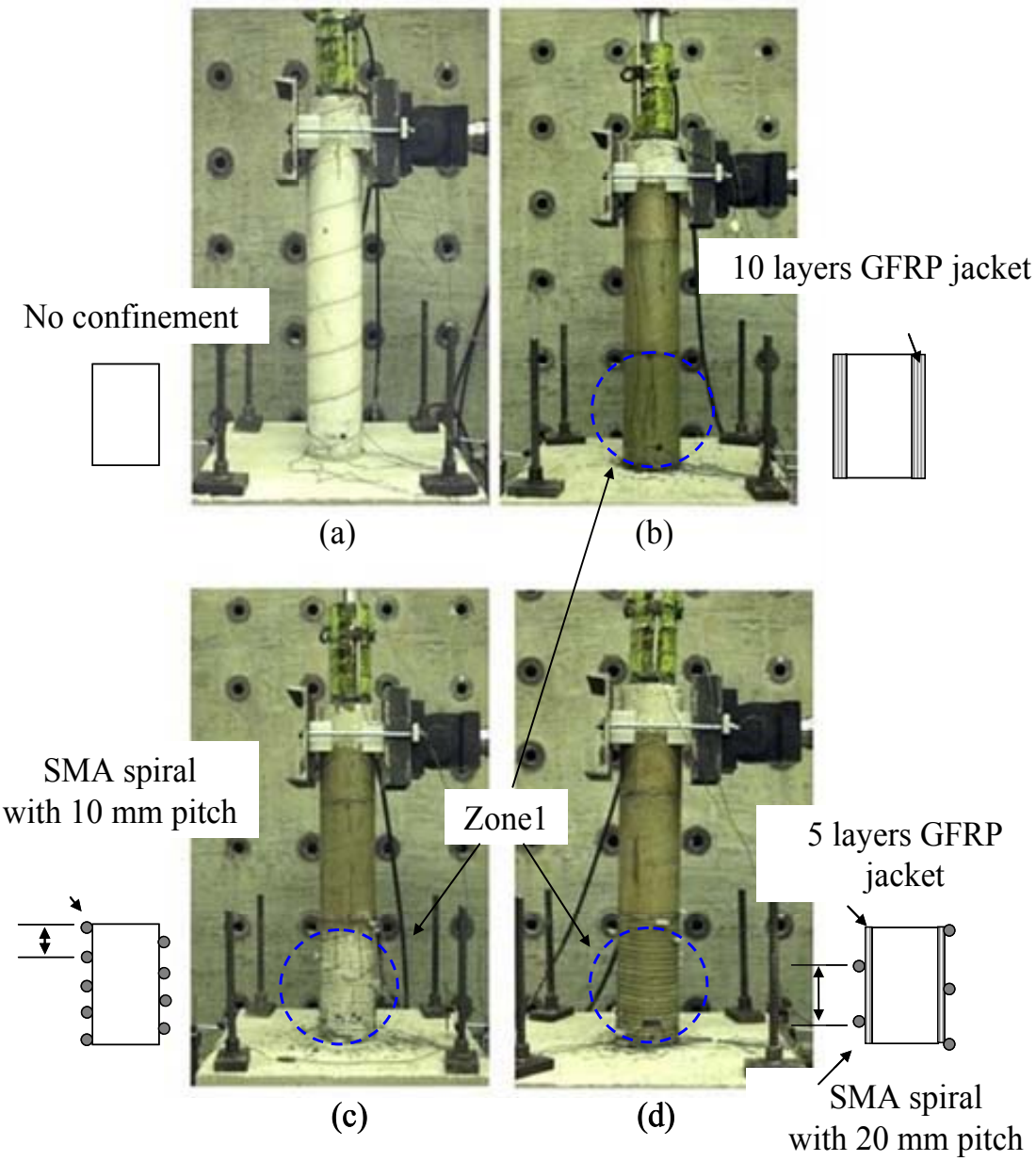

Figure 6.8 Four column specimens before testing: (a) As-built, (b) GFRP, (c) SMA and (d) SMA/GFRP.

Each column was divided into three zones (Zone 1, 2 and 3) as shown in Figure 6.4. Zone 1 represents the most critical region in terms of flexure, where the plastic hinge is expected to occur. While Zones 2 and 3 are less critical than Zone 1, they can still sustain damage either due to shear stresses or due to the over-strength of the retrofitted Zone 1, which will force the damage to be shifted upward. To ensure that the damage is localized in Zone 1, Zones 2 and 3 were wrapped with glass-FRP (GFRP) jackets. The GFRP jackets used in this study were made of 0.11 mm (0.0043 in)-thick fiberglass (E-glass) sheets and epoxy resin was applied using hand lay-up method. For consistency, Zones 2 and 3 in all three columns were wrapped with 5 and 2 layers of GFRP sheets, respectively, which correspond to GFRP volumetric ratio of 0.87% and 0.35%, respectively. Figure 6.9 shows a picture taken when retrofitting the RC columns at the testing site.

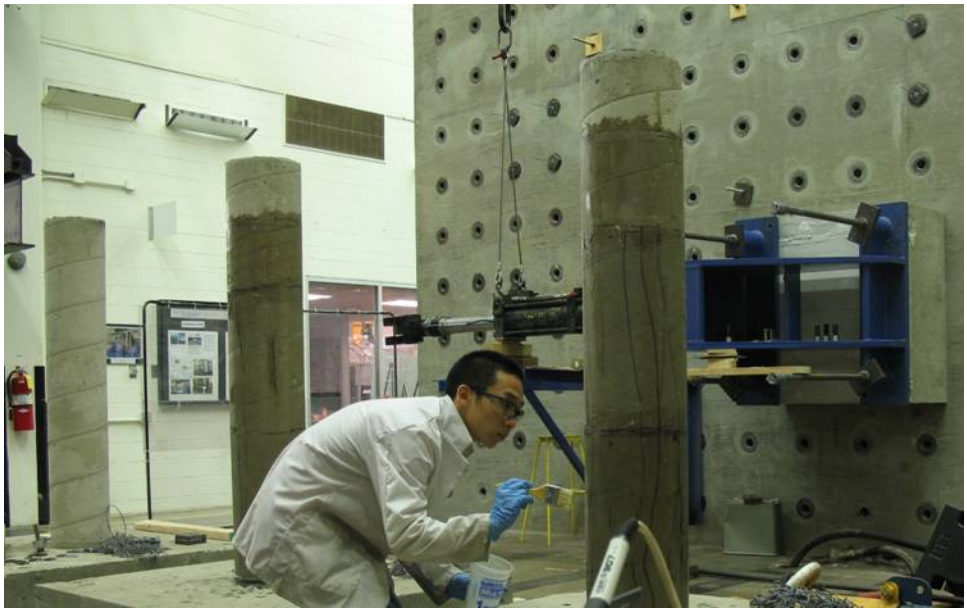

Figure 6.9 Retrofitting RC columns with GFRP/epoxy sheets using hand lay-up method.

Table 6.1 shows a summary of the properties of the retrofitting methods used for each of the three columns. The only difference between the three retrofitted columns was in the type of retrofit applied at Zone 1. One column was wrapped with GFRP jacket, which represents a passive confinement technique. The second was retrofitted with SMA spirals, which represents an active confinement technique. While in the third column, a hybrid confinement (i.e. passive + active) technique was applied by wrapping the column with both SMA spirals and GFRP sheets (SMA/GFRP). Combining GFRP and SMAs was sought in this study as a more economical approach for applying active confinement since the amount of SMAs will be reduced significantly compared to the case with only SMA spirals. Reducing the amount of SMAs will cause the spiral pitch to increase and thus the GFRP will help in confining the concrete between the SMA wires.

The SMA spirals used were made of 2438 mm (8 ft)-long segments of 2 mm (0.08 in)-diameter NiTiNb wires. The wires were provided by the manufacturer in their prestrained condition (≈ 6%-prestrain). The length of the segments was a standard of the manufacturer. To form a complete spiral, the wires were spliced using U-clamps which was tested and found to be capable of sustaining the ultimate strength of the wires as presented in the previous chapter. The prestrained spiral was wrapped around the column with the desired pitch.

Table 6.1 Confining techniques at each column

Specimen	Zone1	Zone2	Zone3
GFRP Column	10-layer GFRP jacket	5-layer GFRP jacket	2-layer GFRP jacket
SMA Column	SMA spiral w/10mm pitch	5-layer GFRP jacket	2-layer GFRP jacket
SMA/GFRP Column	SMA spiral w/20mm pitch + 5-layer GFRP jacket	5-layer GFRP jacket	2-layer GFRP jacket

To provide basis for the comparison between the three retrofitted columns, the confinement pressure applied on Zone 1 was taken as the same in the three cases. Since the confinement pressure in the GFRP jacket case is expected to increase with concrete dilation, the target pressure used in the comparison was at the onset of the GFRP jacket rupture. Therefore, the pressure applied in the case of the GFRP retrofitted column was determined first, and then the spirals and jacket used on the other two columns were designed accordingly. Ten layers of GFRP sheets with 0.11 mm (0.0043 in) thickness were used to wrap the GFRP retrofitted column. Tensile tests of GFRP coupons from section 5.3.1 revealed that Young's modulus and the ultimate strain of the used GFRP were 19131 MPa (2774 ksi), and 0.018mm/mm, respectively.

A jacket efficiency factor of 0.5, which is typical in the case of GFRP jackets, was assumed in this study (Xia and Wu 2000; Lorenzis and Tepfers 2003). The confining

pressure corresponding to the 10-layer GFRP jacket was founded to be 1.5 MPa (218 psi) based on the Eq. 5.1. This passive confinement pressure was used to calculate the pitch spacing of the SMA spiral used on the SMA retrofitted column, and the pitch spacing of the SMA spiral (*s*) was computed as follows:

$$s = \frac{2A\sigma_{SMA}}{Df_l} \qquad (6.1)$$

where *A* is the cross-sectional area of the SMA wire, σ_{SMA} is the SMAs recovery stress, *D* is the column diameter, and f_l is the desired confinement pressure.

It is worth mentioning that the recovery stress (f_{SMA}) used in Eq. 6.1 was adjusted to account for the effect of SMAs prestrain loss. From the material tests presented in Chapter 5, it was found that the relationship between recovery stress and prestrain is linear (see Figure 5.5). Hence, the adjusted recovery stress values were obtained from the previously determined relationship. Since this loss could only be obtained after installing and heating SMA spirals, a prestrain loss of 1%-strain was assumed prior to installing the spirals based on a previous testing on the SMA spirals in this design stage in order to determine the pitch spacing of the spirals. The study revealed that the predicted 1% prestrain loss would produce post-losses residual recovery stress of approximately 440.7 MPa (64 ksi) (versus 460 MPa (68 ksi) with no losses, see Figure 5.4). Using Eq. 6.1, the predicted recovery stress resulted in a pitch spacing of 10 mm (0.39 in), which was used in wrapping the SMA retrofitted column (SMA column). It is important to mention,

however, that the value of the prestrain loss was later checked and compared with the predicted value after the spiral was installed and heated.

As mentioned earlier, the last column (SMA/GFRP column) was tested to examine the effect of applying hybrid confinement pressure (i.e. active + passive). Half of the confinement pressure of 1.5 MPa (218 psi) was applied from SMA spirals and the other half was applied from GFRP jackets. To do so, the pitch spacing of the SMA spiral was doubled to 20 mm (0.79 in) compared to that was used in the SMA column, and the number of GFRP layers was cut into half (i.e. 5 layers instead of the 10 layers was used in the GFRP column (see Table 6.1)). To retrofit the column with SMA/GFRP, the five layers of GFRP were wrapped first with epoxy resin using the hand lay-up method. After curing, the prestrained SMA spiral was wrapped and heated by passing an electric current.

6.3 LOADING PROTOCOL

Figure 6.10 shows the load protocol that was used in the test. The columns were loaded cyclically with a rate of 5.1 mm (0.2 in)/min up to 1.5% drift and 15.3 mm (0.6 in)/min thereafter. Initially a load increment of 0.5% drift was adopted until a drift of 6% was reached, after which an increment of 1% was used until 12% drift. An increment of 2% drift was used afterward until the test was stopped.

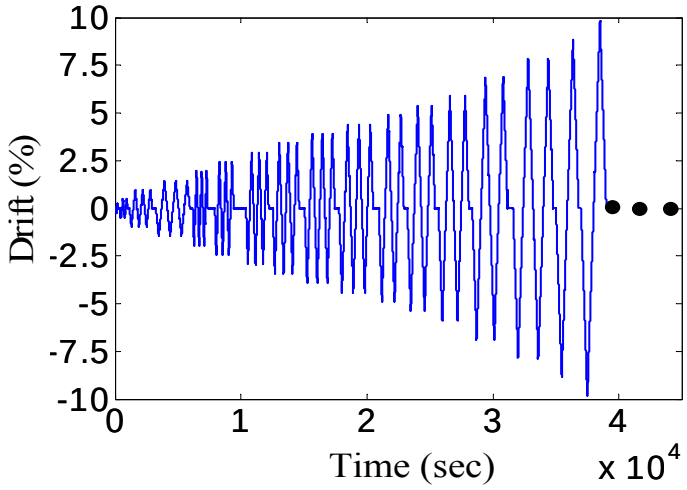

Figure 6.10 Loading protocol used in the study.

6.4 TEST RESULTS

6.4.1 Experimental confinement pressure

To design the GFRP jackets and the SMA spirals, the GFRP jacket efficiency factor and the SMA prestrain loss were assumed to be 0.5 and 1%-strain, respectively. It was deemed important to confirm these values using actual strain measurements acquired during heating the spirals and testing the columns. Several strain gauges were attached to the surface of the GFRP jacket and at different locations along the SMA spiral. GFRP circumferential strain experimental results were recorded using one of the strain gauges that bridged one of the early cracks that developed vertically in the jacket. As recorded, the ultimate strain of the jacket in the hoop direction was found to be 0.007 mm/mm, which indicated that the jacket efficiency factor is 0.4 rather than the originally predicted 0.5. Using the 0.4 efficiency factor in Eq. 5.1 resulted in a modified confinement pressure

of 1.2 MPa (174 psi) instead of 1.5 MPa (218 psi) applied on Zone 1 of the GFRP retrofitted column.

Similarly, the predicted prestrain loss of the SMA spirals used in retrofitting the other two columns were confirmed using the strain gauge's data that was acquired while heating the spirals. Figure 6.11 shows the strain recovered during the heating of the spirals in the cases of the SMA and SMA/GFRP columns. As illustrated by the lower figures, the spirals were heated up to approximately 160 ^{o}C (320 ^{o}C). The strain recovered (lost) reached a plateau at a strain level of 0.97% for the SMA column and 1.0% for SMA/GFRP column, which corresponds to a recovery stress of 441.1 MPa (64 ksi), and 440.7 MPa (64 ksi), respectively (see Figure 5.5). A comparison between the target confinement pressure and the actual confinement pressure, which was determined based on the experimental data obtained from the three retrofitted columns at Zone 1 is presented in Table 6.2. It is worth mentioning that the pressure applied by the SMA spirals was slightly increased to account for the effect of passive confinement applied by the spirals due to concrete dilation. The results in the table illustrate that the values of the confinement pressures applied on the three columns were close enough with a maximum difference of approximately 3%.

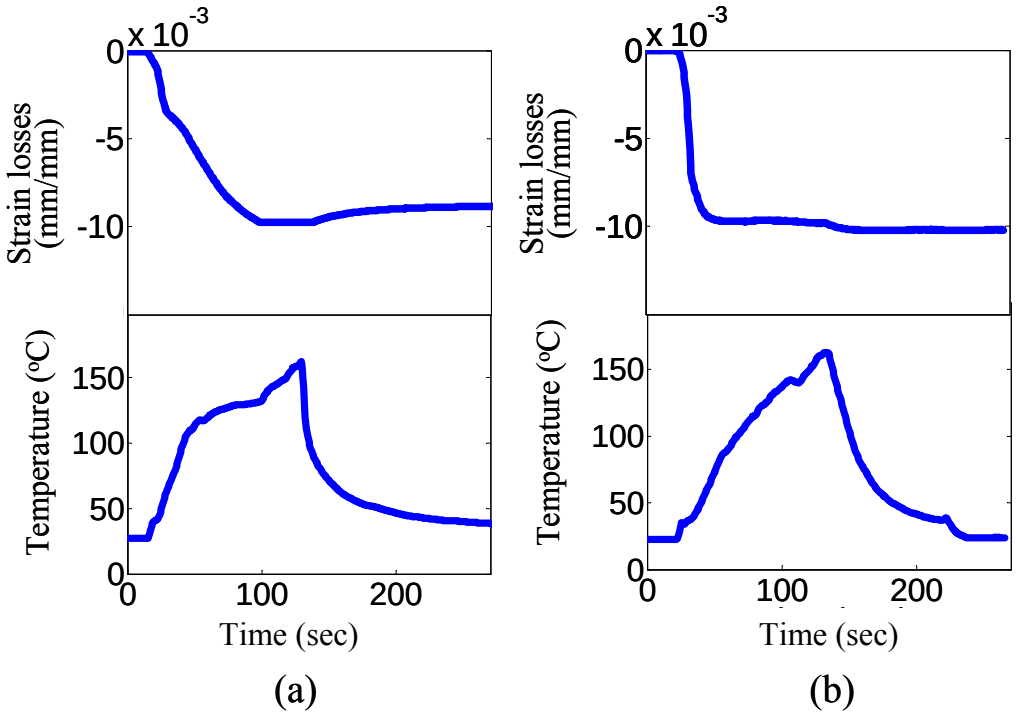

Figure 6.11 Variation of SMA prestrain losses and temperature with time for SMA column (a) and SMA/GFRP column (b).

Table 6.2 Comparison between target and actual confinement pressure applied at zone 1 of the three retrofitted columns

	GFRP Column	**SMA Column**	**SMA/GFRP Column**
Target Confinement Pressure	1.5 MPa	1.5 MPa	1.5 MPa
Actual Confinement Pressure	1.2 MPa	1.24 MPa	1.22 MPa

6.4.2 Force vs. Drift results

Figure 6.12 and Figure 6.13 show lateral force versus lateral drift relationships of the four tested columns. A detailed description of the damage sustained by each specimen is presented in the next section. The steel rebars in all four columns started yielding at a drift ratio of approximately 1.5%. When the as-built column reached 4.2%-drift, one of

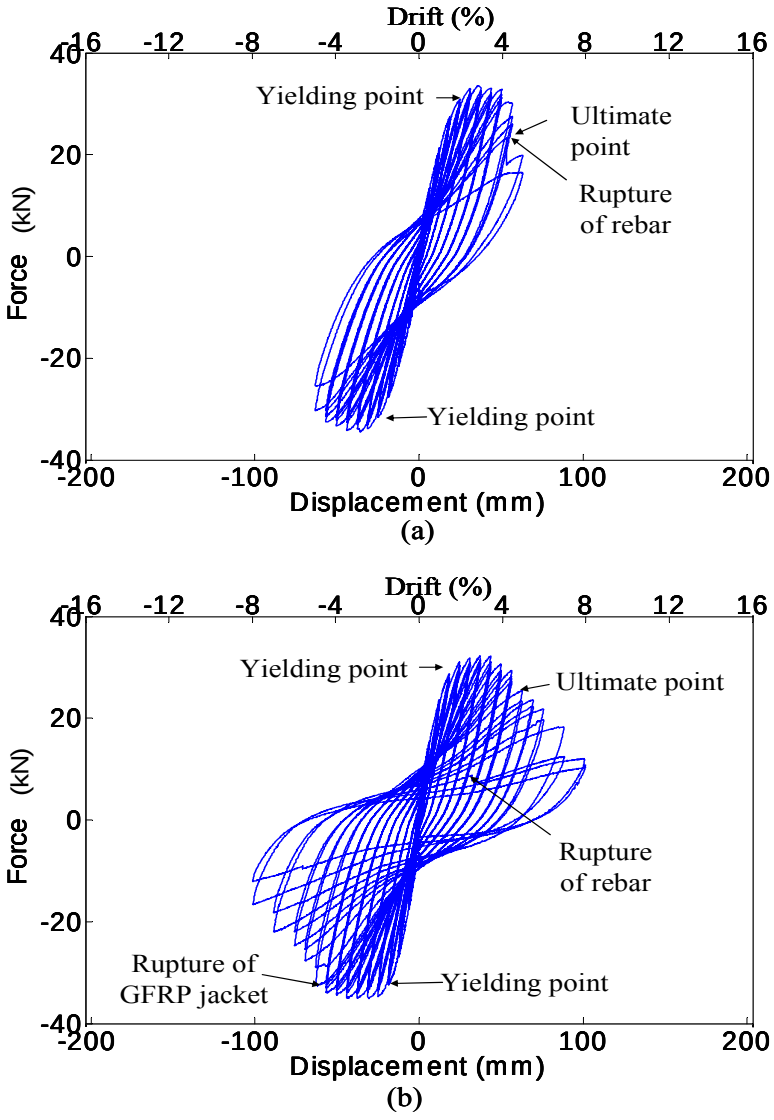

Figure 6.12 Lateral force vs. lateral drift of the As-built column (a) and GFRP column (b).

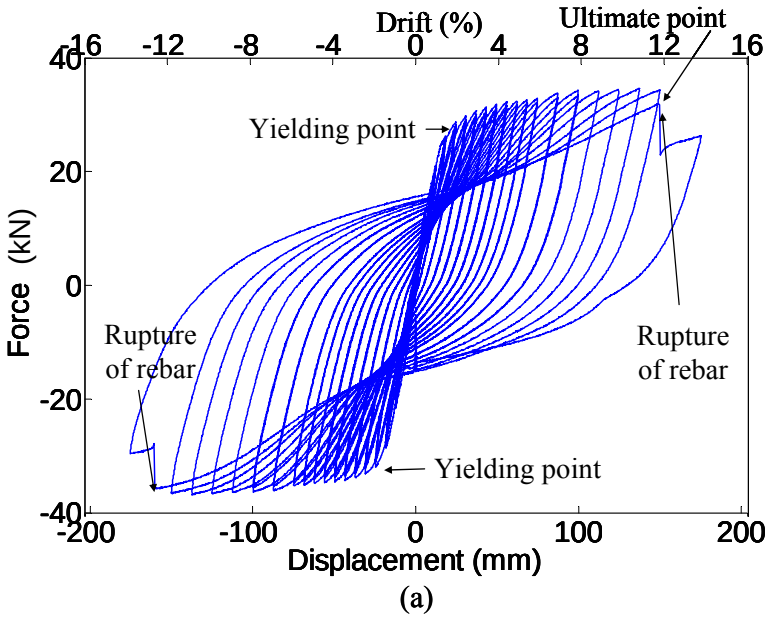

Figure 6.13 Lateral force vs. lateral drift of the SMA column (a) and SMA/GFRP column (b).

its longitudinal rebars ruptured, which caused the strength to drop abruptly by 23% (See Figure 6.12.a). For the GFRP column (See Figure 6.12.b), the maximum strength was recorded at a drift ratio of 3.5%, where the first vertical crack in the jacket was observed. After the 3.5%-drift, the column started showing signs of gradual strength degradation and stiffness deterioration. At 8%-drift, the column strength reached 34.6% of the maximum strength. Taking a closer look at the behaviors of the SMA and SMA/GFRP columns (Figure 6.13.a and Figure 6.13.b), it is shown that after steel yielded, a hardening behavior was observed in both columns. This behavior could be attributed to the elastic behavior of the already stressed SMA spirals as was evident by the SMAs cyclic behavior shown in Figure 5.6. Testing of SMA and SMA/GFRP columns was stopped when the strength deteriorated to below 80% of the maximum strength. The primary reason for strength deterioration in both columns was due to the rupture of one of the longitudinal rebars and not due to damage in the concrete as was the case in the GFRP column. The rebars of the SMA and SMA/GFRP columns ruptured at 12%-drift and 10%-drift, respectively.

To assess the overall performance of the new SMA retrofitting technique, three important response parameters were evaluated and compared. These parameters are strength, displacement ductility, and hysteretic energy. The summary of the comparisons is presented in Table 6.3, while the details are discussed in the following subsections.

6.4.3. Strength

Due to the slightly unsymmetrical behavior of the columns, the column strength was taken as the average of the maximum strengths recorded when the column was pushed and pulled. As illustrated in Table 6.3, the strength values recorded for the as-built and GFRP columns were the same. However, the third row in the table which presents the strength values after being normalized using the as-built column strength indicates that the SMA and SMA/GFRP columns exhibited a slight strength increase of 6% and 3%, respectively compared to both the as-built and GFRP columns.

Table 6.3 Comparisons between the columns strength, ductility, and hysteretic energy

	As-built	**GFRP**	**SMA**	**SMA/GFRP**
Max. Avg. Strength (kN)	34	34	36	35
Normalized Strength	1	1	1.06	1.03
Displacement Ductility (μ)	2.8	3.3	8.0	6.7
Normalized Ductility	1	1.18	2.85	2.39
Hysteretic Energy (kJ)	16.1	20.1	75.9	62.0
Normalized Hysteretic Energy	1	1.25	4.71	3.85
Equivalent Viscous Damping Ratio, ξ_{eq} (%)	10.1	12.7	17.4	16.2

6.4.4 Displacement ductility capacity

The displacement ductility capacity ratio (μ) is one of the important parameters in structural seismic design. It defines the ability of the structural element to withstand large inelastic deformations without collapse. This parameter is defined as the ratio of the drifts at the ultimate and yielding points. In order to determine the displacement ductility ratio for each column, the ultimate point was taken as the point on the backbone curve corresponding to 80% of the column strength. Figure 6.14 shows a comparison between the push/pull force-displacement backbone curves of the four columns. As indicated on the figure, the ductility ratios (μ) of the as-built, GFRP, SMA, and SMA/GFRP columns were 2.8, 3.3, 8.0, and 6.7, respectively. Although the ultimate drift ratios of the SMA and SMA/GFRP columns (12% and 10%, respectively) exceeded the typical ultimate drift limit states, they clearly illustrated the potential and capability of the new retrofitting technique. Table 6.3, also presents the ductility ratios after being normalized using the as-built column ductility ratio. The conventional passive confinement technique using GFRP wraps showed an increased ductility by 18% compared to that of the as-built column. However, the SMA and SMA/GFRP columns exhibited an increased ductility by 185% and 139%, respectively compared to that of the as-built column.

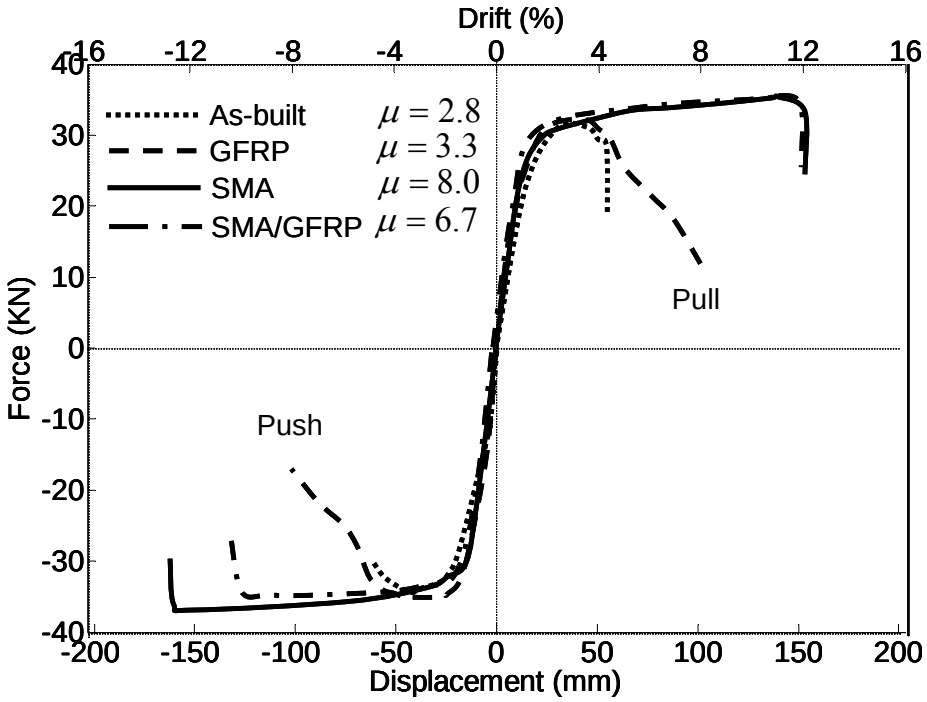

Figure 6.14 Force-displacement backbone curves of the four columns.

6.4.5 Hysteretic energy

Another important factor for seismic design is the ability of the structural element to dissipate energy during an earthquake. In this study, this ability was evaluated by comparing the cumulative hysteretic area enclosed within the force-displacement curves of the four columns until the ultimate point is reached (see Figure 6.12 and Figure 6.13). Table 6.3 presents for each column the cumulative hysteretic energies computed, their normalized values based on the hysteretic energy of the as-built column, and the equivalent viscous damping ratio (ξ_{eq}). The equivalent viscous damping ratio was computed as (Chopra, 2000)

$$\xi_{eq} = \frac{1E_D}{4\pi E_{So}} \qquad (6.2)$$

where E_D is the dissipated energy in a cycle and E_{So} is the elastic strain energy of a structure. Figure 6.15 illustrates the definition of dissipated energy and elastic strain energy in a structure undergoing cyclic loading.

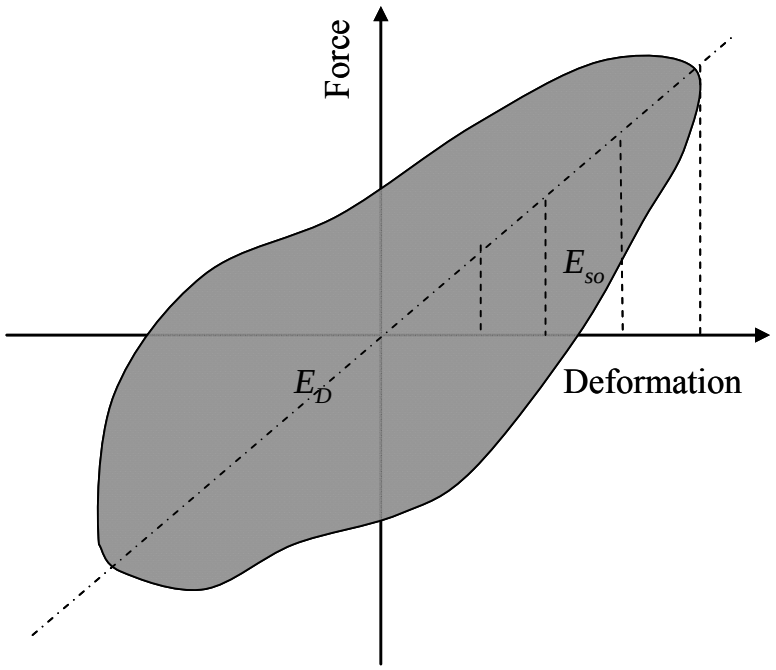

Figure 6.15 Schematics of the dissipated energy (E_D) and the strain energy (E_{So}) of a structure in a cycle loading.

While the GFRP column dissipated 25% more hysteretic energy compared to the as-built column, the SMA and the SMA/GFRP columns were far superior since they dissipated 371% and 285% more hysteretic energy, respectively compared to the as-built column. While the as-built and GFRP columns exhibited an equivalent viscous damping

ratio of 10.1% and 12.7%, respectively, the equivalent viscous damping ratios of the SMA and the SMA/GFRP columns were 17.4% and 16.2% respectively. Figure 6.16 shows relationship between the ductility ratio and the equivalent viscous damping ratio of the four tested columns. The greater the ductility ratio is, the higher the equivalent viscous damping ratio is.

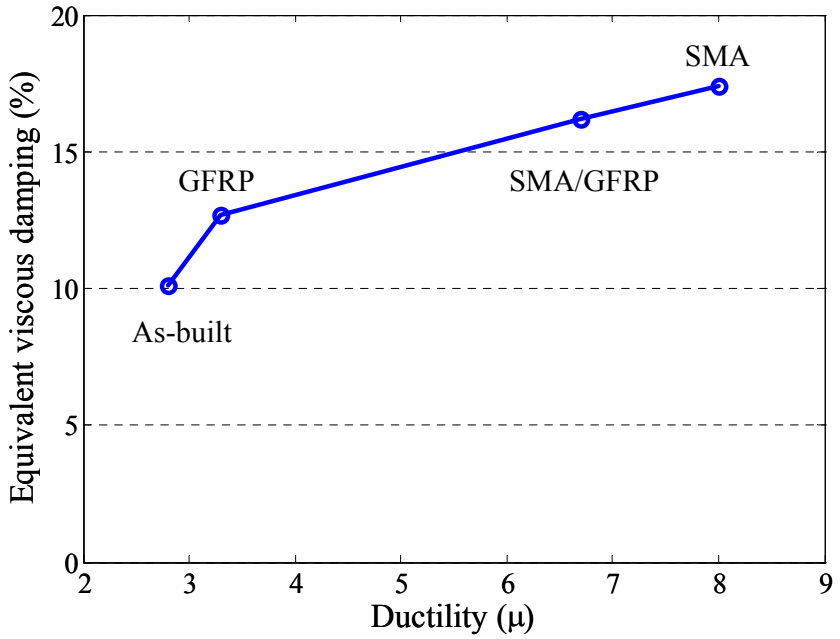

Figure 6.16 Relationship between the ductility ratio and the equivalent viscous damping ratio of the columns.

6.4.6 Results of strain measurements

Strain gauges were installed on surface of concrete, longitudinal reinforcement, GFRP wraps and SMA spirals to monitor the variations of strain of materials.

6.4.6.1 Concrete strains

Figure 6.17 shows examples of the variations of surface concrete axial strain (CLW1 and CLE1) with respect to the drift ratio of column. It is noticed that due to the damage sustained by the strain gauges during testing, it was only possible to obtain data until a drift ratio of approximately 3.0% or less was reached. The maximum strains recorded for the columns with GFRP wraps (i.e. GFRP and Hybrid columns) were less than that of the other two columns. This is primarily due to the fact that the strain gauges used in the case of GFRP wrapped columns were attached to the surface of the GFRP and not directly to the concrete surface. It is also interesting to note that the strains measured from the SMA column were the highest among all four columns (0.005 mm/mm), and the strain gauges installed in the SMA column and the Hybrid column lasted longer than the gauges attached to the other two columns.

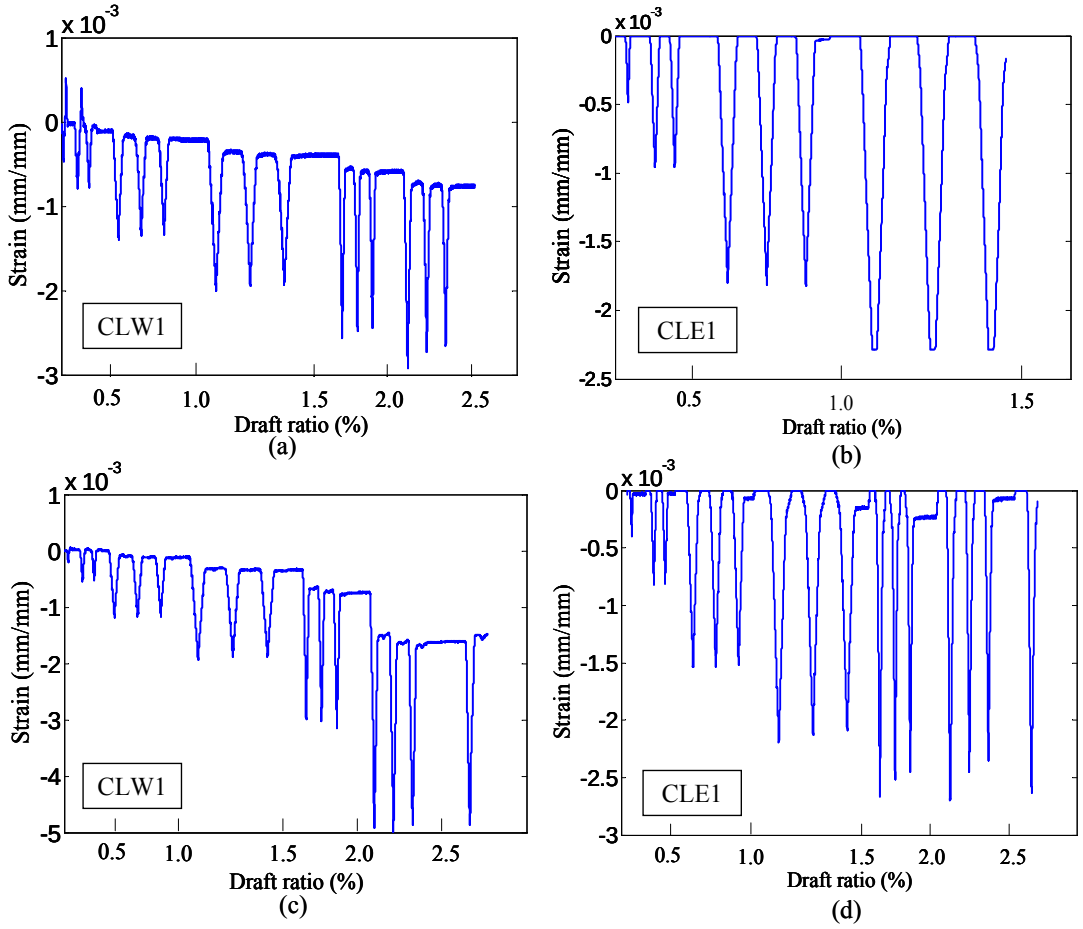

Figure 6.17 Variations of strain on surface of As-built column (a), GFRP column (b), SMA column (c) and Hybrid column (d).

6.4.6.2 Longitudinal reinforcement strains

Figure 6.18 shows examples of the variations of longitudinal reinforcement strains that were installed in the west side of each column (SLW1). The measured data of the longitudinal reinforcement strain gauges were reliable until a 3.0%-drift ratio or less was reached due to damage of the strain gauges during testing. It is noticed that longitudinal reinforcement strain recorded in the SMA column showed less strain than other columns (As-built and Hybrid column) at the same drift ratio. For example, at

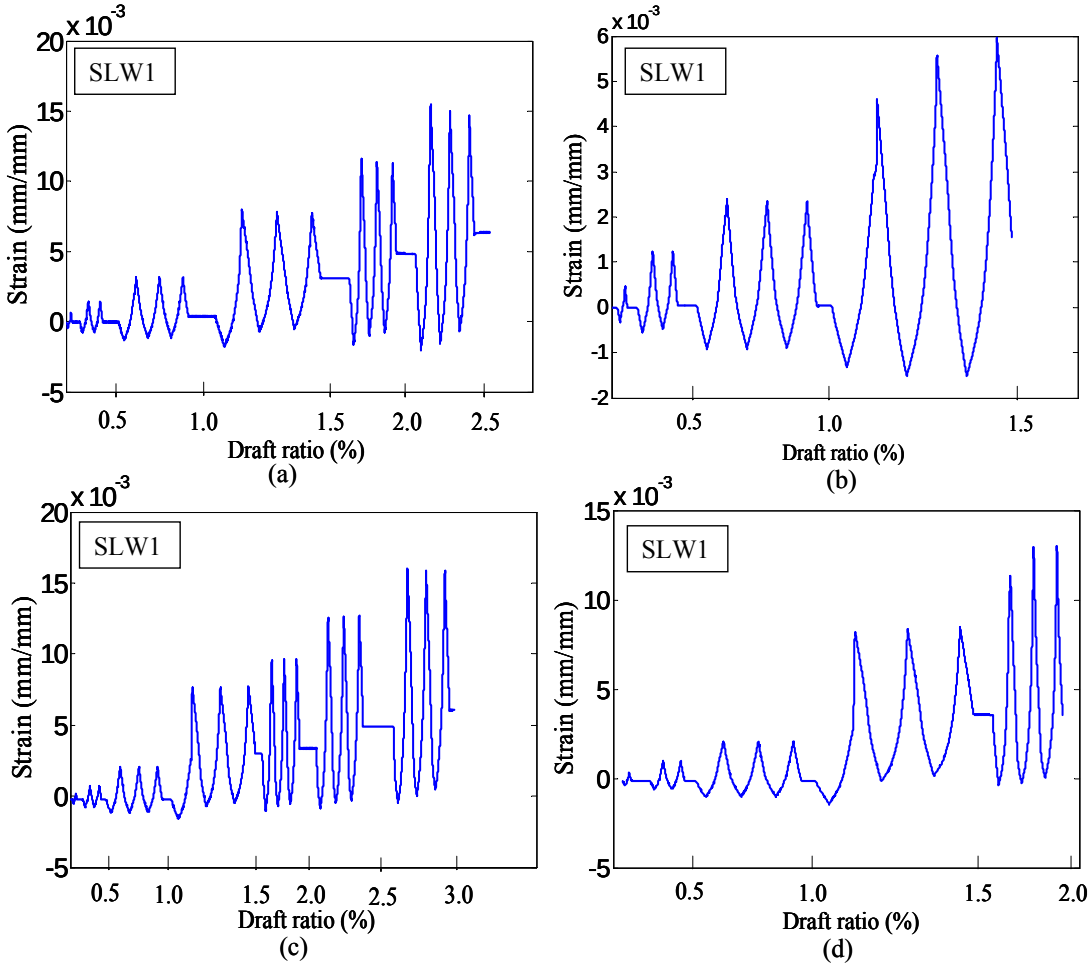

Figure 6.18 Variations of strain on surface of longitudinal reinforcement in: As-built column (a), GFRP column (b), SMA column (c) and Hybrid column (d).

2.5%-drift ratio, the measured strain from the SMA column was 0.013 mm/mm, while the strain from the As-built column was 0.015 mm/mm. The experimental strain values obtained from the GFRP and SMA columns were used to validate the numerical models that will be discussed in the following chapter.

6.4.6.3 GFRP and SMA strains

Figure 6.19 is presented to illustrate the variations of strains of the GFRP wraps in the GFRP column, and the SMA spirals in the SMA and Hybrid columns. The strain gauges were installed horizontally to monitor dilation of concrete through horizontal strains of the GFRP wraps and the SMA spirals. Figure 6.19.a shows the rupture of GFRP wraps where the rupture strain was recorded as 0.0067 mm/mm from GFRP4 at 4.5%-drift ratio. Four strain gauges were evenly attached on the surface of the SMA spirals in the SMA and the Hybrid columns (see Figure 6.6.b). Figure 6.19.b and c are the variations of average strain of SMA spirals until a 12%-drift ratio for the SMA column was reached, and a 9%-drift ratio for the Hybrid column was reached, respectively. The maximum average strain of the SMA spirals was recorded as 0.002 mm/mm in the SMA column. Therefore, the SMA spirals helped significantly to limit the dilation of concrete even at the greater drift ratio compared with the case of the GFRP column. Furthermore, the less dilation of concrete with the SMA spirals indicates that the passive confinement effect from the SMA spirals was not significant.

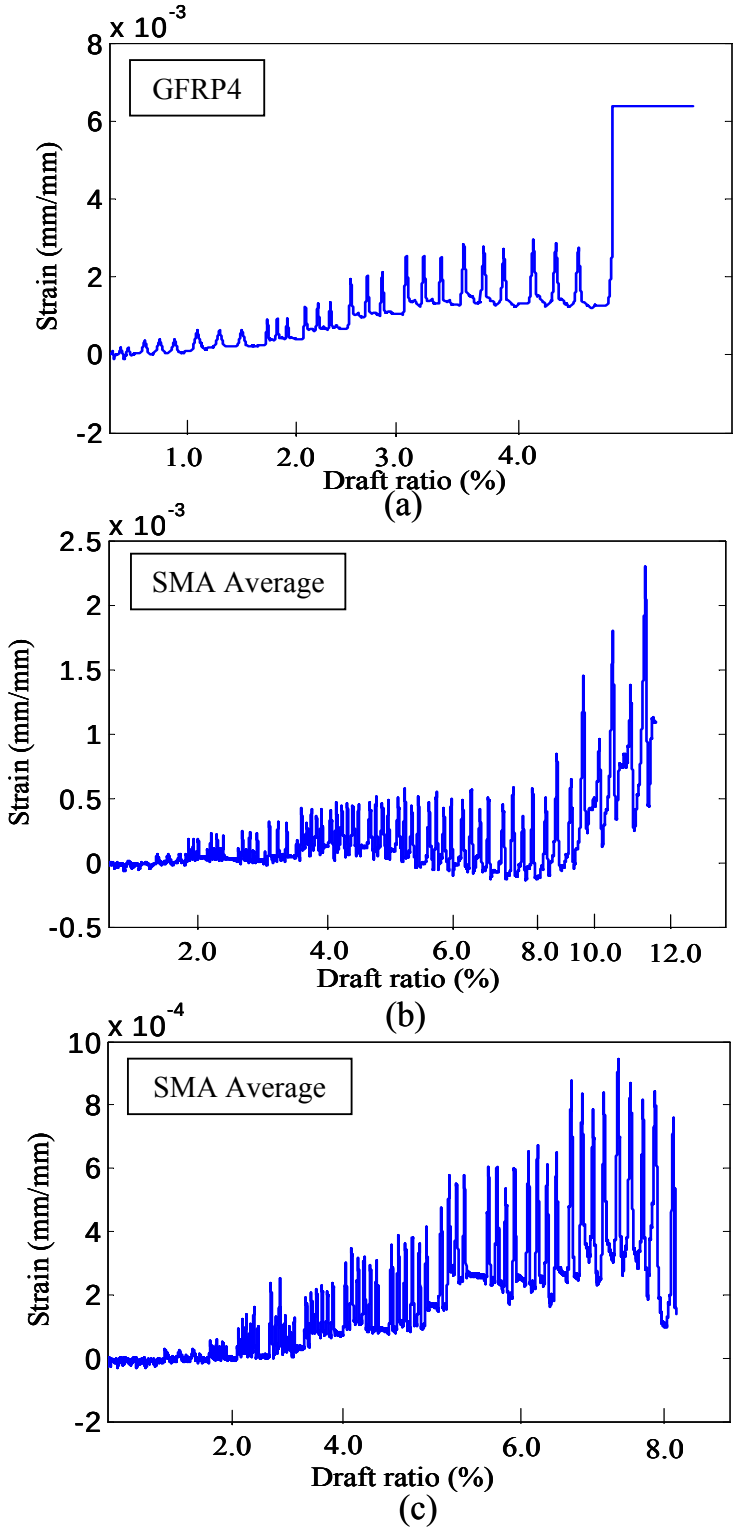

Figure 6.19 Variations of strain on surface of confinements: GFRP for GFRP column (a), SMA spirals for SMA column (b) and SMA spirals for Hybrid column (c).

6.5 DAMAGE ASSESSMENT

An important goal of the columns' testing was to explore the ability of the prestressed SMA spirals to limit the damage sustained by actively confined concrete during severe earthquakes. This section focuses on discussing the type and level of damage sustained by each of the four tested specimens.

6.5.1 As-built column

Figure 6.20 shows the progressive damage of the As-built column at various drift levels: (a) before testing, (b) at 1.5%-drift, (c) at 3.5%-drift and (d) at 5.0%-drift (after testing). After the steel rebar yielded at 1.5%-drift and when the as-built specimen reached a drift ratio of 3.5%, a significant portion of the cover concrete was already spalled. After which, the core concrete and the two longitudinal bars near the extreme fibers started crushing and buckling, respectively. When the column reached 4.2%-drift, one of the longitudinal rebars was ruptured. The bar rupture caused the strength of the column to drop suddenly by 23%. The test was stopped at 5%-drift, and a picture was taken for the column (see Figure 6.20.d). Figure 6.21.a-d shows a picture of each column when it was pushed at its maximum drift: (a) As-built column at 5%-drift, (b) GFRP column at 8%-drift, (c) SMA column at 14%-drift and (d) SMA/GFRP column at 14%-drift.

(a)

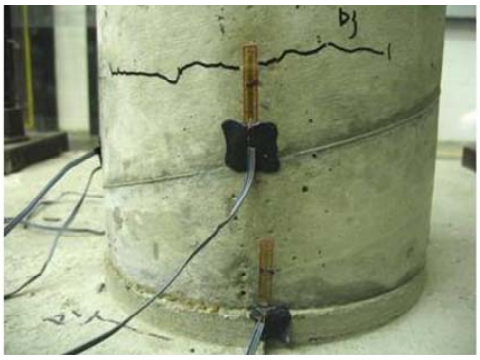

(b)

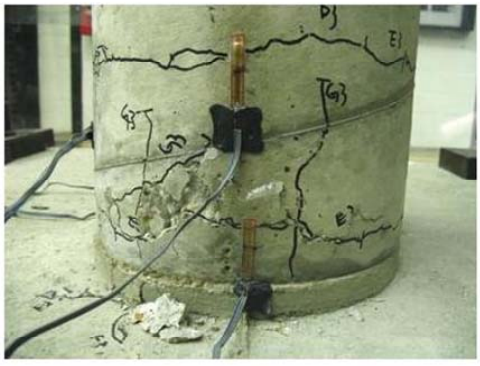

(c)

(d)

Figure 6.20 Progressive damage of the As-built column at various drift levels: (a) before testing, (b) at 1.5% drift, (c) at 3.5% drift and (d) at 5.0% drift.

(a)

(b)

(c)

(d)

Figure 6.21 Pictures of each column at its maximum drift: (a) As-built column at 5%-drift, (b) GFRP column at 8%-drift, (c) SMA column at 14%-drift and (d) SMA/GFRP column at 14%-drift.

6.5.2 GFRP column

Figure 6.22 shows the progressive damage to the GFRP column before testing (a), at a drift of 3.5% (b), at a drift of 5.0% (c) and at a drift of 8.0% (d), which was the last drift cycle of the test. The first vertical crack on the surface of GFRP jacket was developed when the column reached a drift ratio of 3.5% (see Figure 6.22.b). At 5%-drift, significant cover concrete spalling was observed and the transverse reinforcement was exposed (see Figure 6.22.c). In subsequent cycles, significant progressive damage to the jacket was noticed which caused the force to degrade rapidly until the test was stopped at 8%-drift. The damage observed in the specimen at the end of the test is depicted in Figure 6.22.d. After testing, when the jacket was removed and the crushed concrete was cleaned, it was found that one of the longitudinal bars was ruptured.

6.5.3 SMA column

The progressive damage of the SMA column is depicted in Figure 6.23. At 1%-drift, horizontal crack lines started appearing on the concrete surface between the SMA spirals. These cracks started progressing gradually while the drift was increased. However, no vertical cracks were observed until the test was stopped at 14%-drift. Along with the horizontal cracking, there was a gradual and moderate spalling of the concrete cover between the SMA spirals. At a drift ratio of 12%, a loud noise was heard which indicated the rupture of one of the longitudinal rebars. Figure 6.23.e and Figure 6.23.f show the damaged specimen at 8%-drift (maximum drift exerted on GFRP column) and 14%-drift, respectively. Comparing these two pictures with the picture of the GFRP

(a)

(b)

(c)

(d)

Figure 6.22 Progressive damage of the GFRP column at various drift levels: (a) before testing, (b) at 3.5% drift, (c) at 5.0% drift and (d) at 8.0% drift.

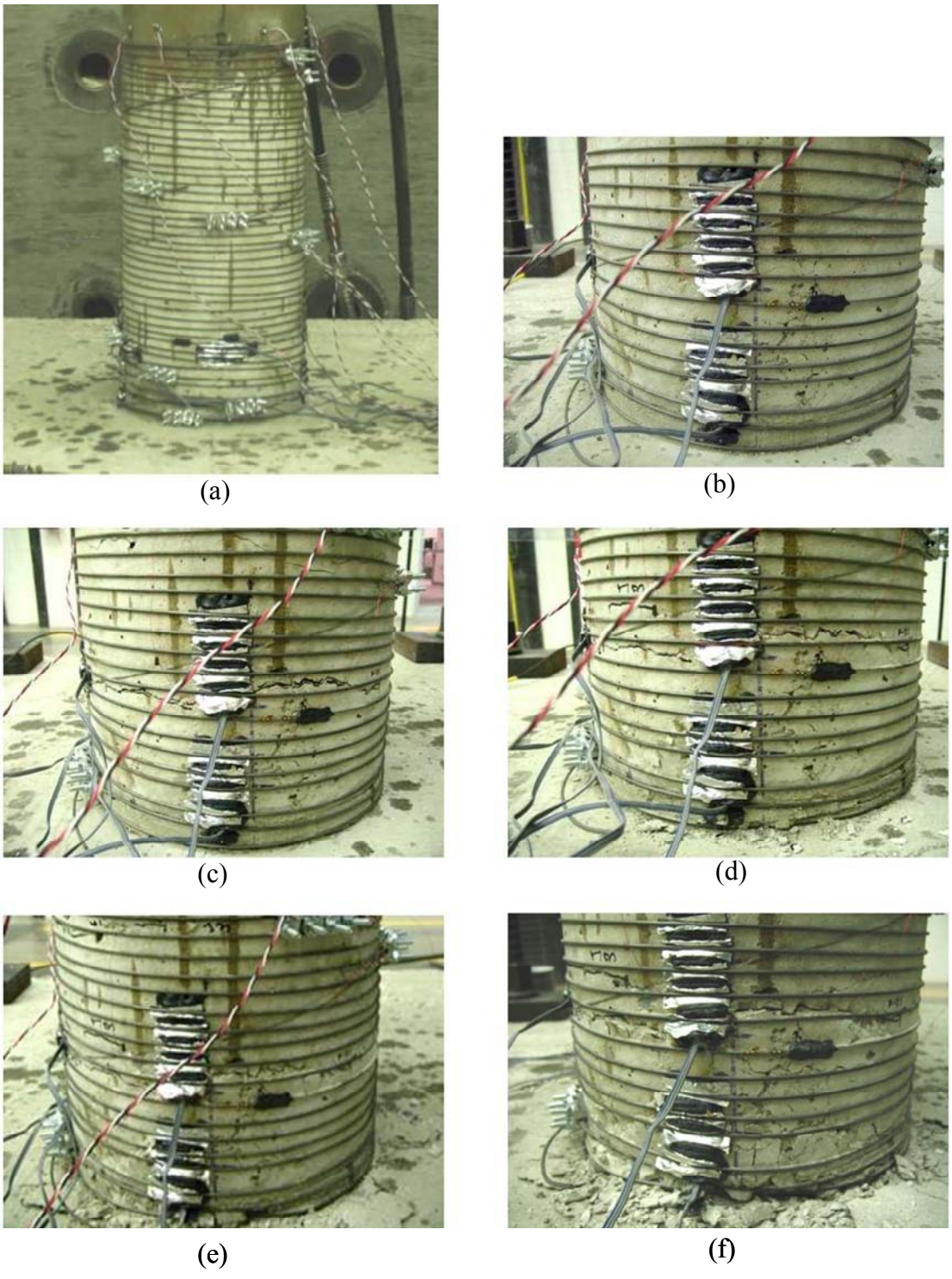

Figure 6.23 Progressive damage of the SMA column at various drift levels: (a) before testing, (b) at 1.0% drift, (c) at 3.5% drift, (d) at 5.0% drift, (e) at 8.0% drift, and (f) at 14.0% drift.

column at 8%-drift (in Figure 6.22.d) demonstrates that even with 75% more drift, the SMA column sustained extremely less damage than that of the GFRP column.

6.5.4 SMA/GFRP column

The progressive damage of SMA/GFRP column is presented in Figure 6.24.a - Figure 6.24.f. The GFRP jacket delayed the development of the horizontal crack lines until a drift ratio of 2.5% (compared to 1% for the SMA column) was reached. The first vertical crack on the surface of the GFRP jacket was observed at 4.5%-drift (compared to 3.5% for the GFRP column). The SMA spiral helped in prestressing the GFRP jacket in the hoop direction which delayed the rupture of the GFRP, despite using half of the number of the GFRP layers that were used in the GFRP column. The prestressed spirals also helped in limiting the progression of damage throughout the test until it was stopped at 14%-drift. When the column drift ratio reached 10%-drift, concrete spalling was observed at one side and a rebar was ruptured on the opposite side. Figure 6.24.d and Figure 6.24.f present the pictures of the column at 8%-drift (maximum drift exerted on GFRP column) and 14%-drift, respectively. Again, comparing these two pictures with the picture of the GFRP column at 8%-drift (in Figure 6.22.d) illustrates that using the hybrid confinement technique (despite the reduced number of GFRP layers) resulted in a significant reduction in the level of damage sustained even under excessive drifts (14%).

To assess the damage more closely, Figure 6.25 is presented. The figure shows the four columns after testing when the GFRP jackets and SMA spirals were removed and the crushed concrete was cleaned. The damage was extended to a height (measured

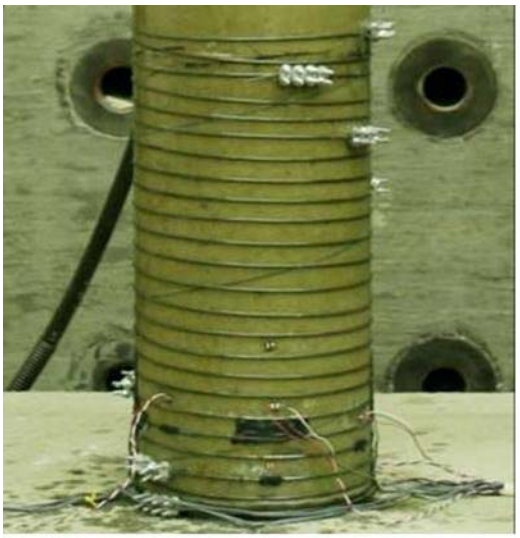

(a)

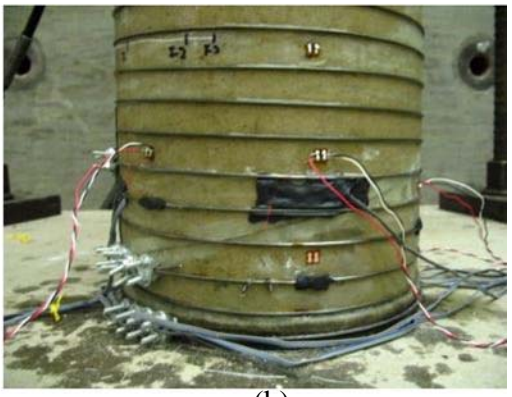

(b)

(c)

(d)

(e)

(f)

Figure 6.24 Progressive damage of the SMA/GFRP column at various drift levels: (a) before testing, (b) at 2.5% drift, (c) at 4.5% drift, (d) at 8.0% drift, (e) at 10.0% drift, and (f) at 14.0% drift.

from the base) of 330 mm (13 in), 178 mm (7 in), 76 mm (3 in) and 114mm (4.5 in) for the as-built column, GFRP column, SMA column, and SMA/GFRP column, respectively. On the other hand, the average width of the remaining concrete in the damaged plastic hinge was 102 mm (4 in), 102mm (4 in), 216 mm (8.5 in), and 191 mm (7.5 in) for the as-built column, GFRP column, SMA column, and SMA/GFRP column, respectively. The limited area of damage in the SMA retrofitted columns compared to the GFRP column is attributed to the high ultimate strain of actively confined concrete compared to the passively confined concrete. By looking at the pictures it is evident that before reaching the point of steel rupture, the two SMA retrofitted columns would require minimal repairs, which will help maintain the bridge functionality after major earthquakes.

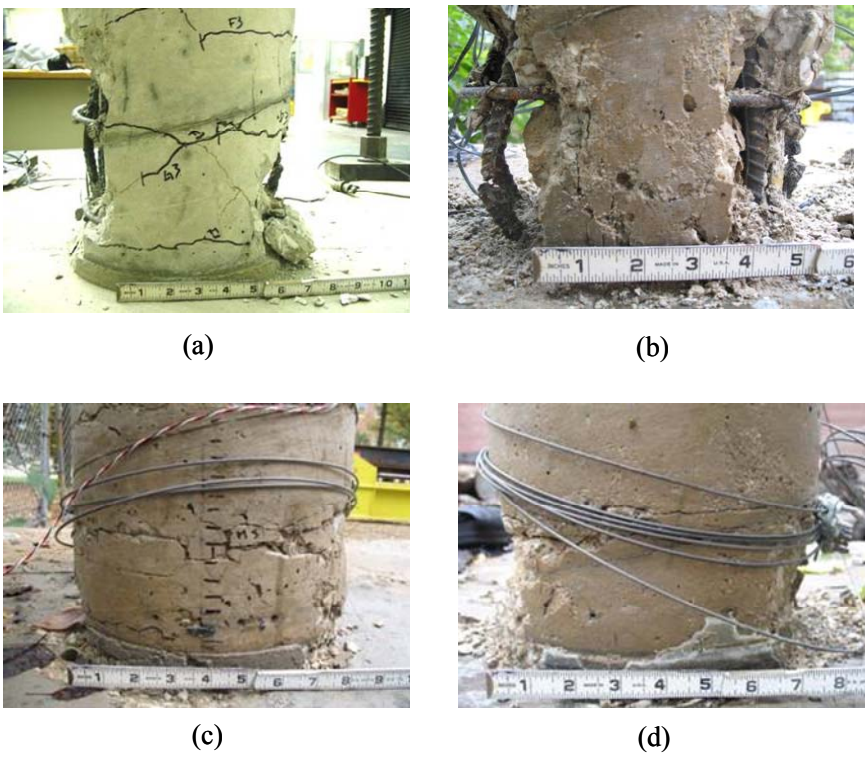

Figure 6.25 Damage sustained by the four columns after the GFRP sheets and SMA spirals are removed: (a) As-built, (b) GFRP, (c) SMA and (d) SMA/GFRP column.

CHAPTER 7 EMERGENCY REPAIR OF RC COLUMNS

From the literature review presented in chapter 2, it is clear that the currently available RC column repair technologies (e.g. concrete or FRP jackets) lack the ability to be implemented and used immediately after an earthquake event. Hence, there is a dire need for an effective repair technology that could be implemented in the field in timely manner. The experimental investigation of the new confinement technique using SMA spirals was further expanded in this chapter to include column "emergency" repair application. Two severely damaged RC columns (the as-built column from the retrofit study and another column which was accidentally damaged during testing) were repaired and tested. A detailed description of the repair technique, the testing procedure and the results are discussed in this chapter.

7.1 SPECIMENS DESCRIPTION AND DAMAGE HISTORY

7.1.1 As-built specimens

The two tested columns were identical and they were damaged in the previously discussed retrofit study (see section 6.1). One of the columns (C1 column) was damaged under an incrementally increasing displacement-controlled lateral cyclic load, while the other column (C2 column) was damaged accidentally due to an error in the control system during testing which caused the actuator to exert an excessive monotonic load on the specimen. The cyclic force versus displacement behaviors of the as-built C1 and C2 columns are shown in Figure 7.1.a and Figure 7.1.b, respectively along with the backbone curves. Both columns were subjected to the same load protocol shown in Figure 6.10.

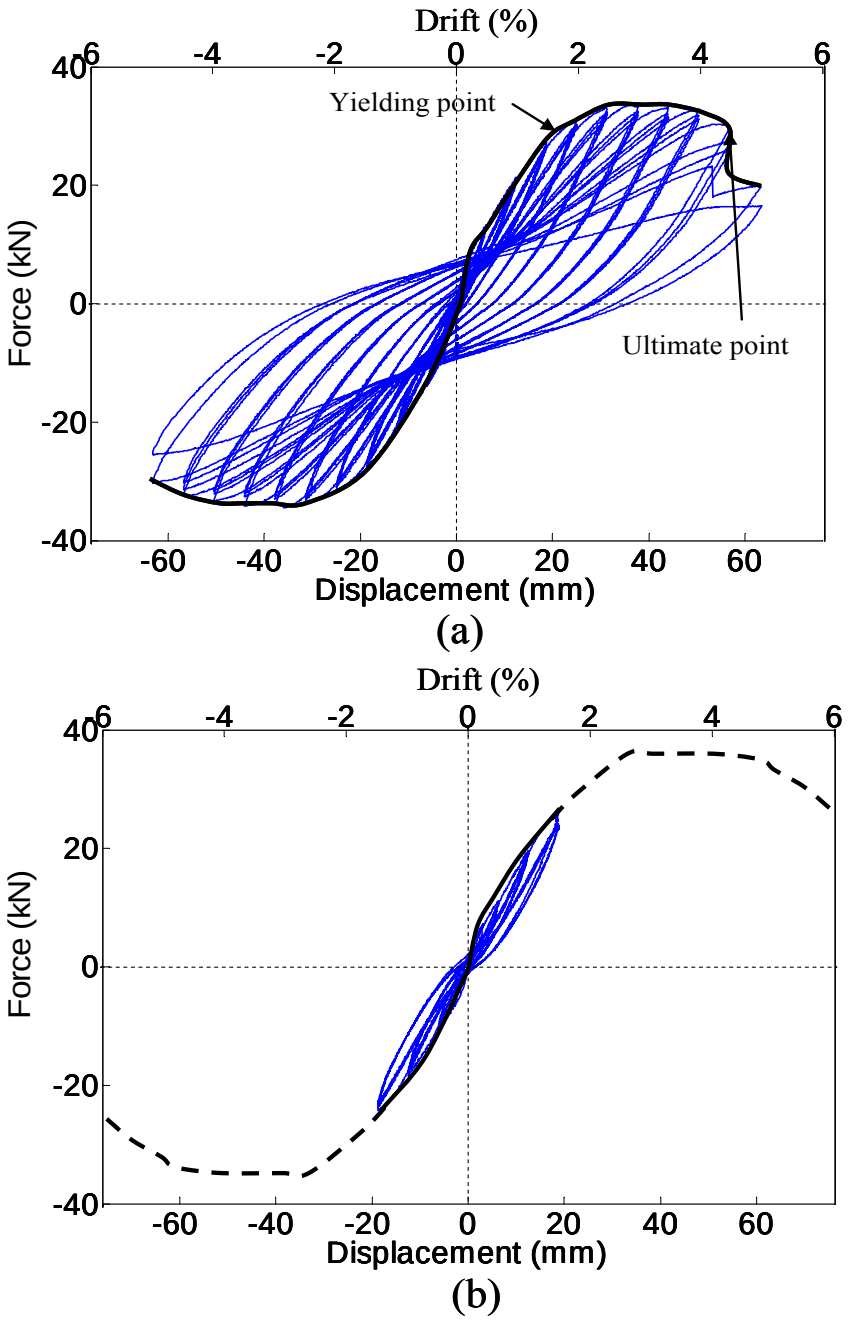

Figure 7.1 Force vs. displacement cyclic behaviors of the as-built columns: (a) C1 column and (b) C2 column.

7.1.1.1 Behavior and Damage of As-built Column C1

Figure 7.2 shows a picture of the damaged C1 column. The details of the cyclic behavior and damage of the C1 column were discussed in section 6.4 and section 6.5.1, respectively.

(a) (b)

Figure 7.2 Damage of C1 column: (a) front view and (b) side view.

7.1.1.2 Behavior and Damage of As-built Column C2

Column C2 was tested under the same load protocol as column C1. However, at a drift ratio of 1.5% the hydraulic actuator went out of control in one direction exerting a maximum drift ratio of about 7% on the specimen. The cyclic behavior shown as a solid line in Figure 7.1.b was recorded prior to the accidental displacement of the specimen. Due to the problem encountered during the testing, no data was recorded after 1.5% drift. The dashed line shown in Figure 7.1.b represents the predicted backbone curve based on the behavior of the identical column C1. Pictures of the accidentally damaged specimen are shown in Figure 7.3. Since the column was damaged primarily under monotonic

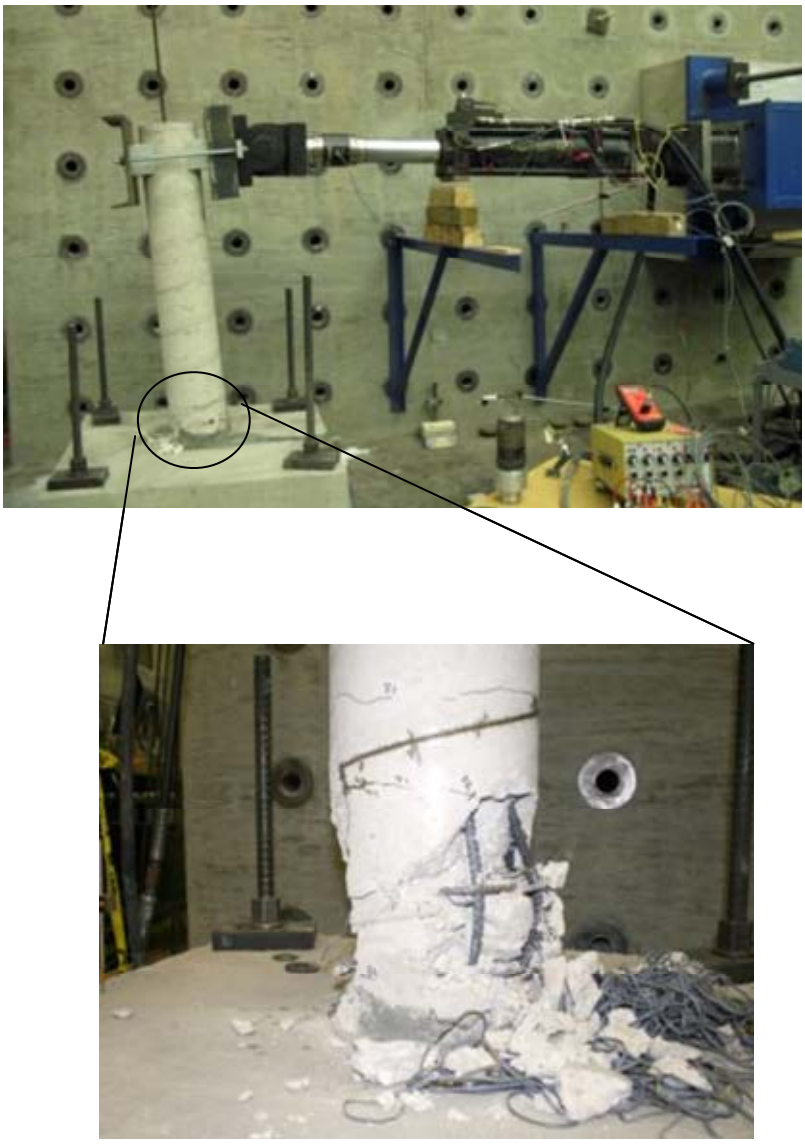

Figure 7.3 Damage of C2 column.

loading, the concrete at one side was completely crushed, while at the other side the concrete was cracked due to excessive tension. While recentering the damaged column after the accident, cracked concrete spalled significantly. Therefore the concrete damage was unsymmetrical unlike column C1 which was damaged symmetrically. In addition, since column C2 was not subjected to significant cyclic loading at high drift ratios as in

the case of column C1, the rebars in column C2 showed severe buckling without experiencing any rupture. The height of the damaged plastic region was 330 mm (13 in).

7.2 DESIGN OF SMA SPIRALS

Since no guidelines are available for designing columns under active confinement, the guidelines provided by the California Department of Transportation (Caltrans) for passive confinement using FRP wraps (Caltran, 2008) was adopted in this study. Caltrans recommends applying a passive pressure of 2.07 MPa (300 psi) at a radial strain of 0.004 in the FRP wraps. Using these requirements and the required thickness of FRP wraps, t_j, is written as

$$t_j = \frac{f_l D}{2\alpha_f E_f \varepsilon_j} \qquad (7.1)$$

where f_l is the target confinement pressure (2.07 MPa (300 psi)), D is the diameter of the cross section of the column (254 mm (10 in)), E_f is the modulus of elasticity of the FRP which was found to be 19,000 MPa (2755 ksi) for the GFRP used in this study, α_f is a reduction factor of 0.9 recommended by Caltrans (2008), and ε_j is the radial strain (0.004). Therefore, it was found that using 32 layers of 0.11 mm (0.0043 in) thick GFRP sheets (3.52mm (0.14in)-thick) is required.

The pitch spacing of the SMA spirals (with 2 mm (0.8 in) wire diameter) used in the repair of the damaged columns was selected by comparing the numerical behaviors of the tested columns with SMA spirals and GFRP sheets. The numerical models for RC

columns used in the comparison were based on the confined concrete models that were discussed in Chapter 4. In the analysis, the pitch was varied until the displacement capacity (i.e. displacement corresponding to the onset of concrete core crushing) of the column retrofitted with SMA spirals matches that of the column wrapped with 32 layers of GFRP sheets. The finite element program OpenSees (Mazzoni et al. 2009) was utilized again. In these models, nonlinear displacement-based beam–column elements were used to model the columns at the plastic hinge region (Figure 7.4.a). Fiber sections were assigned to the beam–column elements to capture the unique nonlinear constitutive stress–strain behavior of the section's cover concrete, core concrete, and longitudinal steel reinforcement. The numerical models for columns were subjected to incrementally increasing cyclic displacement until the core concrete in each column reached its crushing (ultimate) strain. After several iterations it was found that a SMA spiral pitch of 25 mm (1.0 in) resulted in close enough ultimate points of both columns; therefore, a pitch of 25 mm (1.0 in) was used in the repair of the damaged columns. Based on the previously determined recovery stress of the SMA wires (460 MPa (67 ksi)), the active confinement pressure induced by the 25 mm (1.0 in)-pitch spiral was calculated as 0.6 MPa (90 psi). Figure 7.4.b shows the lateral force versus lateral displacement relationships of both SMA and GFRP retrofitted columns. As shown, both columns reached the ultimate point at a drift ratio of 7.8%, and the behaviors were in good agreement.

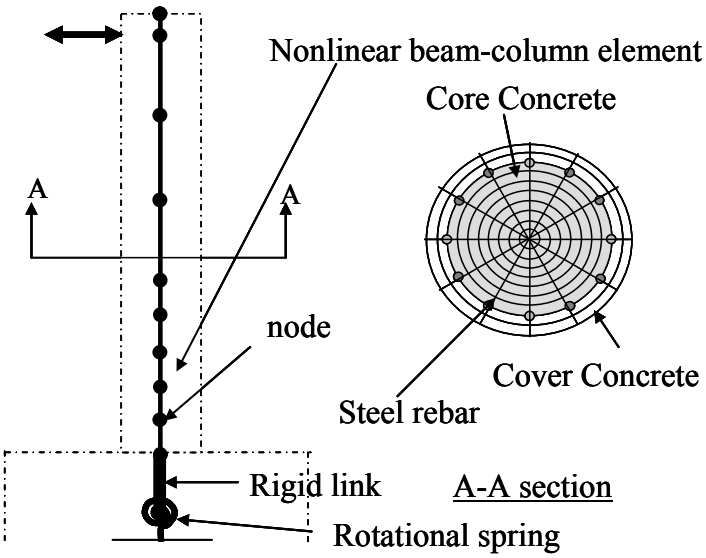

(a)

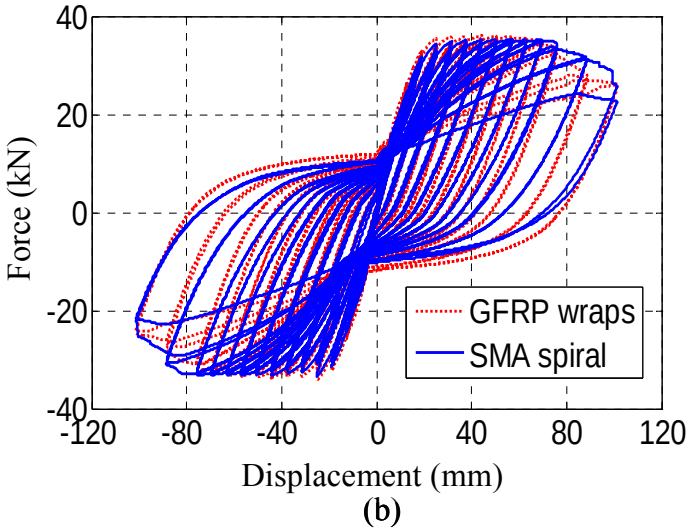

(b)

Figure 7.4 Analytical model of RC column (a) and analytical force vs. displacement relationships of RC columns retrofitted with SMA spiral and GFRP wraps (b).

7.3 REPAIRED SPECIMENS

In an attempt to restore the lateral strength and ductility of the two damaged columns in less than 24 hours, the columns were subjected to a five-step repair process. Figure 7.5 presents pictures illustrating the steps of the repair process. First, crushed and loose pieces of concrete were removed from the damaged region of the columns and the steel reinforcement was exposed. Figure 7.5.a shows the concrete surface of column C1 after removing the crushed concrete. A picture before removing the crushed concrete can be seen in Figure 7.2. and Figure 7.3. Second, longitudinal steel bars which were slightly buckled were straightened, while the bars which were ruptured were connected using rebar couplers (Figure 7.5.b). As noted earlier, only one bar was ruptured and needed coupling in column C1. For column C2, however, no longitudinal rebars were ruptured, but three of the rebars experienced severe buckling. To adjust these bars, it was deemed necessary to cut and reconnect these bars with couplers. The third step in the repair process involved the use of injected pressurized epoxy to fill the cracks of the columns (Figure 7.5.c). Injection ports were installed on the surface of the column, and the cracks were sealed by removable paste glue to allow the injected epoxy to fully penetrate the cracks. Steps one through three took approximately three hours. In the fourth step, quick-setting mortar was applied at the damaged region (Figure 7.5.d). The nominal compressive strength of the mortar under controlled environmental conditions at an age of 24 hours was 31.0 MPa (4.5 ksi). To examine the strength of the mortar in the laboratory environment where the columns were tested, three 76 mm × 152 mm (3 in x 6 in) cylinders were cast using the quick-setting mortar and tested after 24 hours.

(a)

(b)

(c)

(d)

(e)

(f)

Figure 7.5 Pictures of the five-step emergency repair process: (a) Concrete removal, (b) steel adjustment, (c) epoxy injection, (d) mortar application, (e) heating of SMA spirals, and (f) repaired column.

The strength of the cylinders was found to be 21 MPa (3.0 ksi), which is 53% of the compressive strength of the concrete used in casting the columns. While the mortar was curing, the fifth step of the repair process was conducted. The columns were wrapped with the SMA spirals at the repaired region (i.e. 330 mm (13 in) from the column base) and heated using a blowtorch as shown in Figure 7.5.e. A picture of the column after the completion of the repair process is shown in Figure 7.5.f. The total time from the first step of repair until the onset of the column testing was approximately 24 hours. It is worth noting however that the repair process itself was conducted in less than 15 hours.

7.4 TEST-SETUP

Figure 7.6 shows an isometric view of the test setup that was used in the testing of the repaired columns. The columns were subjected to the quasi-static lateral cyclic loading protocol previously shown in Figure 6.10. The same test-setup described in section 6.1.1 was used. During testing, the axial force on the column was maintained at a value of 116 kN (26 kips), which represented 5% of the gross section compressive strength of the as-built columns.

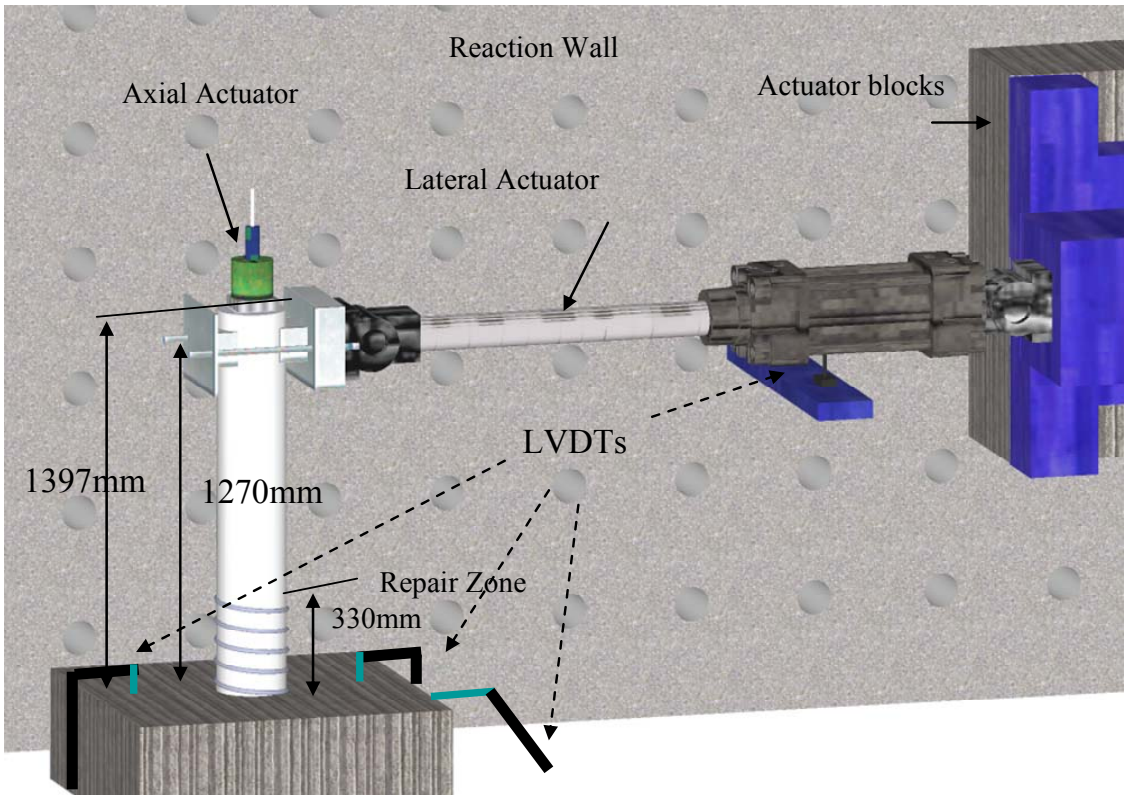

Figure 7.6 Isometric view of the test set-up.

7.5 TEST RESULTS

7.5.1 Column C1

Figure 7.7 shows a comparison between the lateral force versus displacement relationships of the as-built and the repaired C1 column. The repaired column started yielding at a drift ratio of 0.7%, and the average maximum strength recorded was 34.2 kN (7.7 kips). At a drift of 2%, the strength of the repaired column dropped suddenly by 28% due to the rupture of one of the longitudinal rebars. In the subsequent cycle, another rebar was ruptured reducing the strength to 52% of its peak value. Comparing the average strength of the repaired and as-built columns reveals that the emergency repair technique

performed on the severely damaged column was able to fully restore the as-built column's lateral strength and exceeded it by 3%. Furthermore, the average initial stiffness of the repaired column was found to be 3.4 kN/mm (19.4 kips/in), which is 54% higher than that of the as-built column and 930% higher than the residual (secant) stiffness of the damaged column.

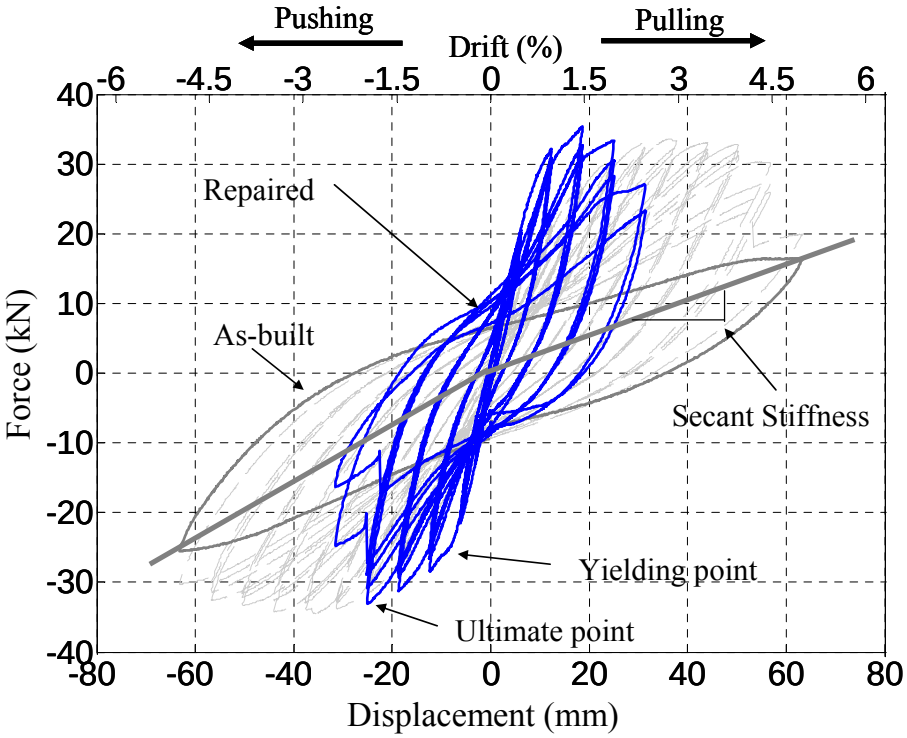

Figure 7.7 Comparison between the force-displacement relationships of the as-built and repaired column C1.

Although the column experienced significant degradation in its strength at 2% drift, its overall displacement ductility ratio (i.e. ratio between the lateral displacement at the ultimate and yielding points) was 2.9 compared to a ductility ratio of 2.8 for the as-built column. This was due to the significant increase in the initial stiffness of the repaired column compared to the as-built column. The displacement ductility ratio of each column was the minimum value of the ductility ratios determined from pushing and pulling. The yielding points and the ultimate points of the repaired column and the as-built column are depicted on the backbone curves presented in Figure 7.8. After testing, it was confirmed that the couplers were successful in connecting the ruptured rebar. Figure 7.9 shows pictures of the repaired column C1 after the test was complete.

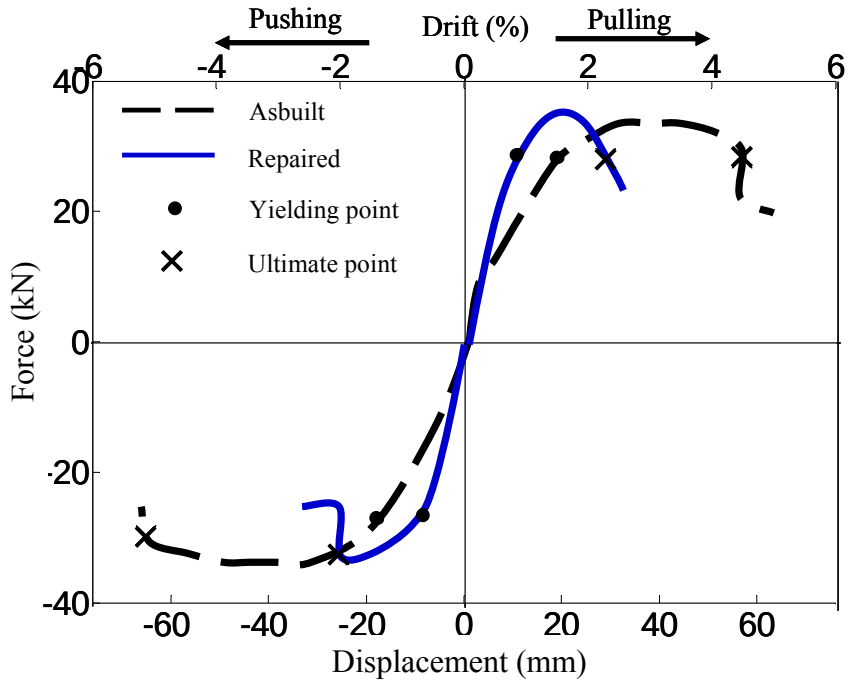

Figure 7.8 Backbone curves of the repaired and as-built column C1.

Figure 7.9 Pictures of column C1 after the test was complete.

7.5.2 Column C2

Figure 7.10 shows a comparison of the lateral force versus displacement relationship between the as-built and the repaired column C2. The repaired column started yielding at a drift ratio of 0.6%, and the maximum strength recorded was 41.3 kN (9.3 kips) at 1.5% drift ratio. The cyclic behavior of the repaired column was unsymmetrical, and the lateral strength of the column degraded gradually, instead of dropping suddenly. The unsymmetrical behavior of the repaired column was confirmed later to be mainly due to the slippage of the coupled rebars located on one side of the column during testing. Figure 7.11 shows a picture of the rebars that slid from the couplers after testing. The failure of the couplers to fully connect the rebars resulted in a reduced strength of the rebars, which led to significantly less strength for the column when 'pushed' (see Figure 7.10). On the other hand, when the column was 'pulled', it showed satisfactory behavior since the rebars resisting tension were in good condition and only sustained minimal damage during the first round of testing. Assessing the

behavior of the column when pulled, one can observe that the strength of the repaired column exceeded that of the as-built column by 21% (based on the predicted maximum strength of the as-built column, 34.5 kN (7.8 kips)). Also, the average initial stiffness of the repaired column in both pulling and pushing directions was 4.2 kN/mm (24.0 kips/mm), which exceeded the initial stiffness of the as-built column by 47%.

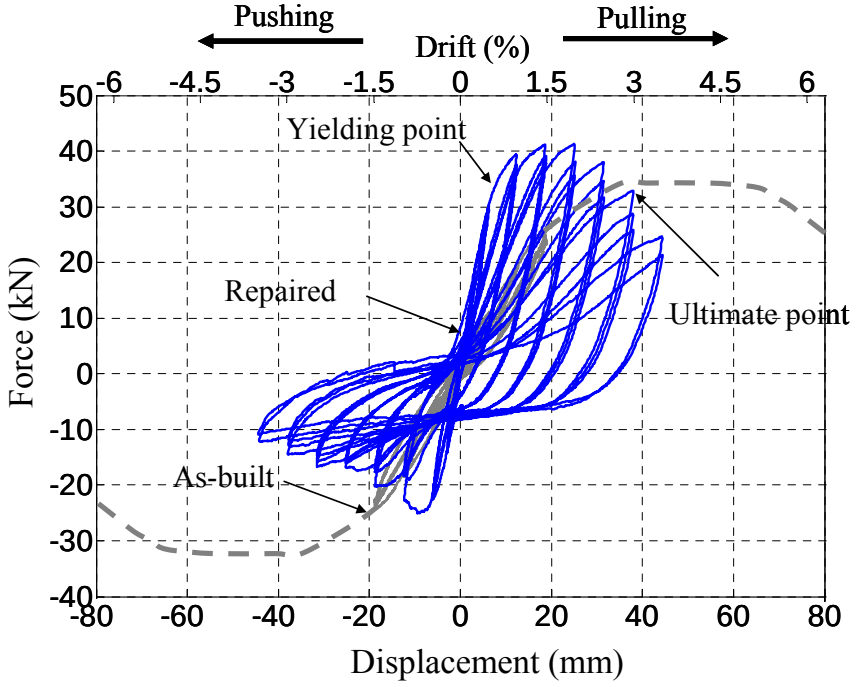

Figure 7.10 Comparison between the force-displacement relationships of the as-built and repaired column C2.

Figure 7.11 Slippage of rebars from the couplers.

In order to examine the displacement ductility ratio, the backbone curves of the repaired and as-built C2 column are presented in Figure 7.12. Due to the previously discussed unsymmetrical behavior of the column, only the backbone curve under pulling is shown. From the yielding and ultimate points shown in the figure, it was determined that the displacement ductility ratio of the repaired column C2 is equal to 5.0, which is 79% greater than the ductility ratio of the as-built column. It is worth noting that since the strength degradation of the repaired column occurred gradually, the ultimate point of the repaired column was taken at force level corresponding to 80% of the peak lateral strength of the column.

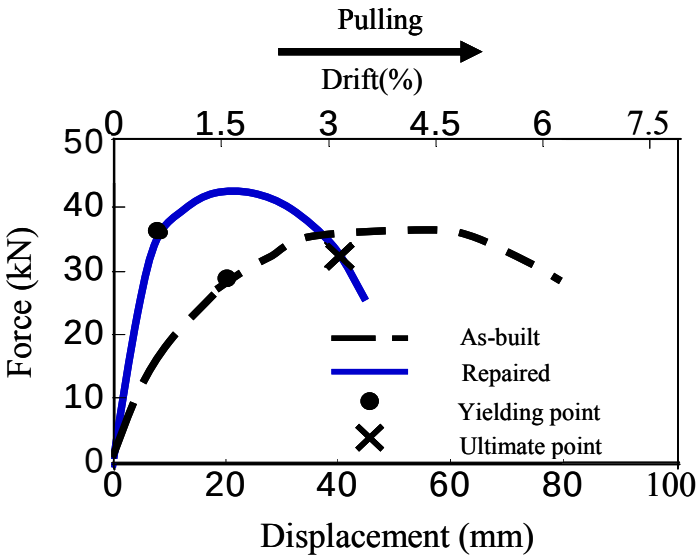

Figure 7.12 Backbone curves of the repaired column and as-built column C2.

CHAPTER 8 MODELING AND VALIDATION

In this chapter of the thesis, a numerical model of RC bridge columns retrofitted with SMA spirals was developed and validated using the experimental results of the 1/3-scale columns presented in chapter 6. In the preliminary analysis discussed earlier in chapter 4, a RC column model using OpenSees (Mazzoni et al. 2009) was introduced. Continually, the RC column model with fiber sections was utilized to develop the models presented in this chapter after considering new factors such as passive pressure of SMA confinement, tensile strength of concrete, and rupture of longitudinal reinforcement.

8.1 NUMERICAL MODELING OF THE TESTED SMA COLUMN

One of the main objectives of this study was to develop a numerical column model capable of describing the behavior of RC columns with external confinements especially when using SMA spirals. The model should be able to take into account the effect of the internal steel transverse reinforcement as well. Schematics showing the tested column and its analytical model are presented in Figure 8.1. Based on experimental tests, the compressive strength of the unconfined concrete was taken as 44.8 MPa (6500 psi) and the yield strength of the longitudinal and lateral steel reinforcements were 414 MPa (60 ksi) and 248 MPa (36 ksi), respectively. The OpenSees nonlinear displacement-based beam-column element was utilized to develop the numerical model of the column (elements E2-E9 in Figure 8.1.b) and a rigid element was used to model the footing (element E1) with a rotational spring which was introduced at the mid height of the footing to capture the column's flexibility at the base. The retrofitted column was divided into three regions (Zone1, Zone2, and Zone3) as shown in Figure 8.1.a. Zones 2 and 3

were retrofitted using GFRP sheets, while Zone 1 (Plastic hinge zone) was retrofitted using SMA spirals. More details about the retrofitting schemes used in the experimental tests can be found in Chapter 6. A fiber section was assigned to the beam-column elements to describe their nonlinear behavior. In the fiber section, different constitutive relations are utilized for the cover concrete, core concrete, and longitudinal steel reinforcement fibers (see Figure 8.1.c). The numerical results of the developed column models were compared with the experimental results in terms of global hysteretic behavior, damage states, and material strains. The details of the material constitutive relationships used in the model are discussed in the next subsection.

8.1.1. Material constitutive behaviors

8.1.1.1 Unconfined and Confined Concrete

The constitutive relationship used to describe unconfined concrete followed the uniaxial Concrete04 model in OpenSees. The compressive stress-strain curve is expressed numerically using one continuous equation showing the concrete strength, f_{co} as the peak strength at the strain, ε_{co} suggested by Popovics (1973). Also, the uniaxial Concrete04 material model was used to simulate the behavior of the concrete confined with SMA as described in section 4.2.2. As described previously, in order to incorporate the effects of active confinement lateral pressure induced by the external SMA spirals, a modified version of the analytical model that was developed by Mander et al. (1988) was utilized.

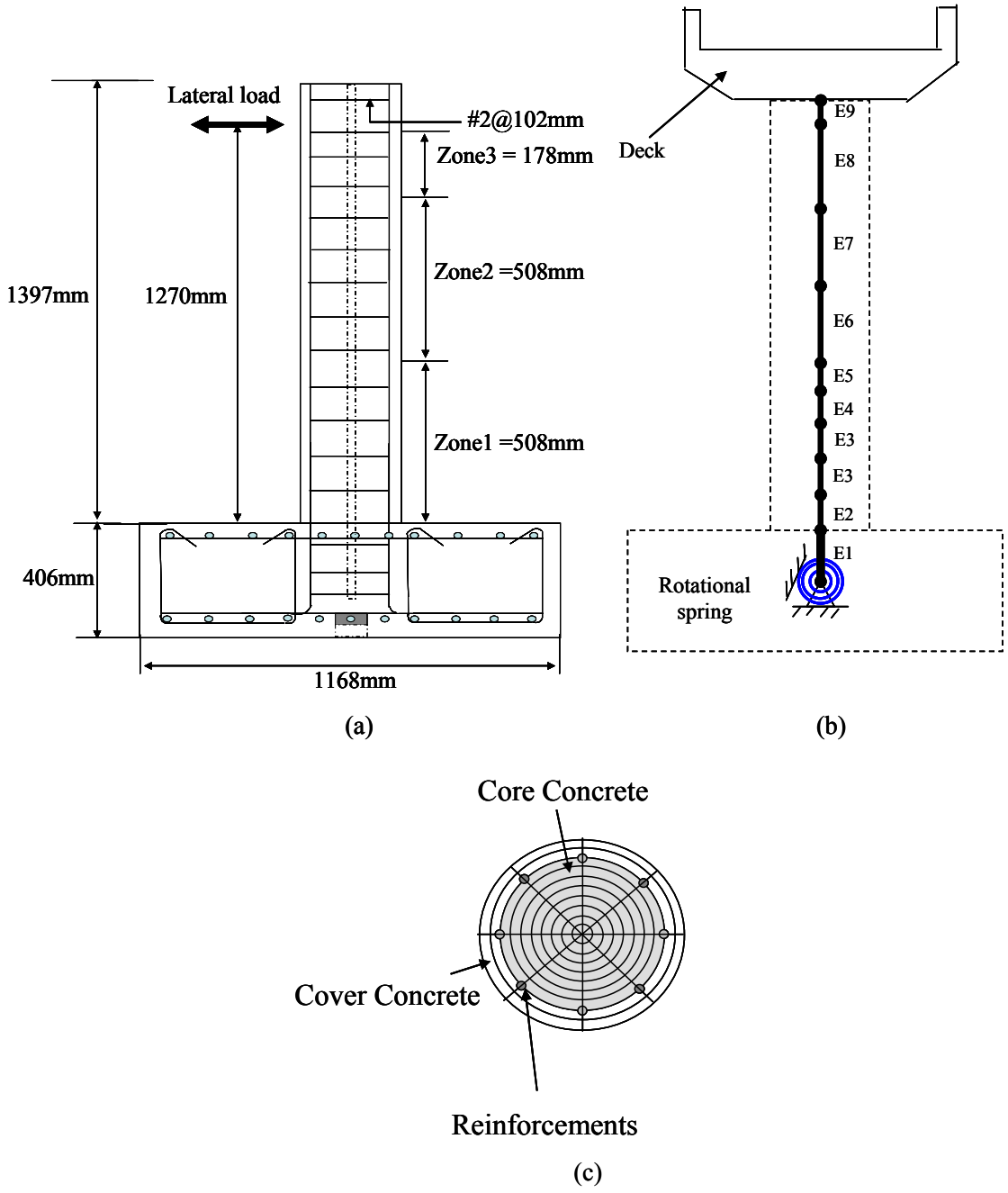

Figure 8.1 Schematics of tested column (a), numerical model for column (b) and fiber section of the numerical model for column (c).

According to Mander et al., the stress and strain values at the peak point on the envelope curve of confined concrete could be computed using Eqs 4.5 and 4.6, respectively. To compute the values, the lateral confining pressure is the most important variable in the equations. However, the model needs to be modified further to account for the passive confinement pressure that was determined experimentally from the thermo-mechanical tests of NiTiNb SMA wires (see Figure 5.6). Therefore Eq.4.7 was modified as follows:

$$f_l = f_{l\_tie} + f_{l\_SMA\_active} + f_{l\_SMA\_passive} \quad (8.1)$$

where f_{l_tie} is the confining pressure induced by the internal steel ties at yielding, $f_{l\_SMA\_active}$ is the active confinement pressure from the SMA spiral, and $f_{l\_SMA\_passive}$ is the additional passive confinement pressure from the SMA spiral. Once the actively confined concrete starts dilating under the axial load, the column is expected to sustain additional passive confinement pressure induced by the SMA spiral. For circular columns, the total confinement pressure f_{l_SMA} is directly related to the properties of the SMA wire through the following formula:

$$f_{l\_SMA} = k_e^{SMA}(2A_{SMA}(\sigma_{SMA} + \sigma_{passive}))/(d \times s) \quad (8.2)$$

where k_e is a correction factor suggested by Mander et al. to account for the reduction in the confining pressure due to the spacing between the wires, A_{SMA} is the cross sectional

area of the SMA wire, σ_{SMA} is the SMAs recovery stress, $\sigma_{passive}$ is the additional stress induced in the SMAs due to the dilation of concrete, *d* is the diameter of the circular column, and *s* is the spiral pitch. In this analysis and based on previous experimental tests in Chapter 5 and 6, the recovery stress of SMAs was 413.8 MPa (60 ksi) after taking into account prestrain losses of 1% (see Figure 5.5 and Figure 6.11).

8.1.1.2. Longitudinal Reinforcement

The behavior of the longitudinal steel reinforcement in the SMA confined column was represented using the uniaxial Steel02 model in OpenSees again as described in section 4.2.3. Steel02 material model is based on the Giuffré-Menegotto-Pinto model (1973), and it is capable of simulating the hysteretic behavior of steel reinforcement under cyclic loading. In order to mimic the rupture of one or more of the longitudinal rebars, the rupture option of reinforcement was incorporated in the numerical simulation using the "MinMax" uniaxial material command with Steel02 material in OpenSees. When a predefined value of strain is reached, the program eliminates the stress and modulus of elasticity of Steel02 material. The predefined values for longitudinal reinforcement used in the numerical models for columns were calibrated with the experimental data, and in this study, 0.17 and 0.09 were assigned as the ultimate strain values for the longitudinal reinforcement used in the SMA column simulation and the GFRP column simulation, respectively. One of the possible reasons for the large difference in the ultimate strain values in both cases is the effect of active confinement on limiting the buckling of longitudinal reinforcement compared to passive confinement. This could significantly increase the ultimate tensile strain of the reinforcing bars.

8.2. MODEL RESULTS AND VALIDATION

8.2.1 SMA column

The numerical SMA column model was subjected to the same lateral cyclic loading protocol that was used in the test (see Figure 6.10). Figure 8.2 shows a comparison between the force-displacement relationships of the experimental result and the numerical simulation of the SMA retrofitted column. In general, there is good agreement between both behaviors. The numerical model was able to capture the loading and unloading behaviors including the rupture of the longitudinal rebar which resulted in the abrupt drop in the column strength at a drift ratio of 12%. A minor difference between the strengths of the experimental and analytical columns was observed on the pulling side. This difference was attributed to the unsymmetrical response of the experimental column due to the accidental application of the axial load during testing with an eccentricity of approximately 15 mm (0.59 in).

Moreover, a detailed validation was performed by comparing the physical damage states observed during testing and the numerical strain-based damage states obtained from the numerical model. In order to assess the damage states of the numerical model, the stress-strain behaviors of cover and core concretes and longitudinal reinforcement of the fiber section at the plastic hinge were thoroughly investigated at various locations. Figure 8.3 shows schematic of the fiber section where the stress-strain behaviors were investigated. The damages of the numerical model were defined when the concrete and steel strains reached their ultimate strain levels. Table 8.1 summarizes the damage states of the experiment and the numerical simulation at various drift levels. It shows that

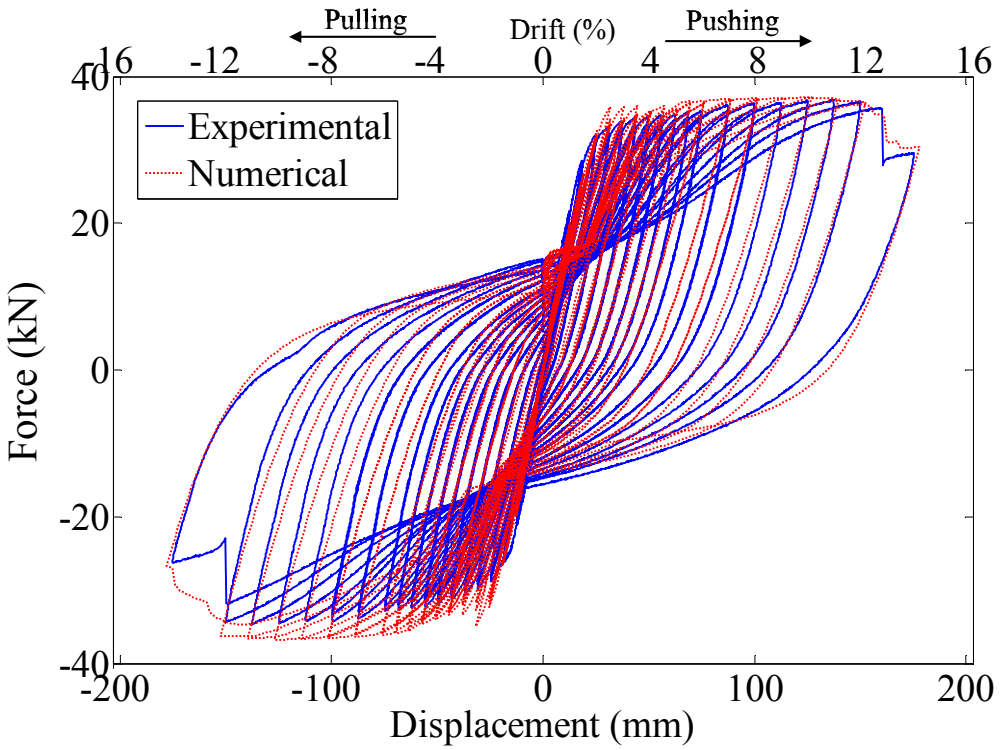

Figure 8.2 Comparison between the force-displacement relationships of the experimental and analytical SMA columns.

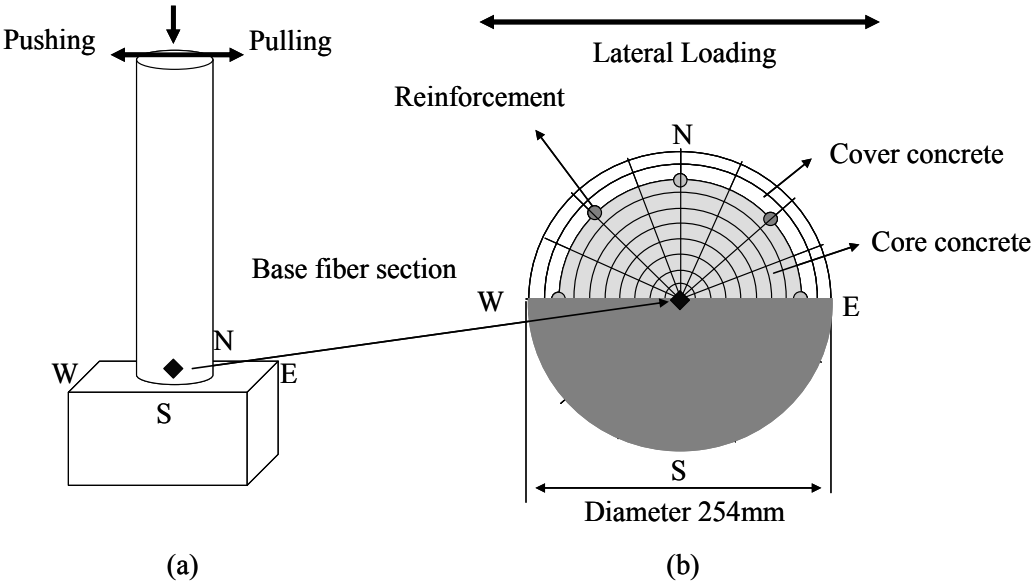

Figure 8.3 Schematics of the numerical model for column (a) and fiber section (b) for damage assessment.

the analytical model was capable of capturing the physical damage states of the tested column including concrete cover spalling, longitudinal steel yielding, and concrete core crushing. It is worth noting that the damage of the SMA column was not severe until the longitudinal rebars located near the extreme fibers were ruptured at 12%-drift ratio. Similarly, the simulation showed that the rebar was ruptured at a drift ratio of 12% when the ultimate strain reached 0.17. After the test was completed, the average diameter after excluding the damaged concrete was found to be 191 mm (7.5 in) from the experimental result and 173 mm (6.8 in) from the simulation. Figure 8.4 shows the comparison of the damage between the experiment and the simulation after the test. Based on the fiber section of the numerical model (see Figure 8.4.b), the points where concrete strain

Table 8.1 Summary of the damage states of the SMA column

Drift (%)	**Experiment**	**Simulation**
1	Horizontal crack lines were developed	Cover concrete reached the tensile strength
1.5	Steel started yielding	Steel started yielding
11	Cover concrete started spalling	Cover concrete reached the ultimate strain
12~14	Longitudinal reinforcement was ruptured	Longitudinal reinforcement was ruptured
14	Average diameter of column after damage: 191 mm	Average diameter of column after damage : 173 mm

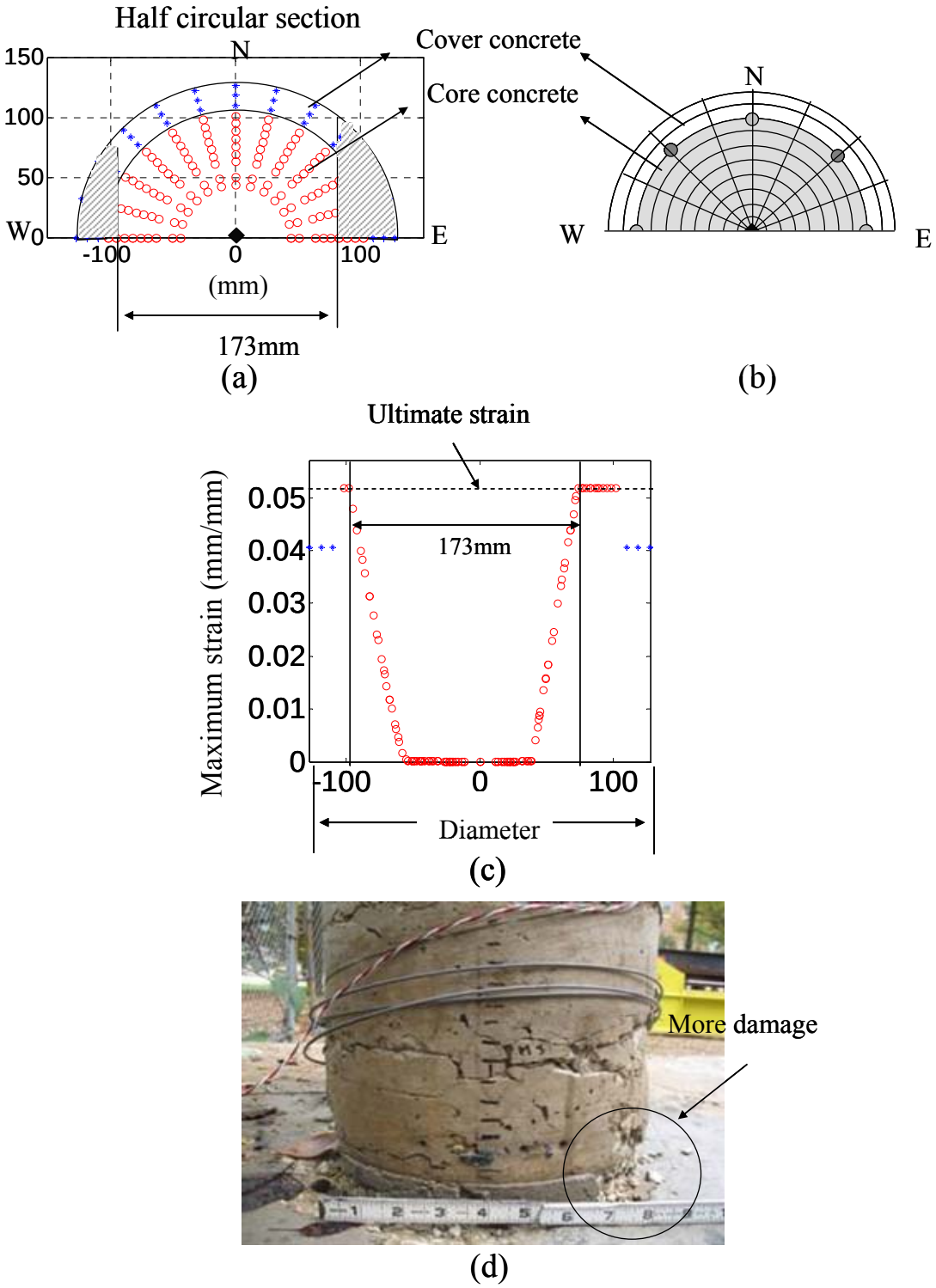

Figure 8.4 Damaged area of the SMA column in the sectional view (a), the fiber section of the numerical model (b), the maximum strains of concrete in the front view (c), and picture of damaged column (d).

was examined are shown in Figure 8.4.a, and the hatched regions in the figure represented the points that exceeded the ultimate concrete compressive strain. The asymmetric damage from the numerical simulation (Figure 8.4.a and c) and the experimental results (Figure 8.4.d) is evident by the more damage sustained on the east side of the column.

Comparisons between the experimental and numerical strains of longitudinal reinforcement and concrete are presented in Figure 8.5. Strain gauges were mounted on the surfaces of longitudinal reinforcement at the west and east sides of the column and on the surfaces of the concrete as described in Chapter 6. However, most of strain gauges on the concrete surface were damaged during the heating of the SMA spirals except one strain gauge attached to the west side of the column. The strain data were available until the third cycle of the 3.0%-drift ratio for reinforcement and the first cycle of the 3.0%-drift ratio for concrete, since the strain gauges were damaged severely afterward due to the cyclic loading. Tensile strain was not observed from the strain gauge on concrete, and this is due to crack openings that were developed above and below where the strain gauge was attached, so only longitudinal compressive strains were compared (see Figure 8.5.c). Also, strain gauges tended to have residual strains due to accumulated damage in the strain gauges themselves as the testing progressed, but the strain values obtained from the numerical model did not exhibit any residual strain. Therefore, when considering the residual strains in each loading cycle from the experimental data, the experimental strain values showed good agreement with the numerical values. For instance, at a 2.5%-drift ratio, the experimental compressive strain was recorded as -0.0034 mm/mm after subtracting the residual strain from the maximum compressive strain, and the numerical

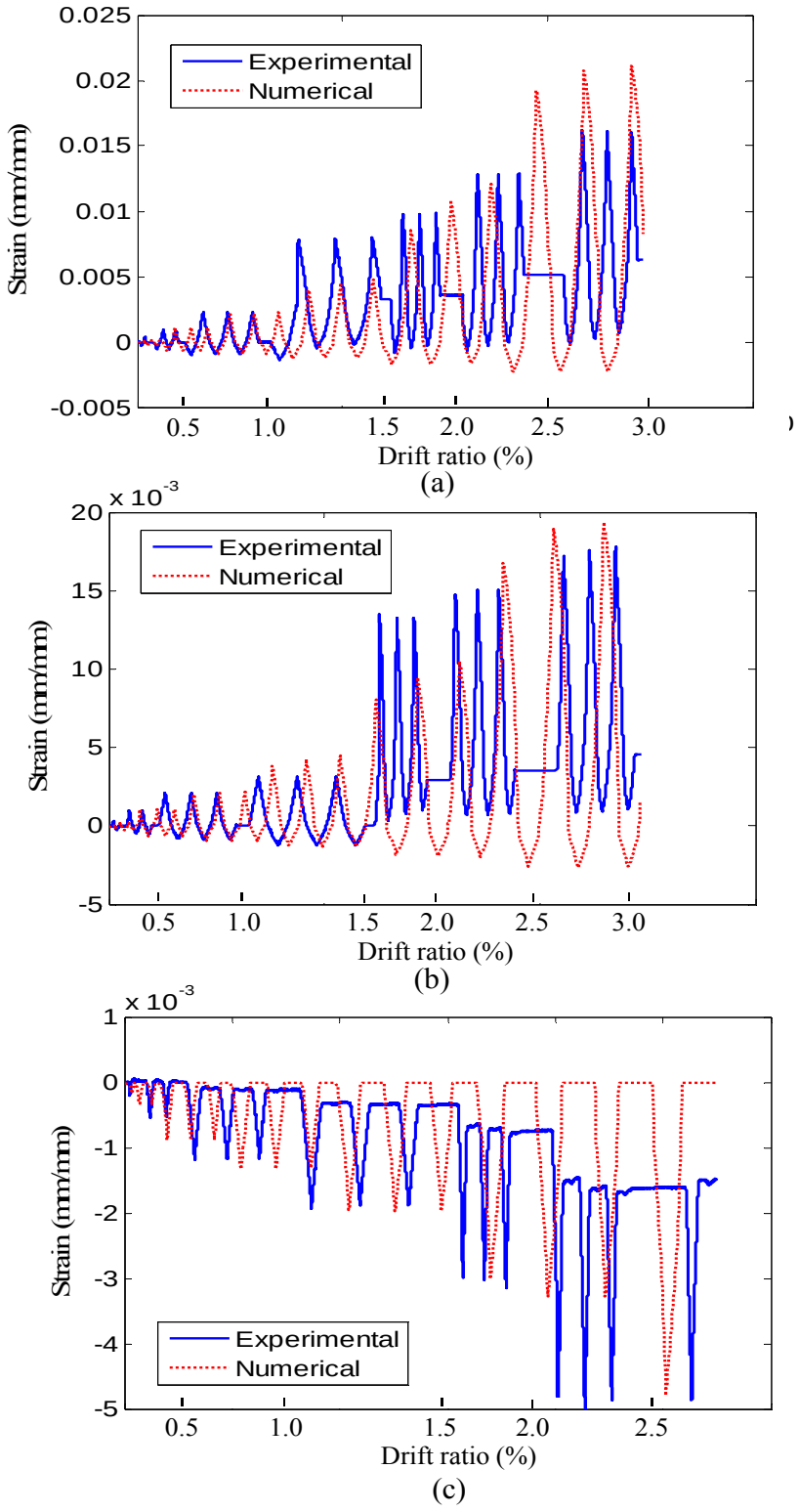

Figure 8.5 Experimental vs. analytical strains of steel reinforcement and concrete of SMA column: (a) steel at the west side, (b) steel at the east side and (c) concrete at the west side.

strain was -0.0033 mm/mm. Also, at a 2.0%-drift ratio, the numerical compressive strain (-0.002 mm/mm) was 91% of the experimental strain (-0.0022 mm/mm).

8.2.2 GFRP column

To describe the stress-strain behaviors of concrete confined with GFRP with and without internal steel ties, the Kawashima et al. (2001) model described in Chapter 4 was used again, and the Uniaxial Concrete02 material model in OpenSees which is capable of considering the tensile strength of concrete was modified in order to mimic the rupture of GFRP wraps used to confine concrete for the numerical simulation (see Figure 4.1). Zone1, Zone2 and Zone3 were wrapped with 10 layers, 5 layers and 3 layers of GFRPs, respectively, and the properties of confined concrete were assigned accordingly. For the longitudinal reinforcement, Steel02 material was used like the SMA column. However, Steel02 was not suitable for mimicking the severe buckling of reinforcement sustained by the GFRP column during testing. Therefore, the comparisons between the numerical model and the experimental result were limited up to a drift ratio of 5.5%. Figure 8.6 shows the comparisons of the force-displacement relationships between the experiment and the numerical simulation of the GFRP column. The figure indicated good agreement between the experiment and the analytical simulation of the GFRP column.

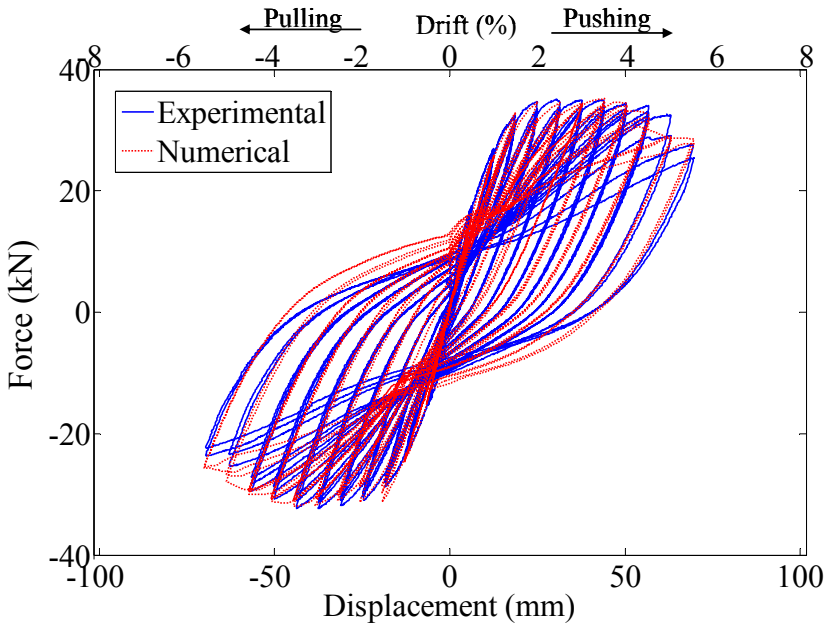

Figure 8.6 Comparison between the force-displacement relationships of the experimental and numerical GFRP columns.

The comparison of the progressive damages of the column between the experiment and the numerical simulation was performed, and the results were summarized in Table 8.2. The first vertical crack which indicated the local rupture of GFRP was observed under a 3.5%~4.0%-drift ratio, and the vertical cracks had propagated further as the lateral drift was increasing. Also the numerical simulation showed that the GFRPs ruptured when the column reached close to a 4%-drift ratio, which means that the cover concrete started spalling numerically. The core concrete started crushing experimentally and numerically just below a 5%-drift ratio.

Table 8.2 Summary of the damage states for the GFRP column

Drift (%)	Experiment	Simulation
1.5	Steel started yielding	Steel started yielding
3.5~4	Vertical cracks were developed and started propagating	GFRPs were ruptured
4.5	Cover concrete started spalling	Core concrete started crushing
5	Core concrete started crushing	

Figure 8.7 shows the comparisons of the variations of strain between numerical simulation and experimental test results. The strain variation of longitudinal reinforcement and surface of column were available until a 1.5%-drift ratio, since the strain gauges were damaged severely afterward due to the cyclic loading. As shown in the figures, the strain values of the numerical simulation showed good agreement with the experimental values. In this case, the concrete strain from the experimental test did not show noticeable residual strain unlike the concrete strain from the SMA column since the strain gauge was actually attached on the GFRP wraps, which experienced no crack openings during the early stage of the cyclic loading. At 1.5%-drift ratio, the maximum compressive strains were recorded as -0.0022 mm/mm and -0.0023 mm/mm from the numerical model and from the experimental data, respectively. Later in Chapter 9, this numerical model was used to perform a cost analysis as a comparison model to the SMA active confinement technique.

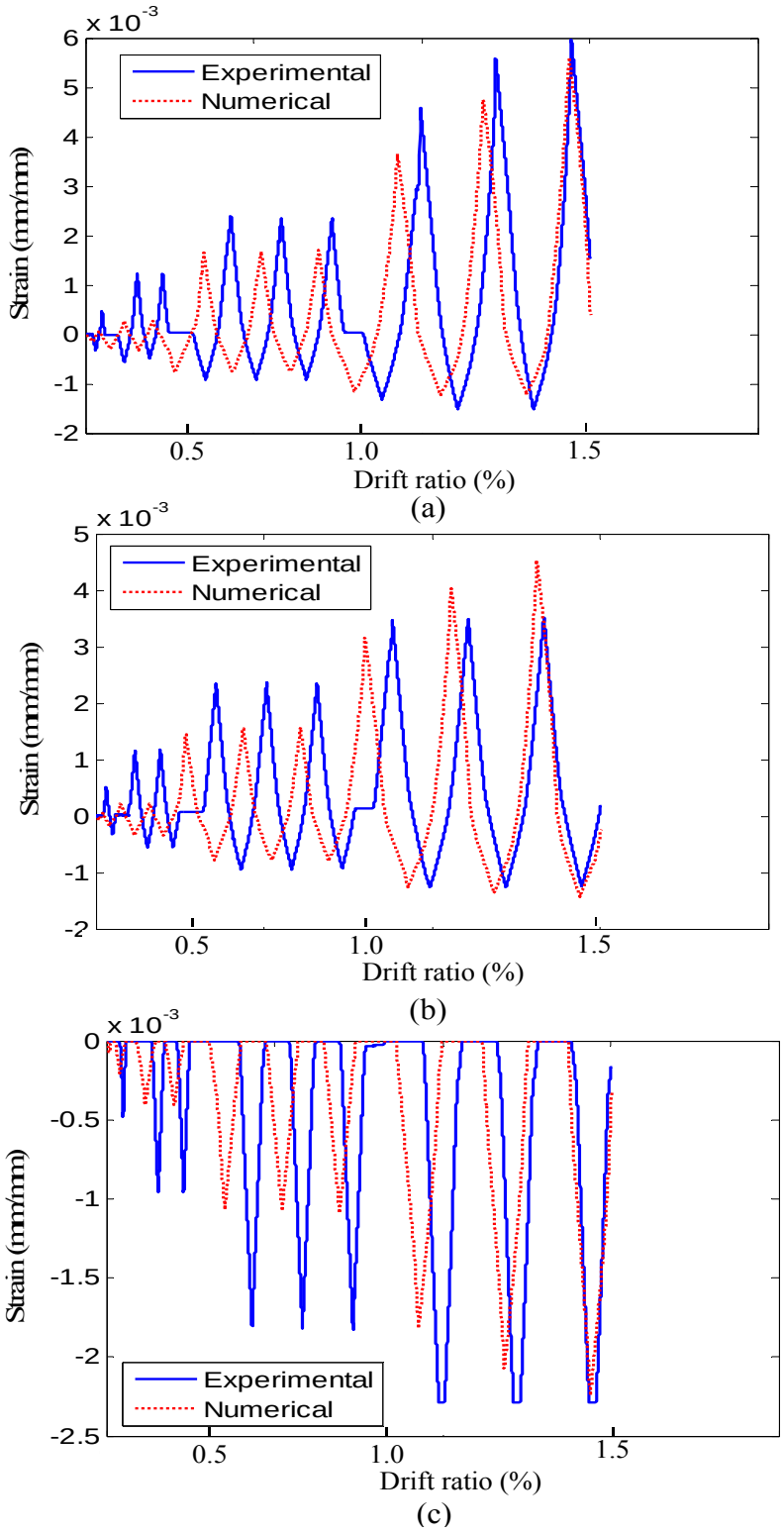

Figure 8.7 Experimental vs. analytical strains of steel reinforcement and concrete of GFRP column: (a) steel at the west side, (b) steel at the east side and (c) concrete at the west side.

CHAPTER 9 PARAMETRIC STUDY

The work presented in the previous chapters helped in proving the concept of using thermally prestressed SMA spirals for retrofitting/repairing RC bridge columns. It also introduced a simplified and validated method for modeling concrete columns that are retrofitted/reinforced with these spirals. To this end, there was still a significant lack of knowledge related to the design of the new retrofit technique and the impact of various geometrical and design parameters of the RC columns on the overall efficacy of the new active confinement technique. In order to address this issue, the validated modeling method that was presented in chapter 8 was used in a parametric study that aimed at investigating the effects of the interactions between active confinement pressure and other common design and geometrical parameters such as axial load, volumetric ratio of longitudinal reinforcement, and slenderness ratio of retrofitted columns. The results of the parametric study will provide practical information that is useful in setting a design guideline for retrofitted bridge columns using the newly developed SMA active confinement technique. A detailed description of the parametric study and its results are presented in this chapter.

9.1 PARAMETERS

Using the validated analytical model of RC columns retrofitted with SMA spirals, intensive parametric study was performed to examine the impact of several parameters on the cyclic behavior of the retrofitted columns. Four parameters were considered in the study: 1) confinement pressure from the SMA spiral, 2) volumetric ratio of the longitudinal reinforcement (ρ_l), 3) axial load, and 4) slenderness ratio of the column

(diameter of the column was kept constant and equal to 1524 mm (60 in) throughout the study, while the column length varied). The ranges of the four parameters and their base values are listed in Table 9.1. The base values of each parameter are representative values used when conducting two- or three-parameter parametric study that will be discussed in the following sections.

Table 9.1 Range of parameters considered in the parametric study

Parameters	**Range of values**	**Base values**
Confinement Pressure (MPa)	0~2.07	N/A
ρ_l (%)	1~4	2
Axial load (%)	10~40	10
Slenderness ratio	4:1~7:1	5:1

The range selected for each parameter was based on common practices or design code recommendations. For example, the longitudinal reinforcement volumetric ratio (ρ_l) was based on Caltrans Seismic Design Criteria (SDC) (2009). Volumetric ratios of 1%, 2%, 3% and 4% corresponding respectively to the use of 24#10 (32 mm (1.27 in)), 26#14 (43 mm (1.69 in)), 38#14 (43 mm (1.69 in)) and 28#18 (57 mm (2.25 in)) rebars, were considered in the study. The ultimate stain value of longitudinal reinforcement was taken as 0.17 based on the calibrated value from the numerical SMA column simulation

in Chapter 8, and based on Caltrans recommendations (2009) the ultimate strain for rebars larger than #10 was reduced by 25%. For the axial load range selected for the study, a minimum value of 10% of the column's gross section nominal capacity is regarded as the lower bound for axial load on RC columns (Aviram et al. 2008). Recent studies showed, however, that in the case of earthquakes with strong vertical excitations, the axial force could reach up to 40% of the nominal column's capacity (Kim et al. 2011). Kim et al. (2011) showed that axial force could be doubled to the applied dead load.

9.2. MULTI-FACTOR ANALYSIS OF VARIANCE (ANOVA)

A multi-factor analysis of variance (ANOVA) (Walpole et al. 2008) was performed to design the parametric study by utilizing the statistical tool available in MATLAB program. The ANOVA served as a statistical tool to assess the impact of possible interactions between the studied parameters on the columns' behavior prior to conducting the parametric study. The goal was to determine the most significant interactions that ought to be studied and discard those interactions with a low level of impact. In order to perform the multi-factor ANOVA, only the minimum and maximum values (levels) of each factor were considered (see Table 9.1). The sum-of-squares and the mean squares of individual factors, interactions between the four factors, and error were calculated for an *f*-test (Walpole et al. 2008). Finally, a probability value (P-value) testing a null hypothesis of each factor was computed and used as an indicator whether the interactions between a specific factor and the other three factors are significant. In this study, a P-value of 25% was considered as a threshold indicating the significance of the interaction (i.e. a P-value less than or equal to 0.25 indicates statistically significant

interaction). To complete the ANOVA using the four factors, seismic performance parameters of numerical RC columns including displacement ductility (μ) and equivalent viscous damping ratio (ξ_{eq}) were regarded as the response factors of the analysis. Therefore, an ANOVA table was generated and used to examine which factors would have a significant impact on the μ and ξ_{eq} parameters of the columns based on the interactions with the confinement pressure induced by SMA spirals.

9.2.1 Results of multi-factor ANOVA

A total of 16 (=2^4) numerical simulations were performed using OpenSees. The validated numerical modeling technique of SMA confined columns was used with different combinations of the four parameters. The four parameters assigned to each column are summarized in Table 9.2. For instance, Col. 1 is a column confined with 0.34 MPa (50 psi) of confinement pressure from SMAs with 1% of longitudinal reinforcement under an axial load of 10% of the column's gross section capacity, and finally, its slenderness ratio is 4:1.

Since the study was primarily focused on the column's behavior, the properties of the foundation were not considered. Instead, the columns were assumed to be fixed at the base, and the Bond-slip material model in OpenSees was implemented at the base of column using a zero-length fiber section element (Zhao and Sritharan 2007). In their study, the backbone curve of the relationship between bar stress and loaded-end slip was described as

Table 9.2 Parameter values assigned to each of the ANOVA columns

Column	Confinement (MPa)	ρ_l (%)	Axial load (%)	Slenderness ratio
Col.1	0.34	1	10	4:1
Col.2	2.07	1	10	4:1
Col.3	0.34	1	10	7:1
Col.4	2.07	1	10	7:1
Col.5	0.34	1	40	4:1
Col.6	2.07	1	40	4:1
Col.7	0.34	1	40	7:1
Col.8	2.07	1	40	7:1
Col.9	0.34	4	10	4:1
Col.10	2.07	4	10	4:1
Col.11	0.34	4	10	7:1
Col.12	2.07	4	10	7:1
Col.13	0.34	4	40	4:1
Col.14	2.07	4	40	4:1
Col.15	0.34	4	40	7:1
Col.16	2.07	4	40	7:1

$$\tilde{\sigma} = \frac{\dfrac{\tilde{s}}{\mu - \tilde{s}}}{[(\dfrac{1}{\mu b})^{R_e} + (\dfrac{\tilde{s}}{\mu - \tilde{s}})^{R_e}]^{1/R_e}} \qquad (9.1)$$

where $\tilde{\sigma} = (\sigma - f_y)/(f_u - f_y)$, $\tilde{s} = (s - s_y)/s_y$, $\mu = (s_u - s_y)/s_y$, b is the initial hardening ratio, and R_e is a power index of the curve. f_y and f_u are the yielding strength and the ultimate strength of the bar, respectively. s_y and s_u are the loaded-end slip of the bar when the bar reaches the yielding and ultimate state, respectively. This element takes into

account the additional flexibility in the columns due to the slip between the longitudinal reinforcement and the concrete. The columns were subjected to the cyclic loading protocol shown in Figure 9.1, which was adopted from the Federal Highway Administration (FHWA) recommendation (2004). The protocol comprises three cycles at each displacement level, and the incremental displacement is equal to the yielding displacement (Δ_y). The columns were loaded until they reached their ultimate displacement. The yielding displacement was defined as the displacement where the secant stiffness line at 75% of the ultimate lateral load intersects the horizontal line corresponding to the ultimate load, while the ultimate displacement was defined as the displacement where the load carrying capacity reduces by 15% of the maximum lateral strength or the displacement corresponding to the rupture of one of the longitudinal rebars—whichever is smaller (Elnashai and Sarno 2008) (see Figure 9.2).

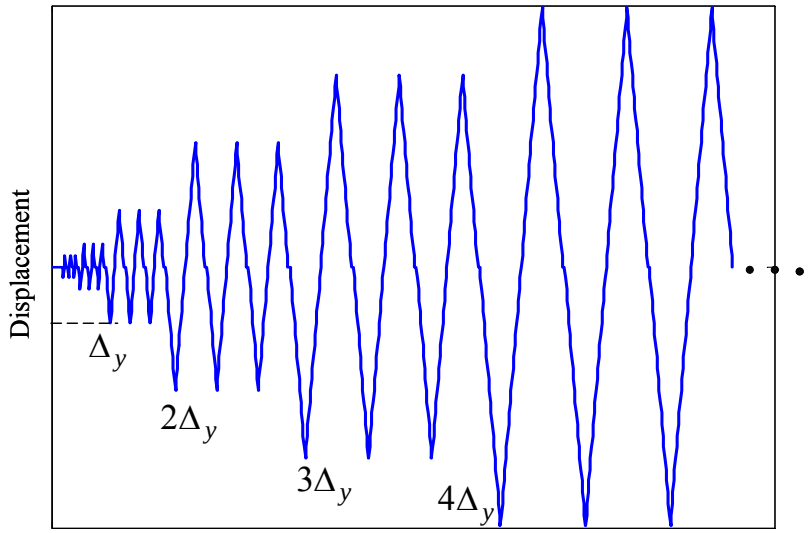

Figure 9.1 Cyclic loading protocol.

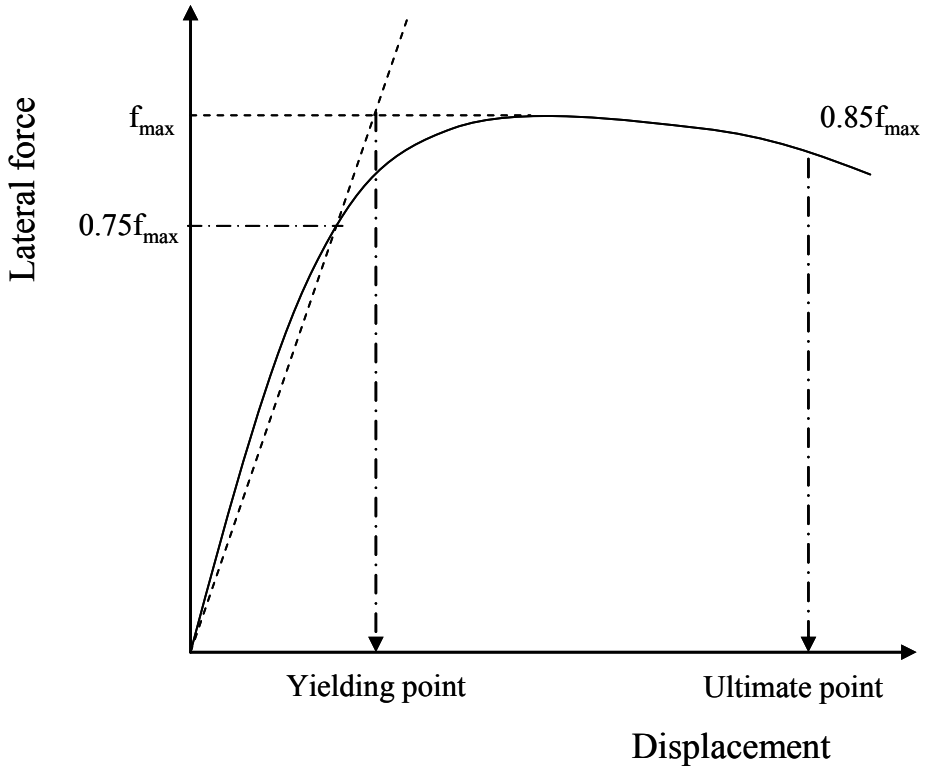

Figure 9.2 Force-displacement sketch illustrating the definition adopted in the parametric study for a RC column yielding and ultimate points.

After performing the multi-factor ANOVA, the parameters that showed significant interactions with the confinement pressure were identified. Table 9.3 summarizes the P-values obtained from the ANOVA results based on the displacement ductility (μ) and equivalent viscous damping ratio (ξ_{eq}), respectively. In order to compute the P-values, Eqs. 9.2 and 9.3 were used. In these equations, the *f* value is the ratio of mean squares, v_1 and v_2 are degrees of freedom of each variable, and Γ is the chi-square distribution of each variable:

$$h(f)=\begin{cases}\dfrac{\Gamma[(v_1+v_2)/2](v_1/v_2)^{\frac{v_1}{2}}}{\Gamma(v_1/2)\Gamma(v_2/2)}\dfrac{f^{(\frac{v_1}{2})-1}}{(1+v_1 f/v_2)^{\frac{v_1+v_2}{2}}}, & f>0\\ 0, & f\le 0\end{cases} \qquad (9.2)$$

By integrating the F-distribution from the f value of each case to the infinite, the probability was computed as follows (Walpole et al. 2008):

$$P=\int_{f_{value}}^{\infty} h(f)df \qquad (9.3)$$

Based on the P-values corresponding to the displacement ductility response parameter it was found that considering the effects of interaction among three parameters namely "Confinement*Axial load*Slenderness ratio" and "Confinement*Slenderness ratio*Longitudinal reinforcement ratio" is statistically significant. Hence, more in-depth analysis of these interactions was carried out. Furthermore, based on the results of the equivalent damping ratio response parameter, none of the three parameter interactions showed a P-value less than 0.25. Therefore, it was safe to assume that the effect of three-parameter interactions has negligible impact on the damping ratio. However, the two-parameter interactions, namely "Confinement*Axial load" and "Confinement*Longitudinal reinforcement ratio" seem to be statistically significant; hence, they were studied in more depth. With these results, the parametric study was designed using smaller increments of the selected parameters.

Table 9.3 P-values of multi factor-ANOVA based on displacement ductility and equivalent viscous damping ratio

Interaction	P-value	
	Ductility	Equivalent damping ratio
Confinement*Axial load	0.0768	0.2184
Confinement*Slenderness	0.0735	0.7486
Confinement*Longitudinal	0.3532	0.1844
Confinement*Axial load*Slenderness	0.1155	0.9748
Confinement*Axial load*Longitudinal	0.9576	0.3786
Confinement*Slenderness*Longitudinal	0.1225	0.7358

9.3 RESULTS OF PARAMETRIC STUDY

9.3.1 Displacement ductility

Based on the P-values in Table 9.3, two detailed three-parameter parametric studies were carried out. The first study involved: confinement pressure, axial load and slenderness ratio, while the second study involved: confinement pressure, slenderness ratio, and longitudinal reinforcement ratio. The results of the first and second studies are shown in Figure 9.3 and Figure 9.4, respectively. Both figures show that in general, increasing the active confinement pressure increases the displacement ductility of the columns. The largest ductility ratio in Figure 9.3 is the value corresponding to the smallest axial load (10% of column's gross section nominal capacity), smallest

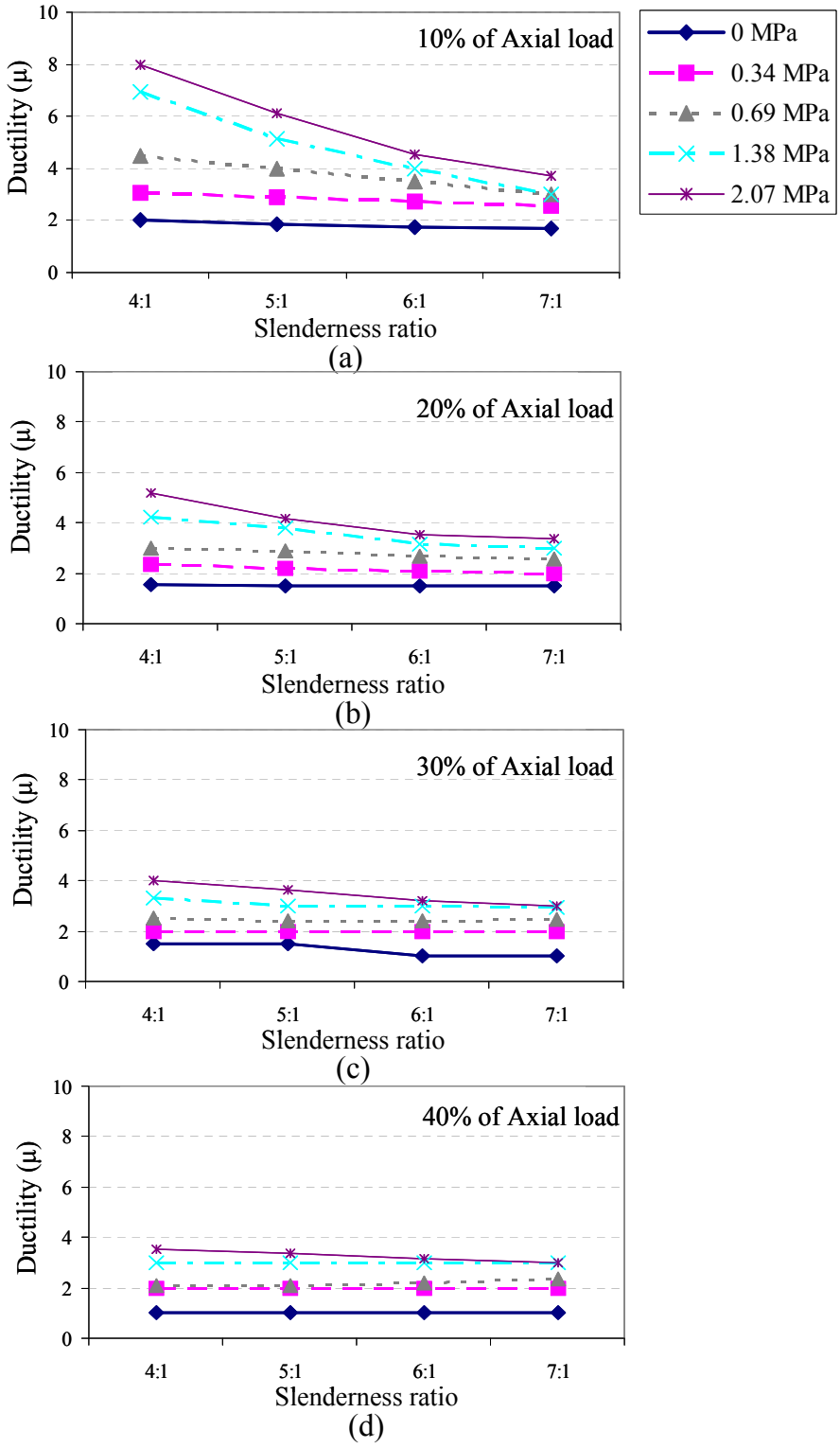

Figure 9.3 Variation of the displacement ductility of the RC columns with respect to confinement pressure, slenderness ratio and axial load: (a) 10% of axial load, (b) 20% of axial load, (c) 30% of axial load and (d) 40% of axial load.

slenderness ratio (4:1), and largest confinement pressure (2.07 MPa (300 psi)) (Figure 9.3.a). In terms of efficiency, a confinement pressure of 1.38 MPa (200 psi) seems to be the most efficient confinement pressure in the sense that it results in a ductile behavior close to that of the 2.07 MPa (300 psi) confinement pressure case but with 33% cut in the SMA spirals used. Taking a closer look at Figure 9.3.a-d reveals that as the slenderness ratio increases, the ductility ratio decreases at a variable rate depending on the confinement pressure and the axial load. For axial loads greater than 20%, the variation in the ductility ratio as a result of the increase in the slenderness ratio tends to be minor. Furthermore, as the axial load increases, the ductility ratio of the columns decreases regardless of the slenderness ratio and the confinement pressure, and the lines become more linear indicating that the effects of interactions between the three parameters become insignificant. Under small axial load (10%), the ductility of the columns improved significantly as the level of the confinement pressure increased when the slenderness ratio of the columns was 4:1 and 5:1. On the other hand, the ductility of columns with slenderness ratios of 6:1 and 7:1 was less affected by increasing the axial load and confinement pressure.

A total of 80 simulations were carried out to generate Figure 9.4 which shows the variations of the displacement ductility with respect to the level of confinement pressure, the level of slenderness ratio, and the level of volumetric ratio of longitudinal reinforcement of actively confined RC columns. As shown in Figure 9.4, increasing the ratio of the longitudinal reinforcement decreases the ductility of the columns slightly. As observed in Figure 9.3, the effect of confinement seems to be more prominent in the

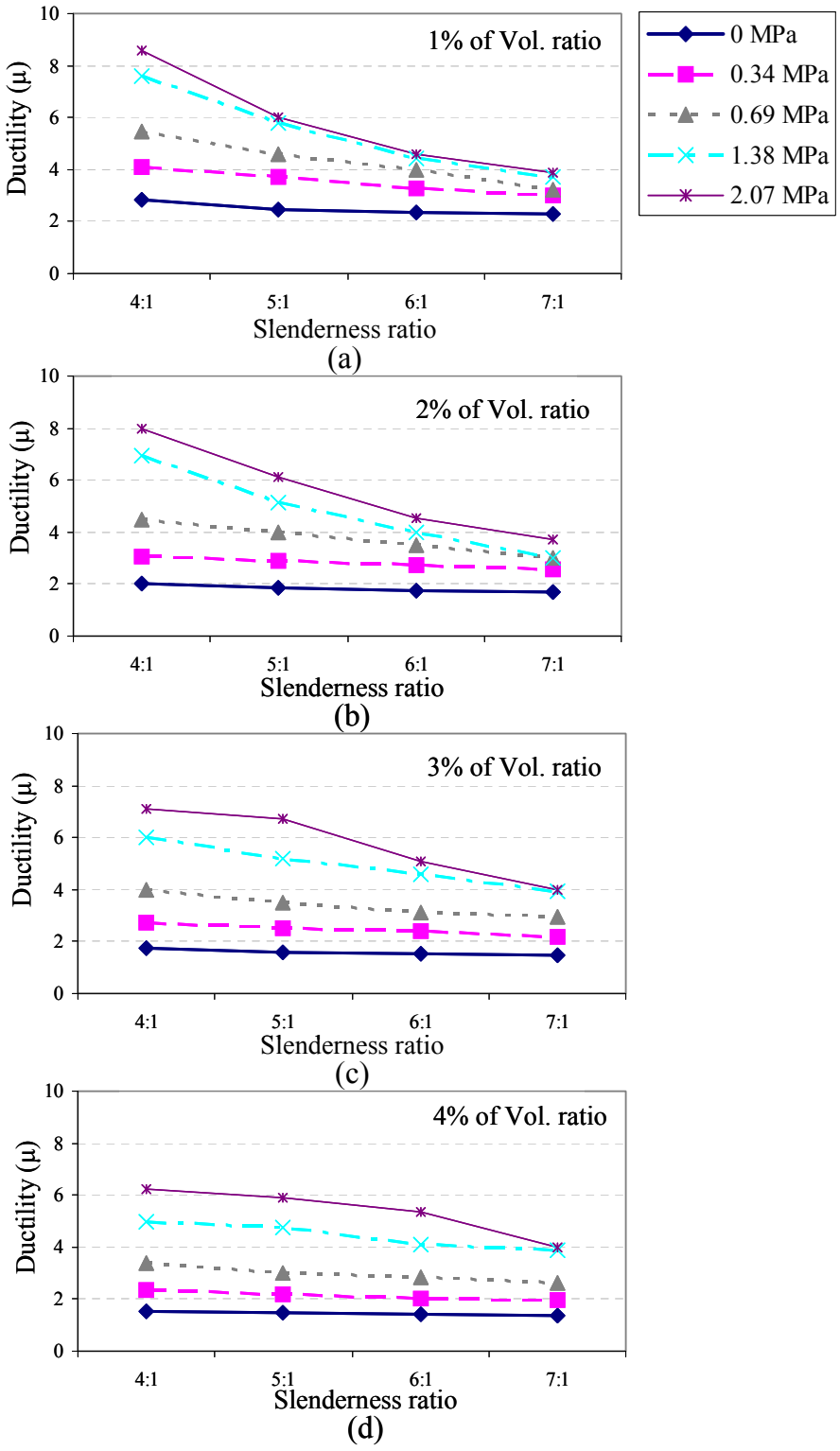

Figure 9.4 Variation of the ductility of the RC columns with respect to confinement pressure, slenderness ratio and reinforcement volumetric ratio: (a) 1% of Vol. ratio, (b) 2% of Vol. ratio, (c) 3% of Vol. ratio and (d) 4%% of Vol. ratio.

columns with slenderness ratios less than 6:1 regardless of the longitudinal reinforcement ratio. However, even in the case of reinforcement ratio as high as 4%, an active confinement pressure of 1.38 MPa (200 psi) seems to be quite effective in improving the column's displacement ductility by more than 2.5 times that of as-built column. Comparing the improvements in ductility in Figure 9.4.a-d illustrates that as concluded from Figure 9.3, using a target confinement pressure of 1.38 MPa (200 psi) seems to be an efficient design for the spirals.

9.3.2 Equivalent viscous damping ratio

As illustrated earlier using the P-values presented in Table 9.3, the equivalent viscous damping ratio of the column was not significantly affected by any of the three-parameter interactions; however, the two-parameter interactions between confinement pressure and axial load and between confinement pressure and longitudinal reinforcement ratio were statistically significant. Therefore, these two interactions were studied in more depth. Figure 9.5 shows the variations of equivalent viscous damping ratio (ξ_{eq}) with respect to confinement pressure and axial load (Figure 9.5.a) and confinement pressure and reinforcement ratio (ρ_l) (Figure 9.5.b). As illustrated in the figure, ξ_{eq} generally increases as the level of confinement pressure increases. The results show that active confinement pressure seems to have less impact on damping ratio under high axial loads, and more impact in the case of columns with a larger ratio of longitudinal reinforcement. Studying the results presented in Figure 9.5.a reveals that the damping ratio decreased as the applied axial load increased in the cases of the columns under higher confinement pressure. Compared to the column with no external confinement, applying external active

confinement pressure of 2.07 MPa (300 psi) improved the damping ratio by 221%-1990% under the axial load values considered in the study.

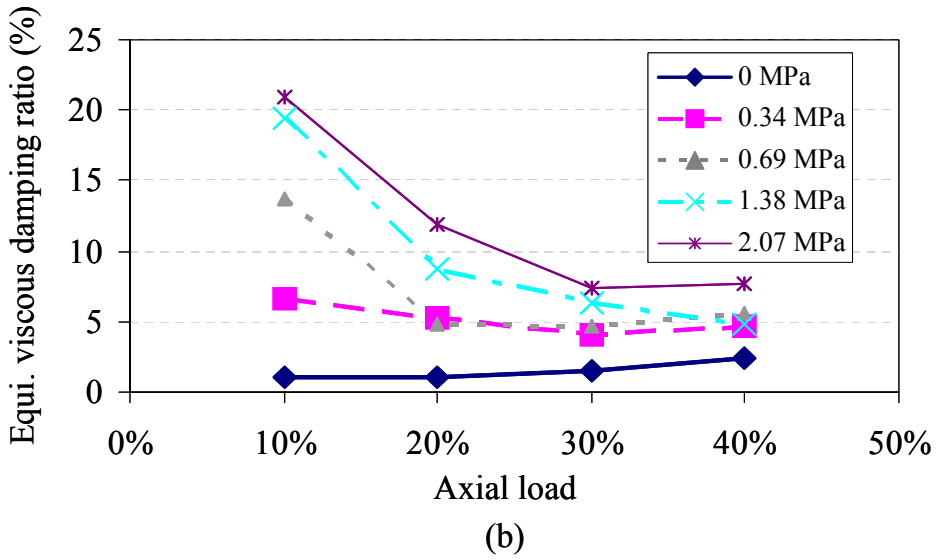

(b)

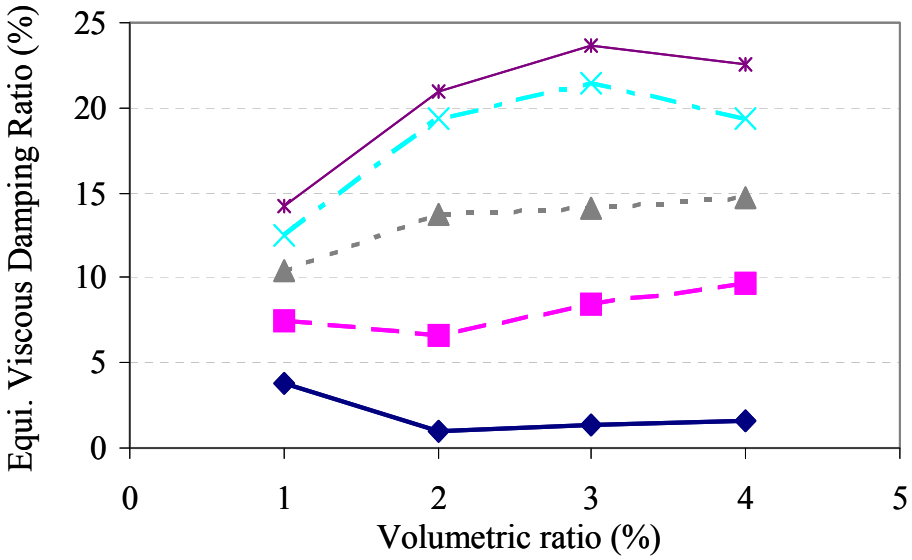

(b)

Figure 9.5 Variation of the equivalent viscous damping ratio of the RC columns with respect to confinement pressure and axial load (a) and volumetric ratio of longitudinal reinforcement (b).

Figure 9.5.b shows an opposite pattern to that observed in Figure 9.5.a in the sense that the damping ratio increased with the increase of the longitudinal reinforcement ratio. Hence, confinement pressure value had the least impact on the damping ratio when the volumetric ratio of the longitudinal reinforcement was equal to 1%. When this reinforcement ratio was used, the columns failed due to gradual strength degradation since concrete carried out most of the compressive force. However, the impact of adding external confinement pressure was much more prominent at higher volumetric ratios since with a higher reinforcement ratio steel contributes significantly in resisting compressive stresses, which helps in reducing the rate of strength degradation due to concrete crushing. It is important to note that the reduction in the columns' ductility when the columns were heavily reinforced (4%) resulted in a slight reduction in the damping ratio especially under relatively higher confinement pressure values. Again, it is noticed from Figure 9.5 that using SMA spirals that provide a confinement pressure of 1.38 MPa (200 psi) seem to be the most efficient design based on the range of confinement pressure values considered in this study.

9.4. HYSTERETIC BEHAVIOR

The hysteretic behaviors of the columns that were observed throughout the parametric study varied significantly. To provide better understanding of the influence which various parameters have on the columns' hysteretic behaviors, some example columns were presented. The four parameter values corresponding to each of column are summarized in Table 9.4.

Table 9.4 Values of the four parameters assigned to each column in Figure 9.6 - Figure 9.8.

Graph number	Confinement pressure (MPa)	ρ_l (%)	Axial load (%)	Slenderness ratio
Fig.9.6.a	2.07	2	10	4:1
Fig.9.6.b	2.07	2	40	4:1
Fig.9.7.a	2.07	1	10	4:1
Fig.9.7.b	2.07	1	10	7:1
Fig.9.8.a	2.07	1	10	5:1
Fig.9.8.a	2.07	4	10	5:1

Figure 9.6 - Figure 9.8 show six examples of the force-displacement relationships from the numerical simulations performed during the parametric studies. As shown, the active confinement pressure was kept constant in all shown cases. In Figure 9.6.a and Figure 9.6.b all parameters were kept the same except the axial load, which was taken as 10% in Figure 9.6.a and 40% in Figure 9.6.b. Although the columns in both figures were subjected to the same confinement pressure (2.07 MPa (300 psi)), the column under 10% axial load exhibited ductility and damping ratios of 8.0 and 23.31%, respectively, while the column under 40% axial load exhibited ductility and damping ratios of 3.57 and 8.27%, respectively. Under this relatively high confinement pressure, both columns did not experience any concrete crushing (i.e. ultimate strain of concrete was not reached)

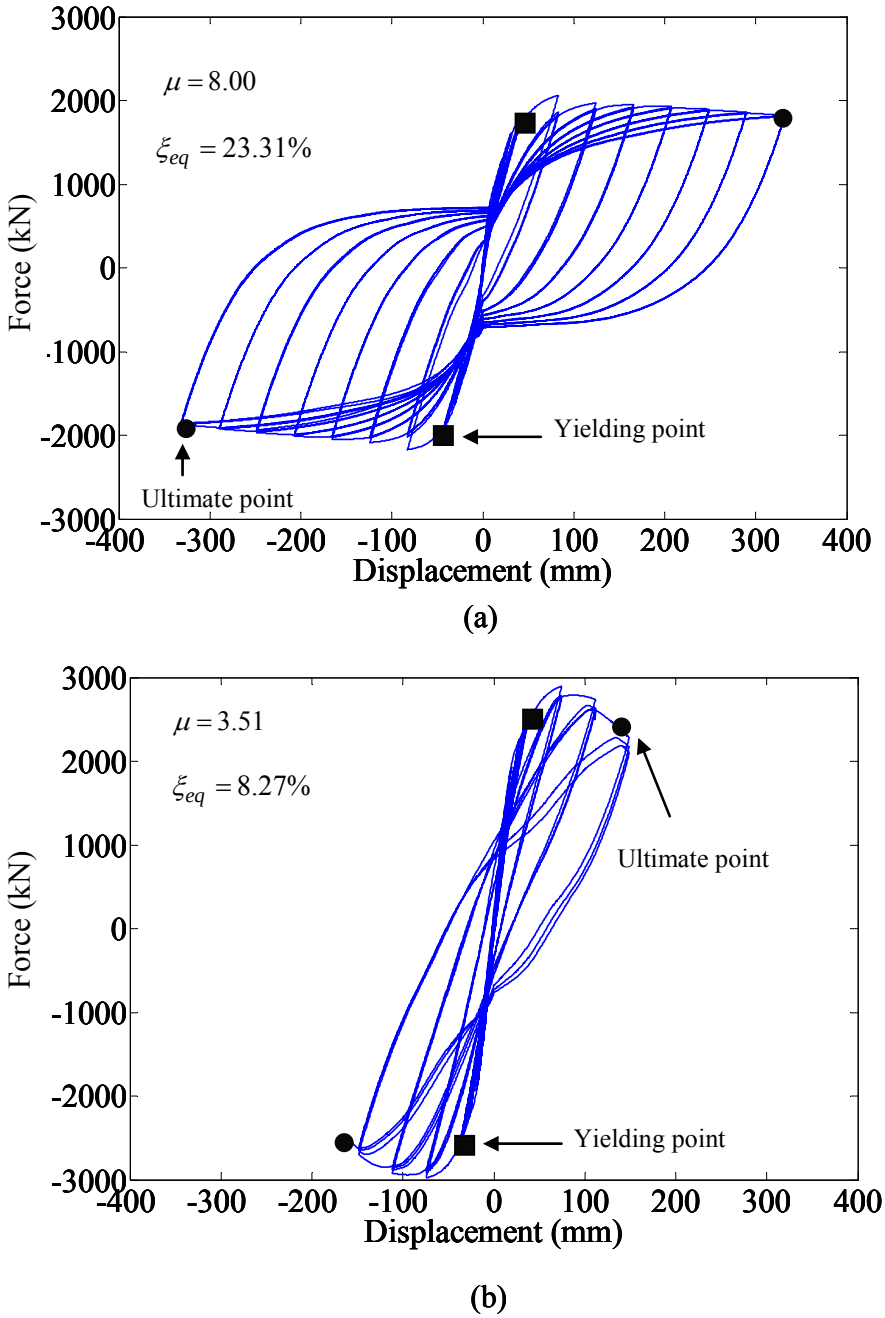

Figure 9.6 Force vs. displacement relationships of two examples of actively confined RC columns from the parametric studies: (a) 10% of axial load and (b) 40% of axial load.

until they reached their ultimate point, but with higher axial load, the degradation in the strength in each cycle was more pronounced. Hence, the column under 40% axial load reached the ultimate point more rapidly. However, the maximum lateral strength of the RC column under 40% axial load was 37% higher than that of the RC column under 10% axial load since increasing the axial force delays the yielding of the longitudinal rebars in tension and thus increases the column's lateral strength.

Figure 9.7.a and Figure 9.7.b show the hysteretic behaviors of the two columns with 4:1 and 7:1 slenderness ratio, respectively while the rest of the parameters are kept constant. Although both columns were subjected to the same confinement pressure, the displacement ductility and the equivalent viscous damping ratio of the column with 4:1 slenderness ratio marked 120% and 160% higher, respectively than those of the 7:1 slenderness ratio column. However, the displacement capacity of the 7:1 column was 10% greater than that of the 4:1 column. The main reason that the more slender column had less ductility although it had greater displacement capacity was that the yielding displacement of the 7:1 column was 2.4 times that of the 4:1 column. Since the 7:1 column had longer length of moment arm, the maximum lateral strength of the column was 51% of that of the 4:1 column.

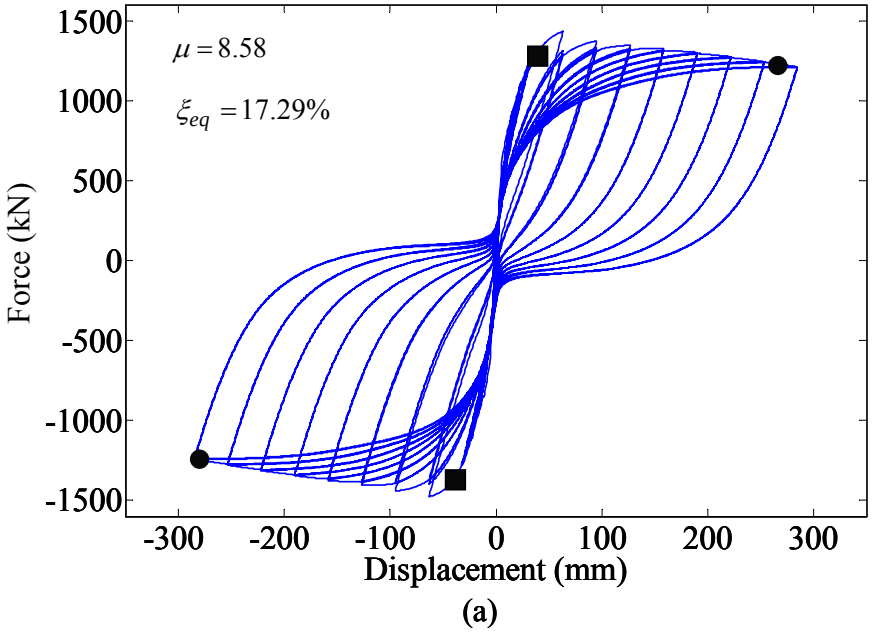

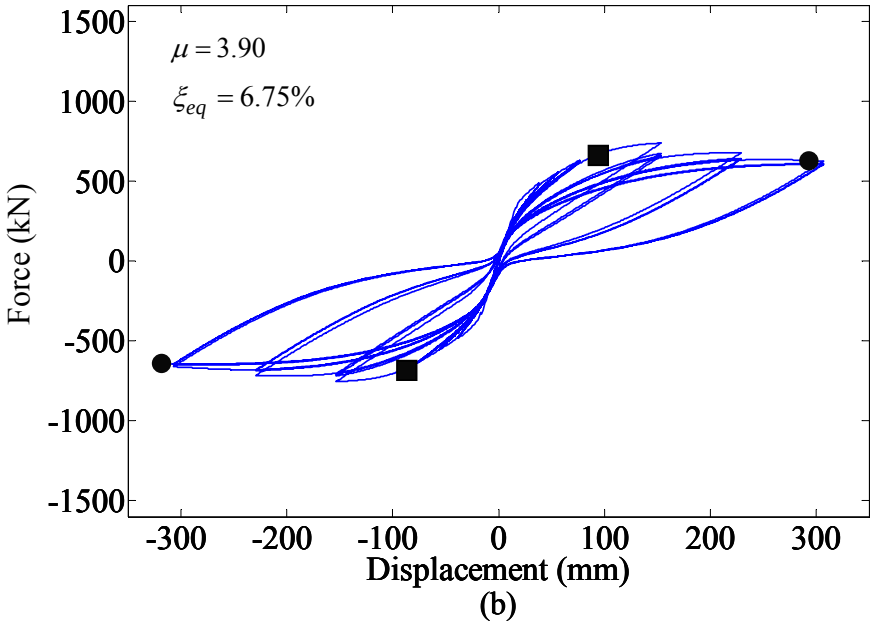

Figure 9.7 Force vs. displacement relationships of two examples of actively confined RC columns from the parametric studies: (a) 4:1 of slenderness ratio and (b) 7:1 of slenderness ratio.

Figure 9.8.a and Figure 9.8.b show the hysteretic behaviors for columns with 1% and 4% volumetric ratio of longitudinal reinforcement (ρ_l), respectively, while other parameters were kept constant as indicated in Table 9.4. The column with less reinforcement (Figure 9.8.a) showed slightly better displacement ductility and less damping ratio compared to that of the heavily reinforced column (Figure 9.8.b). As the reinforcement ratio increased, both yielding and ultimate displacements increased with almost the same percentage causing a minor change in the ductility ratio. This was not the case for the column's lateral strength, which increased significantly by 135%. It is also noticed in the figures that the column with low volumetric ratio (1%) exhibited more pinching during unloading compared to the column with a high volumetric ratio (4%). This resulted in a higher damping ratio for the column with greater reinforcement as discussed earlier in Figure 9.5.

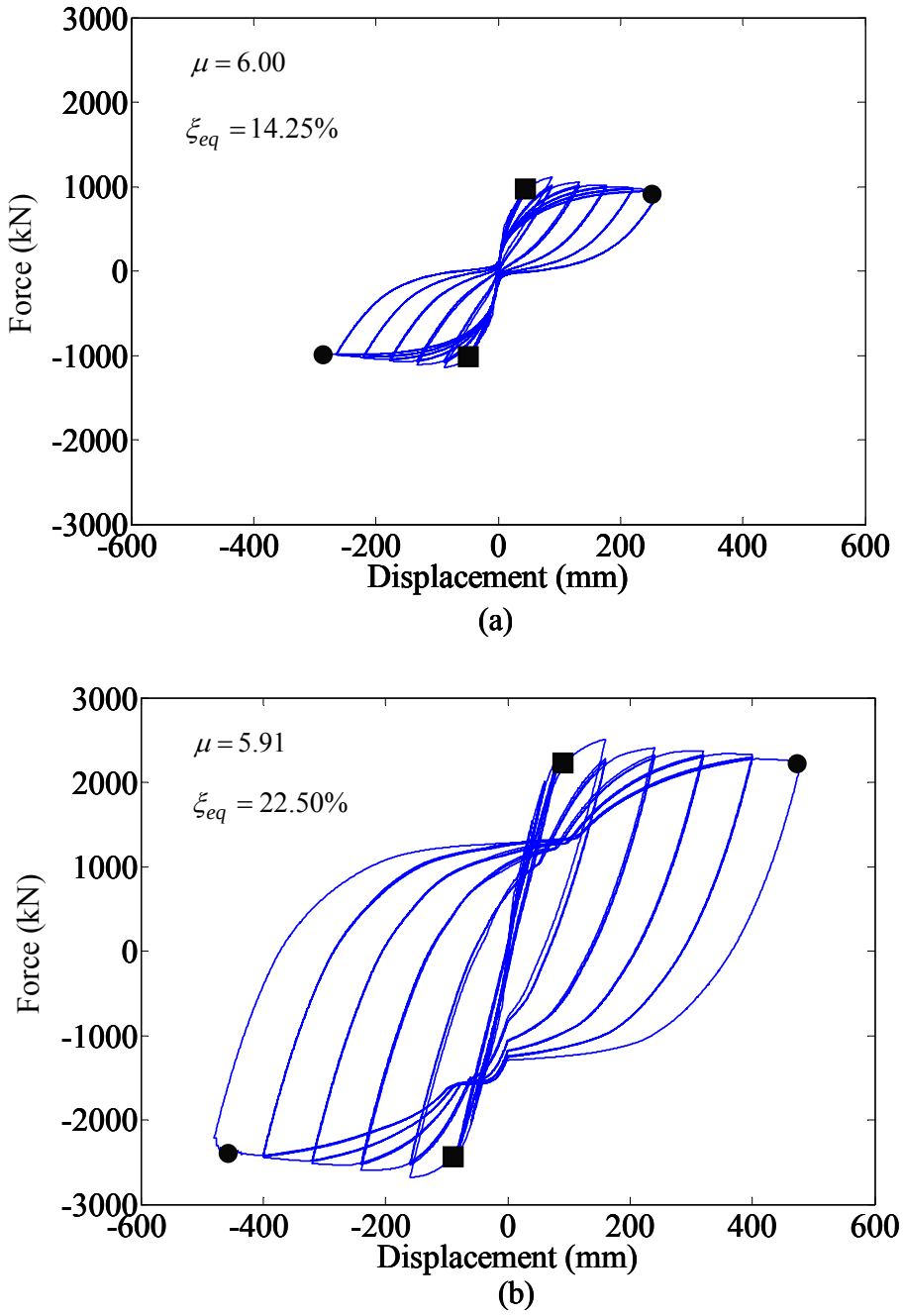

Figure 9.8 Force vs. displacement relationships of two examples of actively confined RC columns from the parametric studies: (a) 1% of volumetric ratio and (b) 4% of volumetric ratio.

9.5 COST ANALYSIS

In addition to investigating the impact of the previously discussed parameters on the structural behavior of the columns, the study was also expanded to investigate the cost associated with the new retrofit technique. Cost of using SMAs has been an issue that hindered the application of SMAs in civil structures. However, based on the numerical models described earlier in Chapter 8, it revealed that the studied retrofit technique using SMA spirals could potentially be more cost-effective or comparable to the currently used passive technique using FRP jackets. The cost analysis study was performed based on the RC columns retrofitted with SMA spirals and GFRP wraps until both numerical models reached a same ductility ratio. The RC columns used in this analysis had 762 mm (2.5 ft), 914 mm (3.0 ft), 1067 mm (3.5 ft), 1219 mm (4.0 ft), 1372 mm (4.5 ft) and 1524 mm (5 ft) diameter for their cross sections, with an axial load of 10% of the their cross section's capacity, 2% of volumetric ratio of longitudinal reinforcement, and 5:1 for slenderness ratio. According to Caltrans recommendations (Caltrans, 2008), the number of GFRP layers was determined such that a confining pressure of 2.07MPa (300psi) is reached at a radial strain of 0.004. The corresponding active confining pressure from the SMA spirals that would result in the same level of target ductility was determined iteratively by varying the pitch of the spiral, hence varying the active confinement pressure. The process described in section 7.4 was utilized again to design both SMA spiral and GFRP wraps.

In order to obtain a similar cyclical behavior of both columns, 0.34 MPa (50 psi) as the active confinement pressure was required for the RC columns with 1372 mm (4.5 ft) and 1524 mm (5 ft) diameter, while 0.38 MPa (55 psi) was required for the RC

columns with the diameters smaller than 1372 mm (4.5 ft). As an example, Figure 9.9 shows results of the cyclic behaviors of RC columns with the cross section of 1372 mm (4.5 ft) diameter confined with SMA spirals and GFRP wraps. In order to apply 2.07 MPa (300 psi) from GFRPs per Caltrans recommendations, a total GFRP thickness of 19 mm (0.75 in) was required. After several iterations, it was found that a SMA spiral pitch equal to 38 mm (1.5 in) was necessary for the SMA column to obtain a comparable cyclic behavior to the GFRP column in terms of ductility (Fig. 9.9).

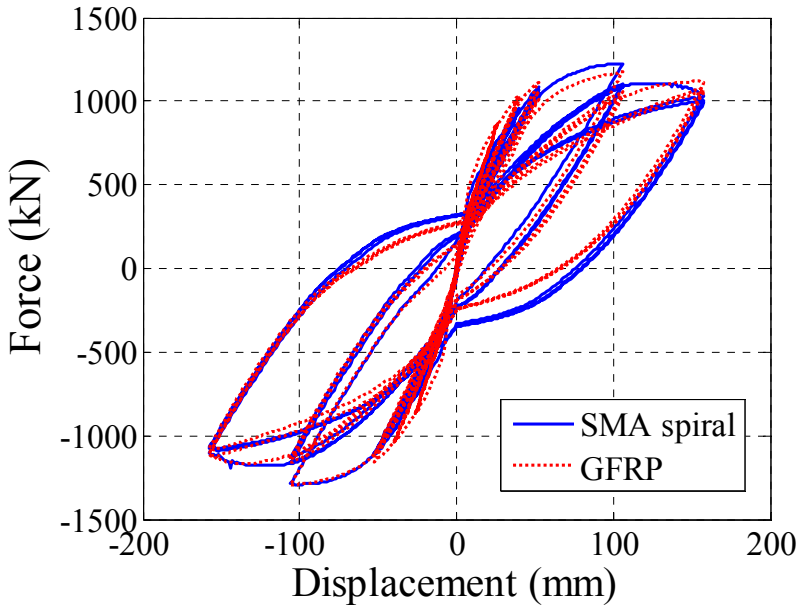

Figure 9.9 Cyclic behaviors of RC columns with the 1372mm diameter confined with SMA spirals and GFRPs.

After determining the number of GFRP layers and SMA spiral pitch for each column size, the cost of the material needed was computed and compared in Figure 9.10. The analysis was based on SMA price of \$300/lb and GFRP/epoxy price of \$10/yd^2. These prices were based on quotes provided by manufacturers from the United States. The figure illustrates that the cost of using SMA spirals is comparative to that of GFRP jackets. The low cost associated with using SMA spirals is attributed to the efficiency of the SMA spirals since small amount of material is sufficient for the column to achieve high ductility compared to passive confinement using GFRP. Furthermore, using SMA spirals could be even more cost effective if the cost of installation is also considered. The relatively small amount of time needed to install and activate the spirals could result in significant cut down in the costs of in-field installation compared to other conventional methods.

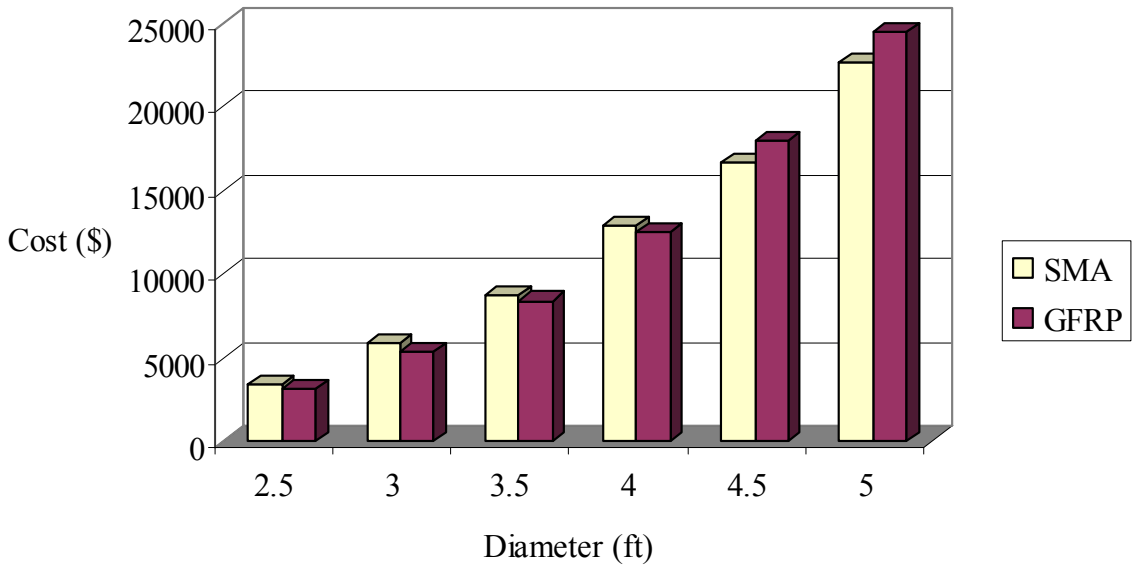

Figure 9.10 Cost analysis using SMA spirals vs. GFRP wraps.

CHAPTER 10 CONCLUSIONS AND RECOMMENDATIONS

10.1 SUMMARY AND CONCLUSIONS

The aim of the research was to investigate the feasibility of using thermally prestressed SMA spirals in the seismic retrofit and repair of RC bridge columns. The spirals were used to apply external active confinement pressure at the columns' plastic hinge zone to enhance the flexural ductility of the columns and mitigate damage. The NiTiNb alloy, which is characterized by wide thermal hysteresis, was used in this study. Heating the spiral activates the shape recovery, which is accompanied by a large recovery stress. The recovery stress in the spirals caused the confinement pressure to be exerted on the column by squeezing the column.

The following tasks of the research were completed: 1) Numerical simulations of single cantilever RC bridge columns confined actively with SMA spirals and passively with FRP jackets in order to prove the concept of the SMA confinement technique. 2) Thermo-mechanical tests on NiTiNb wires to determine their transformation temperatures, recovery stress and cyclic behavior. 3) Uniaxial compression tests on confined concrete cylinders with SMA spirals and GFRP wraps to examine the behaviors of the actively and passively confined concrete cylinders. 4) Quasi-static lateral cyclic tests on four 1/3-scale single cantilever RC columns. The columns were retrofitted with various schemes including SMA spirals, GFRP jackets, and SMA/GFRP wraps. 5) Two damaged columns were repaired using the new confinement technique and re-tested under lateral cyclic load in less than 24 hours. 6) Numerical model for the SMA confined

RC column was developed and validated with the test results. 7) An extensive parametric study based on the validated numerical model was performed to set up a guide-line when using the proposed SMA confinement technique on existing RC columns.

The results of the research proved the superiority of the new confinement technique using SMA spirals to the currently used FRP jackets in terms of: 1) Increasing the flexural ductility of the columns (more than 2.4 times the ductility obtained from using GFRP jacket), and 2) Limiting the damage sustained by the columns even under excessive lateral drifts (14%-drift). The proposed active confinement technique was also proven to overcome the limitations that other active confinement techniques have faced. Furthermore, the amount of SMA used to reach such superior behavior was relatively small and the time and labor required for installing the SMA spirals were minimal. Unlike using prestressed strands or FRP jackets, installing the thermally prestressed SMAs will require minimal labor and hardware. The use of SMA spirals for rapid repair was proven to be successful since the repair process of each column took approximately 15 hours, which makes the SMA spirals very suitable for situations where performing emergency retrofit or repair is required.

Furthermore, in order to describe numerically the nonlinear behavior of a retrofitted RC column, a numerical model for the retrofitted column based on fiber section was developed and validated using the experimental test data obtained in Chapter 6. The constitutive behavior of actively confined concrete was described using a modified version of the Mander et al. model (1988). The modified version of the model took the recovery stress, prestrain losses, and ultimate strain of SMA spirals into account. The numerical results showed that the developed model was capable of capturing, with

acceptable accuracy, not only the hysteretic force vs. displacement behavior of the experimental columns but also their damage states at various drift levels as well as the strain values in steel reinforcement and concrete. Then, the validated model was utilized in a multi-factor ANOVA followed by an extensive parametric study that focused on examining the impacts of several design and geometrical parameters on the flexural ductility and damping characteristic of SMA confined RC columns under cyclic loading. The parametric study results showed that for the range of values considered in this study, the effect of active confinement was more prominent on the displacement ductility of columns with: 1) axial load less than or equal to 20% of the column's gross section nominal capacity, and 2) slenderness ratio smaller than 6:1. As expected, the study showed that using longitudinal reinforcement with a high volumetric ratio had a negative impact on the column's displacement ductility. However, it was shown that for columns with reinforcement volumetric ratios as high as 4%, the use of an active confinement pressure of 1.38 MPa (200 psi) could increase their flexural ductility by 2.5 times compared to that of the as-built columns. The results of the study also showed that active confinement pressure had less impact on damping ratio under high axial loads, and more impact in the case of columns with larger ratio of longitudinal reinforcement. Applying an external active confinement pressure of 2.07 MPa (300 psi) improved the damping ratio of the columns by 221%-1990% under the axial load values considered in the study. In summary, the study revealed that for columns with: 1) slenderness ratio in the range of 4:1~5:1, 2) volumetric ratio of longitudinal reinforcement in the range of 1~2%, and 3) sustained average axial load of about 10% of the column's gross section nominal capacity, a target displacement ductility and equivalent viscous damping ratio of approximately

6.0~7.0 and 20%, respectively, could be attained by applying an external confining pressure of 1.38 MPa (200 psi). It is interesting to note that this value was 33% less than the confinement pressure value recommended by Caltrans when using FRP wraps for passive confinement. Furthermore, using SMA spirals could be an economical confinement technique compared to using a typical passive confinement technique. In conclusion, this study helped in shedding the light on important design aspects of the innovative active confinement technique using thermally prestressed SMA spirals.

10.2 RECOMMENDATIONS FOR FUTURE RESEARCH

This study focused on a single cantilever circular RC column confined with the newly suggested SMA spirals as a means of an active confinement technique, experimentally and numerically. However, shapes of bridge RC columns are not only circular but also rectangular, polygonal or elliptical etc. Therefore it is recommended to examine the feasibility of applying the newly suggested active confinement technique using SMA on the other shapes of bridge RC columns, numerically and experimentally. Furthermore, it is also recommended to study numerically and experimentally the new technique on the bridge system level since the technique only has been studied on the component level. Hybrid simulation is a good approach to examine the performance of the new technique on the bridge system level. The impact of using the new confinement technique on the overall structural behavior would be an important aspect when applying the technique into an existing RC column vulnerable to possible strong lateral excitations. Finally, investigating the possibilities of using other types of SMA such Fe-based SMAs

for active confinement is also recommended, since Fe-based SMAs are more cost-effective compared to NiTi-based SMAs.

APPENDIX A

In order to set up the column tests in Chapter 6, some fixture plates such as left steel channel, aluminum case, right steel box and spool (see Figure A.1, A2, A3 and A.4) were required to be installed. In the Newmark Structural Engineering Laboratory (NSEL) at University of Illinois at Urbana-Champaign, mounting holes for specimens, and actuators on the strong wall and the floor of the laboratory were already in place at these specific locations. Due to the mounted place of the column specimens on the floor of the laboratory and the size of the actuator, the fixture plates were supposed to be manufactured with the proper holes for bolting to have complete connections between the specimen and the actuator. Figure A.1 and A.2 show the fixture plates with dimensions at the top view and at the front view of the testing set-up, respectively. Figure A.3 and A.4 show the dimensions with/without the locations of bolting holes of the aluminum case, left steel channel and right steel box in three different views. Especially, the different patterns of bolting holes on the left side and the right side of the right steel box are presented in Figure A.4. Since an existing spool in the laboratory was used for the testing set-up, the details of the spool are not presented. 12.7 mm (0.5 in) diameter bolts were used for the bolting connections.

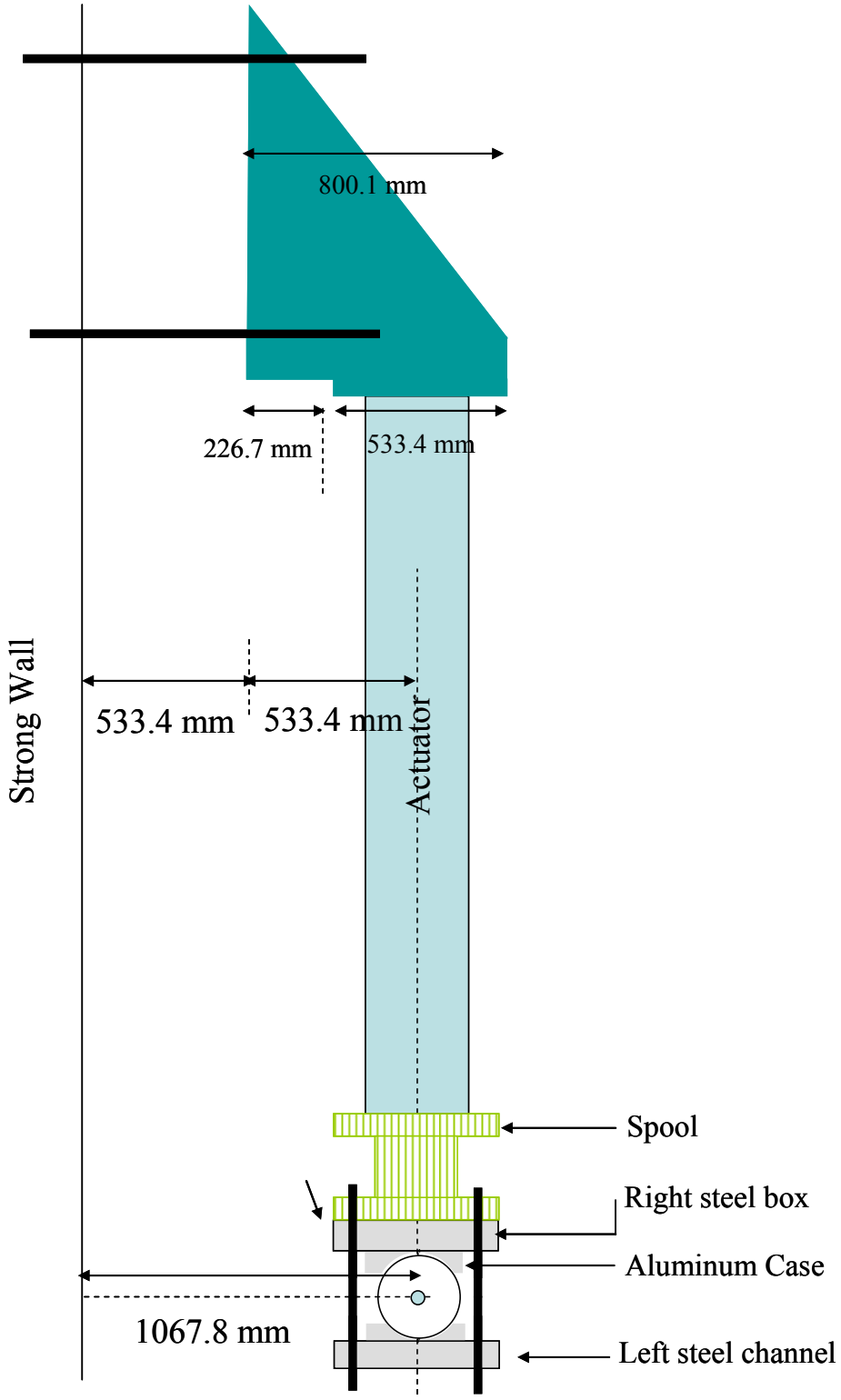

Figure A.1 Top view of the column testing set-up with details of fixture plates.

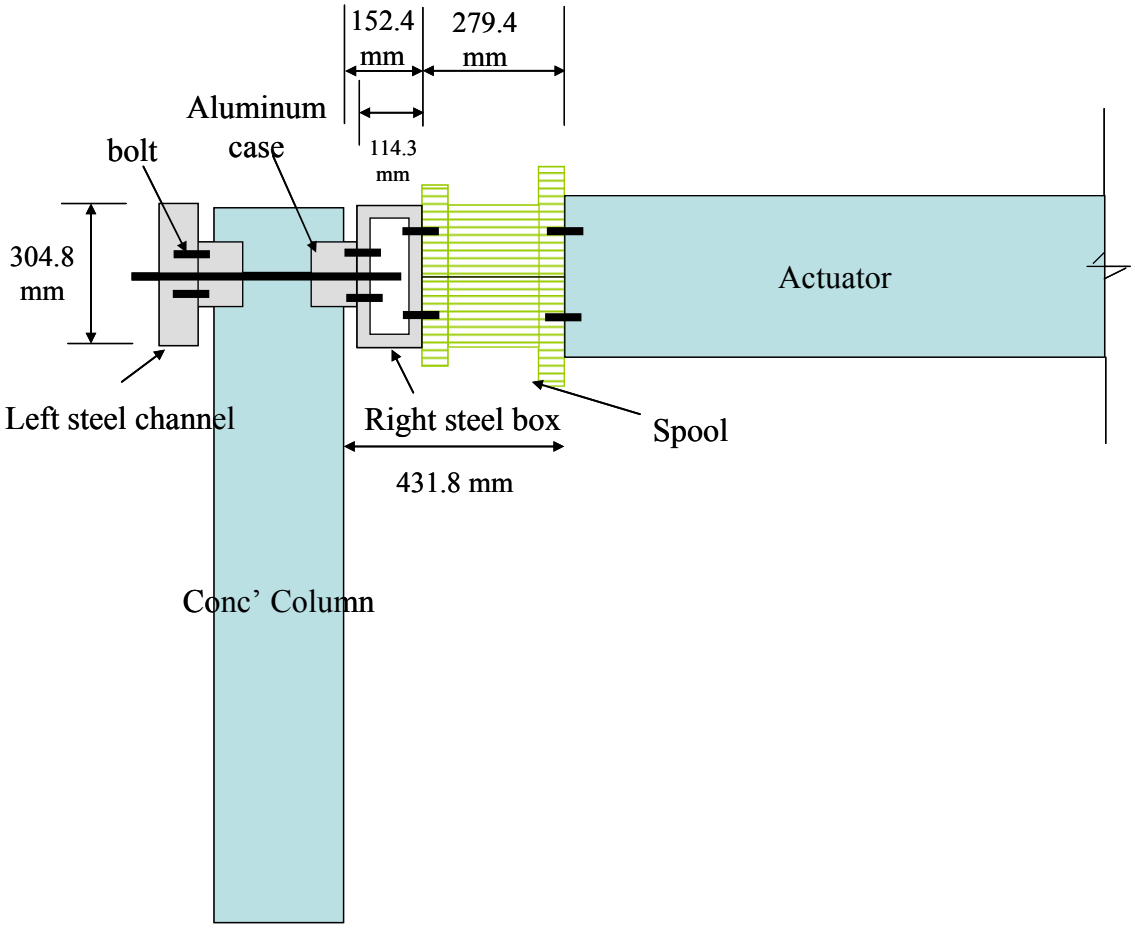

Figure A.2 Front view of the column testing set-up with details of fixture plates.

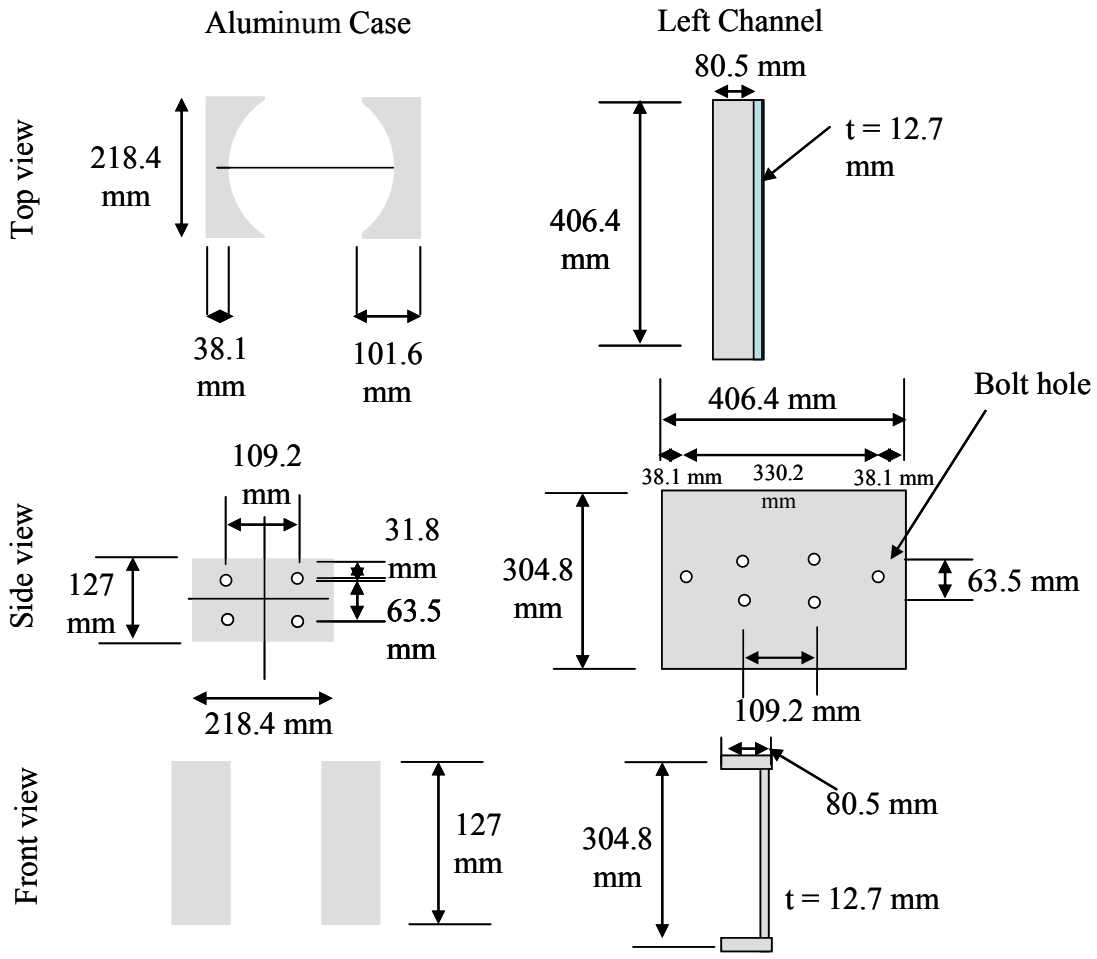

Figure A.3 Detail drawings of aluminum case and left steel channel.

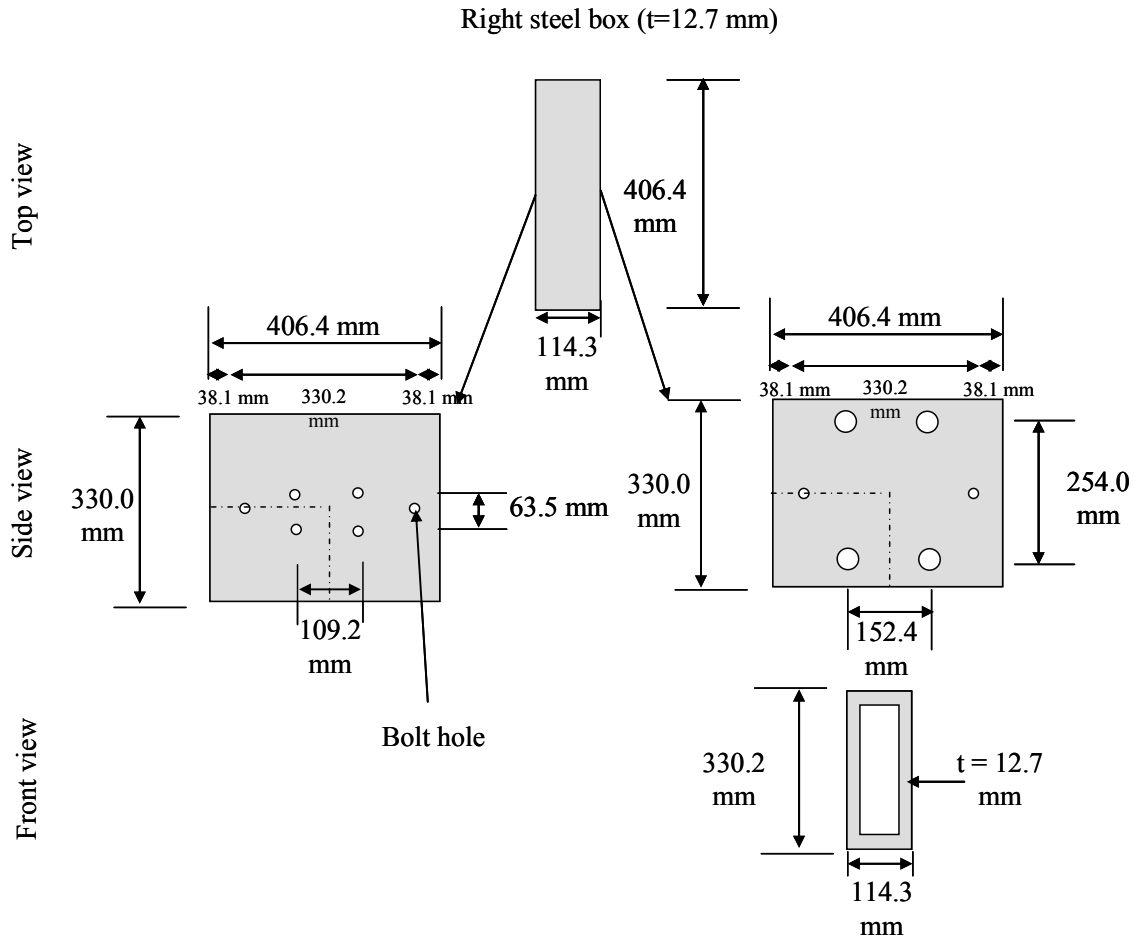

Figure A.4 Detail drawings of right steel box.

REFERENCES

AASHO (1969) "Standard Specifications for Highway Bridges." *American Association of State Highway Officials,* 10th. Edition, Washington, D.C.

Ahmad, S. H. and Shah, S. P. (1982). "Stress-strain curves of concrete confined by spiral reinforcement." *ACI Journal*, 79(6), p.484–490.

Andrawes, B. (2005). "Seismic response and analysis of multiple frame bridges using superelastic shape memory alloys." Ph.D. Thesis, Georgia Institute of Technology, GA

Andrawes, B., Shin, M., and Wierschem, N. (2010) "Active Confinement of Reinforced Concrete Bridge Columns Using Shape Memory Alloys." *J. Bridge Eng.,* 15(1),81-89.

Aviram, A., Mackie, K.R., and Stojadinovic, B. (2008). "Guidelines for Nonlinear Analysis of Bridge Structures in California." Pacific earthquake engineering research center PEER2008/03.

Balmer, G. G. (1949). "Shearing strength of concrete under high triaxial stress - computation of Mohr's envelope as a curve." *Structural Research Laboratory Report SP-23, Bureau of Reclamation,* Research and Geology Division, Denver, Colorado.

Balsamo, A., Colombo, A., Manfredi, G., Negro, P., and Prota, A. (2005). “Seismic behavior of a full-scale RC frame repaired using CFRP laminates.” *Engineering Structures*, 27, p.769–780.

Bellamy, C. J. (1961). “Strength of concrete under combined stress.” *Journal of the American Concrete Institute,* 58(4),p.367–380.

Benson, R.W., Flot, R.F. and Sandburg, C.L. (1983). "The use of shape memory effect allloy as an engineering material." *15th National SMAPE technical Conference*

Besselink, P.A. (1997), "Recent Developments on Shape Memory Applications." *J. PHYS. IV FRANCE 7*, p.581-590

Bett, B.J., Klingner, R.E., and Jirsa, J.O. (1988). “Lateral Load Response of Strengthened and Repaired Reinforced Concrete Column.” *ACI Structural J.* 499-508.

Cai, W., Lu,X.L. and Zhao, L.C. (2005). "Damping behavior of TiNi-based shape memory alloys." *Materials Science and Engineering,* A 394,p.78–82.

Cai, W., Zhang, C. and Zhao L. (1994). “Recovery Stress in a Ni-Ti-Nb Shape Memory Alloy with Wide Transformation Hysteresis.” *J. Mater. Sci. Technol.,* 10, p27-30.

Caltrans (2008). “Bridge design aids” California Department and Transportations.

Caltrans (2009). “Seismic Design Criteria.” California Department and Transportations.

Carey, S.A. and Harries, K.A. (2005). “Axial Behavior and Modeling of Small-, Medium- and Large-Scale Circular Sections Confined with CFRP Jackets.” *ACI Structures Journal*, 102(4), p.596-604.

Chai,Y.H., Priestley, M.J.N., and Seible, F. (1991). “Seismic retrofit of circular bridge columns for enhanced flexural performance.” *ACI Strut. J.*, 88(5), p.572-584.

Chang, G.A. and Mander, J.B. (1994). “Seismic Energy Based Fatigue Damage Analysis of Bridge Columns: Part I – Evaluation of Seismic Capacity.” *Technical Report NCEER-94-0006,* National Center for Earthquake Engineering Research, State University of New York at Buffalo.

Chen, W.F. (1982). “Plasticity in Reinforced Concrete.” McGraw-Hill Book Company.

Cho, C., Kwon, M., and Spacone, E. (2005). “Analytical model of concrete filled fiber reinforced polymer tubes based on multiaxial constitutive laws.” *J. Struc. Eng., ASCE,* 131(9), p.1426-1433.

Chopra A.K. (2000). “Dynamics of Structures: Theory and Applications to Earthquake Engineering.” *Prentice-Hall: Englewood Cliffs, 2nd ed.,* NJ.

Daudey, X. and Filiatrault, A. (2000). “Seismic evaluation and retrofit with steel jackets of reinforced concrete bridge piers detailed with lap-splices.” *Can. J. Civ. Eng*., 27, p.1–16.

Demers, M., and Neale, K. W. (1999). “Confinement of reinforced concrete columns with fiber-reinforced composite sheets—An experimental study.” *Can. J. Civ. Eng.*, 26(2), p.226–241.

Dong, Z., Zhou, S. and Liu, W. (2002). “A study of NiTiNb shape-memory alloy pipe joint with improved properties.” *Material Science Forum (Switzerland),* 394-395, p.107-110.

Duerig, T.W. (1990). "Application of Shape Memrory." *Materials Science Forum,* 56-58, p.679-672

Duerig, T.W., Melton K.N. and Proft, J.L. (1990). “Wide Hysteresis Shape Memory Alloys (*In Engineering Aspects of Shape Memory Alloys*)” p.130- 136.

Duerig, T.W., Pelton, A.R., Sto¨ckel, D. (1999). "An overview of nitinol medical applications." *Mater Sci Eng A*, 273–275, p.149–160.

Duerig, T., Pelton, A. and Trepanier, C. (2011). "Part I: Mechanisms and Behavior: Chapter 9 Alloying and Composition." *Nitinol,* 2011 ASM Internaional.

EERI, Peer, FHWA. (2010). “Performance of highway and railway structures during the February 27, 2010 Maule Chile Earthquake.”

Eid, R. and Paultre, P. (2008). “Analytical Model for FRP-Confined Circular Reinforced Concrete Columns.” *J. OF Composites for Construction,* 12(5), p.541-552.

Eid, R., Roy, N., and Paultre, P. (2006). “Tests of axially loaded circular reinforced concrete columns strengthened with FRP sheets.” *CRGP Rep. No. 2006–03, Dept. of Civil Engineering,* Univ. of Sherbrooke, Sherbrooke, Quebec.

Elnashai, A.S. and Sarno L.D. (2008). “Fundamentals of Earthquake Engineering.” John Wiley and Sons LTD, West Sussex, United Kingdom.

Fardis, M.N. and Khalili, H.H. (1981). “Concrete encased in fiber glass reinforced plastic.” *ACI J*., 78(6), p.440-446.

FHWA (2004). “FHWA’s Recommendations of Seismic Performance Testing on Bridge Piers.” U. S. Department of Transportation Federal Highway Administration.

fib. (2003). “Seismic assessment and retrofit of reinforced concrete buildings.” *Bulletin 24*, Lausanne.

fib (2007) “Seismic bridge design and retrofit - structural solutions.” *Bulletin 39,* Lausanne.

Fu, X., Guojun, M., Xinqing, Z. and Huibin, X. (2009). “Effects of Nb Content on Yield Strength of NiTiNb Alloys in Martensite State.” *Chinese J. Aeronatics*, 22, p.658-662.

Fukuyama, K., Higashibata, Y., and Miyauchi, Y. (2000). “Studies on repair and strengthening methods of damaged reinforced concrete columns.” *Cement & Concrete Composites,* 22, p81-88.

Gamble, W. L., Hawkins, N. M., and Kaspar, I. I. (1996) “Seismic retrofitting experience and experiments in Illinois,” *Proceedings of 5th National Workshop on Bridge Research in Progress*, National Center for Earthquake Engineering Research (NCEER), State University of New York at Buffalo, Buffalo, NY., p.245-250.

Haroun, M.A. and Elsanadedy, H.M. (2005) "Fiber-Reinforced Plastic Jackets for Ductility Enhancement of Reinforced Concrete Bridge Columns with Poor Lap-Splice Detailing." *J. Bridge Eng.* , 10(6), 749-757.

Harrison, J.D. and Hodgson, D.E. (1975). "Shape memory effects in alloys." J. Perkins, ed., Plenum Press, p.517

Hawkins, G.F., Patel, N.R., Steckel, G.I., and Sultan, M. (1996), “Failure Analysis of Highway Bridge Column Composite Overwraps.” *Fiber Composites in*

Infrastructure, First intl. Conference on Composites in Infrastructure, ICCI 96, Tucson, AZ.

Hirano, T., Teraki, J. and Yamada T., (1991). "Application of fuzzy theory to the design of functionally gradient materials." *SMiRT 11 Transactions*, SD1, p.49–54.

Humbeeck, J.V., and Stalmans R. (1998), "in Shape Memory Materials (Eds: K. Otsuka, C. M. Wayman)" *Cambridge University Press*, Cambridge , Ch. 7, p. 149-183.

Hussain, M.A., and Driver, R.G. (2005). "Experimental investigation of external confinement of reinforced concrete columns by hollow structural section collars." *ACI Structural J.*, 102(2), p.242-251.

Janke, L, Czaderski, C., Motavalli, M, and Ruth, J. (2005). "Applications of shape memory alloys in civil engineering structures - Overview, limits and new ideas." *Materials and Structures,* 38, p.578-592.

Jennings, P.C. et al. (1971). "Earthquake Features of the San Fernando Earthquake of February 9, 1971." *EERL 71-02 Report,* Pasadena, CA.

Karsan, I. D., and Jirsa, J. O. (1969). "Behavior of concrete under compressive loading." *Journal of Structural Division ASCE*, 95 (ST12).

Kawashima, K. (2009) “Seismic damage in the past earthquakes.” Chapter 3 – Lecture note, http://seismic.cv.titech.ac.jp/common/PDF/lecture/seismic_design/2009/Chapter3_text.pdf.

Kawashima, K., Hosotani, M., and Yondea, K., (2001) “Carbon fiber sheet retrofit of reinforced concrete bridge piers toward new generation seismic design methodology of bridges.” *Tokyo Institute of Technology*, Tokyo.

Kent, D. C , and Park, R. (1971). "Flexural members with confined concrete." *J. Struct. Div., ASCE,* 97(7), 1969-1990.

Kim, S.J., Holub, C. and Elnashai, A.S. (2011). “Analytical assessment of the effect of vertical earthquake motion on RC bridge piers.” J. Struct. Engrg. (ASCE) 2011, 137(2), 252-260.

Krstulovic-Opara, N., and Thiedeman, P.D. (2000). “Active confinement of concrete members with self-stressing composites.” *ACI Materials J.*, 97(3), p.297-308.

Kupfer, H., Hilsdorf, H. K., and Rusch, H. (1969). “Behavior of concrete under biaxial stresses.” *ACI Journal*, 66,p.656–666.

Kupfer, H. B. and Gerstle, K. H. (1973). “Behavior of concrete under biaxial stresses.” *Journal of the Engineering Mechanics Division,* 99,p.853–866.

Lam, L., and Teng, J. G. (2003). "Design-oriented stress-strain model for FRP-confined concrete." *Constr. Build. Material*, 17(6–7), p. 471–489.

Lam, L., and Teng, J. G. (2004). "Ultimate condition of fiber reinforced polymer-confined concrete." *J. Compos. Constr.*, 8(6), p.539–548.

Launay, P. and Gachon, H. (1972). "Strain and ultimate strength of concrete under triaxial stress." *Concrete for Nuclear Reactors,* p.269–282.

Lehman, D.E., Gookin, S.E., Nacamuli, A.M., and Moehle, J.P. (2001). "Repair of Earthquake-Damaged Bridge Columns." *ACI Structural J.,* 98, p.233-242.

Li, Y.F., Chen, S.H. , Chang, K.C. and Liu, K.Y. (2005). "A constitutive model of concrete confined by steel reinforcements and steel jackets." *Can. J. Civ. Eng.*, 32, p.279–288.

Lorenzis, L.D. and Tepfers, R.(2003). "Comparative Study of Models on Confinement of Concrete Cylinders with Fiber-Reinforced Polymer Composites." *J.Composite for Construction, ASCE,* 7(3), p. 219-237.

Madas, P. and Elnashai, A.S. (1992). "A new passive confinement model for concrete subjected to cyclic and transient dynamic loading." *Earthquake eng. struct. dyn.*, 21, p.409-432.

Maekawa, K., and An, X. (2000) "Shear failure and ductility of RC columns after yielding of main reinforcement." *Eng. Fracture Mechanics*, 65(2), p.335-368.

Malvar, L.J., Crawford, J.E. and Wesevich, J.W. (1994). "A New Concrete Material Model for DYNA3D," *Report TM 94-14* to the Defense Nuclear Agency, Karagozian and Case, CA.

Malvar, L.J., Crawford, J.E. and Wesevich, J.W. (1997). "A Plasticity Concrete Material Model for DYNA3D." *Int. J. Impact Eng*., 19, p.847-873.

Malvar, L.J., Morrill, K.B., and Crawford, J.E. (2004) "Numerical modeling of concrete confined by fiber-reinforced composites." *J. Composites for Construction, ASCE*, 8(4), p.315-322.

Mander, J. B., Priestley, M. J. N., and Park, R. (1988a). "Theoretical stress-strain model for confined concrete." *Journal of Structural Engineering*, 114(8):1804–1826.

Mander, J. B., Priestley, M. J. N., and Park, R. (1988b). "Observed stress-strain behavior of confined concrete. "*Journal of Structural Engineering,* 114(8):1827–1849.

Martlnez-Rueda, E. and Elnashai, A.S. (1997). "Confined concrete model under cyclic load." *Materials and Structures/Matrix Constructions*, (30), p.139-147.

Mazzoni, S., McKenna, F., Scott, M.H. and Fenves, G.L. et al. (2009) “OpenSees Command Language Manual.” Open System for Earthquake Engineering Simulations

Melton, K.N., Simpson, J. and Duerig, T.W. (1986). In Proc. ICOMAT-86, Int. Conf. on Martensitic Transformations, 1053

Menegotto, M. and Pinto, P.E. (1973). “Method of analysis of cyclically loaded RC plane frames including changes in geometry and non-elastic behavior of elements under normal force and bending.” *Preliminary Report IABSE* 13, p.15–22.

Mills, L. L. and Zimmerman, R. M. (1970). “Compressive strength of plain concrete under multiaxial loading conditions.” *ACI Journal*, 67(10),p.802–807.

Mirmiran, A., and Shahawy, M. (1997). "Dilation characteristics of confined concrete." *Mech. of Cohesive-Frictional Mat., Int. J.*, 2(3), 237-249.

Miyazaki, S. (1998). "Medical and dental applications of shape memory alloys." In: Shape Memory Materials, Cambridge, Cambridge University Press, p.267–281.

Moehle, J.P. (2000). “State of research on seismic retrofit of concrete building structures in the US.” *In US–Japan symposium and workshop on seismic retrofit of concrete structures.*

Monti, G., and Spoelstra, M. R. (1997). "Fiber-section analysis of RC bridge piers retrofitted with FRP jackets." *Proc. Struct. Congress, ASCE*, Portland, OR, p.884-888.

Nesheli, K.N., and Meguro, K. (2006). "Seismic retrofitting of earthquake-damaged concrete columns by lateral pre-tensioning of FRP belts." *Proceedings of the 8th. U.S. National Conferenceon Earthquake Engineering,* April 18-22, 2006, San Francisco, CA., USA, Paper no. 841.

OpenSees (2010). Steel02 Material http://opensees.berkeley.edu/wiki/index.php/Steel02_Material_--Giuffr%C3%A9-Menegotto-Pinto_Model_with_Isotropic_Strain_Hardening

Otsuka, K. and Ren X. (1999). "Recent developments in the research of shape memory alloys." *Intermetallics*, 7, p.511–528.

Otsuak, K. and Wayman, C.M.(2002). "Shape memory material." *Cambridge University Press,* New edition.

Park, R., Priestley, M. J. N., and Gill, W. D. (1982). "Ductility of square-confined concrete columns." *J. Struct. Div., ASCE,* 108(4), p.929-950.

Popovics, S. (1973). "A numerical approach to the complete stress strain curve for concrete." *Cement and concrete research*, 3(5), 583-599.

Priestley, M.J.N., Seible, F., Xiao, Y., and Verma, R. (1994a). "Steel Jacket Retrofitting of Reinforced Concrete Bridge Columns for Enhanced Shear Strength—Part 1: Theoretical Considerations and Test Design." *ACI Structural Journal*, 91(4), p.394-405.

Priestley, M.J.N., Seible, F., Xiao, Y., and Verma, R. (1994b). "Steel Jacket Retrofitting of Reinforced Concrete Bridge Columns for Enhanced Shear Strength— Part 2: Test Results and Comparison with Theory." *ACI Structural Journal*, 91(5), p.537-551.

Priestley, M. J. N. and Seible, F. (1995). "Design of seismic retrofit measures for concrete and masonry structures." *Construction and Building Materials*, 9(6), 365-377.

Reiter, T. and Dvorak, G.J., (1998). "Micromechanical models for graded composite materials: II. Thermomechanical loading." *J. Phys. Solids*, 46(9), p.1655–1673.

Richart, F.A., Brandtzaeg, A. and Brow, R. L. (1928) "A study of the failure of concrete under combined compressive stress." *Bulletin 185, University of Illinois Engineering Experiment Station*, Urbana IL.

Richart, F. E., Brandtzaeg, A., and Brown, R. L. (1929). “The failure of plain and spirally reinforced concrete in compression.” *Technical Report Bulletin No. 190, Engineering Experiment Station,* University of Illinois, Urbana. IL

Roy, H. E. H., and Sozen, M. A. (1964). "Ductility of concrete." *Proc. Int. Symp. on the Flexural Mech. of Reinforced Concrete, ASCE-American Concrete Institute*, p.213-224.

Saatcioglu, M., and Yalcin, C. (2003) “External prestressing concrete columns for improved seismic shear resistance.” *J. Struct. Eng., ASCE*, 129(8), p.1057-1070.

Sadaamantesh, H., Ehsani, M.R, and Li, M.W. (1994). “Strength and ductility of concrete columns externally reinforced with fiber composite sheets”, *ACI Structural Journal,* 91(4), p.434-447.

Saadatmanesh, H., Ehsani, M.R., and Jin, L. (1997). “Repair of Earthquake-Damaged RC Columns with FRP Wraps.” *ACI Structural J.,* 94,p.206-214.

Saiidi, M. S., Sureshkumar, K., and Pulido C. (2005) “Simple carbon-fiber-reinforced-plastic-confined concrete model for moment-curvature analysis.” *J. Composites for Construction,* 9(1), p.101-104.

Samaan, M., Mirmiran, A. and Shahawy M. (1998) "Model of concrete confined by fiber composites." *Journal of Structural Engineering, ASCE,* 124, p.1025-1031.

Schickert, G., and Winkler, H. (1977). "Results of tests concerning strength and strain of concrete subjected to multiaxial compressive stresses." Deutscher Ausschuss fur Stahlbeton, Heft 277, Berlin, West Germany.

Scott, B. D., Park, R. and Priestley, M. J. N. (1982). "Stress-Strain Behavior of Concrete confined by Overlapping Hoops at Low and High Strain Rates" *ACI,* 79(1), p.13-27.

Scott, M. and Fenves, G. (2006). "Plastic Hinge Integration Methods for Force-Based Beam–Column Elements." *J. Struct. Eng.*,132(2), p.244-252.

Shanmuganathan, S. (2005). "Performance of highway bridges under Chuetsu Earthquake, Japan." *2005 NZSEE Conference,* Tsukuba-shi, Japan

Sheikh, S.A. and Uzumeri, S.M., (1979) "Properties of Concrete Confined by Rectangular Ties" *Bulletin 132*, C.E.B. Paris .

Shin, M. and Andrawes, B. (2010). ""Experimental investigation of actively confined concrete using shape memory alloys." *Engineering Structures*, 32(3), p.656-664.

Southern California Earthquake Data Center (2011) http://www.data.scec.org/significant/northridge1994.html#e

Spoelstra, M.R, and Monti, G. (1999). "FRP confined concrete model." *Journal of composites for construction, ASCE,* 3 (3), p.143-150.

Stice, J. (1990). "The use of superelasticity in guidewires and arthroscopic instruction." In: Engineering Aspects of Shape Memory Alloys, London, Butterworth-Heinemann, p.483–487.

Tadaki, T., Otsuka, K. and Shimizu, K. (1988). "Shape memory alloys." *Ann. Rev. Material Sci.*, 18, p.25-45.

Takagi, T., Sutou, Y., Kainuma, R.,Yamauchi, K. and Ishida, K. (2005). "Effect of Prestrain on Martensitic Transformation in a $Ti_{46.4}Ni_{47.6}Nb_{6.0}$ Superelastic Alloy and its Application to Medical Stents." *Journal of Biomedical Materials Research Part B: Applied Biomaterials*, 76B(1), p.179-183.

Toutanji H. A. (1999). "Stress-Strain characteristics of concrete columns externally confined with advanced fiber composite sheets." *ACI Materials Journal*, 96(3), p.397-404.

USGS photographic library (2006a)

http://libraryphoto.cr.usgs.gov/htmllib/batch34/batch34j/batch34z/kach0024.jpg

USGS photographic library (2006b)

http://libraryphoto.cr.usgs.gov/cgi-bin/show_picture.cgi?ID=ID.%20Wilshire,%20H.G.%20%203ct

USGS (2010) http://earthquake.usgs.gov/earthquakes/world/events/1995_01_16.php

USGS (2011)

http://earthquake.usgs.gov/earthquakes/eqinthenews/2010/us2010tfan/#summary

Vellenas, J. Bertero, V.V., and Popov, E. (1977) "Concrete confined by rectangular hoops subjected to axial loads." *Report 77/13, Earthquake Engineering Research Center,* University of California, Berkley, CA.

Vokoun, D., Kafka, V., and Hu, C.T. (2003) “Recovery stresses generated by NiTi shape memory wires under different constraint conditions.” *Smart Material Structures,* 12, 680–685.

Vosooghi, A, Saiidi, M.S., and Gutierrez, J. (2008). “Rapid repair of RC bridge columns subjected to earthquakes.” *Proceedings of 2nd International Conference on*

Concrete Repair, Rehabilitation, and Retrofitting (ICCRRR 2008), Cape Town, South Africa

Walpole, R.E., Myers, R.H., Myers, S.L., and Ye K. (2008). "Probability and Statistics for Engieering and Scientists." 8th ed. Pearson Prentice Hall, NJ.

Wang, L., Rong, L.J., Yan, D.S., Jiang, Z.M. and Li, Y.Y. (2005). "DSC study of the reverse martensitic transformation behavior in a shape memory alloy pipe-joint." *Intermetallics*, 13,p.403–407

Wayman, C.M. and Duerig, T.W. (1990). "An Introduction to Martensite and Shape Memory (in *Engineering Aspects of Shape Memory Alloys).*", p.3-20.

Wei, L., and Xinqing, Z. (2009). "Mechanical Properties and Transformation Behavior of NiTiNb Shape Memory Alloys." *Chinese Journal of Aeronautics*, 22, p.540-543.

Willam, K. J. and Warnke, E. P. (1975). "Constitutive model for the triaxial behavior of concrete." *In Proceedings of the International Association for Bridge and Structural engineering: Seminar on Concrete Structures Subjected to Triaxial Stress,* Bergamo, Italy, 19. p.1-30.

Wolf, J. (2008). "A plasticity model to predict the effects of confinement on concrete." *Ph.D Thesis,* California Institute of Technology Pasadena, California.

Wu, M.H. and Schetky, L. McD. (2000). "INDUSTRIAL APPLICATIONS FOR SHAPE MEMORY ALLOYS." *Proceedings of the International Conference on Shape Memory and Superelastic Technolgies*, Pacific Grove, California, p.171-182.

Wu, T. and Wu, M.H. (2000). "NiTiNb PLUGS FOR SEALING HIGH PRESSURE FUEL PASSAGES IN FUEL INJECTOR APPLICATIONS." *Proceedings, International Conference on Shape Memory and Superelastic Technologies (SMST-2000),* Pacific Grove, California, p.235

Xiao, Y., and Wu, H. (2000). "Compressive behavior of concrete confined by carbon fiber composite jackets." *J. Mater. Civ. Eng.*, 12(2), p.139–146.

Xiao, Y. and Wu, H. (2003). "Retrofit of reinforced concrete columns using partially stiffened steel Jackets." *Journal of Structural Engineering*,129(6), p.725-732.

Yamakawa, T., Banazadeh, M., and Fujikawa, S. (2004). "Emergency retrofit of damaged RC columns right after seismic attack using pre-tensioned aramid fiber belts." *1st Conference on Applications of FRP Composites in Construction and Rehabilitation of Structures,* May 4, 2004, Tehran, Iran.

Yin, H.M., Sun, L.Z., and Paulino, G.H. (2004). "Micromechanics-based elastic model for functionally graded materials with particle interactions." *Acta Materialia*, 52, p.3535-3543.

Youm, K.S., Lee, H.E. and Choi, S. (2006). "Seismic performance of repaired RC columns." *Magazine of Concrete Research*, 58, p.267–276.

Zhao, J., and Sritharan, S. (2007). "Modeling of strain penetration effects in fiber-based analysis of reinforced concrete structures." *ACI Structural Journal*, 104(2), 133-141.

Zhao, X., Yan, X., Yang, Y., Xu, H. (2006). "Wide hysteresis NiTi(Nb) shape memory alloys with low Nb content (4.5at.%)." *Materials Science & Engineering A (Structural Materials: Properties, Microstructure and Processing)*, 438-440, p.575-578.